AURORAE OF IO AND EUROPA: OBSERVATIONS AND MODELING

INAUGURAL-DISSERTATION
ZUR
ERLANGUNG DES DOKTORGRADES
DER MATHEMATISCH-NATURWISSENSCHAFTLICHEN FAKULTÄT
DER UNIVERSITÄT ZU KÖLN

VORGELEGT VON
LORENZ ROTH
AUS MÜNCHEN

KÖLN 2012

Berichterstatter:	Prof. Dr. Joachim Saur
	Prof. Dr. Bülent Tezkan

Tag der mündlichen Prüfung: 11.10.2012

Abstract

In the present dissertation we study the auroral emissions emanating from the tenuous atmospheres of Jupiter's satellites Io and Europa. The satellites are embedded in a dense magnetospheric plasma environment. Due to Jupiter's fast rotation the corotating magnetospheric plasma particles constantly flow past Io and Europa causing a complex interaction and triggering auroral emission in the atmospheres. Therefore, aurora observations are a useful tool to explore both the magnetospheric environment and the neutral gas clouds of the satellites. For our analysis, images of Io's and Europa's ultraviolet (UV) emissions are extracted from a large data set of observations by the Space Telescope Imaging Spectrograph (STIS) of the Hubble Space Telescope (HST). Additionally, high-resolution images taken by the Long-Range Reconnaissance Imager (LORRI) of the New Horizons spacecraft of Io's visible aurora and a simultaneous observation by the HST Advanced Camera for Surveys (ACS) are examined.

Io's aurora is characterized by bright emissions on the sub-Jovian and anti-Jovian flanks close to the equator and a fainter limb glow around the polar regions. Analyzing the STIS images we demonstrate that the variations of Io's UV aurora observed over a period of five years can be attributed to changes in the magnetospheric environment as well as to the varying viewing perspective. Based on these findings, an analytical model for the three-dimensional distribution of the UV emission around Io is developed. By fitting the parameters of this phenomenological model to the STIS observations, we are able to derive universal, quantitative properties of the emission distribution. Thereby, we find that the aurora above the sunlit part of Io's surface is brighter than on the night side or during an eclipse event, when Io moves through Jupiter's shadows. By comparing the LORRI and ACS observations of Io's aurora in eclipse to results from a three-dimensional two-fluid plasma simulation model, we show that the reduced auroral brightness originates from a lowered atmospheric density. Our results are a strong indication, that Io's atmosphere is driven by sublimation of SO_2 frost rather than direct volcanic outgassing. The ultimate source for Io's atmospheric gas is widely debated for many years.

We also investigate the observed variation or rocking of the bright auroral spots around Io's equator. The location of the spots has been shown to be correlated to the Jovian magnetic field orientation at Io. The exact correlation is, however, not 1:1, but is presumably affected by local perturbations of the magnetic field. Therefore, we analyze the influence of the magnetic field perturbations due to the plasma interaction as well as due to induced fields from Io's interior on the expected variations of the aurora spots. According to our calculations, the observed rocking of the aurora is not consistent with a conductive magma ocean below Io's surface. A rough estimation of the plasma interaction effects on the auroral spots does not yield conclusive results.

Furthermore, we examine the morphology and brightness of the OI 1304 Å and OI] 1356 Å emissions in the STIS observations of Europa's UV aurora. We find that most emission is observed on the disk of Europa rather than around the limb like in comparable observations of Io's aurora. We show that an increasing O_2 density towards the sub-solar point possibly explains the observed morphology as well as previous observations. While the OI] 1356 Å emission pattern appears to vary periodically in correlation with the changing magnetospheric environment, the OI 1304 Å morphology is clearly dominated by a very bright locally confined emission in the northern, anti-Jovian quadrant of Europa's disk. The location of this anomaly coincides exactly with the longitude, where a peak in water vapor production is predicted due to increased shear heating at the surface cracks. Estimating the emission brightnesses expected for a local water plume, we find that the observed UV emission intensities are principally consistent with a locally confined abundance of water vapor with a column density of $N_{H_2O} = 2.6 \times 10^{16}$ cm^{-2}. However, due to observational uncertainties and since we have neglected the effects of the plasma interaction for the approximation of the H_2O abundance, our results can not be seen as prove for the existence of water plumes on Europa. To accurately determine the effects of an asymmetric O_2 atmosphere and the influence of a local water plume, the plasma interaction has to be simulated.

Zusammenfassung

Die vorliegende Dissertation beschäftigt sich mit Beobachtungen der Auroraerscheinungen bei den Jupitermonden Io und Europa. Die beiden Monde befinden sich tief in der riesigen Magnetosphäre Jupiters und sind in eine dichte Plasmaumgebung eingebettet. Das Plasma rotiert in Verbindung mit dem Magnetfeld mit der Rotationsperiode des Planeten und umströmt somit stetig die langsamer kreisenden Monde. Durch die Stöße der Plasmateilchen mit der Atmosphäre entsteht eine komplexe Wechselwirkung. Zudem werden die Atmosphären der Monde durch Stöße mit den vorbeiströmenden Elektronen zum Leuchten angeregt. Die Auswertung von Beobachtungen dieser Leuchterscheinungen liefert daher interessante Einblicke sowohl in die plasmaphysikalischen Prozesse in der Umgebung also auch in die Natur der Atmosphären der Monde. Zur Untersuchung der Auroraerscheinungen extrahieren wir Abbildungen der Ultraviolettemissionen von Io und Europa aus einer Reihe von Beobachtungen des Space Telescope Imaging Spectrograph (STIS) an Bord des Hubble Space Telescope (HST). Die Prozessierung der STIS Beobachtungen beinhaltet den Abzug der Hintergrundstrahlung sowie des am Mond reflektierten Sonnenlichts. Zusätzlich untersuchen wir hochaufgelöste Bilder von Ios Aurora im sichtbaren Wellenlängenbereich, die vom Long-Range Reconnaissance Imager (LORRI) der Raumsonde New Horizons aufgenommen wurden, in Kombination mit einer zeitgleichen UV-Beobachtung der Advanced Camera for Surveys (ACS) des Hubble Space Telescope.

Die Atmosphäre von Io besteht zu großen Teilen aus Schwefeldioxid (SO_2). Eine bislang ungeklärte Frage ist der genaue Entstehungsmechanismus der Atmosphäre. Verschiedenen Studien zufolge ist die Hauptquelle entweder Sublimation von Schwefeldioxidablagerungen auf der Oberfläche, oder aber die Atmosphäre wird direkt von vulkanischen Ausgasungen gespeist (*Lellouch et al.* 2007). Die Emissionen aus Ios Atmosphäre im Bereich von Ultraviolettstrahlung (UV) bis hin zu Strahlung im sichtbaren und infraroten Bereich wurden bereits von verschiedenen Teleskopen und Raumfahrzeugen beobachtet und untersucht (siehe z.B. *Roesler et al.* 1999, *Geissler et al.* 1999, 2004). In den meisten Beobachtungen ergibt sich ein Strahlungsmuster, das von zwei hellen Punkten in der Nähe des Äquators am linken und rechten Rand der in den Beobachtungen abgebildeten Scheibe des Mondes dominiert ist. Die Entstehung dieser hellen Aurora-Punkte ist auf die Umlenkung der anströmenden Elektronen aufgrund von ionosphärischen Strömen zurückzuführen (*Saur et al.* 2000). Die Lage dieser Punkte wiederum schwankt periodisch in Verbindung mit den Schwankungen des Jupitermagnetfeldes am Ort von Io (*Retherford et al.* 2000, *Geissler et al.* 2001). Außerdem wird bei Io ein heller schmaler Bereich am Rand der Mondscheibe beobachtet, den man als *limb glow* bezeichnet. Die Helligkeit dieses *limb glow* auf der nördlichen und südlichen Hemisphäre ist gekoppelt an das Energiereservoir der Elektronen oberhalb und unterhalb von Io (*Retherford et al.* 2003).

Mit einer genauen Analyse der STIS UV-Beobachtungen von Io, die in einem Zeitraum von fünf Jahren aufgenommen wurden, können wir nachweisen, dass die Variationen des beobachteten

Strahlungsmusters überwiegend auf die Änderungen der magnetosphärischen Umgebung sowie den jeweiligen Beobachtungswinkel zurückgeführt werden können. Darauf basierend entwickeln wir ein analytisches Modell für die räumliche Verteilung der Strahlung in der Umgebung des Mondes. Mithilfe des Modells können wir künstliche Strahlungsbilder erstellen, die wir durch Variation der Modellparameter an die Beobachtungen anpassen. Dabei leiten wir einen Parametersatz für das Modell ab, mit dem die modellierten Strahlungsbilder alle wesentlichen Merkmale der Beobachtungsbilder bestmöglich reproduzieren und bestätigen damit die zeitliche Beständigkeit von Ios UV-Aurora. Dadurch dass unser Modell durch die Berücksichtigung der Variation der magnetosphärischen Bedingungen universell gültig ist, ist es sogar möglich, die erwarteten Strahlungsmuster für zukünftige Beobachtungen vorherzusagen.

Aus den angepassten Modellparametern leiten wir zusätzlich eine Reihe quantitativer Eigenschaften der Verteilung und Intensität der Aurora ab. Die abgeleitete Ausdehnung der Äquatorpunkte sowie die radiale Abnahme der globalen Komponente der Strahlung zeigen, dass ein Großteil der Strahlung innerhalb von 100 km oberhalb der Oberfläche emittiert wird. Wir zeigen zudem, dass sich die Äquatorpunkte weit in den Schweifbereich des Mondes erstrecken, wodurch Strahlungsmerkmale, die als *wake emission* bezeichnet werden, erklärt werden können. Die gemessene relative Helligkeit der beiden Äquatorpunkte zueinander deuten auf einen systematischen Helligkeitsunterschied der Emission zwischen der sonnenzugewandten und sonnenabgewandten Hemisphäre hin. STIS-Beobachtungen der Aurora während einer Io-Finsternis, wenn der Mond sich im Kernschatten Jupiters befindet, weisen im Vergleich zu Beobachtungen im Sonnenlicht eine deutlich geringere Strahlungsintensität auf. Sowohl die abgeschwächte Intensität auf der Nachtseite, also auch die niedrige Helligkeit in totaler Finsternis deuten auf einen deutlichen Rückgang des Neutralgasvorkommens im Schatten hin.

Ähnliche Ergebnisse liefert auch die Analyse der LORRI- und ACS-Beobachtungen, bei denen sich der Mond ebenfalls im Schatten Jupiters befand. Zur Auswertung dieser Beobachtungen wenden wir ein dreidimensionales Zwei-Fluid-Plasmamodell zur Beschreibung der Plasmawechselwirkung im Nahbereich von Io an, das von *Saur et al.* (1999) entwickelt wurde. Damit ist es möglich, den Einfluss der Atmosphärenverteilung und -dichte auf die Strömung der Elektronen zu berechnen, die wiederum durch Stöße mit den Atmosphärenteilchen die beobachtete Aurora auslösen. Mit der Berechnung dieses wechselseitigen Einflusses der Atmosphäre und der Plasmaströmung schätzen wir eine Säulendichte der Atmosphäre im Schatten von $N = (1-4) \times 10^{15}$ cm^{-2} ab, was in etwa 10% des Gasinhalts der Atmosphäre über der sonnenbeschienen Oberfläche entspricht. Damit bestätigen auch die numerischen Simulationen der LORRI- und ACS-Bilder einen Rückgang der Atmosphärendichte im Schatten in Übereinstimmung mit den Ergebnissen der Auswertung der STIS-Beobachtungen. Unsere Ergebnisse sprechen also dafür, dass die Sublimation der SO_2-Ablagerungen die wesentliche Quelle der Atmosphäre ist und die vulkanischen Ausgasungen nur zu einem kleinen Teil zum Gasvorkommen beitragen. Zudem zeigen die LORRI-Aurora-Bilder zum ersten Mal eine deutlich leuchtende Vulkanfontäne nahe des Nordpols, die der Vulkanregion "Tvashtar" zugeordnet wird. Das zeigt einerseits, dass vulkanische Ausgasungen auch zur Atmosphäre beitragen, andererseits schätzen wir durch Vergleich mit unseren Simulationsrechnungen eine vergleichsweise niedrige Säulendichte in der Vulkanregion ab, was die Theorie der Sublimationsatmosphäre weiter stützt.

In einem weiteren Teil der Arbeit untersuchen wir die Schwankungen der hellen Äquatorpunkte von Ios Aurora. Dafür messen wir den Winkel der Neigung der Punkte in den STIS-Beobachtungen und setzten die gemessenen Winkel in Beziehung zur Orientierung des Hintergrundmagnetfeldes. Es zeigt sich, dass die Auroraschwankungen gegenüber der Schwankung des ungestörten

Magnetfeldes um etwa 20% abgeschwächt sind und einen leichten Versatz aufweisen. Wir zeigen, dass diese Abweichungen nicht durch atmosphärische Inhomogenitäten erklärt werden können. Als weitere mögliche Ursache für die Abweichungen untersuchen wir die Magnetfeldstörungen in der Nähe des Mondes durch die Effekte der Plasmawechselwirkung und durch mögliche induzierte Magnetfelder aus dem Inneren des Mondes. Während die generellen Eigenschaften der Plasmawechselwirkung oft untersucht und wohl bekannt sind, wurde die Messung von Induktionssignalen aus einer unterirdischen elektrisch leitfähigen Magmaschicht erst kürzlich von *Khurana et al.* (2011) postuliert. Eine Abschätzung der Plasmawechselwirkung zeigt keinen eindeutigen Zusammenhang zwischen den erwarteten Störungen und den Abweichungen der gemessenen Winkel vom Hintergrundfeld. Die Berechnung der induzierten Magnetfelder ergibt zwar eine gedämpfte Schwankung der Äquatorpunkte, jedoch führt das überlagerte induzierte Magnetfeld zu einer zeitlichen Verschiebung der Variationen, die den beobachteten Abweichungen genau entgegengesetzt ist. Starke Induktionssignale würden zudem zu einer übermäßigen Abschwächung der Schwankung führen. Daher ist nach unseren Berechnungen die beobachtete Schwankung nicht vereinbar mit der Existenz einer stark leitenden Magmaschicht unter der Kruste Ios. Für eine genaue Bestimmung der Magnetfeldtopologie in der Umgebung Ios ist jedoch eine gleichzeitige Simulation der Plasmaeffekte sowie der Induktion im Inneren notwendig.

Europas Atmosphäre besteht im Wesentlichen aus molekularem Sauerstoff mit geringen Anteilen von atomarem Sauerstoff und Wasserdampf. In den Aufnahmen der UV-Aurora zeigen sich dementsprechend Emissionen aus der Atmosphäre bei den Sauerstofflinien OI] 1356 Å und OI 1304 Å (*Hall et al.* 1995, 1998). Die räumliche Verteilung dieser Strahlung wurde bisher nur wenig untersucht (z.B. *Cassidy et al.* 2007, *Saur et al.* 2011). Bei unserer Auswertung der STIS-Bilder zeigt sich, dass die meiste Strahlung der Sauerstoffemissionen bei Europa auf der Scheibe zu finden ist. Darin unterscheidet sich Europas Aurora wesentlich von der Emission bei Io, wo die hellsten Bereiche in den Beobachtungen mit vergleichbarem Blickwinkel außerhalb der Scheibe des Mondes detektiert werden. Theoretische Überlegungen ergeben, dass dieses Strahlungsmuster durch eine Asymmetrie in der Sauerstoffatmosphäre entstehen könnte, wie sie im Atmosphärenmodell von *Plainaki et al.* (2012) vorausgesagt wird. Außerdem ergeben sich deutliche Abweichungen der Strahlungsmuster der OI] 1356 Å- und OI 1304 Å-Aurora. Während die OI] 1356 Å-Emission im Wesentlichen Schwankungen ausgesetzt ist, die sich durch die Variation der magnetosphärischen Umgebung erklären lassen, zeigt sich in der OI 1304 Å-Aurora ein auffällig heller Bereich im nördlichen, jupiterabgewandten Quadranten der Scheibe. Berechnungen der Erwärmung der Risse in Europas Eisoberfläche durch Scherspannungen von *Saur et al.* (2011) sagen bei exakt dem Längengrad der beobachteten Anomalie ein Spannungsmaximum und somit eine hohe Wahrscheinlichkeit für die Entstehung von Wasserfontänen voraus. Solche Wasserfontänen wurden vor kurzem beim Saturnmond Enceladus entdeckt (*Porco et al.* 2006). Daher schätzen wir die Helligkeiten der Sauerstoffemissionen für ein lokal stark erhöhtes Vorkommen von Wasserdampf ab und zeigen, dass die beobachtete Anomalie durch eine lokale H_2O-Säulendichte von etwa $N_{H_2O} = 2.6 \times 10^{16}$ cm^{-2} erklärt werden könnte. Zur genauen Bestimmung des Einflusses einer solchen Wasserfontäne ist es jedoch notwendig, die Wechselwirkung der Atmosphäre mit räumlichen Inhomogenitäten auf die Strömung des Plasmas zu berechnen.

Mit unserer Auswertung der Aurora-Beobachtungen bei Io und Europa können wir eindrücklich nachweisen, welche vielfältigen Möglichkeiten zur Erforschung des Inneren, der Atmosphäre sowie der Plasmaumgebung der Monde sich aus den beobachteten Strahlungserscheinungen ergeben.

Contents

1 Introduction

From time immemorial, auroral lights have been an intriguing and inspiring phenomenon. The auroral ovals around the North and South pole of the Earth, often referred to as *Aurora Borealis* and *Aurora Australis*, have been observed over centuries before people began to understand what these atmospheric lights are. The English astronomer Edmund Halley (1656–1742) was the first to detect a connection of the shape of the auroral emissions to the Earth's magnetic field. In 1859, Richard Carrington (1826–1875), another English astronomer, observed a strong solar flare, a bright eruption of magnetic energy from the sun, 18 hours before auroral activity was seen over much of the world, and brought up the idea of a correlation between solar activity and aurora occurrence for the first time (*Eather* 1980). Although today's understanding of the terrestrial aurora is still incomplete, it is clear that the solar wind, a stream of plasma particles coming from the sun, controls the strength of the brightest auroral emissions. The interaction of this solar wind with the Earth's magnetosphere, which is the region around the planet that is controlled by the planetary magnetic field, leads to an acceleration of electrons and ions. The accelerated charged particles can reach the upper atmosphere at higher northern and southern latitudes moving along the magnetic field lines of the Earth. There, the plasma particles collide with the neutral atmospheric gas triggering the auroral emissions.

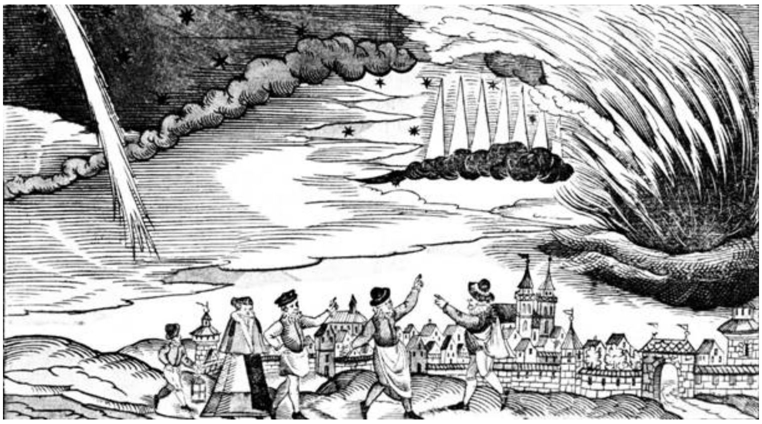

Figure 1.1: *Aurora Borealis seen from Nuremberg (Germany) in a medieval engraving from 1591 (Eather 1980). Strong solar activity presumably triggered this rare event of aurora at low geographic latitudes in Central Europe.*

It turned out, that aurora is not a unique phenomenon at the Earth. After the detection of auroral emissions at Jupiter with intensities more than hundred times higher than at the Earth (e.g., *Broadfoot et al.* 1979), it was clear that interaction with the solar wind is not the only possible generator for aurora. Since the energy in the solar wind is considerably lower at Jupiter and its planetary magnetic field, which shields the incoming solar wind, is much stronger, an internal energy source for the acceleration within the magnetosphere had to be present. It was found that a current system forms to maintain the corotation, i.e., rotation with the orbital velocity of Jupiter and its intrinsic magnetic field, of the plasma particles within the magnetosphere. This current system triggers the almost continuously radiating auroral ovals around Jupiter's poles (*Hill* 2001). Additionally, spatially confined auroral spots have been found to correspond to the location of Jupiter's large satellites in the magnetosphere. These localized emissions have been named *footprints* of the satellites. The four large satellites, Io, Europa, Ganymede and Callisto are also called Galilean moons after their discoverer Galileo Galilei (1564–1642). In the footprints, the interaction of the fast rotating magnetosphere with the relatively slowly orbiting moons becomes visible. Currents originating from the moons' atmosphere are mapped along the magnetic field into Jupiter's atmosphere, where they generate the footprints. For a complete overview of Jupiter's aurora the interested reader is referred to *Clarke et al.* (2004).

Not only in dense planetary atmospheres, but also in the tenuous gas envelopes of the Galilean moons the magnetospheric plasma triggers observable auroral emissions. As the magnetospheric plasma is confined to Jupiter's magnetic field, it rotates roughly with the period of Jupiter's rotation around the planet. The orbital velocity of the moons is considerably lower and the plasma particles therefore flow constantly past the moons. Thereby, collisions between the magnetospheric electrons and the neutral atmospheric gas, excite the latter to higher electronic states. When returning to the lower state the excited neutral gas emits photons. Since the brightness and shape of the auroral radiation depend on both the abundance of neutral gas and the properties of the impinging plasma particles as well as the magnetic field, observations of these auroral emissions from the atmospheres of the satellites are a valuable tool to explore the diverse nature of the Galilean moons and their environment in plasma physical, atmospheric and geological aspects.

Since the spacecrafts Pioneer, Voyager and Galileo visited Jupiter, numerous fascinating phenomena of Jupiter and its four large satellites have been discovered. The two Galilean moons that are subject of the present thesis, Io and Europa, turned out to be very different in many ways, although being direct neighbors in the Jovian system. On the surface of Io, the innermost Galilean moon, an extreme and ongoing volcanic activity can be observed with lava flows and huge volcanic eruptions. Large surface areas are covered with sulfur dioxide frost originating from these eruptions. Io's atmosphere is produced by volcanic plumes and sublimation of these surface frost. The relative contribution of the two processes, however, could not be determined yet and is widely debated. Europa, in contrast, orbiting Jupiter only 250 000 km further out, is completely covered with ice and its surface is one of the smoothest in our solar system. The smoothness of the surface and several other hints led to the conclusion that Europa harbors a subsurface ocean under its icy crust. These features, Europa's icy surface and Io's volcanic activity also affect the appearance of the auroral emission of the satellites.

Observations of the Hubble Space Telescope (HST), which is in orbit around Earth since 1990, played a major role in exploring the aurorae at Io and Europa. Spectra obtained by the HST Goddard High Resolution Spectrograph (GHRS) brought evidence for the neutral atmosphere around Europa (*Hall et al.* 1995). Spatially resolved UV observations of Io by the Space Telescope Imaging Spectrograph (STIS), which was installed on HST in 1997 in replacement of the GHRS, revealed that the magnetic field topology is essential for the morphology of the auroral emissions. Besides HST, observations of the imaging systems on board the spacecrafts Galileo and Cassini also contributed to the understanding of the aurorae, particularly in case of Io where a direct influence of volcanically active regions on the aurora has been found (e.g., *Geissler et al.* 1999). On the one hand, aurora observations can therefore be used as remote sensing tool to probe the local plasma and magnetic field in the environment of the satellites. In-situ measurements by spacecrafts of e.g., the plasma density or the magnetic field, might provide a higher accuracy and precision. However, they lack a separation of spatial and temporal resolution, as the spacecraft is always in motion and hardly ever passes through exactly the same region twice. The aurora observations cover the entire environment of the satellites at a time. In addition, the HST STIS observations principally allow an analysis of the temporal evolution of the aurora over the exposure time, which is on the order of tens of minutes. On the other hand, the auroral radiation is emitted by the excited neutral gas in the vicinity of the satellites, i.e., in the images atmospheric properties are more or less directly "mapped" to the observer. The observations therefore contain useful information about atmospheric densities and abundances. Hence, observations of the aurorae of the Galilean moons have been proven to provide valuable insights into the nature of the atmospheres of the satellites as well as of the ambient magnetospheric properties.

In the case of Io, the principals of the observed morphological pattern has been analyzed frequently yielding a basic understanding of the formation. However, the exact distribution and the possible time variability of the auroral emission is still not clear. Furthermore, as the role of volcanic eruptions as direct source for Io's atmosphere has not been unambiguously determined, the influence of the plumes on the aurora and its variability is unclear. The most prominent feature of Io's aurora are bright spots around the equator. The location of these spots depends on the orientation of the background magnetic field, but the exact correlation is also not clear yet. In this thesis we will therefore analyze a set of HST STIS observations taken over a period of five years between September 1997 and December 2001 to accurately investigate the spatial distribution and temporal variations of Io's UV aurora. Additionally, we will investigate high-resolution images of Io's aurora in eclipse obtained by the Long-Range Reconnaissance Imager (LORRI) on board the New Horizons spacecraft (NH) and the Advanced Camera for Surveys (ACS) of the Hubble Space Telescope. Using a three-dimensional two-fluid plasma simulation developed by *Saur et al.* (1999) we study these eclipse images and infer atmospheric properties during eclipse from a comparison of the observation images with the plasma simulation results.

In the case of Europa, the observed morphology of the UV aurora is not at all understood at present. Europa was the objective of only one STIS observation campaign in October 1999. The observations have been briefly discussed in two review papers by *McGrath et al.* (2004, 2009). In this thesis a detailed analysis of the images obtained during five HST orbits is carried out. We will investigate dependencies of the morphology and the brightness of the observed radiation on the magnetospheric environment and examine possible atmospheric compositions that explain the relative strength of the different observed spectral lines.

The thesis is organized as follows: In Chapter 2 we describe the properties of the interior, atmospheres and plasma environment of Io and Europa. In particular, we will reflect the previous observations of the aurorae of the satellites. For Io, a description of the local interaction between the moon and the magnetosphere is given including a short overview of simulation models dealing with it. Chapter 3 contains a detailed description of the HST STIS data, the processing of it and the extraction of the spatial two-dimensional images. The characteristics of the NH LORRI and HST ACS eclipse images are specified and a short description of the methods used for the data analysis is given. The processed STIS images of Io's aurora are analyzed in detail in Chapter 4. We summarize the findings on the brightness and morphology of Io's aurora and develop a phenomenological model for the three-dimensional emission distribution. By adjusting the model to the observations we derive quantitative properties of the aurora. The bright auroral spots and their correlation to the magnetic field are investigated in detail. In Chapter 5, the NH LORRI and HST ACS observations are analyzed by comparing the results of a numerical simulation of Io’s aurora with the images. Chapter 6 contains the analysis of the 1999 STIS Europa observations with a detailed discussion. The final Chapter 7 summarizes the main findings and conclusions of this thesis.

2 Previous observations and models

In this chapter the current understanding of the interior, the atmosphere and the plasma environment of the two satellites, Io and Europa, is described. Thereby, we will particularly address the previous observations that are of interest for the generation of the auroral emission.

2.1 Io and its environment

The first images of Io taken by the Voyager I spacecraft in March 1979 provided spectacular evidence for active volcanism outside the Earth showing a huge plume on the limb of the satellite. It turned out that Io's volcanic activity plays an essential role in the Jovian magnetosphere.

The atmosphere of Io and how it interacts with the surrounding plasma and magnetic field are the key factors that control the formation of the auroral emissions. After a short introduction of the satellite and its volcanism, we therefore summarize the current state of research on both Io's atmosphere and the interaction with the Jovian magnetosphere including a description of simulation models. We then give an overview of the previous observations of auroral emission emanating from Io's atmosphere at ultraviolet, visible and infrared wavelengths.

2.1.1 Interior, surface and volcanism

Io is a differentiated body consisting of a metallic core and a silicate mantle with a rigid, cold crust. The average density of 3.56 $\mathrm{g\,cm^{-3}}$ is the highest of all moons in the solar system. The core represents about 20% of the total mass, its size depends on the mixing ratio of iron and silicate, which is not exactly known. The estimated mass and density imply an extension between 0.2 and 0.5 times Io's radius ($\mathrm{R_{Io}}$). The physical state of the core could not be unambiguously determined by Galileo measurements. A dynamo-driven intrinsic magnetic field, which could arise in a partially or fully molten convective core, has not been found (*Saur et al.* 1999). Hot lava flows and high temperature eruptions of up to 1450 °C observed on Io's surface indicate that the mantle might be partially molten with an increasing melt fraction from the mantle base up to the base of the rigid lithosphere (*Keszthelyi et al.* 2004, 2007). The surface heat flow from the interior is extremely high with an estimated total flux of 1.5−4 $\mathrm{W\,m^{-2}}$, where volcanic hot spots apparently contribute most (*Moore et al.* 2007). The main internal heat source is tidal dissipation resulting from the eccentricity of Io's orbit, which is maintained by a 1:2:4 orbital resonance with Europa and Ganymede, called Laplace resonance. Estimating the dissipated tidal energy *Peale et al.* (1979) had predicted the existence of volcanic surface features shortly before the first volcanic activity was observed by *Morabito et al.* (1979).

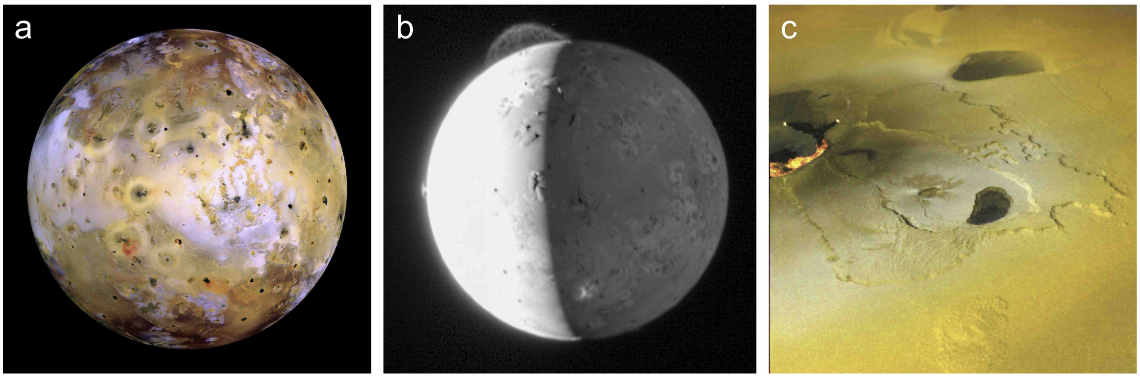

Figure 2.1: *(a) Three-color, 16-frame mosaic of Io taken during Galileo orbit 21 in August 1999 with a resolution of 1.3 km per pixel. (b) Image taken by New Horizons in February 2007 with a resolution of 12 km per pixel showing the enormous 300-km high plume from the volcano Tvashtar near Io's north pole. (c) Active eruption and lava lakes at the Tvashtar Catena as seen by Galileo in November 1999. This picture is about 250 km across. (Courtesy of NASA)*

Today after several spacecrafts visited Jupiter, more than 400 volcano-tectonic depressions called paterae, over 150 hot spots and 16 volcanic plumes have been observed on Io's surface (*Williams and Howell* 2007, *Geissler and Goldstein* 2007). Io is thus the most volcanically active body in our Solar System. Its volcanic eruptions consist of lava effusions as lava flows and lava lakes as well as of explosive plumes of gas and dust. The plumes on Io have been categorized in two classes (*McEwen and Soderblom* 1983): The most common Prometheus-type plumes form over ends of compound lava flow fields and are long-lived and dust-rich plumes with white mostly SO_2 deposits (see bright areas in false color image, Figure 2.1a). Pele-type plumes, in contrast, are short-lived high-temperature eruptions that can reach heights of up to 400 km depositing red (probably sulfurous) material on the surface. The huge Tvashtar plume close to Io's north pole is one example of these mostly faint Pele-type plumes, though clearly visible in an image taken by NH LORRI in 2007, see Figure 2.1b. As expected for a Pele-type plume, Tvashtar appears to undergo considerable activity variations. Lava flows and eruptions have been observed during the Galileo (Figure 2.1c, and e.g., *McEwen et al.* 1998, *Marchis et al.* 2001) and *New Horizons* (Figure 2.1b, and *Spencer et al.* 2007a) encounters, but no enhanced thermal emission has been detected with Earth-based infrared observations by *Marchis et al.* (2005) in late 2001. Several months before in February 2001, Tvashtar has been clearly detected in identical observations (*Marchis et al.* 2002).

Next to the relatively flat volcanic plains, huge mountains are found on major parts of Io's surface. They reach heights of more than 10 km, with the highest being $\sim$17 km high (*Schenk et al.* 2001). Models suggest compressional uplift of cold crustal blocks as major formation mechanism (*Turtle et al.* 2001). Rather than volcanoes the moutains are thus of tectonic origin, although a global tectonic pattern has not been identified. Analyzing a large set of Galileo and Voyager images *Williams et al.* (2011) produced the first gobal geological map of Io, where the surface is subdivided in four major categories: plains (65.8% of surface), lava flow fields (28.5%), mountains (3.2%), and patera floors (2.5%).

Galileo infrared observations showed that SO_2 frost originating from plumes is omnipresent on Io's surface covering over 60% (*Douté et al.* 2001). Other expected surface compounds are e.g., silicates and various sulfur chains (S_3, S_4 and S_8) produced by polymeralization of S_2, which has been observed in the Pele and Tvashtar plumes by *Spencer et al.* (2000a) and *Jessup and Spencer* (2012). However, they have never been definitely indentified (*Carlson et al.* 2007). For detailed descriptions of the interior, surface and volcanism the reader is referred to the review papers by *Moore et al.* (2007), *Carlson et al.* (2007) and *Williams and Howell* (2007).

2.1.2 Atmosphere

The first unambiguous detection of Io's atmosphere was achieved, when the Voyager infrared experiment (IRIS) measured gaseous sulfur dioxide (SO_2) above Loki Patera (*Pearl et al.* 1979). In numerous subsequent studies SO_2 has been confirmed to be the main constituent (e.g., *Ballester et al.* 1990), but Io probably possesses the most species-rich atmosphere of the four Galilean satellites. Besides SO_2, various minor species, such as Na, K, O, S, S_2, SO and Cl, have already been observed in the vicinity of the satellite (*Brown and Chaffee* 1974, *Trafton* 1975, *Ballester et al.* 1987, *Spencer et al.* 2000a, *Lellouch et al.* 1996, *McGrath et al.* 2000, *Feaga et al.* 2004).

While sputtering of surface material has been ruled out as dominant source (see review of *Lellouch et al.* 2007), there is an ongoing debate about the relative roles of direct volcanic outgassing and sublimation of surface frost for maintaining the atmosphere. Since the abundance of SO_2 frost is found to be correlated with active volcanic regions (*Douté et al.* 2001), the surface distribution of the atmosphere is related to the distribution of the volcanic regions on global scales, no matter if sublimation or direct outgassing is the main source (*Spencer et al.* 2005). The frequency of both the active volcanic regions and the paterae decreases with increasing latitude (*Lopes-Gautier et al.* 1999, *Radebaugh et al.* 2001). Observations of surface reflected solar Lyman-α radiation that is absorbed in the atmosphere (Figure 2.2) indicate that the SO_2 gas is concentrated likewise at lower latitudes (*Feldman et al.* 2000, *Strobel and Wolven* 2001).

Numerous observations of emission and absorption signals have been obtained over the years to get further insight in the nature of Io's neutral gas atmosphere. Millimeter-wave observations of SO_2 rotational lines by *Lellouch et al.* (1992) suggested a spatially confined or patchy atmosphere with a SO_2 column density of 6×10^{17} cm^{-2}, which is likely of volcanic origin. Observations of SO_2 gas absorption at UV wavelengths by the HST Faint Object Spetrograph (FOS) (*Ballester et al.* 1994) and the Galileo ultraviolet spectrometer (*Hendrix et al.* 1999) were generally in agreement with these findings. On the other hand, several recent observations support the picture of a sublimation driven atmosphere. *Jessup et al.* (2004) analyzed spatially resolved UV spectra ($2000 - 3000$ Å) and conclude that the atmosphere is at least in some regions primarily maintained by sublimation of surface frost with a SO_2 column density of $\sim (1-2) \times 10^{17}$ cm^{-2}. Disk-resolved millimeter (*Moullet et al.* 2008) and submillimeter (*Moullet et al.* 2010) observations of SO_2, SO and NaCl rotational lines imply a surface distribution that is in good agreement with results of SO_2 frost sublimation models. The authors thus conclude that the contribution of volcanic plumes to the atmospheric SO_2 is small. Using the HST STIS observations of the reflected Lyman-α radiation *Feaga et al.* (2009) derived a global map of SO_2 column density (Figure 2.2), which shows a relatively sharp density decrease at approximately $30-45°$ north and south. They derive a maximum column density of 5×10^{16} cm^{-2} and find that the atmosphere is denser and more extended on the anti-Jovian hemisphere. A sub-anti-Jovian asymmetry was first noted by *Jessup et al.* (2004) and *Spencer et al.* (2005) and later confirmed by *Moullet et al.* (2010). *Spencer et al.* (2005) analyzed a set of disk-integrated 19-μm infrared spectra taken between 2001 and 2004 and found a longitudinal variations in the equatorial column density between 1.5×10^{16} cm^{-2} and 1.5×10^{17} cm^{-2} in correlation with the abundance of SO_2 frost patches. In a

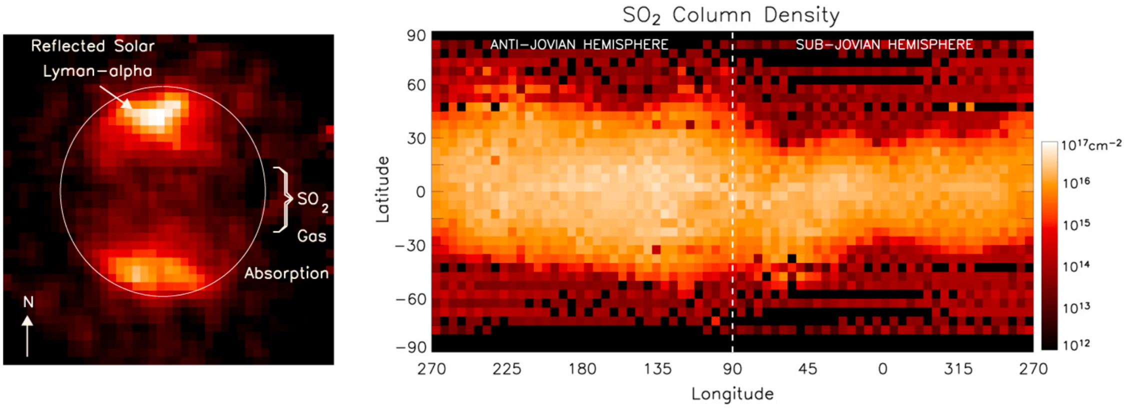

Figure 2.2: *(Left) HST STIS observation of reflected solar Lyman-α radiation, which is absorbed in the dense equatorial atmosphere. (Right) Global SO$_2$ distribution derived from Lyman-α observations (Feaga et al. 2009).*

follow-up study of the 2001-2004 data (which has been already analyzed by *Spencer et al.* 2005) and new 19-μm spectra obtained between 2005 and 2010, *Tsang et al.* (2012) detected a correlation of increasing SO$_2$ abundance with decreasing distance to the sun, which clearly indicates a contribution of sublimated gas to the atmosphere. However, the authors also state, that they would expect larger seasonal variations than are observed, which in turn is an indication for a substantial season-independent volcanic contribution. Hence, the search for the main source of Io's atmospheric gas must be continued.

Additionally, several analytical and numerical models for Io's atmosphere have been developed (e.g., *Summers and Strobel* 1996, *Wong and Smyth* 2000, *Austin and Goldstein* 2000). In a recent study of a sublimation-driven atmosphere *Walker et al.* (2010) investigated effects of plasma heating as well as surface frost, molecular residence time and surface temperature distribution in a sophisticated SO$_2$ gas dynamics simulation, which also includes direct volcanic outgassing. The simulation results indicate the gas distribution is mainly controlled by effectiveness of the frost sublimation, which strongly depends on the surface temperature. *Walker et al.* (2012) improved the atmospheric model of *Walker et al.* (2010) including thermophysical surface properties and found that the observed asymmetry of gas abundance between the anti-Jovian and sub-Jovian hemispheres can be explained by the diurnally averaged effect of eclipse on the sub-Jovian side.

The response of the atmosphere to ceasing sunlight has been subject of many studies with unambiguous results and findings (*Binder and Cruikshank* 1964, *Ingersoll* 1989, *Nelson et al.* 1993, *Bellucci et al.* 2004). The observed SO$_2$ abundances on the day side hemisphere imply temperatures around 110−120 K of the sunlit surface (e.g., *Strobel et al.* 1994, *Wong and Smyth* 2000). Galileo radiometer measurements of Io's night side by *Spencer et al.* (2000b) revealed a decreased surface temperature of ∼90 K, which probably leads to an essential condensation of atmospheric SO$_2$ gas as frost on the surface. Observations of the SO$_2$ abundance on the night side or during eclipse might thus provide the possibility to determine the relative importance of the volcanoes as a direct source of the atmosphere, versus sublimation of SO$_2$ surface frost. Recent Monte Carlo simulations of the response to eclipse of the neutral gas by *Moore et al.* (2009) indicate a strong dependence on the abundance of non-condensable species for an atmospheric collapse. In case of a mole-fraction of 0.35 of non-condensable gas, such as O$_2$, a near-surface diffusion layer forms and the SO$_2$ density decreases only slowly and does not drop below 0.18 of the initial column density during an eclipse event. There have been several measurements of the response of the auroral emission to eclipse, which we will discuss in Section 2.1.4.

Considering results from modeling and from millimeter, infrared and ultraviolet observations *Lellouch et al.* (2007) concluded in their review paper that Io's atmosphere has a mean vertical column density of $\sim (1-5) \times 10^{16}$ cm^{-2}, covering 50−70% of Io's day-side hemisphere. The density variations across the surface are still unclear, even though it is proven that the equatorial atmosphere is significantly denser than the polar. The day side surface pressure of Io's atmosphere thus corresponds to roughly one billionth of the atmospheric pressure at the Earth's surface. The properties of the night side atmosphere are, however, hardly constraint yet.

Through primarily sputtering, ionization and charge exchange, Io's atmosphere is constantly being lost to the Jovian magnetosphere where the particles arrive partly ionized and partly as neutrals. *Saur et al.* (2003) investigated the relative importance of elastic and inelastic collisions in Io's atmosphere and found that at least 80% of the material leaves the atmosphere as neutrals accelerated by elastic collisions with the corotating plasma. The neutrals in the magnetosphere are finally ionized by UV radiation or electron impact. All ions are then picked-up by the rotating magnetic field of Jupiter due to the Lorentz force and form the so-called *Io torus* or *plasma torus*. The total mass that is fed into the magnetosphere is estimated to be as much as ∼1 ton per second (*Broadfoot et al.* 1979).

Io's circles Jupiter on a Keplerian orbit at 5.9 Jovian radii (R_J = 71492 km) with a velocity of 17 km s^{-1}. Io's orbit is thus located deep inside the planet's huge magnetosphere, which is thought to extend up to the orbit of Saturn on the night side. On the day side the magnetopause is located at ∼60 R_J on average. In inner magnetosphere the plasma corotates rigidly with the planet's period (*Hill* 1979). As Io's orbital period is ∼4 times larger than Jupiter's rotation period, the Jovian magnetic field and corotating torus plasma in turn constantly overtake the moon. The satellite's *trailing* hemisphere is thus the *upstream* hemisphere regarding the plasma flow and the *leading* hemisphere corresponds to the wake side or *downstream* hemisphere. Hence, the particles that originally are lost by the satellite orbit significantly faster and catch up with Io. The resulting complex interaction between the plasma and magnetic field on the one side and the moon and its atmosphere on the other side is described in the next section.

2.1.3 Interaction with the Jovian magnetosphere

The magnetic field and plasma environment in the vicinity of Io is strongly disturbed by the interaction with the satellite and its atmosphere-ionosphere. Additionally, induced magnetic fields from the interior possibly influence the environment. We first explain the well established picture of the plasma interaction, before we briefly describe effects of the induction.

Plasma interaction

The ambient magnetic field strength in Io's orbit is roughly 2000 nT. A comparison of the thermal pressure of the plasma to the magnetic pressure, which is commonly referred to as plasma β, reveals that the magnetic field plays the dominant role in the interaction of the plasma with Io. The magnetic pressure is given by $p_{mag} = B^2/2\mu_0$, with the vacuum permeability μ_0. Due to the comparably strong magnetic field the gyroradii and gyroperiods of ions and electrons are

Table 2.1: *Physical properties of Io and the local magnetospheric plasma (Neubauer 1998, Kivelson et al. 2004, and references therein).*

Radius	$\mathrm{R_{Io}}$	1821 km
Semi-major axis	$\mathrm{a_{Io}}$	5.9 $\mathrm{R_J}$
Orbital period	$\mathrm{T_{Io}}$	1.77 days
Orbital velocity	$\mathrm{v_{Io}}$	17 $\mathrm{km\,s^{-1}}$
Average Jovian magnetic field	B_0	∼2000 nT
Corotational velocity	v_{corot}	74 $\mathrm{km\,s^{-1}}$
Relative plasma velocity	v_0	57 $\mathrm{km\,s^{-1}}$
Electron number density	n_e	1200−3800 $\mathrm{cm^{-3}}$
Temperature of thermal electrons	k_BT_e	5 eV
Ion temperature	k_BT_i	20−90 eV
Ion gyrofrequency	ω_{ci}	9 $\mathrm{s^{-1}}$
Ion gyroradius	r_{ci}	2-3 km
Alfvén Mach number	M_A	∼0.3
Thermal pressure / magnetic pressure	β	∼0.04
Alfvén conductance	Σ_A	∼4.4 S
Pedersen conductance	Σ_P	∼200 S
Hall conductance	Σ_H	100-200 S

considerably smaller than the spatial and time scales of the obstacle, i.e., Io's radius, atmospheric scale heights and plasma convecting times. Therefore, it is valid to treat the plasma as fluid and neglect the small scale kinetic effects in a theoretical description of the interaction. Within the fluid descriptions for plasmas two different theoretical formulations have been successfully applied to calculate Io's local interaction with Jupiter's magnetosphere (*Saur et al.* 2004): One treats the electric fields **E** and currents **j** as basic variables, the other solves equations for the plasma velocity **v** and the magnetic field **B** in the first place. The interaction model that we apply to simulate the auroral emission in eclipse was developed by *Saur et al.* (1998,1999) and is based on the $\mathbf{E},\mathbf{j}$ approach. Therefore, we will describe the local interaction in the framework of the modified electric field and the evolving current system rather than starting with a description of the disturbed plasma velocity and magnetic field.

Io's orbital velocity is significantly lower than the corotational speed of the magnetospheric plasma, see Table 2.1. Thus, the plasma particles constantly stream past the moon and its atmosphere with a relative velocity of ∼57 $\mathrm{km\,s^{-1}}$. Inelastic collisions between the torus electrons and the neutral gas particles of the atmosphere and, less important, photo-ionization lead to the formation of an ionosphere around the satellite. In the rest frame of Io, the atmospheric gas as well as the dense ionospheric plasma is at rest with respect to the moving torus plasma and magnetic field. The ionospheric particles are thus exposed to a motional electric field pointing approximately away from Jupiter given by $\mathbf{E}_0 = -\mathbf{v}_0 \times \mathbf{B}_0$, with the Jovian background field $\mathbf{B}_0$ and the undisturbed relative plasma velocity $\mathbf{v}_0$, see small box in Figure 2.3. The electric conductivity along the magnetic field direction $\sigma_{\|}$ is generally high. While outside the ionosphere the electric conductivity $\sigma_{\perp}$ perpendicular to **B** is almost zero, $\sigma_{\perp}$ becomes considerably large within regions of high ionospheric density. Due to the motional electric field a strong current system evolves inside the conductive ionosphere driving electric currents mainly in the anti-Jovian direction (see Figure

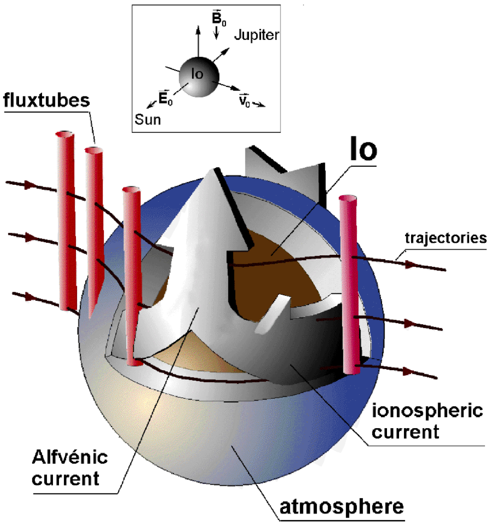

Figure 2.3: *Sketch of Io's local plasma interaction. The coordinate system of the sketch and the Saur model is depicted in the small box. In the model the magnetic field is spatially homogeneous and parallel to the z-axis. Due to the relative motion of the magnetic field ionospheric currents flowing in the anti-Jovian direction are generated. The upstream plasma flow is strongly decelerated inside Io's atmosphere, and deflected around the body. The flux tube (red) trajectories are shown with the black lines (Saur et al. 2000).*

2.3). The electric field is partially short-circuited and thus modified by the ionospheric currents. The perturbation of the electric field in turn changes the local Lorentz forces, which implies an acceleration or deceleration of the streaming plasma leading to a strongly diverted flow around Io. Inside the ionosphere the electric field and the plasma velocity are significantly reduced.

In the $\mathbf{v}$,$\mathbf{B}$ picture, mass loading and collisions are compensated by $\mathbf{j} \times \mathbf{B}$ forces in the momentum equation. Through the deceleration of the plasma flow, the magnetic field piles up in the upstream region and convects slowly through the ionosphere bending around it. The local perturbation excites several wave modes with the Alfvén wave being the most important as it carries the electric currents almost lossless parallel and anti-parallel to the magnetic field.

The ionospheric currents, however, can not be maintained perpendicular to $\mathbf{B}$ outside the ionosphere where $\sigma_\perp$ is low, and the current system is continued along the magnetic field lines carried by Alfvén waves. The Alfvén waves propagate with the velocity

$$\mathbf{v}_A = \frac{\mathbf{B}}{\sqrt{\mu_0 \rho}} \quad , \tag{2.1}$$

where ρ represents the plasma mass density in the torus. In case of Io, the Alfvén velocity $\mathbf{v}_A$ is always larger than the velocity of the corotating plasma $\mathbf{v}_0$, i.e., the Alfvén Mach number $M_A = v_0/v_A$ is smaller than one. The sonic and the Alfvén Mach numbers determine the fast Mach number, which is also smaller than one and thus no bow shock forms. *Neubauer* (1980) developed the first analytical model that describes the far-field Alfvénic current system showing that the waves travel along characteristics given by $V_A^\pm = \mathbf{v}_0 \pm \mathbf{v}_A$. The characteristics are inclined with respect to the Jovian field lines creating the *Alfvén wings*. The yellow lines in Figure 2.4 show the propagation of the Alfvén waves (which are partly reflected at the boundary of the torus) through the Jovian magnetosphere. The currents are finally short-circuited due to the non-vanishing per-

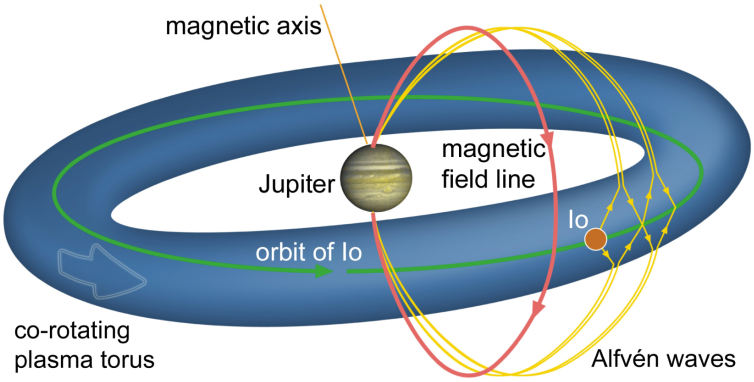

Figure 2.4: *Sketch of the far-field interaction of Io with the magnetosphere (Jacobsen 2011). The roughly dipolar Jovian field line is shown in red, the Alfvén wings are illustrated with the yellow lines. The plasma torus (blue) is inclined with respect to Io's orbit (green) due to the tilt of the Jovian dipole moment.*

pendicular conductivity in Jupiter's ionosphere, where they also trigger auroral emission creating the *footprint* of Io (*Clarke et al.* 2002).

As the auroral emission from Io's atmosphere originates from the close vicinity of the moon (i.e., from within a few hundreds of km above the surface), the formation of Io's aurora is controlled mainly by the local interaction. Therefore, we will focus on the ionospheric interaction and describe the basic ideas of the theoretical description of the ionospheric currents and electric field in the model of *Saur et al.* (1999), referred to as *Saur* model.

***Saur* plasma model**

A numerical simulation for the currents and fields in Io's vicinity was developed by *Wolf-Gladrow et al.* (1987) connecting a model for the local interaction to the far-field solution by *Neubauer* (1980). Starting from the momentum equations for electrons and one ion species the authors derive an equation for the perpendicular ionospheric currents. Due to the high conductivity parallel to **B** they assume a vanishing parallel electric field and derive a two-dimensional elliptic differential equation for the electric potential. Based on the same approach *Saur et al.* (1999) developed their three-dimensional, stationary, two-fluid plasma model for a magnetic field geometry, where **B** is given by the constant, homogeneous Jovian background field $\mathbf{B}_0$ at all times. Again with the assumption of vanishing parallel electric fields, the perpendicular electric field is reduced to two dimensions in the xy-plane with $\mathbf{B}_0$ pointing in the negative z-direction of the coordinate system (see small box in Figure 2.3). As mentioned earlier, inside Io's ionosphere currents are induced by the motional electric field. The perpendicular ionospheric currents can be expressed as

$$\mathbf{j}_\perp = \sigma_P \mathbf{E} + \sigma_H \frac{\mathbf{B}_0 \times \mathbf{E}}{B_0} \quad . \tag{2.2}$$

The Pedersen conductivity σ_P governs the currents in the direction of the electric field **E** (Pedersen currents), the Hall conductivity σ_H determines the Hall currents in the direction perpendicular to both the electric and magnetic fields ($\mathbf{B}_0 \times \mathbf{E}$ direction). Using the electric potential Φ instead of the field ($\mathbf{E} = -\nabla\Phi$), Equation (2.2) becomes

$$\mathbf{j}_\perp = -\left(\sigma_P \frac{\partial\Phi}{\partial x} + \sigma_H \frac{\partial\Phi}{\partial y}\right)\mathbf{e}_x - \left(\sigma_P \frac{\partial\Phi}{\partial y} - \sigma_H \frac{\partial\Phi}{\partial x}\right)\mathbf{e}_y \quad , \tag{2.3}$$

for the assumed constant magnetic field $\mathbf{B}_0 = B_0\mathbf{e}_z$. The divergence of (2.3) is thus

$$\nabla\cdot\mathbf{j}_\perp = -\left[\sigma_P\Delta\Phi + \left(\frac{\partial\sigma_P}{\partial x} - \frac{\partial\sigma_H}{\partial y}\right)\frac{\partial\Phi}{\partial x} + \left(\frac{\partial\sigma_P}{\partial y} + \frac{\partial\sigma_H}{\partial x}\right)\frac{\partial\Phi}{\partial y}\right] \quad . \tag{2.4}$$

Ampére's law for a steady state ($\nabla\times\mathbf{B} = \mu_0\mathbf{j}$) implies

$$\nabla\cdot\mathbf{j} = 0 \quad , \tag{2.5}$$

and thus

$$\frac{\partial}{\partial z}\mathbf{j}_\parallel + \nabla\cdot\mathbf{j}_\perp = 0 \quad . \tag{2.6}$$

The parallel currents can be expressed as

$$\mathbf{j}_\parallel = -\Sigma_A\Delta\Phi \tag{2.7}$$

(cf. Eq. (9) of *Neubauer* 1980). For small Alfvén Mach numbers $M_A \ll 1$, the parallel Aflvén conductance is $\Sigma_A = \frac{1}{\mu v_a}$. By integrating (2.6) along the field lines

$$\int_{z_0}^{z'} \frac{\partial}{\partial z}\mathbf{j}_\parallel(x,y,z)\,\mathrm{d}z + \int_{z_0}^{z'} \nabla\cdot\mathbf{j}_\perp(x,y,z)\,\mathrm{d}z = 0 \quad , \tag{2.8}$$

a differential equation for the electric potential Φ in the plane perpendicular to $\mathbf{B}_0$ can be derived using (2.4) and (2.7)

$$(\Sigma_P + \Sigma_A)\Delta\Phi + \left(\frac{\partial\Sigma_P}{\partial x} - \frac{\partial\Sigma_H}{\partial y}\right)\frac{\partial\Phi}{\partial x} + \left(\frac{\partial\Sigma_P}{\partial y} + \frac{\partial\Sigma_H}{\partial x}\right)\frac{\partial\Phi}{\partial y} = 0 \tag{2.9}$$

(see also *Neubauer* 1998, Eq. (40)). The respective conductances Σ_P and Σ_H are then calculated by an integration of σ_P and σ_H along the flux tubes (along z since $\mathbf{B}_0 \parallel \mathbf{e}_z$) over the collision region, i.e., where the neutral gas density is non-zero. It is important to note that the overall modification of the electric field in the ionosphere therefore does not depend on the local conductivity, but only on the integrated conductances in the entire flux tubes along $\mathbf{B}_0$.

Neubauer (1998) has shown that the electron gyrofrequency ω_{ce} exceeds the effective electron collision frequency $\tilde{\nu}_{en}$ in Io's vicinity by roughly an order of magnitude. Assuming $\omega_{ce} \gg \tilde{\nu}_{en}$, the ionospheric conductivities depend only on the ion cyclotron frequency ω_{ci} and the effective collision frequency $\tilde{\nu}_{in}$. The effective collision frequencies take into account elastic collisions and the acceleration of the newly produced ionospheric plasma (see also *Neubauer* 1998). In the two-fluid model with one positively charged ion species the conductivities are then given by

$$\sigma_P = \frac{en}{B_0}\frac{\omega_{ci}\tilde{\nu}_{in}}{\omega_{ci}^2 + \tilde{\nu}_{in}^2} \quad , \tag{2.10}$$

and

$$\sigma_H = \frac{en}{B_0}\frac{\tilde{\nu}_{in}^2}{\omega_{ci}^2 + \tilde{\nu}_{in}^2} \quad , \tag{2.11}$$

with the plasma number density $n = n_i = n_e$ (ion, electron number density) (cf. Equations (27) and (28) in *Saur et al.* 1999). By integrating along z, *Saur et al.* (1999) calculate the Pedersen and Hall conductances for Equation 2.9, which is solved numerically yielding the perturbed electric field $\mathbf{E} = -\nabla\Phi$.

In the description of the electron velocity *Saur et al.* (1999) take into account only the Lorentz force neglecting collisions with neutral gas as well as the pressure gradient and the inertia. The electron velocity is thus reduced to the xy-plane and can be expresses by

$$\mathbf{v}_e = \frac{\mathbf{E} \times \mathbf{B}_0}{B_0^2} \tag{2.12}$$

(cf. Equation (7) of *Saur et al.* 1999). The perpendicular ion velocity is derived from the ionospheric currents given by Ohm's law. Following the flow of the flux tubes, i.e., the homogeneous field lines and the plasma connected to them, through Io's atmosphere the model calculates the plasma density and ion and electron temperature including inelastic collisions, recombination and photo-ionization (cf. Equations (4), (16) and (21) of *Saur et al.* 1999). The flux tube trajectories are illustrated in Figure 2.3. Hence, the model calculates self-consistently the evolution of the plasma density, the velocity and the ion and electron temperatures for a given distribution of the neutral atmosphere around Io. Since aurorae are triggered by collisions between electrons and the neutral gas, a self-consistent simulation of the electron density and temperature (as the collisional cross sections strongly depend on the electron temperature) is essential to model Io's auroral emission. *Saur et al.* (2000) successfully applied the plasma model to simulate HST STIS observation of the aurora explaining the observed aurora morphology, when Io is located at western elongation to Jupiter. We will elaborate on these results in Section 2.1.4. In Chapter 5 of the present work, the *Saur* model is adapted to the scenario, when Io is located in Jupiter's shadow, to simulate for a given atmospheric distribution the plasma interaction and the aurora formation in eclipse self-consistently. Therefore, the continuity, electron velocity and electron temperature equations are slightly modified. The equations and our modifications are explained in detail in Section 5.2.

Saur et al. (1999) additionally present an analytical solution for constant ionospheric conductances (and the constant background field as in the numerical model) describing the general perturbation of the plasma quantities in the ionosphere (Appendix A of *Saur et al.* 1999). For a cylindrical homogeneously conducting body, they derive an expression for the perturbed ionospheric electric field in the xy-plane

$$\mathbf{E}_i = -E_0 \frac{2\Sigma_A}{\Sigma_H^2 + (\Sigma_P + 2\Sigma_A)^2} \begin{pmatrix} -\Sigma_H \\ \Sigma_P + 2\Sigma_A \end{pmatrix} = \mathbf{E}_0 + \begin{pmatrix} \sin\Theta_P \\ \cos\Theta_P \end{pmatrix} \quad , \tag{2.13}$$

as a function of the ionospheric Hall- and Pedersen conductances Σ_H and Σ_P and the field parallel Alfvén conductance Σ_A. The angle Θ_P is given by

$$\tan\Theta_P = \frac{2\Sigma_A\Sigma_H}{\Sigma_H^2 + \Sigma_P(\Sigma_P + 2\Sigma_A)} \quad , \tag{2.14}$$

and describes the deviation of the ionospheric currents from the negative y-direction. For an electron flow given by (2.12) the trajectories of the electrons are twisted towards Jupiter by the angle Θ_{twist}, with

$$\tan\Theta_{twist} = \frac{\Sigma_H}{\Sigma_P + 2\Sigma_A} \quad . \tag{2.15}$$

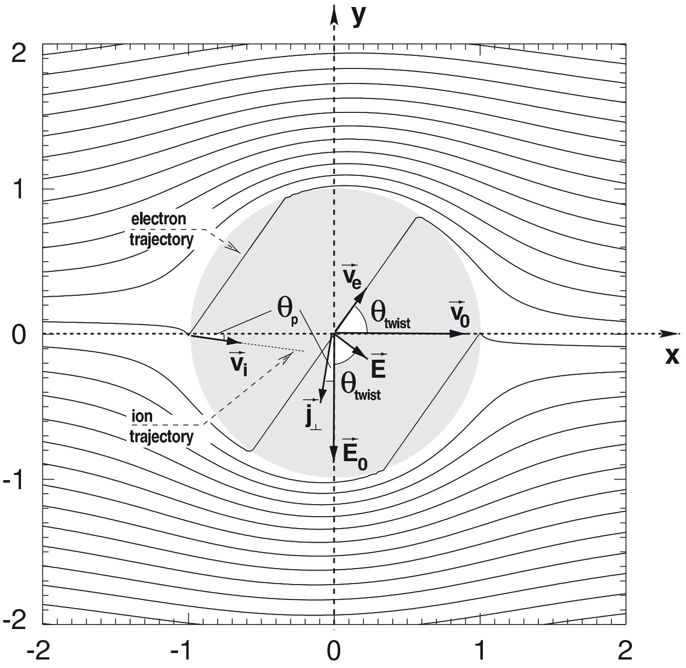

Figure 2.5: *Basic properties Io's local plasma interaction in the plane perpendicular to the magnetic field (Saur et al. 1999). Displayed are the iso-contours of the electric potential, which are also the trajectories of the electrons. The plasma velocity is strongly reduced inside the grey shaded circles, which indicates the interaction region. Due to the Hall conductivity, the electron flow is diverted towards Jupiter, whereas the ion flow rotated in the opposite direction. On the flanks the plasma is accelerated with respect to the upstream velocity.*

Figure 2.5 illustrates the flow pattern, the isolines of the electric potential (which are at the same time the trajectories of the electrons) and the derived angles Θ_P and Θ_{twist} for estimated ionospheric conductances for Io. With the conductances given in Table 2.1 the angles are $\Theta_P \approx 10^\circ$ and $\Theta_{twist} = 26-44^\circ$. The electric field inside the ionosphere is significantly reduced and rotated towards the positive x-direction leading to an increased electron velocity. Using (2.13), one can therefore define an interaction parameter

$$\alpha = \frac{E_i}{E_0} = \frac{2\Sigma_A}{\sqrt{\Sigma_H^2 + (\Sigma_P + 2\Sigma_A)^2}} \quad , \tag{2.16}$$

which quantitatively specifies the reduction of the field in the ionosphere as a function of the conductances. With (2.12) and $\nabla \cdot \mathbf{v}_w = 0$, (2.16) also describes the fraction of the upstream electrons that can enter Io's atmosphere and is commonly assumed to be $\alpha_{Io} \approx 0.1$ in case of Io.

The electron flow direction is rotated towards the positive y-direction (towards Jupiter), the ions drift into the anti-Jovian direction. Note that for a vanishing Hall conductance the flow pattern is symmetric with respect to the xz-plane, i.e., the Hall currents break the anti-sub-Jovian symmetry. Estimated values for the ionospheric and Alfvén conductances (see Table 2.1) show that Σ_H is on the order of Σ_P indicating a considerable influence of the Hall effect.

Saur et al. (1999) investigated flow asymmetries due to Hall conductance and estimated a total electric current of 5×10^6 A through the Alfvén wings as well as a Joule heating rate of 4×10^{11} W for the dissipated power on the other end of the field lines in Jupiter's ionosphere. Using a slightly

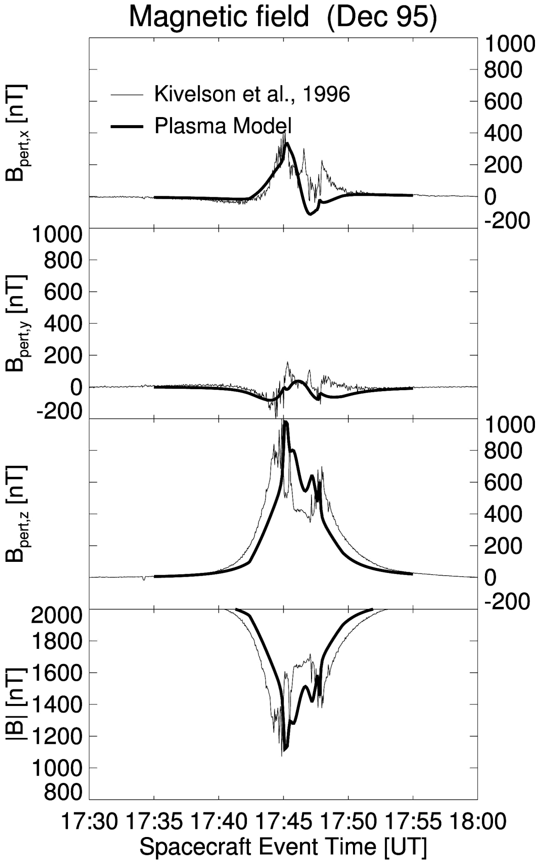

Figure 2.6: *Galileo magnetometer measurements of the magnetic field perturbations (from top: δB_x, δB_y, δB_z and B) in the vicinity of Io during Galileo flyby I0 (thin solid line, Kivelson et al. 1996), and simulation results of an improved numerical model by Saur et al. (2002) (thick solid line). The conspicuous double-peak magnetic field signature in B_z could be reproduced by the Saur model and is attributed to diamagnetic and inertia currents in the wake of Io (Figure from Saur et al. 2004).*

modified version of the numerical *Saur* model (e.g., including impact-ionization by high energetic electron beams) *Saur et al.* (2002) were able to explain and interpret key features of Galileo plasma and magnetic field observations, such as the double-peak magnetic field signature during Galileo flyby I0, see Figure 2.6. Note that the perturbation of the **B** becomes as high as 30% of the background magnetic field strength. Although, in the model a constant background field is assumed, the magnetic field disturbances can be calculated from the ionospheric currents using Biot-Savart's law.

Other plasma models

Io's interaction has also been simulated in the one-fluid framework by *Linker et al.* (1988, 1989, 1991, 1998), who solve the full set of resistive magnetohydrodynamic (MHD) equations for the magnetic field and the plasma density, momentum and pressure. The results confirmed the formation of the Alfvén wings, but indicated a significant contribution of the slow and fast MHD modes to the perturbation features in Io's vicinity. *Combi et al.* (1998) applied a three-dimensional, ideal single fluid MHD code not including resistivity, but with a very good spatial resolution. While *Linker et al.* (1998) were not able to unambiguously explain the measured plasma and field perturbations during Galileo flyby I0, the model by *Combi et al.* (1998) reproduced the general

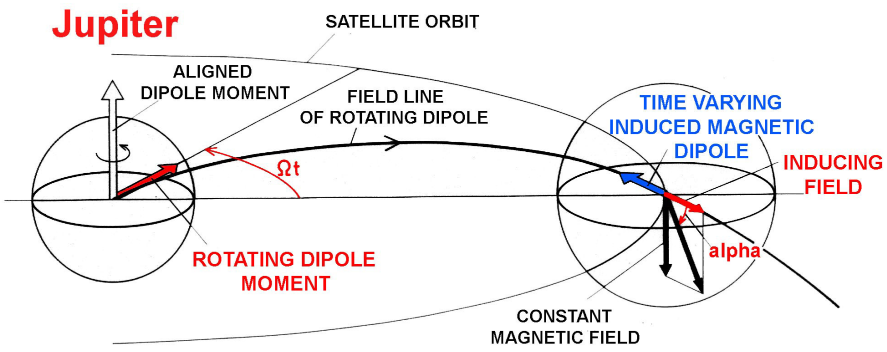

Figure 2.7: *Changing magnetic field direction at a satellite due to the rotating tilted dipole moment of Jupiter (after Neubauer 1999). The red arrow at Jupiter and the red arrow at the satellite show the time varying magnetic field components, which rotate around the z-axis (in the orbital plane) with the synodic rotation of Jupiter. A possible induced magnetic field inside the satellite (blue arrow) are roughly opposed to the inducing fields.*

appearance of the variations of density, magnetic field and ion pressure and temperature along the trajectory. Including a day-night asymmetry in model of *Combi et al.* (1998) and with an improved description of the ion pick-up and magnetic field tilt, *Kabin et al.* (2001) were able to reproduce all the qualitative features of the Galileo measurements during flyby I0. *Lipatov and Combi* (2006) presented the first hybrid model for Io's interaction, which treats the ions as single particles and describes the electrons (and neutrals) as fluid, and found good agreement of the simulation and results of the Galileo flyby I0. All the models described in the present paragraph do not include a self-consistent calculation of the electron temperature and are therefore not suitable to simulate the formation of the auroral emissions.

Induction effects

Another aspect of the interaction between Jupiter's magnetosphere and Io results from the variation of Jupiter's magnetic field in the orbit of the satellites. Jupiter's internal magnetic field can be approximated by a dipole field from a magnetic moment, which is tilted by ~9.5° against the planet's rotation axis (see also Figure 2.4) towards longitude 201° in Jovian System III coordinates (λ_{III}) as defined by *Seidelmann and Divine* (1977) . With an inclination of ~0.04° of Io's orbit, the moon's orbital plane is almost perpendicular to the rotational axis of Jupiter. Thus, during a synodic rotation of Jupiter, Io is exposed to a varying magnetic field environment. The components of Jupiter's dipole moment can be separated into time varying components and a constant component, see Figure 2.7. The magnetic field in Io's orbit can thus be decomposed accordingly. In a conductive layer inside the satellite electric currents are induced by the changing external magnetic field after Faraday's law. These currents generate a secondary or induced magnetic field, which can be measured in the vicinity of the satellite as perturbation of the external, inducing field. Conclusive induction signals have been identified at Europa and Callisto (e.g., *Khurana et al.* 1998, *Kivelson et al.* 2000) indicating global oceans of liquid water underneath the icy crusts. In case of Io, dissipation of tidal energy in the interior might lead to a partially molten layer at the base of the lithosphere (e.g., *Peale et al.* 1979, *Keszthelyi et al.* 2004). In such a global partially molten magma layer measurable secondary fields could be induced (*Seufert et al.* 2011). Assuming a highly conductive layer with a thickness of at least 50 km *Khurana et al.* (2011) claimed that

Galileo measurements of the magnetic field perturbations during Galileo flybys I24 and I27 prove the existence of a highly conductive global asthenosphere with melt fractions >20%. In their study they did not test other possible explanations for the observed magnetic field perturbations like an asymmetric or patchy atmosphere. The influence of induced magnetic fields from a putative magma ocean in Io's interior on the morphology of Io's aurora will be analyzed in Chapter 4 of this work.

2.1.4 Aurora

UV spectra obtained by the International Ultraviolet Explorer revealed oxygen and sulfur emissions from the close vicinity of Io for the first time (*Ballester et al.* 1987). The first observations of these UV emissions with an appropriate spatial resolution were taken by the HST STIS in September and October 1997 (*Roesler et al.* 1999). The spectral range covers wavelengths from 1140 Å to 1730 Å, including several sulfur and oxygen emission lines and the hydrogen Lyman-α line. In the present work, we will analyze the auroral emission in the full set of images, where Io was monitored by STIS with the 52"×2" aperture between 1997 and 2001. A detailed description of the spectral STIS far-ultraviolet (FUV) images is given in Section 3.2.

Roesler et al. (1999) provided the first short, but comprehensive discussion of the observed spatial distribution in the STIS images and characterized the morphology of the O and S emission by distinguishing between the bright *equatorial spots*, the fainter *limb glow* and a rapidly decreasing *extended emission*. An observation of the spatially resolved OI] 1356 Å emission is shown in Figure 2.8a. The observed oxygen and sulfur emission are found to originate from collisional excitation of the neutral gas of Io's atmosphere by impinging magnetospheric electrons. *Roesler et al.* (1999) find that the latitudinal location of the equatorial spots and the brightness asymmetry of the limb glow are correlated to the changing magnetospheric environment. The varying orientation of the background field leads to a *rocking* of the auroral spots about the equator. The equatorial spots, the limb glow and the extended emission in the STIS aurora observations are analyzed in-depth by *Retherford et al.* (2000), *Retherford et al.* (2003) and *Wolven et al.* (2001), respectively. *Retherford et al.* (2000) found that the rocking follows to ∼80% the orientation of the magnetic field direction. Additionally, the spots appear to be shifted from the sub- and anti-Jovian meridian towards the wake side by about 10−30°.

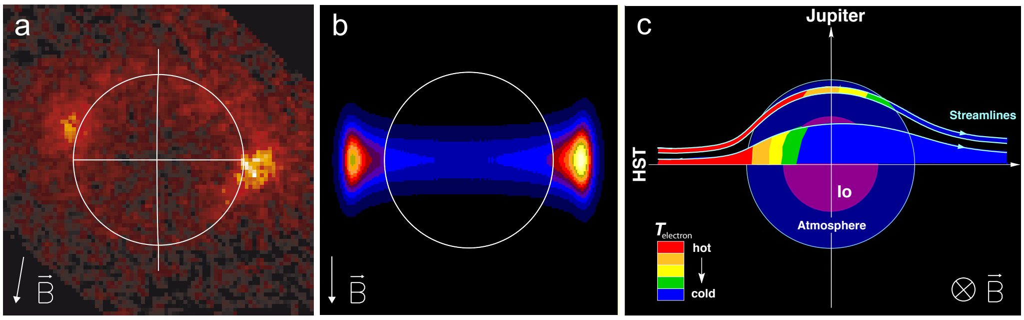

Figure 2.8: *(a) HST STIS image of the oxygen emission OI] 1356 Å showing the bright equatorial spots, which are shifted up and down from the equator in correlation with the varying orientation of the magnetic field (Roesler et al. 1999). (b) Simulated oxygen emission for a southward oriented magnetic field (Saur et al. 2000). (c) Sketch of the plasma flow pattern and the different decrease of electron temperature along the streamlines (after Saur et al. 2000).*

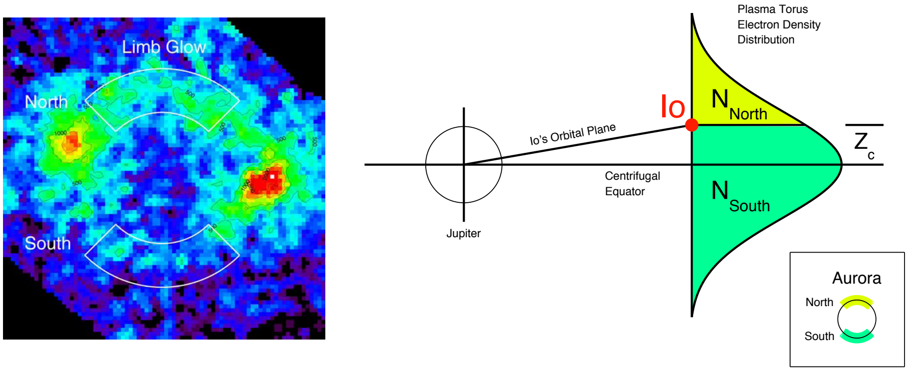

Figure 2.9: *(Left) HST STIS image of the OI] 1356 Å emission showing a stronger limb glow on the northern hemisphere. (Right) Sketch of the limb glow variation due to Io's position with respect to the torus (Figures 1 and 3 of Retherford et al. 2003).*

By applying the plasma model described in the previous section to simulate the emission *Saur et al.* (2000) showed that the OI] 1356 Å aurora morphology and brightness is produced by collisional excitation of the atomic oxygen gas with impinging thermal torus electrons, for a mixing ratio of O/SO$_2$ of $\sim$20%. They observed morphology is explained by the flow pattern of the magnetospheric plasma in the vicinity of Io in combination with the anisotropy of the thermal electron conductivity in a magnetized plasma. While the electrons can move almost loss-free parallel to the magnetic field leading to an extremely high thermal field parallel conductivity, there will be essentially no heat conducted perpendicular to the magnetic field (*Banks and Kockarts* 1973). Hence, although the local torus electrons lose their energy by inelastic collisions with the neutral gas, the heat conduction along the magnetic field prevents the electrons from cooling. At the same time, the flow of the magnetospheric plasma is strongly deflected around Io by the plasma interaction. Consequently, the torus electron energy in the flux tubes directly upstream of Io is spread over a larger area than the electrons of the flux tubes reaching the flanks of Io, see Figure 2.8c. The energy is thus deposited preferentially on Io's flanks, where the bright spots arise. The modeled emission pattern is depicted in Figure 2.8b. A tilt of the magnetic field leads to a tilted distribution of the magnetospheric electrons and the equatorial spots are thus correlated with the background field. Furthermore, the simulation showed that the brighter anti-Jovian spot might be produced by the ionospheric Hall effect, which diverts the electron flow toward Jupiter, see Figure 2.5. Contributions of field-aligned energetic electrons to triggering the UV aurora as proposed by *Michael and Bhardwaj* (2000) are presumably low as their distribution (*Frank and Paterson* 1999) and the expected time variability (*Jacobsen et al.* 2010) are not in agreement with the observed emission pattern.

Retherford et al. (2003) found that the limb glow on the hemisphere facing the plasma torus is up to two times brighter than on the opposite hemisphere. They correlate the brightness to the electron density and temperature in the torus above and below Io, see Figure 2.9. Estimating the electron motion along the field lines *Retherford et al.* (2003) derive a density distribution for the electrons in the flux tubes, which explains the observed limb glow ratios. The morphological characteristics of the sulfur aurora are similar to the oxygen emission pattern (*Feaga et al.* 2002). Analyzing the relative intensities of the detected sulfur emission lines at 1479 Å (see Figure 2.10) *Feaga et al.* (2002) estimate that a mixing S/SO$_2$ ratio of 0.04−0.3% is consistent with the measured intensities.

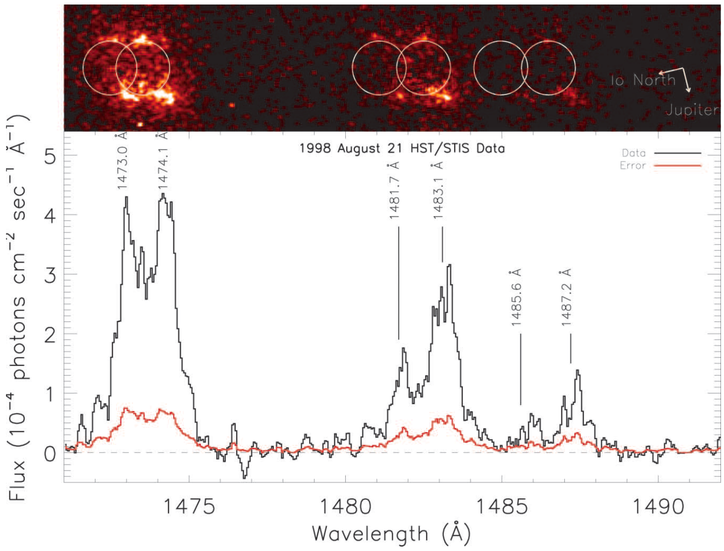

Figure 2.10: *STIS G140M medium resolution observation images (top) and extracted spectra (bottom) showing the SI 1479 Å multiplet (Feaga et al. 2002).*

An oxygen and sulfur aurora has also been observed at wavelengths in the visible wavelength range. *Trauger et al.* (1997) found a bright feature in the oxygen and sulfur emission around 6300 Å and 6716 Å/6731 Å in Io's wake with spatially resolved observations taken by the HST Wide Field and Planetary Camera 2 (WFPC2). *Moore et al.* (2010) simulated the excitation mechanism of these emissions with a Monte Carlo model and found that the north/south asymmetry of the wake emission feature depends on Io's position relative to the torus similar to the limb glow variations in the STIS images. With ground-based observations *Oliversen et al.* (2001) monitored Io's OI 6300 Å emission over a period of ten years (1990−1999) finding both periodic long term variations in correlation with the changing magnetospheric environment, and short-term fluctuations on timescales of tens in minutes, which they attribute to non-thermal field aligned electron beams (e.g., *Frank and Paterson* 1999).

After the arrival of the Galileo probe at the Jovian system and the flyby of the Cassini spacecraft in 2000, Io's auroral emission has been observed extensively by the on-board imaging systems Galileo SSI (Solid State Imager) and Cassini ISS (Imaging Science Subsystem). The images include wavelengths from the near infrared to visible and near-UV (NUV). For longer wavelengths the surface albedo increases considerably. The visible aurora observations are thus restricted to eclipse events, when no sunlit overlays the weaker auroral radiation. In the comprehensive analysis of the Galileo aurora images *Geissler et al.* (2001) found many similarities in morphology and time variability to the STIS UV observations including the correlation of the spots with the magnetic field, see Figure 2.11 (left). Additionally, *Geissler et al.* (2001) observed enhanced visible aurora near active volcanic plumes and stronger emissions in the wake than on the upstream side. In their analysis of the Cassini ISS filter observations of the eclipse aurora *Geissler et al.* (2004) investigated morphological differences between different wavelengths in the images, which they attribute to differing distributions of the emitting species SO_2, O, Na and K (Figure 2.11, right). Limb glows, which are attributed to minor components, indicate that O, Na and K are abundant all over the surface, whereas the emission attributed to SO_2 appears to be confined to equatorial regions.

The general appearance and variability of the auroral emission, while Io passes through eclipse,

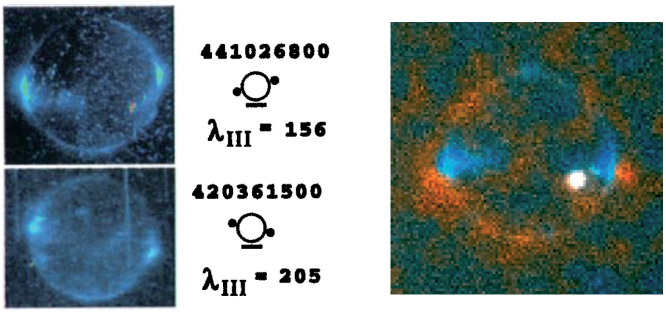

Figure 2.11: *(Left) Galileo SSI clear-filter eclipse images of Io showing the rocking of the brightest emission around the equator correlated to the magnetic System III longitude λ_{III} (Plate 1 e and j of Geissler et al. 2001). (Right) Cassini ISS multispectral ecplise observation composed of UV filter (blue), visible-red filter (red) images on a clear-filter image (white). The red emission is attributed to O abundant a higher altitudes, the bluish glow is from SO_2. Thermal emission from the hot spot of Pele volcano appears bright in the clear-filter image, the faint blue emission close to the north pole might the glowing Tvashtar plume (Plate 1 b of Geissler et al. 2004).*

possibly provide very instructive information about the nature of the atmosphere. When Io enters Jupiter's shadow, two opposing effects control the evolution of the aurora (*Saur and Strobel* 2004). On the one hand, since the atmospheric gas partly freezes out, there is less neutral gas abundant, which potentially can be excited. On the other hand, a decrease of atmospheric density after eclipse ingress leads to a decreasing interaction strength. The deflection and cooling of the plasma flow is lower and the streamlines of the electrons are less divergent leading to a higher α parameter defined by Equation (2.16). *Saur and Strobel* (2004) calculated the response of Io's electrodynamic interaction and auroral radiation to a temporal change in the atmosphere. Depending on the total atmospheric decay they find three qualitatively different scenarios with two of them including a transient post-eclipse brightening. Generally, the total emission intensity in eclipse was found to be lower than out of eclipse. *Saur and Strobel* (2004) conclude that the sublimation driven part clearly dominates the direct outgassing. The aurora response to eclipse has also been subject of multiple observations. *Clarke et al.* (1994) observed a decrease in UV aurora intensity by a factor of 3 within 20 minutes after eclipse ingress. *Retherford* (2002) investigated the variation of key features of the eclipse aurora in the STIS images and inferred a reduction factor of ~1.5 to 2 for the emission close to Io during eclipse. Time series of Io's auroral UV emissions in eclipse were obtained during the New Horizons flyby in 2007 by the on-board UV spectrometer Alice (*Retherford et al.* 2007a). For an atmosphere with 1 to 3% volcanic support the measured variations were in best agreement with simulated eclipse brightness curves by *Saur and Strobel* (2004), see Figure 2.12. Surprisingly, recent high-spectral FUV observations of Io emerging from eclipse by the HST Cosmic Origin Spectrograph (COS) did not show obvious brightness changes related to eclipse emergence (*Spencer et al.* 2012).

Even though numerous observations of the auroral emissions emerging from Io's neutral gas cloud have not yet solved the question of the true nature of the satellites atmosphere, they remain a valuable exploration tool. Solely, the data set of spectral FUV images taken by the HST STIS between 1997 and 2001 has provided many insights into the spatial and temporal variability and composition of Io's neutral gas cloud. In Chapter 4 of the present work, we will develop a comprehensive picture of the aurora formation using the full set of STIS observations, which explains the morphological variation and its correlation to the magnetospheric changes. Thereby, we will show that the observed aurora varies very systematically and is indeed strongly coupled to the plasma environment.

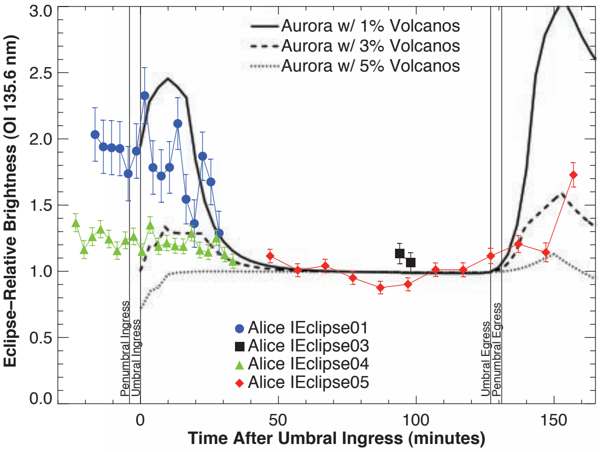

Figure 2.12: *Times series of OI] 1356 Å brightness during four eclipse events taken by the NH Alice spectrograph in comparison with modeled brightness curves by Saur and Strobel (2004) (Retherford et al. 2007a).*

In 2007, Io's auroral emission in eclipse has been observed simultaneously by the NH Long Range Reconnaissance Imager (LORRI) and by the HST Advanced Camera for Surveys (ACS) and the observations revealed detailed features of the aurora, such as a huge glowing plume at the Tvashtar paterae close to the north pole (*Spencer et al.* 2007a, *Retherford et al.* 2007a). In Chapter 5, we will infer constraints on the atmospheric abundances, when Io is in Jupiter's shadow, by comparing the LORRI and ACS eclipse images to simulations results from the *Saur* plasma model.

2.2 Europa and its environment

After more and more observations had substantiated the existence of liquid water under Europa's icy crust, the satellite captured copious attention. The putative subsurface ocean is supposed to cause not only numerous interesting surface features but also the observed magnetic field perturbations at Europa. An influence on the atmosphere or aurora has not yet been detected. As our study of Europa's aurora emission is restricted to the analysis of the one STIS observation campaign of 1999, we will give only a short introduction to Europa's interior, surface structure and interaction, before we summarize all previous observations of the atmosphere and the emerging auroral emission.

2.2.1 Interior, surface and subsurface ocean

Like Io, Europa is differentiated, probably consisting of a metallic core and a rocky mantle (*Anderson et al.* 1998). The outer crust and surface, however, differ significantly in terms of composition and appearance as they mainly consist of solid or partially molten water. This ice-liquid water shell is about 80−200 km thick (*Sohl et al.* 2002, *Schubert et al.* 2004). Europa's surface is one of the smoothest in the Solar System with very few craters and small elevations, but a variety of particular and sometimes unique features. The average age of the surface is estimated to 40−90 million years (*Bierhaus et al.* 2009), which implies that ongoing resurfacing takes place at Europa.

The most prominent surface features are elongated streaks crisscrossing the entire globe, called

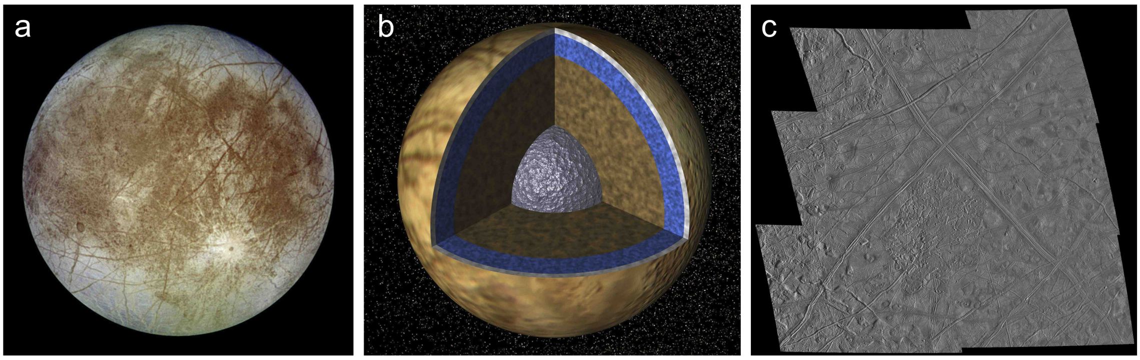

Figure 2.13: *(a) Galileo SSI natural color image of Europa's trailing hemisphere. Dark brown areas resemble rocky material derived from interior or exterior sources. (b) Sketch of Europa's interior showing a solid ice crust over a layer of liquid water, a silicate mantle and a metallic core. (c) Galileo SSI images showing an area, where the icy crust of Europa has been disrupted by activity from below (known as chaos terrain) just below the long crossing lineae. The image is 300 km by 300 km across with a resolution of 180 m per pixel. (Courtesy of NASA)*

lineae, see Figure 2.13a and c. These markings may appear curved or straight, brighter or darker than the surrounding surface depending on the formation and age, and they can be troughs or ridges (e.g., *Doggett et al.* 2009). *Geissler et al.* (1998) systematically studied the global distribution and appearance of this lineaments and presume the formation of the various cracks to be the major resurfacing mechanism. The young surface age including relaxation of craters, apparently mobile ice blocks, smooth deposits and the so-called chaos terrains (Figure 2.13c) provides indirect evidence for a subsurface ocean (e.g., *Carr et al.* 1998, *Pappalardo et al.* 1998). The observed tectonic patterns can be explained by a non-synchronous rotation of the interior (*Greenberg et al.* 1998), which in turn requires a decoupled crust e.g., due to a subsurface liquid or convective layer. Additionally, thermal models of the interior come to the conclusion that Europa most likely possesses a liquid water ocean below the crust (e.g., *Spohn and Schubert* 2003). The energy to keep such a subsurface molten layer from freezing is thought to be supplied by tidal heating due to the mentioned three-body Laplace resonance with Io and Ganymede and the arising eccentricity of Europa's orbit (see Section 2.1.1). This energy source possibly compensates the loss due to heat conduction or convection through the crust (e.g., *Cassen et al.* 1979, *Spohn and Schubert* 2003).

A more direct, but less apparent, i.e., less visible evidence for the existence of liquid water in Europa's interior is brought by Galileo magnetic field measurements (e.g., *Khurana et al.* 1998, *Kivelson et al.* 2000, *Zimmer et al.* 2000, *Schilling et al.* 2007). Similar to the situation at Io, the background magnetic field at Europa changes with time, where the tilt of the Jovian dipole moment contributes most to the variability, see Figure 2.7. A layer of liquid and salty water could have a sufficient conductivity to generate measurable magnetic field perturbations through induction. Hydrated minerals observed on the surface (*McCord et al.* 1998) are supposed to originate from the underlying ice crust implying a considerable salt concentration and thus a high conductivity for a subsurface ocean (e.g., *Hand and Chyba* 2007). Hence, the temporal variability of the background magnetic field induces electric currents inside Europa, which in turn produce magnetic field perturbations. The amplitudes and phase shifts of the induction signals detected during several Galileo flybys indicate ocean conductivities comparable to or less than that of terrestrial seawater if the ocean thickness is on the order of 10−200 km (*Zimmer et al.* 2000, *Schilling et al.* 2007). Very detailed reviews of Europa's interior and surface properties can be found in Parts II and III of *Pappalardo et al.* (2009).

Table 2.2: Physical properties of Europa and the local magnetospheric plasma (Neubauer 1998, Kivelson et al. 2004, and references therein).

Radius	$\mathrm{R_E}$	1569 km
Semi-major axis	$\mathrm{a_{Eu}}$	9.4 $\mathrm{R_J}$
Orbital period	$\mathrm{T_{Eu}}$	3.55 days
Orbital velocity	$\mathrm{v_{Eu}}$	14 $\mathrm{km\,s^{-1}}$
Average Jovian magnetic field	B_0	$\sim$400 nT
Corotational velocity	v_{corot}	118 $\mathrm{km\,s^{-1}}$
Relative plasma velocity	v_{plasma}	104 $\mathrm{km\,s^{-1}}$
Electron number density	n_e	18-250 $\mathrm{cm^{-3}}$
Temperature of thermal electrons	k_BT_e	20 eV
Ion temperature	k_BT_i	$50-400$ eV
Ion gyrofrequency	ω_{ci}	3 $\mathrm{s^{-1}}$
Ion gyroradius	r_{ci}	8-19 km
Alfvén Mach number	M_A	$\sim$0.5
Thermal pressure / magnetic pressure	β	$\sim$0.06
Alfvén conductance	Σ_A	$\sim$4.9 S
Pedersen conductance	Σ_P	$\sim$30 S
Hall conductance	Σ_H	$\sim$10 S

2.2.2 Interaction with the Jovian magnetosphere

Europa also possesses a tenuous atmosphere, which will be described in the following section. Therefore, collisions between the fast rotating plasma and the neutrals perturb the plasma flow and magnetic field around the satellite, which leads to the formation of Alfvén wings similar to the interaction scenario at Io, see Section 2.1.3. Likewise, the plasma β of $\sim$0.06 shows that the magnetic field, although lower than at Io by factor 10, mainly controls the plasma flow. Properties of Europa and the magnetospheric environment are given in Table 2.2.

The *Saur* model, which has been applied to the Io's sub-Alfvénic plasma interaction by *Saur et al.* (1999), was first used to simulate the Europa scenario by *Saur et al.* (1998). For an atmospheric column density of 5×10^{14} $\mathrm{cm^{-2}}$, *Saur et al.* (1998) calculated a deflection of the plasma quantified by the interaction parameter (Eq. 2.16) of $\alpha_{Eu} \approx 0.2$. The authors estimate a total current of 7×10^5 A through the wings, which is $\sim$14% of the total current estimated for Io. Since the atmospheric densities are lower at Europa than at Io, the Pedersen conductance dominates the Hall conductance (see also Table 2.2) leading to an only slightly asymmetric plasma flow (*Saur et al.* 1998). To understand the Galileo magnetometer and plasma observations both the induction effect in the interior and the atmospheric interaction have to be studied (*Neubauer* 1999) . The only numerical model accounting for both effects has been developed by *Schilling et al.* (2007). The model results showed that the induced magnetic fields cause time varying asymmetries in the Alfvén current system and the plasma flow outside Europa (*Schilling et al.* 2008).

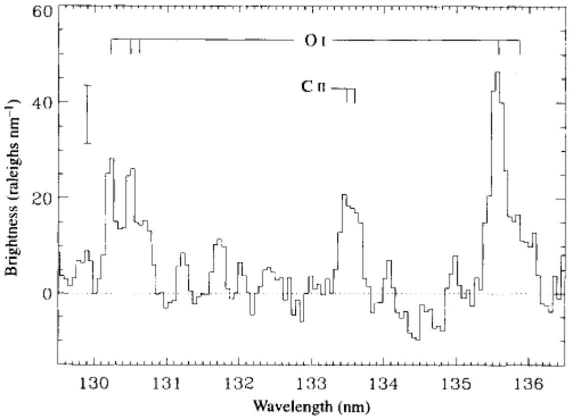

Figure 2.14: *UV spectrum of Europa's trailing hemisphere obtained by the HST GHRS with two oxygen emission features from the tenuous atmosphere (Hall et al. 1995).*

2.2.3 Atmosphere and aurora

Based on laboratory sputtering measurements, molecular oxygen was predicted to be the primary neutral species in Europa's atmosphere (*Brown et al.* 1982), yet before neutral gas has been clearly detected in the vicinity of Europa. More than ten years later, *Hall et al.* (1995) detected oxygen emission in UV spectra obtained by the HST Goddard High Resolution Spectrograph (GHRS) observing Europa's trailing hemisphere. Figure 2.14 shows the obtained UV spectrum with intensity peaks at 1304 Å, 1335 Å and 1356 Å. While the CII 1335 Å radiation is reflected sunlight from the surface, the relatively strong oxygen multiplets at 1304 Å and 1356 Å imply that radiation is emitted from atomic or molecular oxygen in Europa's atmosphere. Contributions from reflected and resonantly scattered sunlight is comparably small. Subsequent GHRS observations by *Hall et al.* (1998) of the leading and again the trailing hemisphere confirmed the measured intensities of the oxygen lines. After subtraction of the contributions from backscattered solar light the brightness ratio I(1356)/I(1304) of 1.9−2.2 indicates that the O_2 abundance clearly exceeds the O abundance. For electron impact on O_2 the expected ratio is $\sim$2 over a large range of electron temperatures, whereas electron impact on O would clearly favor OI 1304 Å over OI] 1356 Å. Assuming a homogeneous and constant electron density and temperature and an atmosphere that is confined to the geometric cross section of the visible disk of Europa, *Hall et al.* (1998) infer an O_2 column of $(0.24 - 1.4) \times 10^{15}$ cm^{-2}.

The HST STIS provided the first spatially resolved images of Europa's UV aurora, which revealed an asymmetric oxygen emission pattern in both oxygen multiplets with a maximum in the anti-Jovian northern quadrant (*McGrath et al.* 2004). The observed oxygen and Lyman-α emissions are shown together with a sunlit view of Europa in Figure 2.15. *Cassidy et al.* (2007) investigated the properties of Europa's surface regolith to cause a non-uniform O_2 distribution that could explain the observed morphology. Implementing a zero sticking coefficient for O_2 in the area of enhanced oxygen emission into a Monte Carlo simulation for the atmosphere they are able to reproduce the observed OI] 1356 Å morphology originating from a spatially non-uniform atmosphere. In a review paper by *McGrath et al.* (2009), the authors discuss the spectral STIS images a bit more in detail and mention a time variability of the OI] 1356 Å intensity and morphology over the $\sim$7-h duration of the HST visit. The observed H I Lyman-α morphology is interpreted as solar radiation reflected from an inhomogeneously reflecting surface, where the regions of a higher UV albedo

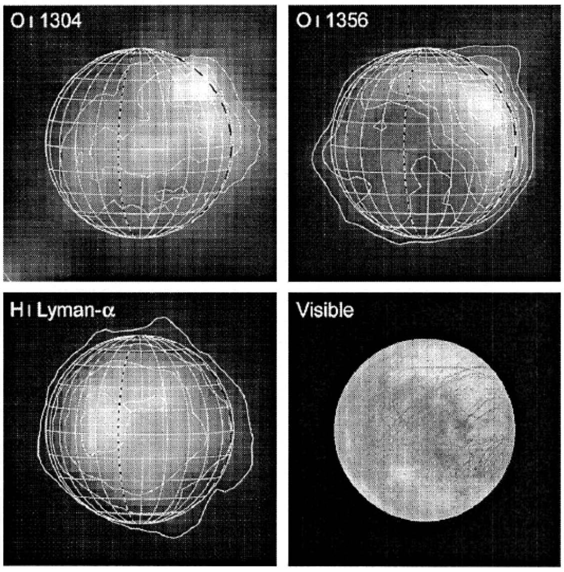

Figure 2.15: Composite HST STIS images of the observed spectral features of OI 1304 Å, OI] 1356 Å and HI 1216 Å Lyman-α during 5 HST orbits in October 1999 and a sunlit view of the observed hemisphere (McGrath et al. 2009).

appear to be correlated with darker visible regions (Figure 2.15, bottom line).

There have been three observation campaigns where the HST ACS monitored Europa's oxygen aurora in and out of eclipse, one of them concurrent with observations by the NH Alice spectrograph (*Retherford et al.* 2007b, *Sparks et al.* 2010, *Saur et al.* 2011). The sunlight observations suffered a severe "red leak" problem, as solar NUV light is scattered into the oxygen emission images, see Figure 2.16a. *Saur et al.* (2011) modeled and subtracted the surface reflected solar light in the images (see Figure 2.16b) and inferred a remaining intensity from atmospheric emissions of ~130−230 Rayleigh depending on the magnetic latitude of Europa's position. By integrating along the north-south axis to achieve a better signal-to-noise ratio *Saur et al.* (2011) detected a surplus of emission around the central longitude (~ 90° west longitude) in the images (Figure 2.16c) coinciding with the longitudes, where the strongest local shear stress on the leading hemisphere is expected. A high shear stress on the surface cracks might lead to a release of water gas and a local increase of atmospheric density.

Observations with higher spectral, but barley spatial resolution by the Cassini UltraViolet Imaging Spectrograph (UVIS) indicate a O/O_2 ratio of ~0.02 of the near surface atmosphere (*Hansen et al.* 2005). In addition, the Cassini UVIS spectra confirmed the presence of an extended neutral cloud consisting of H_2 and to a lesser extent O_2. The particles are lost through thermal escape from the near atmosphere forming a torus in Europa's wake orbit and were first discovered in Cassini measurements of energetic neutral atoms by *Mauk et al.* (2003). Atomic Na and K have also been observed in Europa's extended neutral cloud (*Brown and Hill* 1996, *Brown* 2001). The measured relative abundance of the two alkalis indicates an endogenic source (*Johnson et al.* 2009). The formation of the near surface oxygen aurora that is imaged by the STIS appears to be independent of the extended clouds, as a correlation with or influence of the O_2 abundance on Na or K has not been detected (*Leblanc et al.* 2005, *Johnson et al.* 2009).

A variety of theoretical studies analyzed the production and loss mechanisms for Europa's atmosphere. Impinging of charged particles leads to sputtering and radiolysis of the surface ices

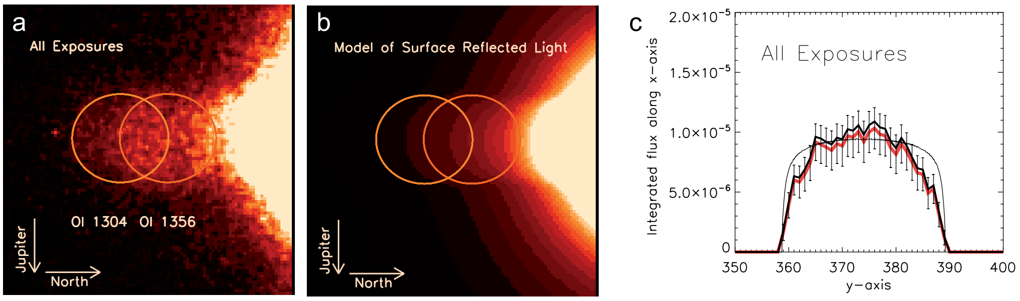

Figure 2.16: *(a) Composite HST ACS images from 2008 showing the strong red leak (to the right in the image), which disguises the atmospheric emissions. (b) Modeled disk-reflected and dispersed solar light, which is subtracted from the observation image. (c) Axis-integrated observed flux on the disk as a function of the sub- to anti-Jovian direction (red and black jagged lines) in comparison to symmetrically radiating disk (thin black line) (Saur et al. 2011).*

releasing directly sputtered H_2O molecules as well as products of H_2O decomposition, see Figure 2.17. The dissociation products can recombine forming primarily O_2 and H_2, where O_2 is less volatile and forms the surface-near bound atmospheric layer (*Johnson et al.* 2004). Sublimation might be a competitive source only near the sub-solar point (*Johnson et al.* 2009). Ionization and pick-up is the dominant loss process for oxygen in Europa's atmosphere (e.g., *Shematovich et al.* 2005). H_2O is lost rapidly due to sticking (freezing) on Europa's cold surface.

Pospieszalska and Johnson (1989) investigated surface sputtering depending on the gyroradii and pitch angles of the impinging ions and propose an asymmetric oxygen abundance with higher densities on the trailing side. The principal generation of the hydrogen-oxygen atmosphere has been studied using kinetic Monte Carlo models (e.g., *Shematovich and Johnson* 2001, *Shematovich et al.* 2005, *Smyth and Marconi* 2006). Recently, *Plainaki et al.* (2012) modeled the different release processes and modifications of the released particles with a Monte Carlo simulation for the case when Europa's leading hemisphere is illuminated by the sun. They estimate column densities of $(0.3-1.5)\times10^{15}$ cm^{-2} for O_2 and $(2-8)\times10^{13}$ cm^{-2} for H_2O, with H_2O dominating at higher altitudes. While H_2 accumulates primarily on the trailing hemisphere where sputtering is more intense, the O_2 abundance peaks at the sub-solar point, which coincides with the leading hemisphere in the simulation.

The only model including the effects of the plasma interaction on the atmosphere and also for the oxygen emission is the *Saur* Europa model. The simulation results of *Saur et al.* (1998) indicate that impact ionization of the neutrals allows the generation of the ionospheric density measured by *Kliore et al.* (1997) (without photo-ionization), leading to an atmospheric loss due to pick-up of 50 kg s^{-1}. For an O_2 column density of 5×10^{14} cm^{-2} the calculated OI] 1356 Å brightness is in agreement with the HST GHRS measurements. The modeled emission morphology, however, is clearly dominated by a strong limb glow due to the line-of-sight effect, whereas the STIS observations by *McGrath et al.* (2004) revealed a completely different pattern with the brightest regions on the disk.

Taken together, Europa's atmosphere consists mainly of O_2 with column densities in the range of $10^{14}-10^{15}$ cm^{-2} corresponding to ∼1% of the atmospheric density at Io. Whereas Io's atmosphere is mainly sustained by sublimation of SO_2 frost or volcanic outgassing, the main source of Europa's gas envelope is the ejection of water molecules from the surface. Although H_2O is the dominant ejecta it sticks efficiently to surface grains, while O_2 does not. So far, observations of the oxygen emissions have provided the most instructive and revealing information about Eu-

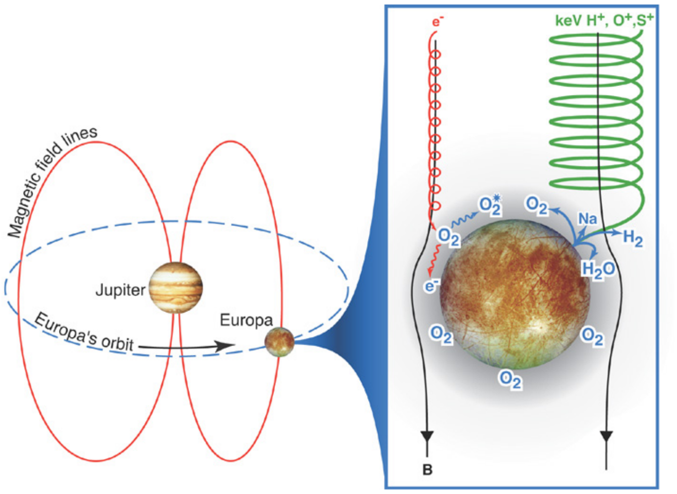

Figure 2.17: *Schematic of the formation of Europa's neutral gas environment. Ions (green) and electrons (red) alter and erode the surface, producing a tenuous atmosphere composed mostly of* O_2*.* H_2 *and Na (and other trace species) form an extended cloud, whereas* H_2O *freezes upon contact with the surface (Johnson et al. 2004).*

ropa's surface-near atmosphere. In Chapter 6, we will analyze the spatially resolved STIS images of the OI 1304 Å, OI] 1356 Å, HI 1216 Å and CII 1335 Å lines in detail and investigate all possible implications for the atmospheric distribution and composition considering influence of plasma interaction and induction in Europa's interior.

Before we start with the evaluation of the observed auroral emissions from the atmospheres of Io and Europa, we will describe the processing of the image data and briefly introduce the applied data analysis techniques in the following Chapter 3.

3 Data processing and analysis

In the first part of this chapter we will elaborate on the characteristics of the spectral-spatial HST STIS observations, before we explain how the image data is processed to extract the two-dimensional images that are analyzed in Chapters 4 and 6. The second part contains a brief technical description of the HST ACS and HN LORRI observations analyzed in Chapter 5. In the last part of this chapter an overview of applied data analysis techniques is given.

3.1 HST STIS spectral UV observations

The HST Space Telescope Imaging Spectrograph (STIS) has three 1024×1024 detector arrays: A charge-coupled device (CCD) with a 52"×52" field of view and two Multi-Anode Multichannel Arrays (MAMA) covering the near-ultraviolet (NUV) and far ultraviolet spectrum (FUV), each with a 25"×25" field of view. STIS can be used to obtain images in undispersed light as well as in the spectroscopic mode, where various gratings and apertures are available to achieve both a spatial and spectral resolution (see STIS Instrument Handbook, *STScI* 2011).

All STIS observations analyzed in this thesis are taken in the first-order spectroscopy mode using the 52" by 2" aperture slit and one of the low or medium resolution gratings G140L, G140M and G230M, see Tables 3.1 and 3.2. This slit allows a spatial resolution of the entire disk of the satellites with a simultaneous spectral resolution determined by the dispersion of the grating. The dispersions are $\Delta\lambda = 0.584$ Å pixel^{-1} for G140L, $\Delta\lambda = 0.053$ Å pixel^{-1} for G140M and $\Delta\lambda = 0.087$ Å pixel^{-1} for G230M with bandwidths of 590 Å, 54 Å and 90 Å, respectively. The effective slit length is 25" determined by the used FUV and NUV MAMA detectors allowing to capture features ~20 satellite radii away in the spatial direction. Thus, on the 1024×1024 pixel detector several distinct images of the satellite and its environment are pictured for various spectral lines sometimes overlapping if the separation between the lines is lower than the satellites' diameter. The coordinate of the spatial or cross-dispersion axis parallel to the slit will be designated y_d. x_d refers to the coordinate of the dispersion axis perpendicular to the slit. Each x_d corresponds to a wavelength λ_d determined by the dispersion $\Delta\lambda$ of the grating through

$$\lambda_d = \lambda_0 + (x_d - x_0) \cdot \Delta\lambda \ , \tag{3.1}$$

for a given reference pixel x_0 and wavelength λ_0. For a given λ_d, the corresponding x_d determines the pixel in horizontal center of the slit. Figure 3.1 illustrates the setup of the observations.

For the studied observations, the STIS is generally used in the time-tag mode, i.e., an event stream containing the pixel (x_d,y_d) and time (t) of each detection is recorded, with a time resolution of 125 μs. Thus, one exposure with an approximate duration of 15–20 minutes could be split in images

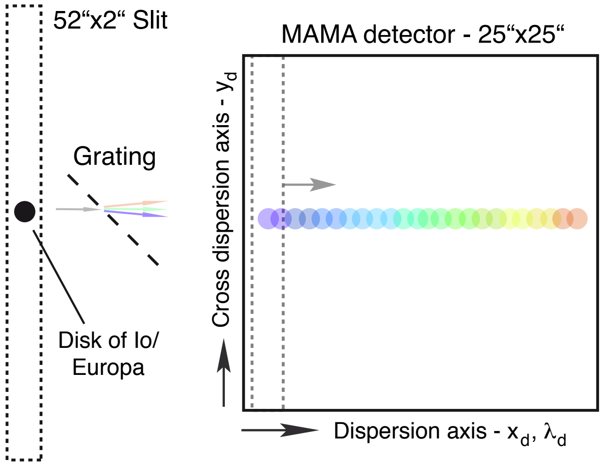

Figure 3.1: *Sketch of the setup of the HST STIS observations. The horizontal dispersion axis contains simultaneous spatial and spectral resolution. The colored circles illustrate the mapped disk of the satellite at different wavelengths.*

of small time intervals. However, as the average signal-to-noise ratio (SNR) of one pixel for the full exposure time is on the order of one and thus very low, a reasonable analysis of smaller time steps is difficult if not impossible.

The raw STIS data passes through a processing pipeline performed by the software *calstis*, which is explained in detail in the STIS Data Handbook (*STScI* 2007). The common processing includes a pixel quality check, a dark signal subtraction and a flat-field correction. The output is the *flat-fielded data* with the file suffix *flt*. In a next step of the processing pipeline, a two-dimensional rectification and a unit conversion from detector counts (*flt* files) to cgs flux (radiance in [$\mathrm{erg\,cm^{-2}\,s^{-1}\,\AA^{-1}\,arcsec^{-2}}$]) is performed. The *rectified spectral images* are written to files with the suffix *x2d*. The rectification corrects a small misalignment between the dispersion axis and the horizontal axis of the detector. The flux conversion accounts for the wavelength dependent system and aperture throughput of the used optical elements assuming the observed object to be a continuum point source. Throughout our work, we use the *x2d* data files, since the rectification allows a simultaneous analysis of images at different spectral lines without correction (or determination) of the satellite's position in each image, separately. The throughput information is obtained from the *calstis* calibration files and the wavelength dependence in the *x2d* images is eliminated for each analyzed undispersed image.
The data files (both *x2d* and *flt*) contain three extensions and file headers with important keywords characterizing the observations and the processing. In the first extension the values for the measured flux $I(x_d, y_d)$ are stored, the second contains the statistical errors $\sigma_0(x_d, y_d)$, and the third stores the data quality values, which flag suspect pixels. The stored error values correspond to the square root of the detected pixel counts propagated through the calibration process. In our error analysis we calculate the errors and their propagation starting from the processed statistical errors given in the file extension. For further explanation on the data handling and processing see Appendix A.

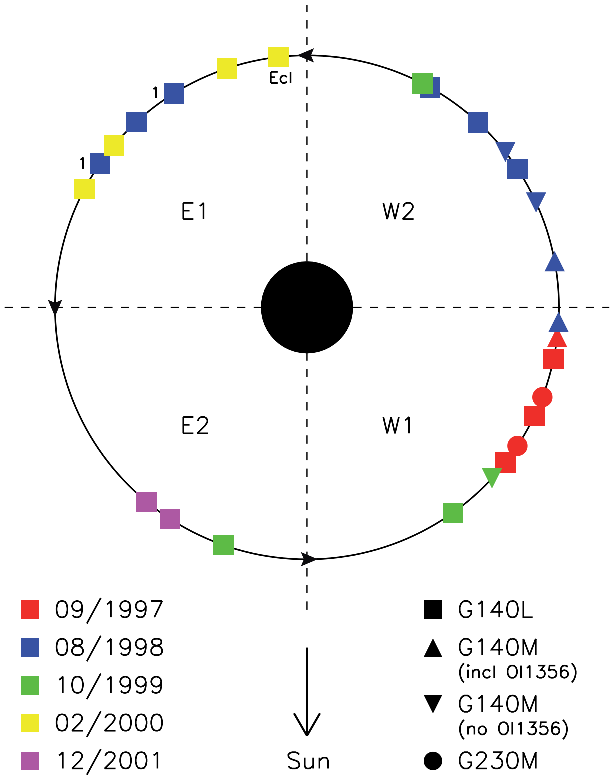

Figure 3.2: *Io's orbital location with respect to Jupiter for all 26 HST orbits of STIS UV observations listed in Table 3.1. "Ecl" marks the eclipse observation, "1" the single exposure orbits. The orbit is subdivided in four sections: W1 and W2 (E1 and E2) are the quarters before and after western (eastern) elongation, respectively. The observation dates are color coded, the observation mode (G140L/G140M/G230M) is illustrated by the shapes.*

3.2 STIS observations: Io

3.2.1 Overview

In the course of four HST observation campaigns the STIS acquired 50 exposures of Io at UV wavelengths with the 52"×2" slit, see Table 3.1. Each of the four campaigns includes several *visits*. Within a *visit*, HST observes Io during consecutive *orbits* of the telescope around Earth acquiring two exposures per *orbit*, with the exception of orbits 14 and 16, where one exposure failed. In Table 3.1, the orbits of all campaigns are numbered continuously from the first in September 1997 until the so far last observation orbit in December 2001. In the images the width of Io's disk varies between 0.92" and 1.27" depending on the distance from the HST. Figure 3.2 shows Io's orbital longitude (OLG) as seen from the Sun for the 26 HST orbits, where STIS monitored Io's UV emission.

Figure 3.3 shows (A) the sum of raw images from three exposures taken with the low resolution grating G140L and (B) the composite image of two exposures with medium resolution grating G140M centered at 1371 Å (*Roesler et al.* 1999, their Figure 1). Horizontally, the spatial information of the 2" wide slit is convolved with the spectral information, whereas the vertical axis is merely spatial. Above, several spectral lines or multiplets are given for various species abundant in

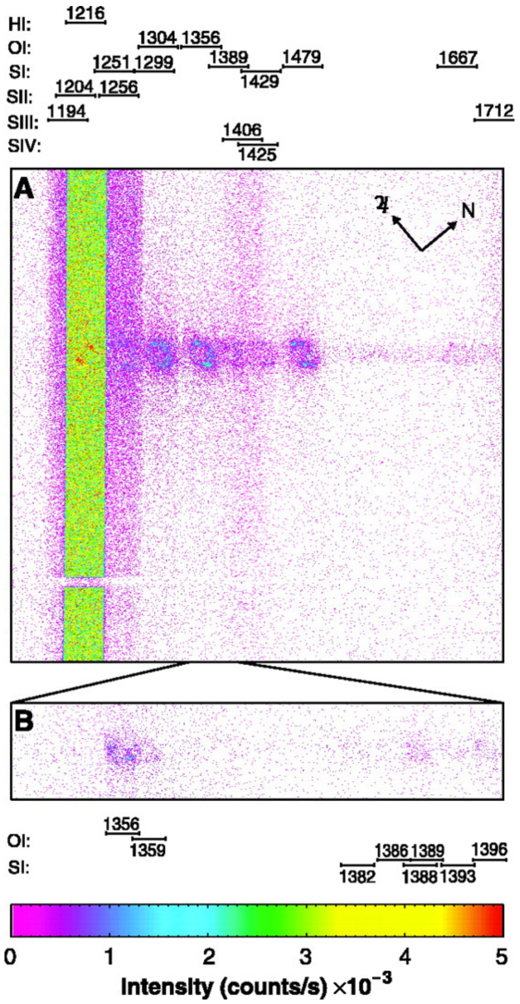

Figure 3.3: *(A) Composite raw image of three exposures obtained during HST orbits 4 to 6 in the G140L mode. (B) Raw image of two G140M exposures. Above, several spetral lines are indicated. The compass shows the direction towards Jupiter (♃) and Jovian North (N). Note, that the intensity specified at the color bar has to be* ***multiplied*** *by* 10^{-3} *for the actual counts per second, see color bar. For further explanations see text (Roesler et al. 1999, their Figure 1).*

Io's atmosphere or the Io plasma torus. We will describe now the observed UV emission features and the current understanding of their formation processes.

Airglow (scattered sunlight) from the geocorona fills the full slit at the HI 1216 Å Lyman-α line. When HST comes closer to the terminator in its orbit, this terrestrial airglow becomes brighter and can be additionally detected along the slit at the oxygen multiplet OI 1304 Å. The Lyman-α emission on and around Io's disk is comprised of solar Lyman-α radiation reflected off Io's surface and attenuated by the SO_2 atmosphere, the geocoronal background, a possible contribution from Iogenic hydrogen and an interplanetary gas component (*Feldman et al.* 2000). The sulfur ion emissions (SII, SIII, SIV) originate primarily from excitation of both torus ions and ionospheric ions, as the emission extends further out in the slit and possesses a maximum in the disk region, most apparent at SII 1256 Å. The two bright disk features to the right of the broad SII 1256 Å torus emission are attributed to the spin forbidden and optically allowed oxygen multiplets OI(^{5}S – ^{3}P)1356 Å and OI(^{3}S – ^{3}P)1304 Å. For OI 1304 Å, reflected and scattered solar radiation and Iogenic emission contribute to the signal. In case of OI] 1356 Å, scattered light

Table 3.1: *List of all HST STIS exposures of Io at UV wavelengths obtained with the 52"x2" slit.* ϕ_{Io} *is the diameter of the disk of Io in the observation.* [1]*orbits with only one exposure.*

HST ID / PI	No	Orb	Dataset	Date	$T_{start}(UTC)$	T_{exp} [s]	ϕ_{Io} ["]	Grid	Bandwidth [Å]
7582	1	1	o49d02010	1997-09-26	10:29	900	1.16	G230M	1888 - 1978
H.W. Moos	2		o49d02a10	1997-09-26	10:47	900	1.16	G230M	1888 - 1978
	3	2	o49d02020	1997-09-26	11:51	1180	1.16	G230M	1888 - 1978
	4		o49d02a20	1997-09-26	12:18	1180	1.16	G230M	1888 - 1978
	5	3	o49d02030	1997-09-26	13:34	1100	1.16	G140M	1344 - 1398
	6		o49d02a30	1997-09-26	13:56	1100	1.16	G140M	1344 - 1398
	7	4	o49d01010	1997-10-14	02:44	920	1.10	G140L	1140 - 1730
	8		o49d01a10	1997-10-14	03:03	920	1.10	G140L	1140 - 1730
	9	5	o49d01020	1997-10-14	04:06	1180	1.10	G140L	1140 - 1730
	10		o49d01a20	1997-10-14	04:33	1180	1.10	G140L	1140 - 1730
	11	6	o49d01030	1997-10-14	05:43	1180	1.10	G140L	1140 - 1730
	12		o49d01a30	1997-10-14	06:10	1180	1.10	G140L	1140 - 1730
7583	13	7	o4xm03010	1998-08-21	18:53	900	1.25	G140M	1344 - 1398
F.L. Roesler	14		o4xm03020	1998-08-21	19:12	920	1.25	G140M	1344 - 1398
	15	8	o4xm03030	1998-08-21	20:25	1200	1.25	G140M	1344 - 1398
	16		o4xm03040	1998-08-21	20:52	1185	1.25	G140M	1344 - 1398
	17	9	o4xm03050	1998-08-21	22:07	1155	1.25	G140M	1442 - 1498
	18		o4xm03060	1998-08-21	22:30	1155	1.25	G140M	1442 - 1498
	19	10	o4xm03070	1998-08-21	23:42	1145	1.25	G140M	1442 - 1498
	20		o4xm03080	1998-08-22	00:05	1145	1.25	G140M	1442 - 1498
	21	11	o4xm01030	1998-08-23	17:35	1300	1.25	G140L	1140 - 1730
	22		o4xm01040	1998-08-23	18:00	1300	1.25	G140L	1140 - 1730
	23	12	o4xm01050	1998-08-23	19:15	1200	1.25	G140L	1140 - 1730
	24		o4xm01060	1998-08-23	19:38	1200	1.25	G140L	1140 - 1730
	25	13	o4xm01070	1998-08-23	20:51	1150	1.25	G140L	1140 - 1730
	26		o4xm01080	1998-08-23	21:14	1150	1.25	G140L	1140 - 1730
	27	14[1]	o4xm02010	1998-08-27	17:15	930	1.25	G140L	1140 - 1730
	28	15	o4xm02020	1998-08-27	18:20	915	1.25	G140L	1140 - 1730
	29		o4xm02030	1998-08-27	18:39	1205	1.25	G140L	1140 - 1730
	30	16[1]	o4xm02040	1998-08-27	19:58	1205	1.25	G140L	1140 - 1730
8169	31	17	o5h9a5010	1999-10-08	12:07	1000	1.26	G140L	1140 - 1730
F. Bagenal	32		o5h9a5020	1999-10-08	12:27	1000	1.26	G140L	1140 - 1730
	33	18	o5h906010	1999-10-11	04:50	800	1.27	G140L	1140 - 1730
	34		o5h906020	1999-10-11	05:07	800	1.27	G140L	1140 - 1730
	35	19	o5h907010	1999-10-11	11:17	800	1.27	G140L	1140 - 1730
	36		o5h907020	1999-10-11	11:34	800	1.27	G140L	1140 - 1730
	37	20	o5h907030	1999-10-11	12:38	1000	1.27	G140M	1244 - 1300
	38		o5h907040	1999-10-11	12:58	1000	1.27	G140M	1244 - 1300
	39	21	o5h909010	2000-02-20	09:51	800	0.93	G140L	1140 - 1730
	40		o5h909020	2000-02-20	10:08	800	0.93	G140L	1140 - 1730
	41	22	o5h909030	2000-02-20	11:09	1100	0.93	G140L	1140 - 1730
	42		o5h909040	2000-02-20	11:35	1100	0.93	G140L	1140 - 1730
	43	23	o5h9a2010	2000-02-25	12:13	600	0.92	G140L	1140 - 1730
	44		o5h9a2020	2000-02-25	12:27	600	0.92	G140L	1140 - 1730
	45	24	o5h9b2010	2000-02-25	13:31	1000	0.92	G140L	1140 - 1730
	46		o5h9b2020	2000-02-25	13:51	1000	0.92	G140L	1140 - 1730
9119	47	25	o6jn03bnq	2001-12-13	18:59	900	1.19	G140L	1140 - 1730
J.R. Spencer	48		o6jn03bpq	2001-12-13	19:17	960	1.19	G140L	1140 - 1730
	49	26	o6jn04tmq	2001-12-29	18:03	900	1.20	G140L	1140 - 1730
	50		o6jn04toq	2001-12-29	18:21	960	1.20	G140L	1140 - 1730

from both the geocorona and Io's atmosphere are negligible, since it is a spin forbidden transition (*Meier* 1991). Besides smaller solar contributions, the sulfur emission around 1479 Å originates from atomic sulfur in Io's atmosphere. The sulfur multiplet consists of several allowed (^{3}D $-$ ^{3}P) and forbidden (^{5}D $-$ ^{3}P) transitions, which are explained in detail by *Feaga et al.* (2002). Longward of ∼1500 Å the signal is principally solar light reflected off the surface (*Feldman et al.* 2000). In the medium resolution G140M spectrum in Figure 3.3B the doublet structure of the OI] 1356 Å feature with two lines at 1355.6 Å and 1358.5 Å is resolved. The color-coded count rates indicate that for an approximate exposure time of 10^3 s the counts per pixel of the raw signal are $\lesssim$1 except around.

During orbits 9 and 10, four spectral images with the G140M centered on 1470 Å were obtained resolving the SI 1479 Å multiplet (*Feaga et al.* 2002). In 1999, the G140M grating was centered at 1272 Å to image the SII 1256 Å torus emission with higher spectral resolution, but these two exposures (Orbit 20) have only been discussed briefly in a conference proceeding by *Woodward et al.* (2001). During the first two orbits in 1997, STIS monitored Io using the G230M grating at NUV wavelengths (1888–1978 Å) observing SI] 1900 Å sulfur emissions. The SI] 1900 Å images are analyzed by *Roesler et al.* (1999) and *Feaga et al.* (2002). Two exposures were acquired when Io was in eclipse by Jupiter, where the solar reflected Lyman-α component vanishes as expected (*Feaga et al.* 2009), and the Iogenic emission features appear fainter (*Retherford* 2002).

3.2.2 Processing

To increase the signal to noise ratio we combine the two exposures per orbit and analyze the resulting images. In the combined images, the signal to noise ratio per pixel of the near surface oxygen and sulfur emissions OI] 1356 Å, OI 1304 Å and SI 1479 Å are higher by a factor of 1.6 to 2 (in the readily processed images). As reference observation time T_{obs} we set the midway between the end time of the first exposure and the start time of the second exposure of one HST orbit disregarding the slightly differing exposure times. All the observational parameters, such as sub-observer longitude φ_{obs} or System III longitude λ_{III}, are set according to the observation time T_{obs}. The second exposure ends ∼40 minutes after the start time of the first one. This corresponds to 2% of Io's orbital period of 42.46 h or a rotation of Io of ∼6°. The change of the observed central meridian from the first to the second exposure is therefore negligible. The synodic rotation period of the magnetosphere and plasma torus at Io is 12.95 h, which implies a variation of the ambient System III longitude of ∼18° within 40 minutes. This change will also be neglected by combining the exposures, but we will discuss possible effects of this variation.

To exclude contributions from geocoronal scattered light, an interplanetary background, torus emissions and possible left-over detector noise a background emission along the slit is determined. Therefore, we sum over the pixels 60 to 200 (which corresponds to 2.4-3.1 R_{Io} to 7.8-10.7 R_{Io}) above and below the disk center in y_d-direction for each x_d value and subtract the average intensity from the x_d column, see Figs. 3.4a and b.

The pixel (x_d,y_d) of the object center (center of Io's disk) is specified in the header of the data files. However, the specified values might have small offsets due to pointing inaccuracy of the HST. To analyze the spatial distribution of the emission in the images, it is necessary to accurately determine the center pixel of Io's disk. The images contain a continuum of reflected solar light between 1520 Å and 1640 Å, where no Iogenic emission is expected (see Figure 3.3). The location of this disk reflected radiation along the slit reflects the position of Io's disk in the y_d-direction on

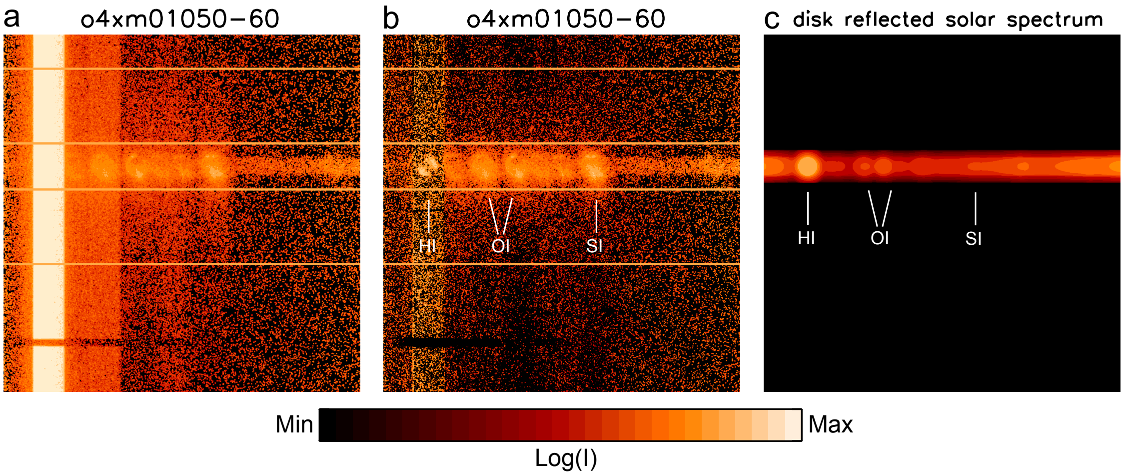

Figure 3.4: *(a) Combined images of orbit 12 as stored in the x2d file. The orange lines above and below the disk trace of Io show the region of the subtracted background emission. (b) Background subtracted image. (c) Model image of disk reflected solar radiation. The dispersed locations of the HI Lyman-α, OI] 1356 Å, OI 1304 Å and SI 1479 Å emissions are indicated. The solar spectrum (Figure 3.6) is adapted to the daily updated solar flux, scaled with the UV albedo and convolved with Io's disk for each λ_d along the spectral direction. The spectral flux is color-coded logarithmically (arbitrary unit), the color scale is identical for all three images.*

the detector. To determine the exact position we calculate a compound continuum intensity for each y_d by integrating over the observed radiation along x_d from 1520 Å to 1640 Å. For a uniform radiating disk and if spreading of the signal is neglected, this intensity profile $I(y_d)$ would be

$$\begin{aligned} I(y_d) &= I_0\sqrt{1-[(y_d-y_{d_0})/\mathrm{R_{Io}}]^2} \quad \text{for} \quad |y_d-y_{d_0}| \leq \mathrm{R_{Io}} \\ I(y_d) &= 0 \quad \text{for} \quad |y_d-y_{d_0}| > \mathrm{R_{Io}}\,, \end{aligned} \tag{3.2}$$

when the center of Io's disk is y_{d_0}. Because the surface is not uniformly reflecting and scattering additionally spreads the emission, the profile is broadened and irregular. We therefore do not try to fit the exact profile, but adjust as Gaussian distribution, although it does not resemble the profile exactly. The fitting methods used in this work are explained in detail in Section 3. Figure 3.5 shows two examples of the continuum radiation versus the offset in y_d and the fitted Gaussian profile for orbits 15 and 17. The maximum of the Gaussian profile indicates the center of the disk in y_d-direction. For most images the offset is between 0 and 3 pixels except for orbits 17, 23 and 24, where the offset is larger than 10 pixels. The inaccuracy of orbit 23 was due the difficulties of acquiring Io in shadow during the eclipse observation (*Retherford* 2002). The error of the Gaussian fit indicates an uncertainty of ~1–2 pixels for the derived location. Because the dispersion axis is aligned with x_d in the *x2d* files, the center pixel applies to all wavelengths.

Principally, the disk reflected solar Lyman-α signal can also be used to reconstruct the location of Io's disk in both directions x_y and y_d. Assuming a uniformly reflecting surface we convolve the two-dimensional Lyman-α image with a synthetic disk image wih a constant intensity on the disk and zero intensity everywhere else. Shifting the modeled disk image in both directions (x_y,y_d) we calculate the maximum total intensity of the convolved image, which gives an estimation of the offset in y_d and x_d. As the signal is partly absorbed in Io's dense equatorial SO$_2$ atmosphere (see Figure 2.2), the asymmetric and irregular observed morphology hampers a straightforward

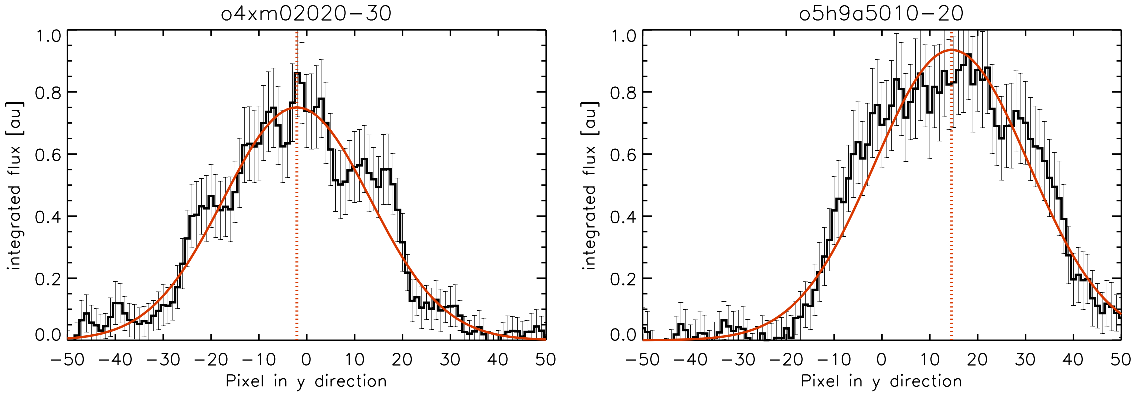

Figure 3.5: *The black bold histogram shows the detector flux integrated along x_d from 1520 Å and 1640 Å in arbitrary unit [au] versus the offset in y_d-direction from the disk center as specified in the data files, with error bars. The solid red line is the fitted Gaussian profile indicating the y_d offset of the actual position of the disk, shown by the dotted vertical line.*

determination of the disk location. Generally, the deviation of the actual disk position from the x_d value specified in the data files appears to be smaller than the offset from the given y_d. However, the difference in determining y_d using the continuum and Lyman-α radiation is on the order of the offset itself. We, therefore use the Lyman-α inferred x_d offset as a first guess, but finally determine the x_d location by comparing the OI] 1356 Å morphology to our modeled emission pattern, see Section 4.2. The G140M and G230M observations do not include a continuum consisting of solely solar reflected radiation. Thus, we locate Io through the comparison between the modeled and observed emission morphologies only.

Solar reflected radiation from Io's disk is present across the entire spectrum. Whereas at Lyman-α the signal on the disk is primarily reflected sunlight (*Feldman et al.* 2000), the contribution at OI 1304 Å and OI] 1356 Å is small, but non-negligible. Daily solar UV spectra measured by the SOLSTICE instrument on UARS are available online (http://lasp.colorado.edu/lisird/) with a spectral resolution of 10 Å (*Woods et al.* 1996). In addition, reference spectra with a higher resolution of 0.5 Å (comparable to the G140L dispersion) have been taken by SOLSTICE during high and moderate solar activity. We adapt the high-resolution (*hires*) UARS spectra to the daily measured spectral flux by calculating the average deviation between the fluxes over the entire spectrum between 1200 Å and 1700 Å. Applying the adaption method the low-resolution (*lowres*) and *hires* spectra of the same day the error of the method is estimated to $< 3\%$. Using the average squared deviation between the spectra yields larger errors due to the missing peaks in the *lowres* spectra. Figure 3.6 (left) shows both the UARS *hires* and *lowres* spectrum of the same day. The adapted high-resolution spectrum is scaled to the distance of Io to the Sun and mapped on a uniform disk of Io's radius for each pixel x_d and the respective wavelength λ_d. The two-dimensional reflected spectrum is then convolved with the STIS point spread function (PSF), which is computed with the TinyTim modeling tool. The STIS PSF and the TinyTim tool are described in detail in Appendix A.5. By summing over the disk in the cross-dispersion direction (from $y_d \approx -1.2$ R$_{\text{Io}}$ to $y_d \approx -1.2$ R$_{\text{Io}}$) in the observation image and the disk reflection image we extract the spectral profiles displayed in Figure 3.6 (right). From these spectra the geometric albedo is derived by minimizing the average squared deviation between the two profiles in the wavelength range, where no Iogenic emission is expected (1520 Å to 1640 Å). An example image of the disk reflected solar radiation scaled with the derived albedo is shown in Figure 3.4c. This method is applicable only

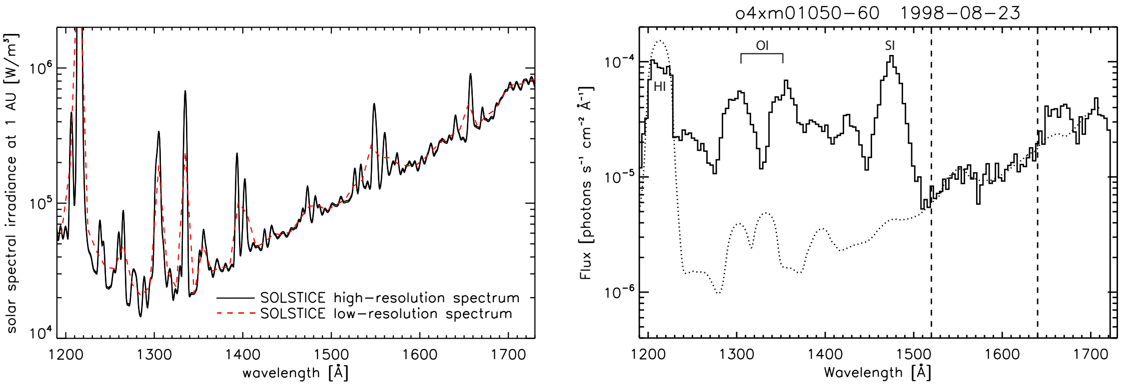

Figure 3.6: *(Left) UARS SOLSTICE spectra with high (solid black) and low (dashed red) spectral resolution of UARS day 200 (1992/3/29). (Right) Extracted and binned STIS spectrum for orbit 12 obtained by summing over the cross-dispersion direction (solid black) and solar spectrum convolved with the uniformly reflecting disk of Io and integrated along the spatial detector axis* y_d *(dotted black). The dashed vertical lines indicate the wavelength range for albedo fit.*

for the 15 orbits, where STIS was used in the G140L mode and the reflected solar continuum is included in the spectrum.

All derived values p for Io's geometric FUV albedo are plotted versus the sub-observer longitude in Figure 3.7. The shown error bars include the uncertainty of the SOLSTICE spectra of $\sim$6% and the relative statistical error of all pixels in the continuum disk area ($\sim 3-6\%$). Additionally, a 3% uncertainty is introduced by the adaption of the *hires* solar spectra. The values are in reasonable agreement with the FUV albedos derived by *Feldman et al.* (2000), who applied principally the same method to the STIS G140L observations obtained in 1997 and 1998 (red lines in Figure 3.7). (*Sartoretti et al.* 1996) derived slightly higher albedo values in the middle UV (MUV) range. However, a decrease towards shorter UV wavelengths is expected from observations by *Nelson et al.* (1987).

Although, there is some scattering in the derived values, the albedo seems to be higher on the sub-Jovian hemisphere ($\varphi_{obs} = 270° - 90°$) than on the anti-Jovian ($\varphi_{obs} = 90° - 270°$). A least-squares fit of the sinusoidal profile

$$p_{fit} = a_1 + a_2 \cdot \cos\left(\varphi_{obs} - a_3\right) , \tag{3.3}$$

with the coefficients a_1, a_2, a_3 yields a maximum albedo at longitude 20° ($= a_3$) and a minimum around 200°. The mean albedo is $a_1 = 0.0168$ with a variation of $a_2 = 0.0018$. A comparison with the phase angles shows that the measured albedo values are mostly lower than the fitted curve for high phase angles ($> 5°$) and vice versa. The variance indicates a relatively strong dependence of the reflected intensity on the solar phase angle θ, i.e., a steep phase function. The MUV observations of *Nelson et al.* (1987) revealed similar albedo variations, but with a higher reflectivity on the trailing hemisphere and a clear phase angle dependence. Analyzing the Lyman-α radiation in the STIS images *Feaga et al.* (2009) found the strongest absorption on the anti-Jovian hemisphere, where the continuum reflectivity appears to be lowest. The longitudinal reflectivity variation thus possibly originates from atmospheric absorption of the continuum radiation. The SO_2 absorption cross section at 1500−1700 Å is $\sigma_{SO_2} \approx 10^{18}$ cm^2 and thus an order of magnitude lower than at Lyman-α (*Manatt and Lane* 1993), which is strongly absorbed around the equator. For the esti-

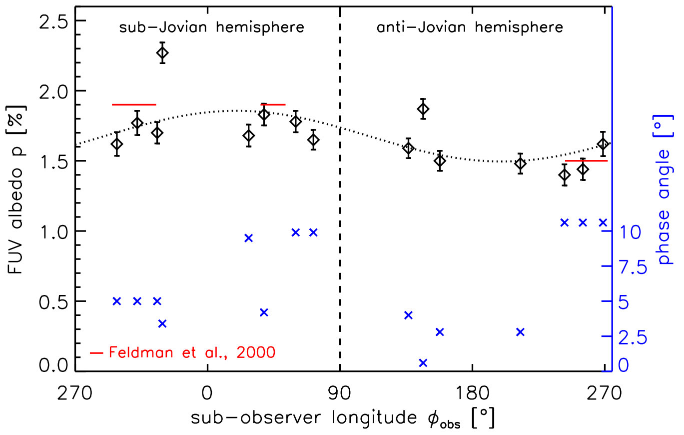

Figure 3.7: *Derived geometric FUV albedo of Io as a function of the sub-observer longitude for all G140L observations (black diamonds with error bars). The dotted black line show as fitted sinusoidal curve. The blue crosses indicate the solar phase angle of the observation.*

mated equatorial SO_2 column density of $\sim 10^{17}$ cm^{-2} absorption is likely to attenuate the signal. Hence, a clear longitudinal dependence of the albedo can not be determined. For the calculation of the reflected sunlight in the G140M observations we assume a constant albedo of 0.017. Surface inhomogeneities probably lead to albedo variations across the disk. The NUV albedo map derived by *Sartoretti et al.* (1995) appears patchy with reflectivity variations between 0 and 3%. Hence, the error of the modeled disk reflected intensity (scaled with the albedo) of a single pixel is presumably high. The uncertainty of the subtracted solar reflected pixel intensity is assumed to be 50% of the modeled reflected flux $I_{sun}(x_d, y_d)$.

In the analyzed SI] 1900 Å images extracted from the G230M observations, the reflected sunlight is not subtracted. Due to the much higher detector dark rate associated with the use of STIS's NUV detector, the background brightness turns out to be very high. The uncertainty of the background subtraction does not allow a proper determination of the albedo. As the reflected sunlight is lower than the strong SI] 1900 Å emission by at least an order of magnitude, a subtraction is therefore omitted here.

When extracting an image for one emission line or multiplet, the wavelength dependent system and aperture throughput is eliminated (see Appendix A.3). The image is then rotated from the detector coordinate system to the Jovian system, where the vertical axis is aligned with Jupiter's rotation axis (see Appendix A.2). All displayed images in Sections 4 and 6 show a region of 3 $R_{moon} \times 3$ R_{moon} centered on the disk center. Throughout this work, the brightness in the analyzed images is given in Rayleigh [R] for Europa and in 10^3 Rayleigh [kR] for Io. The unit conversion to Rayleigh is described in Appendix A.4.

The statistical error σ_0 of each pixel is processed accordingly. The error σ_{bg} due to the subtracted background emission $I_{bg}(x_d, y_d)$ and the error σ_{sun} of solar reflected flux $I_{sun}(x_d, y_d)$ contribute to the propagated pixel error $\sigma_{tot}(x_d, y_d)$ after

$$\sigma_{tot}(x_d, y_d) = \sqrt{\sigma_0^2 + \sigma_{bg}^2 + \sigma_{sun}^2}\,. \tag{3.4}$$

The error of the background emission σ_{bg} and the unit conversion necessary for the error propagation are described in Appendix A.4.

Table 3.2: List of all HST STIS spectral observations of Europa obtained with the 52"x2" slit. ϕ_{Eu} is the diameter of the disk of Europa in the observation. ^{1}orbit with only one exposure.

HST ID / PI	No	Orb	Dataset	Date	T_{start}	T_{exp} [s]	ϕ_{Eu}["]	Grid	Band [A]
8224	1	1	o5d601010	1999-10-05	08:39	830	1.08	G140L	1140 - 1730
M.A. McGrath	2		o5d601020	1999-10-05	09:10	830	1.08	G140L	1140 - 1730
	3	2^1	o5d601030	1999-10-05	10:17	1100	1.08	G140L	1140 - 1730
	4	3	o5d601050	1999-10-05	11:54	1100	1.08	G140L	1140 - 1730
	5		o5d601060	1999-10-05	12:15	1100	1.08	G140L	1140 - 1730
	6	4	o5d601070	1999-10-05	13:31	1100	1.08	G140L	1140 - 1730
	7		o5d601080	1999-10-05	13:53	1100	1.08	G140L	1140 - 1730
	8	5	o5d601090	1999-10-05	15:07	1100	1.08	G140L	1140 - 1730
	9		o5d6010a0	1999-10-05	15:32	1100	1.08	G140L	1140 - 1730

3.3 STIS observations: Europa

3.3.1 Overview

In October 1999, STIS observed Europa's UV emission in the course of HST campaign ID 8224. The exposures taken during five consecutive HST orbits are listed in Table 3.2. The second exposure of the second orbit failed. STIS imaged Europa close to western elongation (see Figure 3.8) using the low-resolution grating G140L throughout the visit. The image parameters and format are identical to the Io G140L observations with a spatial axis and a dispersion axis. In contrast to Io, sulfur emissions from either the torus or the atmosphere/ionosphere are not detected. Besides the prominent Lyman-α radiation, enhanced emission at the two oxygen multiplets OI 1304 Å and OI] 1356 Å is present.

3.3.2 Processing

Principally, processing and image extraction are performed according to the methods described for Io. There are, however, differences due to the differing orbital parameters and atmospheric compositions, which will be explained in this section.

Like for Io, the two exposures obtained during one orbit are combined. Europa's orbital period is twice the period of Io, i.e., the variation of sub-observer central meridian longitude during the combined exposure time of $\sim 3^\circ$ is even lower and thus clearly negligible. The synodic Jovian rotation period is also slightly lower with $T_{\mathrm{Jup,syn}} = 11.25$ h, i.e., the λ_{III} variation of $\sim 21^\circ$ is somewhat higher. A background subtraction is performed in the same way as for Io, see Section 3.2.2. As an example, the observation image of orbit 4, where the oxygen emissions are brightest, is displayed before and after the background correction in Figure 3.9a/b. The single exposure of orbit 2 will be analyzed as well, although the signal-to-noise ratio is lower by roughly $\sqrt{2}$.

The location of the disk center in the spatial direction is determined using the reflected solar continuum and Lyman-α radiation. There is no emission expected from the O_2 atmosphere of Europa longward of 1380 Å (*Feldman et al.* 2000). We thus fit a Gaussian profile to the reflected continuum radiation integrated from $\lambda_d = 1380$ Å to 1700 Å yielding an average offset of 2($\pm$1) pixels

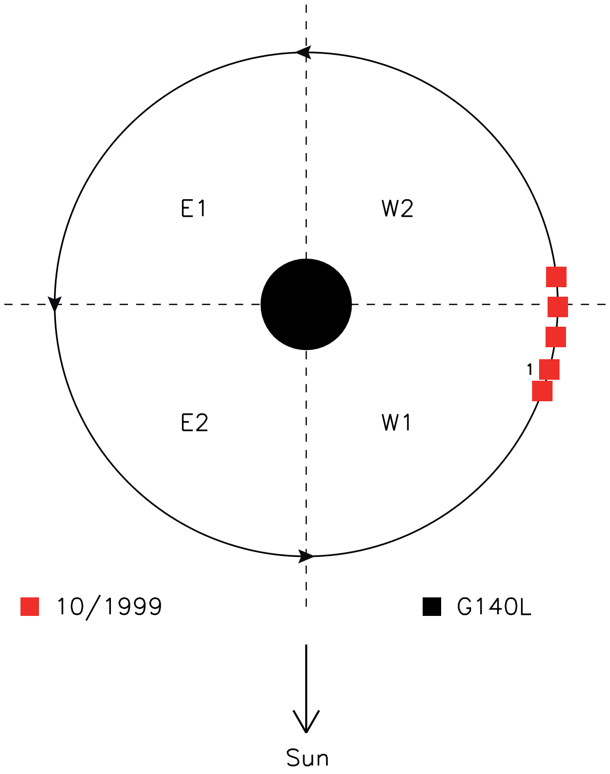

Figure 3.8: *Europa's orbital location with respect to Jupiter for the exposures of the 1999 HST STIS campaign, listed in Table 3.2. Europa orbits Jupiter counterclockwise. All observations were taken when Europa was at western elongation, i.e., the trailing hemisphere is monitored. "1" marks the single exposure orbit. The orbit is subdivided in four sections: W1 and W2 (E1 and E2) are the quarters before and after western (eastern) elongation, respectively.*

for the visit with respect to the y_d value for the disk specified in the *x2d* files. Unlike at Io, the reflected Lyman-α radiation appears to be uniform within Europa's disk, see Figure 3.9b. The Lyman-α signal indicates a slightly higher offset of 2 to 3 pixels on the cross-dispersion axis and a shift of 1 pixel in along the dispersion axis. As H_2O is the main sputtering product, absorption and electron-excited dissociative emission of gaseous water likely affect the observed Lyman-α intensity and morphology. Hence, the y_d offset is set to the value derived from the continuum location.

Since the continuum signal at wavelengths <1500 Å is low and therefore noisy, the modeled disk reflected solar spectrum is fitted to the observed spectrum between 1500 Å and 1700 Å to derive the FUV albedo, see Figure 3.10. We find an albedo of $p = 0.014 \pm 0.002$ for the monitored trailing hemisphere. *Hall et al.* (1998) derive albedos of 0.013 and 0.016 at 1335 Å from HST GHRS observations of the trailing side obtained in 1994 and 1996, respectively. Thus, the derived albedo is in good agreement with the previously inferred values. The observing geometry of the 1996 GHRS campaign ($p = 0.013$) is very similar to the geometry during the STIS observations. This indicates a relatively constant FUV albedo between 1335 Å and 1700 Å, although at wavelengths longward of 2200 Å the albedo increases significantly (*Noll et al.* 1995). *Hansen et al.* (2005) derive an albedo of ~1% with Cassini UVIS observations of Europa's leading hemisphere.

For the analysis of the two oxygen emission images OI 1304 Å and OI] 1356 Å, the disk reflected

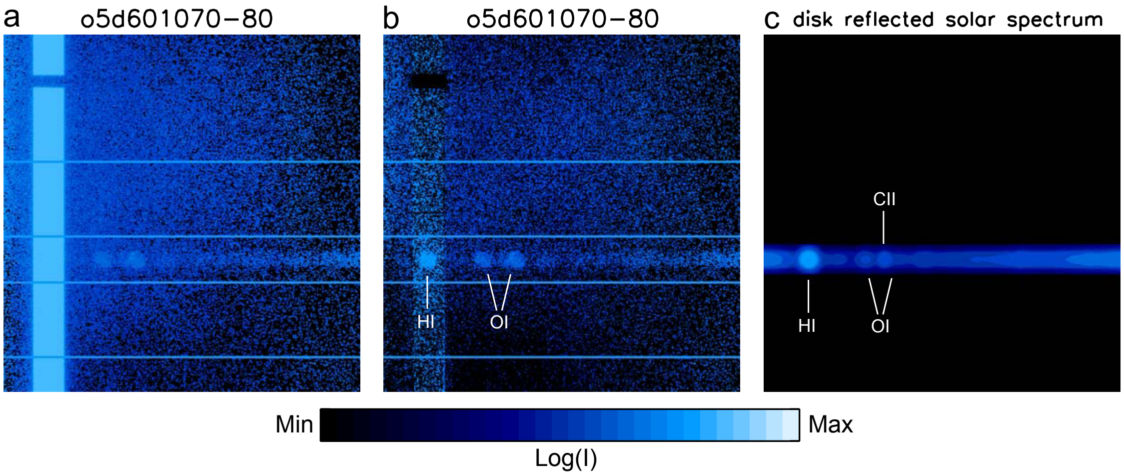

Figure 3.9: *(a) Combined images of orbit 4. The straight blue lines above and below the disk trace of Europa show the region of the subtracted background emission. (b) Background subtracted image. (c) Model image of disk reflected solar radiation. The dispersed locations of the HI Lyman-α, OI] 1356 Å and OI 1304 Å emissions as well as the surface reflected CII 1335 Å radiation are indicated. For further information see also Figure 3.4.*

sunlight (see Figure 3.9c) is subtracted from the observations. Since the emission from the atmosphere are an order of magnitude lower than at Io, the reflected sunlight contributes significantly to the measured intensity of the oxygen multiplets, see Figure 3.10. Therefore, a subtraction of these contributions is essential to analyze the atmospheric emissions quantitatively. The disk reflected solar CII 1335 Å radiation overlaps with the OI] 1356 Å image by ~8 pixels clearly affecting the oxygen morphology with a brightness ratio of roughly $I_{1335}/I_{1356} \approx 1/5$. The albedo appears to be spatially inhomogeneous (*McGrath et al.* 2009), but albedo variations across the surface can not be determined unambiguously in the observations. Assuming an uniformly reflecting disk for the subtraction of the solar radiation might thus slightly distort the oxygen morphology, especially in the overlap region of CII 1335 Å and OI] 1356 Å. In the Lyman-α and CII 1335 Å images the sunlight is not subtracted, since the reflected solar radiation represents most of the analyzed signal.

Solar Lyman-α emission is also backscattered by neutral hydrogen atoms within the interplanetary medium (IPM) throughout the Solar System (*Ajello et al.* 1994). The background Lyman-α is measured above and below the disk with an unobstructed line of sight. Thus, the subtraction of the Lyman-α on the disk might be overestimated, as parts of the IPM Lyman-α is obstructed. However, after the background subtraction, the Lyman-α intensity in the STIS observations is in good agreement with the calculated disk solar reflected Lyman-α, see Figure 3.10. Therefore, possible contributions from interplanetary Lyman-α are presumably small and thus neglected here.

As already mentioned, the average count rate for the emission features is considerably lower than at Io, e.g., for OI] 1356 Å it is reduced by factor 5 to 10. Due to the very low signal-to-noise ratio of a single pixel the spatial resolution is reduced by factor 2 in both directions. Averaging over 2×2 pixels increases the signal-to-noise ratio by $\sqrt{4}$. The error of each pixel $\sigma(x_d, y_d)$ is computed according to the error propagation for Io, see Section 3.2.2.

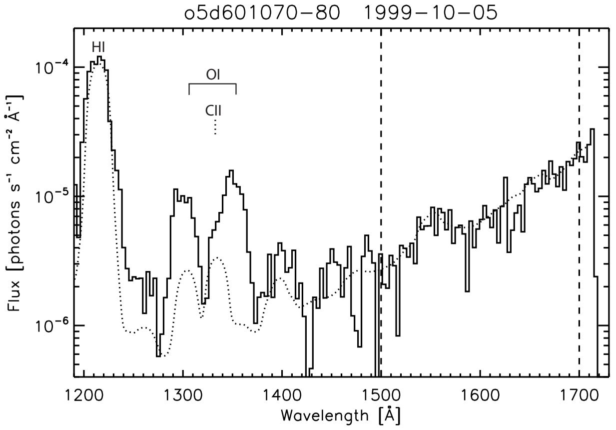

Figure 3.10: *Extracted and binned STIS spectrum for orbit 4 obtained by summing over the cross-dispersion direction (solid black) and solar spectrum convolved with the uniformly reflecting disk of Europa and integrated along the spatial detector axis y_d (dotted black). The dashed vertical lines indicate the wavelength range for albedo fit.*

3.4 NH LORRI and HST ACS observations

In February and March 2007 the New Horizons probe passed the Jupiter system on its way to Pluto. The closest approach to Io occurred on 28 February at a distance of 2.24×10^6 km. Io was observed several times while passing through Jupiter's shadow. During two of the eclipse passages the NH LORRI observed the auroral emission at visible and infrared wavelengths (*Spencer et al.* 2007b). According to the notation of *Retherford et al.* (2007a) these two eclipse occasions will be denoted Ieclipse03 and Ieclipse04. During the Ieclipse03 event simultaneous spatially resolved observations of Io's FUV aurora have been acquired by the Advanced Camera for Surveys Solar Blind Channel (ACS SBC) of the Hubble Space Telescope. The LORRI images were processed by *Spencer et al.* (2007a,b). The emission morphology in the NH LORRI image taken during Ieclipse03 is discussed by *Spencer et al.* (2007a). The ACS observation is processed and reviewed by *Retherford et al.* (2007a). In Chapter 5 we will simulate the formation of the auroral emission in eclipse and compare our results to the LORRI and ACS images. Therefore we will give a short overview over the characteristics of the cameras and observation images here. In addition, the unit conversion to surface brightness is described briefly.

The LORRI is a narrow-angle high-resolution telescope with a 1024×1024 pixel CCD detector. The spatial resolution is 4.96 μrad per pixel, the field of view extends over 0.29°. It provides panchromatic imaging over a bandpass that extends from $\sim$3500 Å to $\sim$8500 Å. A detailed description of the NH LORRI can be found in *Cheng et al.* (2008). For Ieclipse03 one pixel spans an area of $\sim$15 km × 15 km ($\sim$200 pixels per Io diameter) on Io's surface. During Ieclipse04 the LORRI was used in the 4×4 binning mode, which reduces the spatial resolution in both directions by a factor of 4. The pixel size in that case is $\sim$56 km × 56 km, which is equivalent to $\sim$50 pixels per Io diameter.

The observed diffuse emission originates from various emitters. In the blue range of visible wavelengths, SO_2 and S_2 emission bands are the main contributors. Excited atomic oxygen, atomic sodium and potassium are the major emitters in the green, red and infra-red range (*Geissler et al.* 2004). Atomic sulfur contributes only a minor fraction. As parts of the LORRI exposures were

Table 3.3: *Summary of the 2007 NH LORRI and HST ACS eclipse observations. All observations are combinations of several exposures during one eclipse event, as reported in Spencer et al. (2007a). The given observation time refers to the mid-eclipse time and can thus differ for single exposures.*

No	Dataset	Date	$T_{mid-ecl}$	T_{exp} [s]	ϕ_{Io}["]	Filter	Band [Å]
1	LORRI Ieclipse03	2007-02-27	15:24	~16	270	–	3500 - 8500
2	ACS Ieclipse03	2007-02-27	15:24	1200	0.93	F125LP	1250 - 1900
3	LORRI Ieclipse04	2007-03-01	09:53	~10-20	261	–	3500 - 8500

contaminated with instrument scattered light, the analyzed images are combinations of several coaligned exposures during one eclipse event.

The ACS SBC has a 1024×1024 pixels MAMA detector with nominal wavelength coverage from 1150 Å to 1700 Å. Each pixel provides a spatial resolution of 0.034"×0.030". The eclipse observations were acquired using the longpass F125LP filter, which excludes the background from geocoronal Lyman-α emission (*Retherford et al.* 2007a). The transmission for SBC F125LP thus allows imaging of emissions between ~1250 Å to ~1900 Å. This bandpass includes several sulfur and oxygen emission lines, e.g., OI 1304 Å, OI] 1356 Å, SI 1479 Å, as well as disk reflected solar radiation, see Section 3.2.1. Four consecutive exposures with an exposure time of 300 s each were taken by ACS during the Ieclipse03 event resulting in a combined exposure time of 1200 s (*Retherford et al.* 2007a).

The single exposures of the combined LORRI images, which are analyzed and simulated in Chapter 5, are obtained over a period of roughly 1/2 hour during the ~2-h duration of an eclipse. The ACS exposures were acquired within 10 minutes before and after mid-eclipse. All given orbital, geometric and magnetospheric parameters for the eclipse observations refer to the mid-eclipse time $T_{mid-ecl}$. The characteristics of the LORRI and HST ACS observations are summarized in Table 3.3.

The conversion from detector counts to emission brightness depends on the wavelength dependent sensitivity of the respective instrument. Since the spectral profiles of the emissions in the wavelength ranges of LORRI and ACS are unknown, we use the Pivot wavelengths of 6076 Å (LORRI) and 1437 Å (ACS SBC) to convert the detector counts to surface brightness in Rayleigh. To validate this method we use exemplary modeled emission spectra including various emitters (SO_2, O, S, Na and K) and calculate the brightness of the LORRI images using the sensitivity curve of *Cheng et al.* (2008). With this method the intensity differs less than 20% from the intensity derived with the Pivot wavelength.

In Chapter 5 the eclipse observations are simulated using the numerical interaction model to calculate the plasma properties in Io's vicinity. By comparison of the simulated and observed emission morphology and intensity properties of the eclipse atmosphere are derived. As we compare only larger areas in the images, the resolution of model images is not adjusted to the observations and the scattering in the imaging system is neglected.

3.5 Statistics and error analysis

For the evaluation of the STIS observation images, various functions representing the characteristics of the aurora are fitted to the observational data. In Section 4.2, images generated with a phenomenological model are fitted to the STIS images by comparing the intensity of each pixel in each observation and the respective model image. Furthermore, systematic correlations between atmospheric and magnetospheric properties are investigated by adapting functional descriptions to the observed aurora properties. Therefore, we give a short description of fitting methods and the corresponding error analysis used in this work.

3.5.1 Method of maximum likelihood

For fitting an arbitrary function $y(x_i, \mathbf{p})$ to N data points y_i, a Gaussian distribution is often assumed for the measured y_i with the uncertainties σ_i:

$$P_{Gauss}(y_i, \mu_i) = \frac{1}{\sigma_i\sqrt{2\pi}} \exp\left(-\frac{1}{2}\left[\frac{y_i - \mu_i}{\sigma_i}\right]^2\right) \quad . \tag{3.5}$$

μ_i is the actual value or mean of the measured variable y_i. For each independent, measured variable x_i the fitting function computes an expected value $y(x_i, \mathbf{p})$ depending on M parameters or coefficients $\mathbf{p} = (p_1, p_2, ..., p_M)$. The fitting function is optimized if the total Gaussian probability for making the observed measurements y_i with uncertainties σ_i

$$P(\mathbf{p}) = \prod_{i=1}^{N}\left\{\frac{1}{\sigma_i\sqrt{2\pi}} \exp\left(-\frac{1}{2}\left[\frac{y_i - y(x_i, \mathbf{p})}{\sigma_i}\right]^2\right)\right\} \tag{3.6}$$

$$\Leftrightarrow \quad P(\mathbf{p}) = \prod_{i=1}^{N}\left(\frac{1}{\sigma_i\sqrt{2\pi}}\right) \times \exp\left(-\frac{1}{2}\sum_{i=1}^{N}\left[\frac{y_i - y(x_i, \mathbf{p})}{\sigma_i}\right]^2\right) \tag{3.7}$$

is at maximum, when the actual value or mean is given by the fitted function, $\mu_i = y(x_i, \mathbf{p})$ (*Bevington and Robinson* 2003). Thus, to maximize $P(\mathbf{p})$, the weighted sum of the squares of the deviations of all measured data points from the function values, thus second term of the right hand side (RHS) of 3.7, has to be minimized. This standard method is called *least squares method*. The sum is defined as the goodness-of-fit parameter χ^2 given by

$$\chi^2(\mathbf{p}) = \sum_{i=1}^{N}\left[\frac{y_i - y(x_i, \mathbf{p})}{\sigma_i}\right]^2 \quad . \tag{3.8}$$

Assuming the fitting function represents the true values, the measured data points y_i should be spread around $y(x_i, \mathbf{p})$ corresponding to their uncertainty σ_i. If $y(x_i, \mathbf{p})$ depends on M fitted parameters p_k, the expected value for χ^2 is given by

$$\langle\chi^2\rangle = N - M = \nu \quad , \tag{3.9}$$

where ν is the number of degrees of freedom (*Bevington and Robinson* 2003). For convenience, we generally use the reduced chi-square value

$$\chi^2_\nu = \frac{\chi^2}{\nu} \quad , \tag{3.10}$$

with an expectation value of $\langle \chi^2_\nu \rangle = 1$.

At the minimum of χ^2 the derivatives with respect to the M fit parameters or coefficients $\mathbf{p}$ must be zero:

$$\frac{\partial}{\partial p_k}\chi^2 = 0 \qquad \text{for} \quad k = 1, \ldots, M \quad . \tag{3.11}$$

For a χ^2 given by (3.8) we get

$$\frac{\partial}{\partial p_k}\sum_{i=1}^{N}\left[\frac{y_i - y(x_i,\mathbf{p})}{\sigma_i}\right]^2 = 0 \tag{3.12}$$

$$\Leftrightarrow \quad -2\sum_{i=1}^{N}\left[\frac{y_i - y(x_i,\mathbf{p})}{\sigma_i}\frac{\partial y(x_i,\mathbf{p})}{\partial p_k}\right] = 0 \quad . \tag{3.13}$$

If the fitting function is linear in the parameters, i.e., it can be written as

$$y(x_i,\mathbf{p}) = \sum_{l=1}^{M} p_l f_l(x_i) \quad , \tag{3.14}$$

where $f_l(x_i)$ can be any type of function as long as it does not involve a parameter p_k, Equation (3.13) becomes

$$-2\sum_{i=1}^{N}\left[\frac{f_k(x_i)}{\sigma_i}\left(y_i - \sum_{l=1}^{M} p_l f_l(x_i)\right)\right] = 0 \tag{3.15}$$

$$\Leftrightarrow \quad \sum_{i=1}^{N} y_i \frac{f_k(x_i)}{\sigma_i} = \sum_{l=1}^{M}\left[p_l \sum_{i=1}^{N}\left(\frac{f_k(x_i)f_l(x_i)}{\sigma_i}\right)\right] \quad . \tag{3.16}$$

Thus, we obtain M coupled linear equations for the M unknown parameters p_k. Solutions methods for the Equation System (3.16) can be found, e.g., in Chapter 15 of *Press et al.* (2007). Straightforward analytical solutions only exist for linear fitting functions (3.14) (*Bevington and Robinson* 2003). If the function is not linear in the parameters, various methods can be applied for searching the parameter space for the parameter set minimizing χ^2. In this work, the routine *curvefit* provided by the *Interactive Data Language* (IDL) is used for fitting various functions, both linear and non-linear in the parameters, to the data. The routine applies the gradient-expansion algorithm, which is based on the least-squares estimation method for nonlinear functions developed by *Marquardt* (1963).

3.5.2 Uncertainties in the fitting parameters

For fitting functions that are linear in the parameters an analytical solution exists for the parameter set $\mathbf{p}_0$ that minimizes χ^2, i.e., an analytical solution for Equation (3.13). We can thus write p_k as a function of the measured variables x_i and y_i:

$$p_k = p_k(x_1, x_2, \dots, x_N, y_1, y_2, \dots, y_N) \ , \tag{3.17}$$

for all M parameters. The variance of the fitted parameter p_k can then be calculated by a common error propagation of the standard deviations σ_i of the variables y_i

$$\sigma_{p_k}^2 = \sum_{i=1}^{N} \left[\sigma_i^2 \left(\frac{\partial p_k}{\partial y_i} \right)^2 \right] \quad , \tag{3.18}$$

neglecting a possible uncertainty of x_i. Similarly, the covariance of two parameters p_k and p_l is given by

$$\sigma_{p_k, p_l}^2 = \sum_{i=1}^{N} \left[\sigma_i^2 \frac{\partial p_k}{\partial y_i} \frac{\partial p_l}{\partial y_i} \right] \quad . \tag{3.19}$$

A derivation of the error matrix with the variances on the diagonal axis and covariances in the off-diagonal elements from the linear equation system for the parameters p_k (3.16) can be found in Section 15.4 of *Press et al.* (2007). For functions that are non-linear in the parameters, the parameter uncertainties are estimated with a forward difference approximation in the IDL routine *curvefit*. Assuming the functions to be quasi-linear around the best-fit parameters $\mathbf{p}_0$ on scales of the computer-specific floating point precision ε, the partial derivative of $y(x_i, \mathbf{p})$ in Equation (3.13) is estimated to

$$\frac{\partial y(x_i, p_1, \dots, p_k, \dots, p_M)}{\partial p_k} = \frac{y(x_i, \dots, p_k + \varepsilon \cdot p_k, \dots) - y(x_i, \dots, p_k, \dots)}{\varepsilon \cdot p_k} \quad . \tag{3.20}$$

3.5.3 Fitting of the phenomenological aurora model

In Section 4.2, the pixel brightnesses in the STIS images are fitted with a function based on a phenomenological model for the aurora distribution. 18 observation images are fitted for the OI] 1356 Å aurora, 17 images for SI 1479 Å aurora and 16 for the OI 1304 Å aurora. Each image contains approximately $2500 - 4600$ pixels yielding a large number of data points (total number of pixels) of $N \approx 6 \times 10^4$. The model function is determined by $M = 10$ parameters, which are fitted to the observation. The number of degrees of freedom of the fit is

$$\begin{aligned} \nu &= N - M \approx N \\ \nu &\approx 6 \times 10^4 \quad . \end{aligned} \tag{3.21}$$

Hence, the number of equations by far exceeds the unknown parameters, the system is clearly overdetermined.

Poisson distributed data

Detector counts of telescope observations generally obey the Poisson distribution given by

$$P_{Poisson}(y_i, \mu_i) = \frac{\mu_i^{y_i}}{y_i!} \exp(-\mu_i) \quad , \tag{3.22}$$

with the mean μ_i and the measured value y_i of pixel i. If the Gaussian probability is replaced by the Poisson probability for observing y_i counts, when the mean value is given by the fitting function $\mu_i = y(x_i, \mathbf{p})$, the total probability (3.7) for all pixels i becomes

$$P(\mathbf{p}) = \prod_{i=1}^{N} \left(\frac{[y(x_i, \mathbf{p})]^{y_i}}{y_i!} \exp\left[-y(x_i, \mathbf{p})\right] \right) \quad . \tag{3.23}$$

Maximizing P with respect to the fit parameters $\mathbf{p}$ yields the optimized fitting function for Poisson distributed data, where the error is equal to the square root of the measured counts.

However, as the image data has undergone numerous processing steps the processed data values y_i and propagated errors σ_i can not be represented by a Poisson distribution any more. Therefore, the standard least-squares method is applied for fitting the parameters of the phenomenological aurora model to the observation images relating the data uncertainty to a Gaussian probability. Since the data errors are based on the Poisson distributed counts which are strictly bounded on the lower end ($y_i \geq 0$), the standard least-squares method tends to underestimate the values (*Bevington and Robinson* 2003). As the negative tail of the Gaussian distribution is cut off, the probability for a data point y_i to be lower than the mean predicted by the fitting function is underestimated. Thus, the standard least squares method favors lower function values $y(x_i, \mathbf{p})$. In case the count rate is higher than ~20, the Poisson profile is well resembled by the Gaussian distribution. However, in the analyzed images the average pixel count rate is only on the order of 1. Therefore, the least-squares method yields a fit that probably underestimates the actual values.

Minimization method

To minimize the χ^2 of the phenomenological aurora model, we use the *downhill simplex* or *amoeba* method proposed by *Nelder and Mead* (1965). The method does not require calculations of partial derivatives for the parameters p_k, but searches the parameter space using the concept of a simplex, a special polytope of $n+1$ vertices in n dimensions. Starting from an initial parameter set $\mathbf{p}_{init}$, each parameter is first varied individually according to a parameter specific scaling δp_k. For each parameter variation the sum of the least squares is calculated yielding $n+1$ χ^2 values for $n+1$ points in the parameters space. After this initialization, the worst (in terms of the cost function χ^2) of the $n+1$ points in the parameter space is replaced by a point reflected through the centroid of the remaining n points. The algorithm is repeated until a given convergence criteria is reached. Further explanations and an example numerical implementation can be found in Section 10.4 of *Press et al.* (2007).

Depending on the given initial parameters and the variation length scales, the downhill simplex method possibly converges to a local minimum. As the fitting function is a phenomenological model of the aurora distribution, we do not expect to find one unique parameter set as ultimate solution that yields the lowest χ^2. We rather want to examine various points in the parameter space starting from phenomenologically reasonable initial values $\mathbf{p}_{init}$ and using various scaling lengths to test how robust a nearby minimum is. Hence, the downhill simplex method is clearly less efficient in terms of the number of function evaluations than, e.g., the gradient-expansion method by *Marquardt* (1963), but it allows a controlled and stable search of the parameter space.

Goodness of fit

The obtained minima for χ^2 are very shallow, i.e., variations of the parameters $\mathbf{p}$ around the best-fit values $\mathbf{p}_0$ hardly alter χ^2. As the system is completely overdetermined with the data points exceeding the parameters by 3 orders of magnitude, the derived least-square solution is always a kind of compromise between the numerous pixel values. Therefore, the gradient of the resulting chi-squared values from various parameter sets is small. In other words, with a total of 10 parameters the influence of a single parameter on the pixels is relatively low on average. For instance, some parameters control smaller aurora features, which influence only few pixels of an image. The impact of a parameter variation on the total χ^2 is thus limited. On the other hand, a very high noise level of the single pixels with $\sigma_i \approx y_i$, i.e., a signal to noise ratio of 1, leads to a generally low χ^2 value independent of the parameter set. In order to compare the uncertainties in the various parameters, we set a fixed, small deviation from the minimized solution χ^2_{best} of 2% and check the parameters individually. We continue to test values p_k further away from the minimized solution until the associated chi-square is $\chi^2 \geq 1.02\,\chi^2_{best}$. Thereby, we obtain a comparable sensitivity of the model to all parameters.

The analytic methods presented in this section are used throughout our analysis of the STIS aurora observations in Chapters 4 and 6. Whenever an analytical function is fitted to measured values extracted from the observation images, the described gradient-expansion method is applied. The resulting chi-squared values always refer to the reduced chi-squared given in Equation (3.10). The uncertainty of fitted parameters is calculated by (3.18). In the following Chapter 4, the STIS observations of Io's aurora are analyzed and reproduced by a phenomenological model, where the parameters are fitted to the observations with the described downhill simplex method.

4 Io's UV aurora

In this chapter the observed brightness and morphology of the sulfur and oxygen emissions in the STIS images taken between 1997 and 2001 are discussed in detail. We will revise the known properties of the emission patterns and draw a comprehensive picture of the aurora distribution around Io. We will then derive a functional model for the spatial distribution of the aurora depending on several parameters, which are fitted to the observations. Finally, the rocking of the bright equatorial spots is analyzed in detail.

4.1 STIS images of the oxygen and sulfur aurora

All STIS observations taken in the G140L, G140M and G230M mode have been processed as described in Section 3.2. Combining the two processed exposures of an HST orbit, we extract 19 images with a size of 3 $R_{Io} \times 3$ R_{Io} containing the OI] 1356 Å emission, 18 images showing the SI 1479 Å emission, 16 OI 1304 Å images and two SI] 1900 Å images.

4.1.1 OI 1304 Å, OI] 1356 Å, SI 1479 Å and SI] 1900 Å multiplets

Figure 4.1 shows a typical aurora morphology for each of the four oxygen and sulfur multiplets in exemplary emission images. The observed morphology and brightness of the OI] 1356 Å, SI 1479 Å and SI] 1900 Å emission images have been studied previously by *Roesler et al.* (1999), *Retherford et al.* (2000, 2003), *Wolven et al.* (2001) and *Feaga et al.* (2002). The OI 1304 Å observations have not been analyzed yet. After the characterization by *Roesler et al.* (1999), the aurora morphology consists of the bright *equatorial spots*, the *limb glow* and the *extended emission*, see Section 2.1.4. In some aurora observations an enhanced *wake emission* has been identified (e.g., *Retherford et al.* 2000). Additionally, a dimmer emission is seen all over the disk. All these features are not equally prominent and thus not equally visible in the images.

Excitation mechanism

As described in the previous chapter, most of the observed oxygen and sulfur emissions are produced by electron impact excitation of Io's neutral atmosphere. For the oxygen emission, direct excitation of atomic oxygen,

$$e^- + O \rightarrow O^* \rightarrow O + \gamma \quad , \tag{4.1}$$

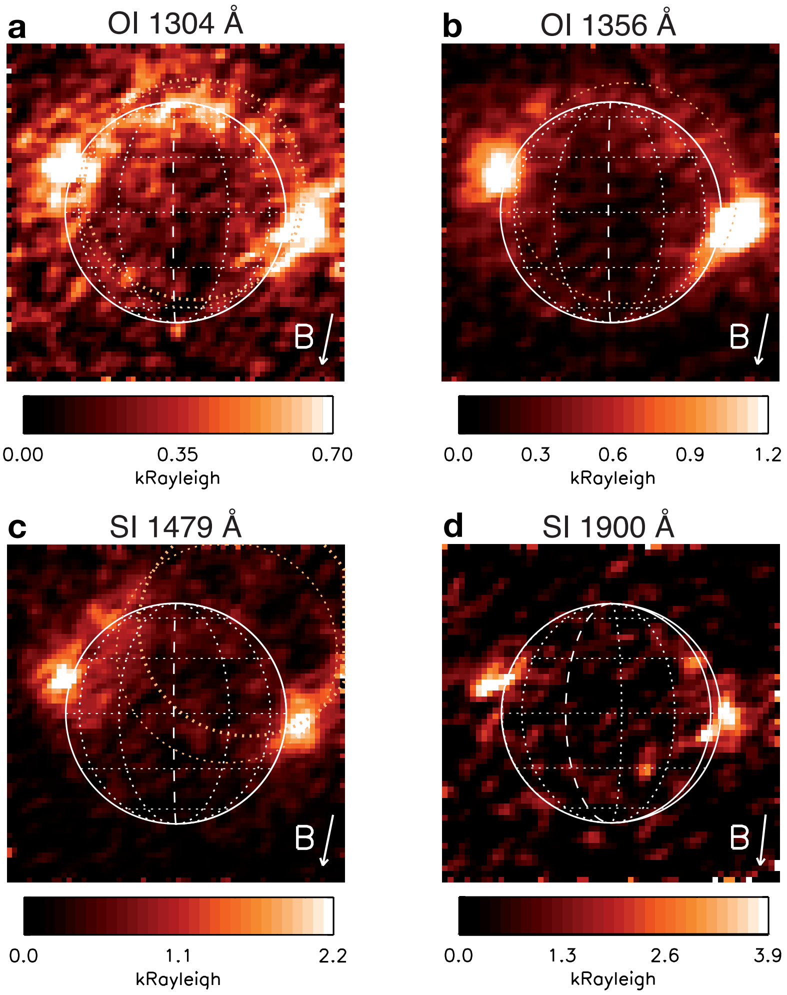

Figure 4.1: *Extracted combined 3 $R_{Io} \times 3$ R_{Io} images of orbit 6 for the (a) OI 1304 Å aurora, (b) OI] 1356 Å aurora and (c) SI 1479 Å aurora. (d) SI] 1900 Å aurora image obtained during orbit 1. All images are taken close to western elongation $\varphi_{obs} \approx 270°$ at a similar System III longitude $\lambda_{III} \approx 85°$. The disk of the brightest line in the multiplets is shown in white with dotted longitudes and latitudes, see Table 4.1. The dashed longitude indicates the upstream/downstream meridian (270°/90° west longitude), the sub-Jovian/anti-Jovian meridian (0°/180° west longitude, hardly visible here) is shown as solid line. The dispersed disk locations of the additional lines of the multiplets are drawn as orange dotted circles. The arrow indicates the direction of the background magnetic field of Jupiter.*

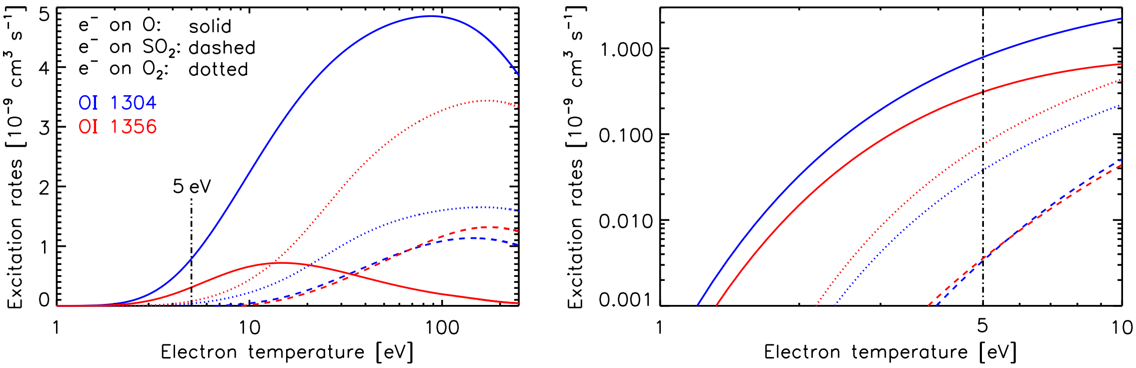

Figure 4.2: *Direct and dissociative excitation rates f_λ for O, O_2 and SO_2 producing OI 1304 Å and OI] 1356 Å emission. The right plot is an enlargement of the left plot on a double logarithmic scale. The temperature of the thermal torus electrons in Io's orbit is approximately $k_B T_e = 5$ eV.*

presumably contributes most for the generally assumed atmospheric mixing ratios of 5−20% of O and O_2. Figure 4.2 shows the excitation rates for direct excitation of atomic oxygen, O, and dissociative excitation of molecular oxygen, O_2, as well as of sulfur dioxide, SO_2. The collisional excitation rates $f_\lambda(T_e)$ can be derived from the energy dependent collision cross sections σ_λ by

$$f_\lambda(T_e) = \int_{E_t}^{\infty} \mathrm{d}E\, f_{\mathrm{Max}}(E, T_e)\sigma_\lambda(E)v(E) \quad . \tag{4.2}$$

Here, E_t is the energy of the excitation threshold, f_{Max} the temperature dependent Maxwellian distribution in energy space and $v(E)$ the electron velocity at a given energy E. The electron impact excitation cross sections used for atomic oxygen emission are based on the laboratory measurements of *Doering and Gulcicek* (1989a,b) and *Doering* (1992). For the O_2 and SO_2 cross sections, we use the values of *Kanik et al.* (2003) and *Vatti Palle et al.* (2004), respectively. Since the dissociative excitation thresholds of SO_2 (∼15 eV) and O_2 (∼10 eV) are higher than the temperature of the thermal torus electrons in Io's orbit of $k_B T_e \approx 5$ eV (*Sittler and Strobel* 1987), the excitation rates for O exceed the O_2 rates roughly by one order of magnitude and the SO_2 rates by even two orders of magnitude.

The respective sulfur excitation rates are shown in Figure 4.3. For excitation of atomic sulfur the adopted cross sections are based on the calculated collision strengths from *Zatsarinny and Tayal* (2002). The calculated SI 1479 Å excitation rate takes into account both the forbidden and allowed lines. The dissociative excitation cross sections of SO_2 producing SI 1479 Å and SI] 1900 Å are taken from *Vatti Palle et al.* (2004) and *Ajello et al.* (1992), respectively. As for oxygen, direct excitation of atomic sulfur,

$$e^- + S \rightarrow S^* \rightarrow S + \gamma \quad , \tag{4.3}$$

presumably accounts for the major part of the observed radiation, unless the mixing ratio of atomic sulfur is considerably lower than 1%. Contributions from dissociative excitation of atmospheric SO and S_2 are not considered here, since no cross sections are available. They are expected to be lower than excitation of the atomic species, as the cross sections for dissociative excitation of SO and S_2 presumably peak at high energies similar to the cross sections of SO_2.

For the electron densities at Io, collisional de-excitation is negligible, so every excitation is balanced by a spontaneous emission (*McGrath et al.* 2000). The probability that a photon will escape

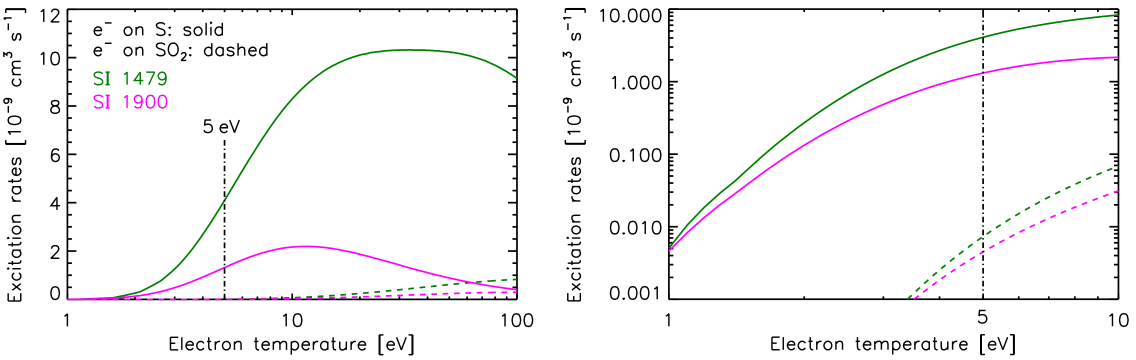

Figure 4.3: Direct and dissociative excitation rates f_λ for S and SO_2 producing SI 1479 Å and SI] 1900 Å emission. The right plot is an enlargement of the left plot on a double logarithmic scale. The temperature of the thermal torus electrons in Io's orbit is approximately $k_B T_e = 5$ eV.

without further scattering and absorption is $\exp(-\tau)$, where $\tau = \sigma_a N_n$ is the optical depth given by the product of the absorption cross sections σ_a and the neutral column density N_n of the line of sight (e.g., *Chamberlain and Hunten* 1987). The measured absorption cross sections for SO_2 are large at the observed wavelengths with values between $\sigma_{SO_2} \approx 3 \times 10^{-18}$ cm^2 for OI] 1356 Å and $\sigma_{SO_2} \approx 1 \times 10^{-17}$ cm^2 for OI 1304 Å (*Manatt and Lane* 1993). Therefore, the optical depth is close to one for emissions that originate from regions very close to the surface, as the estimated column density of Io's dense equatorial SO_2 atmosphere is $\sim 10^{17}$ cm^{-2}. Moreover, the multiplets can undergo self-absorption by the atomic species. The absorption cross section at a given wavelength depends on the line broadening and the oscillator strength of the transition of the atom. For the forbidden transitions, the oscillator strength is very low and the optical depth is therefore $\tau \ll 1$. The atmosphere can, thus, assumed to be optically thin for OI] 1356 Å and SI] 1900 Å (*Morton* 1991, *McGrath et al.* 2000) aside from absorption at very high SO_2 columns. For the allowed transitions of SI 1479 Å and OI 1304 Å, the absorption oscillator strength is considerably higher. The optical depth of SI 1479 Å could not be determined unambiguously, but is assumed to be around 1 (*Feaga et al.* 2002). The oscillator strength of the OI 1304 Å transitions is of the same order, so the atmosphere can not assumed to be optically thin everywhere.

For an optically thin emission the measured brightness can be calculated by integrating the local emission rate i_λ along the line of sight. The local volume emission rate

$$i_\lambda = f_\lambda(T_e)\, n_e\, n_n \tag{4.4}$$

is determined by the density of neutral atmospheric gas n_n, the density of the impinging electrons n_e and the excitation rate f_λ, which depends on the local electron temperature. The local electron parameters are strongly affected by the plasma interaction as described in Section 2.1.3. Hence, to derive atmospheric abundances from the measured auroral intensities both the atmospheric and plasma properties have to be taken into account. In the present chapter, we will focus on the spatial distribution of the auroral emission rather than deducing absolute column densities for the atmospheric species. We will discuss the influence of the emission and absorption processes and roughly analyze the implications of the observed relative brightnesses of the multiplets. In Chapter 5 the plasma interaction for the case when Io is in eclipse will be simulated. Using the simulated spatial distribution of the electron parameters, we can infer atmospheric abundances. As the SO_2 atmosphere is expected to collapse in eclipse, the column density is reduced by approximately one

Table 4.1: *Spectral lines of the observed sulfur and oxygen multiplets and the relative line strengths.*

N_{img} #	Multiplet	Wavelength[a] [Å]	A[b] [s^{-1}]	Theo. rel. intensity[c]	Obs. rel. intensity[d]	G140L disks[e,f]	G140M disks[e]
16	**OI 1304 Å**						
	$^3S^0 \rightarrow {}^3P$	1302.7	3.20×10^8	5	-	1st	-
	(allowed)	1304.9	1.91×10^8	3	-	2st	-
		1306.0	0.64×10^8	1	-	3rd	-
19	**OI] 1356 Å**						
	$^5S^0 \rightarrow {}^3P$	1355.6	4.53×10^3	3.4	3.6	1st	1st
	(forbidden)	1358.5	1.35×10^3	1	1	2st	-
18	**SI 1479 Å**						
	$^3D^0 \rightarrow {}^3P$	1474.1	2.16×10^8	2.5	15.2	1st	1st
	(allowed)	1483.1	1.95×10^8	2.2	11.1	2nd	-
		1487.2	8.70×10^7	1	2.9	3rd	-
	$^5D^0 \rightarrow {}^3P$	1473.0	4.37×10^7	18.3	14.5	1st	2nd
	(forbidden)	1481.7	1.74×10^7	7.4	4.1	2nd	-
		1485.6	2.30×10^6	1	1	3rd	-
2	**SI] 1900 Å**					G230M disk[e]	
	$^5S^0 \rightarrow {}^3P$	1900.3	6.60×10^4	3.5	3 - 3.4	1st	
	(forbidden)	1914.7	1.90×10^4	1	1	-	

[a] The given wavelengths for SI 1479 Å are blended wavelengths as observed by *Feaga et al.* (2002).

[b] Einstein A coefficients (*Morton* 1991, *Tayal* 1998). For SI 1479 Å the given A are combined probabilities for several transitions.

[c] Theoretical relative line strength for a collisionless and optically thin atmosphere derived from the Einstein A coefficients.

[d] Observed relative line strengths. OI 1356 Å: *Retherford* (2002). SI 1479 Å, SI 1900 Å: *Feaga et al.* (2002). The values of the SI 1479 Å forbidden and allowed transitions all refer to the lowest intensity (1485.6 Å).

[e] Disks of Io as displayed in the images, see, e.g., Figure 4.1. 1st refers to the main disk indicated with a white circle and dotted longitudes and latitudes. 2st and 3rd indicate the respective wavelengths of the *secondary disks* plotted with orange dotted circles in the images.

[f] The location of the SI 1479 Å disks in the G140L observations refers to a weighted average wavelength of the nearby forbidden and allowed lines.

to two orders of magnitude and the emissions can be assumed optically thin to major parts in this case.

Dispersion and relative line strengths

Due to the dispersion in the STIS observations, the disk of Io is displaced for the different spectral lines of the multiplets along the dispersion axis by several pixels. The morphology is partially blurred or distorted if the displaced disks overlap. After the rotation of the images into the Jovian coordinate system (see Appendix A.2) the dispersion axis is tilted ~45° with respect to the horizontal image axis. The dispersion axis thus extends from bottom left to top right in the rotated images. The contributing spectral lines and the relative line strengths of the oxygen and sulfur multiplets are listed in Table 4.1.

OI] 1356 Å

The theoretical relative intensities of the lines of the OI] 1356 Å doublet (Figure 4.1b) are 3.4 (1355.6 Å) to 1 (1358.5 Å) given by the Einstein A coefficients, as the emission lines originate from the same upper level (*Morton* 1991, *Tennyson* 2005). *Retherford* (2002) inferred a slightly higher ratio of 3.6 to 1 from the STIS G140M observations. The disk of the 1358.5 Å line (orange circle) is shifted along the dispersion axis by five pixels with respect to the 1355.6 Å line in the G140L observations. For the G140M images the disks do not overlap with a relative displacement of 55 pixels.

OI 1304 Å

The OI 1304 Å multiplet (Figure 4.1a) consists of three lines at 1302.2 Å, 1304.9 Å and 1306.0 Å. Assuming an optically thin atmosphere and neglecting possible contributions from resonantly scattered sunlight, the expected relative intensities are 5:3:1, see Table 4.1. Due to the overlap of the disks in the G140L observations the relative emission strength can not be measured in the images. G140M images containing OI 1304 Å have not been obtained. In the displayed images the disk is centered at the strongest line (1302.2 Å).

SI 1479 Å

The SI 1479 Å multiplet theoretically contains numerous transitions with wavelengths between 1473.0 Å and 1487.2 Å (*Morton* 1991, *Tayal* 1998). In their analysis of the medium resolution STIS observations of the sulfur emission *Feaga et al.* (2002) detect three (partially blended) forbidden lines and three (partially blended) allowed lines, see Table 4.1 and Figure 2.10. In the G140L observation images the disk is centered between the strongest lines at 1473.6 Å. The orange dotted circles show the overlapping disk locations at weighted average wavelengths between the allowed and forbidden lines around 1482 Å and 1486 Å. In the G140M images the main disk is centered at 1474.1 Å, the secondary disk at 1473.0 Å.

SI] 1900 Å

The SI] 1900 Å doublet (1900.3 Å, 1914.7 Å) is well resolved in the G230M observations, i.e., the disks are more than 3 R_{Io} apart in the observations. In our work we will analyze only the stronger emission line at 1900.3 Å.

4.1.2 Variation of the aurora morphology

Although details of the emission morphologies have been described in the previous studies, a comprehensive picture of the local intensities and the spatial extension of the auroral emissions has not been established yet. We will analyze the aurora morphology in all extracted STIS images to infer the three-dimensional distribution of the local oxygen and sulfur emission in the nearby vicinity of Io. The observational parameters for the images are listed in Table 4.2. The sub-observer central meridian almost complies with the orbital longitude as seen from Earth, see Appendix A.2.

The OI] 1356 Å doublet involves a spin forbidden transition and is therefore produced almost exclusively by electron impact. The two lines of the multiplet at 1355.6 Å and 1358.5 Å are only five pixels apart due to the dispersion in the G140L observations and well resolved in the G140M images. Hence, the OI] 1356 Å images reveal the clearest of all observed morphologies originating

Table 4.2: *Observational parameters for the STIS images of Io's aurora.*

Dataset	R$_{\mathrm{Io}}$[a] [pixel]	N_{Pix}[a] [#]	d_{obs}[b] [AU]	d_{sun}[b] [AU]	φ_{obs}[c] [°]	φ_{sun}[c] [°]	λ_{III}[d] [°]	ψ_m[d] [°]	z_c[d] [R$_{\mathrm{Io}}$]	B_x[e] [nT]	B_y[e] [nT]	B_z[e] [nT]
OI 1304 Å, OI] 1356 Å, SI 1479 Å												
o49d020-2a30[*]	19.7	2724	4.4	5.0	272.1	263.2	173.7	8.5	22.8	156	-754	-2147
o49d010-1a10	22.2	3480	4.6	5.0	242.6	232.0	357.4	-8.7	-23.6	-127	545	-1964
o49d010-1a20	22.2	3480	4.6	5.0	255.1	244.5	38.3	-9.1	-24.5	37	631	-2024
o49d010-1a30	22.2	3472	4.6	5.0	268.8	258.2	83.1	-4.4	-11.9	290	428	-2086
o4xm03010-20[*]	21.1	3168	4.1	5.0	261.3	266.7	179.8	8.9	24.1	104	-780	-2145
o4xm03030-40[*]	21.1	3168	4.1	5.0	275.2	280.6	225.4	8.6	23.4	-214	-613	-2086
o4xm03050-60[#]	21.1	3168	4.1	5.0	289.2	294.6	271.5	3.1	8.5	-312	-138	-1988
o4xm03070-80[#]	21.1	3168	4.1	5.0	302.7	308.0	315.7	-4.0	-10.8	-255	289	-1939
o4xm01030-40	25.3	4508	4.0	5.0	298.3	303.3	40.9	-8.9	-24.2	49	630	-2028
o4xm01050-60	25.3	4508	4.0	5.0	312.2	317.2	86.4	-3.9	-10.6	308	395	-2090
o4xm01070-80	25.3	4508	4.0	5.0	325.7	330.7	130.8	3.3	8.8	409	-252	-2134
o4xm02020-30	25.4	4556	4.0	5.0	38.4	42.6	207.5	9.4	25.4	-113	-742	-2117
o5h9a5010-20	25.5	4612	4.0	5.0	329.3	332.7	83.5	-4.4	-11.8	292	425	-2087
o5h906010-20	25.6	4644	4.0	5.0	157.9	160.7	79.9	-4.9	-13.2	272	459	-2082
o5h907010-20	25.6	4644	4.0	5.0	212.6	215.4	259.3	5.0	13.4	-306	-270	-2013
o5h909010-20	18.9	2520	5.4	5.0	59.9	50.0	64.0	-6.9	-18.7	177	569	-2062
o5h909030-40	18.9	2520	5.4	5.0	71.9	62.0	103.4	-1.2	-3.3	386	180	-2109
o5h9a2010-20	18.7	2472	5.5	5.0	16.0	6.5	223.5	8.8	23.6	-205	-630	-2089
o5h9b2010-20	18.7	2472	5.5	5.0	27.9	18.5	262.5	4.5	12.1	-309	-235	-2006
o6jn03bnq-pq	24.1	4120	4.2	5.2	136.5	140.5	189.3	9.3	25.1	25	-794	-2138
o6jn04tmq-oq	24.4	4208	4.2	5.2	146.5	147.1	36.0	-9.2	-24.7	26	631	-2021
SI] 1900 Å												
o49d020-2a10	19.5	2676	4.4	5.0	245.5	236.7	86.5	-3.9	-10.6	309	394	-2090
o49d020-2a20	19.5	2676	4.4	5.0	258.0	249.1	127.4	2.7	7.3	415	-197	-2132

[*] Only OI 1356 Å aurora

[#] Only SI 1479 Å aurora

[a] Radius of Io in pixels, and number of pixels in the image within a radius of 1.5 R$_{\mathrm{Io}}$ around the disk center N_{Pix}.

[b] Distance of Io to the observer (HST) d_{obs}, and to the Sun d_{sun}.

[c] Io-centric sub-observer longitude/orbital longitude as seen from HST/Earth (φ_{obs}) and the Sun (φ_{sun}), see also Appendix A.1. The difference between φ_{obs} and φ_{sun} is the solar phase angle.

[d] Longitude of the Jovian System III λ_{III}, magnetic latitude ψ_m, and the distance between Io and the torus equator z_c, see also Appendix A.1.

[e] Jovian background field after the VIP4 model for the internal field of Jupiter (*Connerney et al.* 1998).

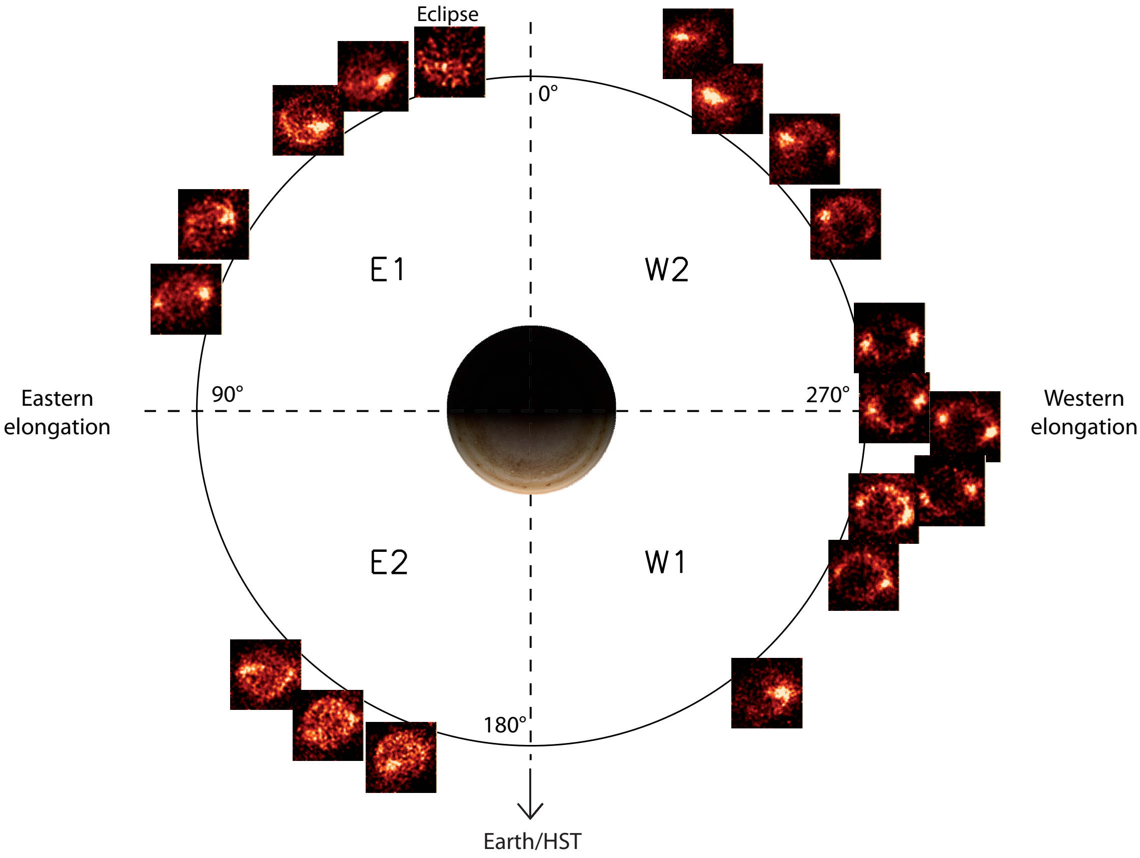

Figure 4.4: *STIS OI] 1356 Å images of Io located at the orbital position of Io during the observation. The orbital position as seen from Earth corresponds to the sub-observer central meridian longitude in the Io-centric coordinate system, see Table 4.2. The color-scale is adjusted to the observed brightness in each image. The orbit is subdivided in four sections: W1 and W2 (E1 and E2) are the quarters before and after western (eastern) elongation, respectively.*

from mostly unattenuated emission by electron impact excited oxygen in Io's atmosphere. Therefore, the properties of the observed morphology in the STIS images is derived in the first place from the OI] 1356 Å images in the next section, although the emission patterns of the OI 1304 Å, SI 1479 Å and SI] 1900 Å aurora principally reveal the same characteristics.

The first STIS images in 1997 were taken when Io was before western elongation revealing the prominent bright equator spots, see Figure 4.1. Until December 2001, Io has been monitored at many orbital longitudes before and after eastern and western elongation, and during one orbit in eclipse by Jupiter. The two morphological features of the near-surface aurora, *equatorial spots* and *limb glow*, were detected in many images, although the observed emission pattern shows considerable variability. In Figure 4.4 all 19 OI] 1356 Å images are located at the approximate orbital position of Io during the observation as seen from Earth allowing a direct comparison of the morphologies along the orbit.

The equatorial spots rock up and down in correlation with the varying direction of the Jovian magnetic field. This can be best observed in the 6 observations around western elongation ($\varphi_{obs} \approx 270°$), where in 3 images the sub-Jovian spot is located above Io's equator and the anti-Jovian spot below it. In the other 3 images close to 270° the spots are shifted in the other directions.

The background magnetic field points southwards and is tilted towards Jupiter in the first case and away from Jupiter in the latter 3 images. The asymmetry of the limb brightness is correlated with the location of the equatorial spots. The northern hemisphere is always brighter, whenever the sub-Jovian spot is above the equator, and vice versa.

The correlated variation is explained by the tilt of the magnetic equator and the centrifugal equator with respect to to the orbital plane. The plasma particles are principally connected to the field and thus stay on one field line. Due to centrifugal forces the plasma concentrates towards the point on the field line that is farthest away from the rotation axis. With the assumption of an ideal magnetic dipole field these points lie in a plane, which is tilted by $\sim 6.3^\circ$ with respect to the rotational equator. The plane is called *centrifugal equator* or *torus equator* and is the symmetry plane for the latitudinal structure of the plasma torus. The magnetospheric geometry for different System III longitudes is sketched in Figure 4.5, when Io is observed at eastern and western elongation.

Above the torus facing hemisphere the electron density is much higher than above the opposite hemisphere. As the field parallel electric conductivity is extremely high, the electrons can propagate almost loss-free along the field lines into the atmosphere. Comparing the average parallel motion of the electrons with the convection speed of the magnetic flux tubes across Io *Retherford et al.* (2003) conclude that most electrons of a flux tube collide with Io (or its atmosphere). The relative aurora brightness of the hemispheres is therefore correlated to the electron column densities in the flux tubes above and below Io.

The deflection and deceleration, when the flux tubes flow past Io, is controlled by the plasma interaction as explained by *Saur et al.* (2000), see Section 2.1.4. The flux tubes that pass Io on the flanks (on less divergent streamlines) are not intersected by the body and transport most energetic electrons into the atmosphere. Assuming a constant electron temperature and density in one flux tube most radiation after (4.4) is emitted, where the highest neutral gas density is found along the flux tube that passes Io on the flank. Further assuming a spatially homogeneous background field and a radially decreasing global atmosphere this location corresponds to the tangential points of the magnetic field on Io's surface. The tangential points build a great circle around Io, which is tilted with respect to the planetographic equator by the angle

$$\beta_0 = \arctan\left(\frac{\sqrt{B_x^2 + B_y^2}}{|B_z|}\right) \quad . \tag{4.5}$$

The circle of the magnetic field tangents on the surface will be designated Io's *magnetic equator*. B_x, B_y and B_z refer to the components of the magnetic field in the IPhiO coordinate system. The IPhiO system is centered at Io with z-axis along Jupiter's spin axis, the x-axis points the azimuthal direction (parallel to the orbital velocity) and the y-axis is the radius vector towards Jupiter. Hence, whenever Io is located above Jupiter's magnetic equator and the centrifugal equator, the limb glow on the southern hemisphere is brighter and the sub-Jovian (anti-Jovian) spot is displaced southward (northward) from Io's equator. This corresponds to the case of $\lambda_{III} \approx 200.8$ in Figure 4.5. For Io being located below the centrifugal equator, i.e., $\lambda_{III} \approx 20.8$, the features are exactly reversed. When Io is situated in the torus center the limb glows of both hemispheres are similar in brightness and the spots located at Io's planetographic equator.

Following Io in its orbit around Jupiter starting from western elongation the sub-Jovian spot moves onto the disk, whereas the anti-Jovian spot disappears behind the limb. In the images that are acquired when Io is further away from eastern and western elongation (before and after

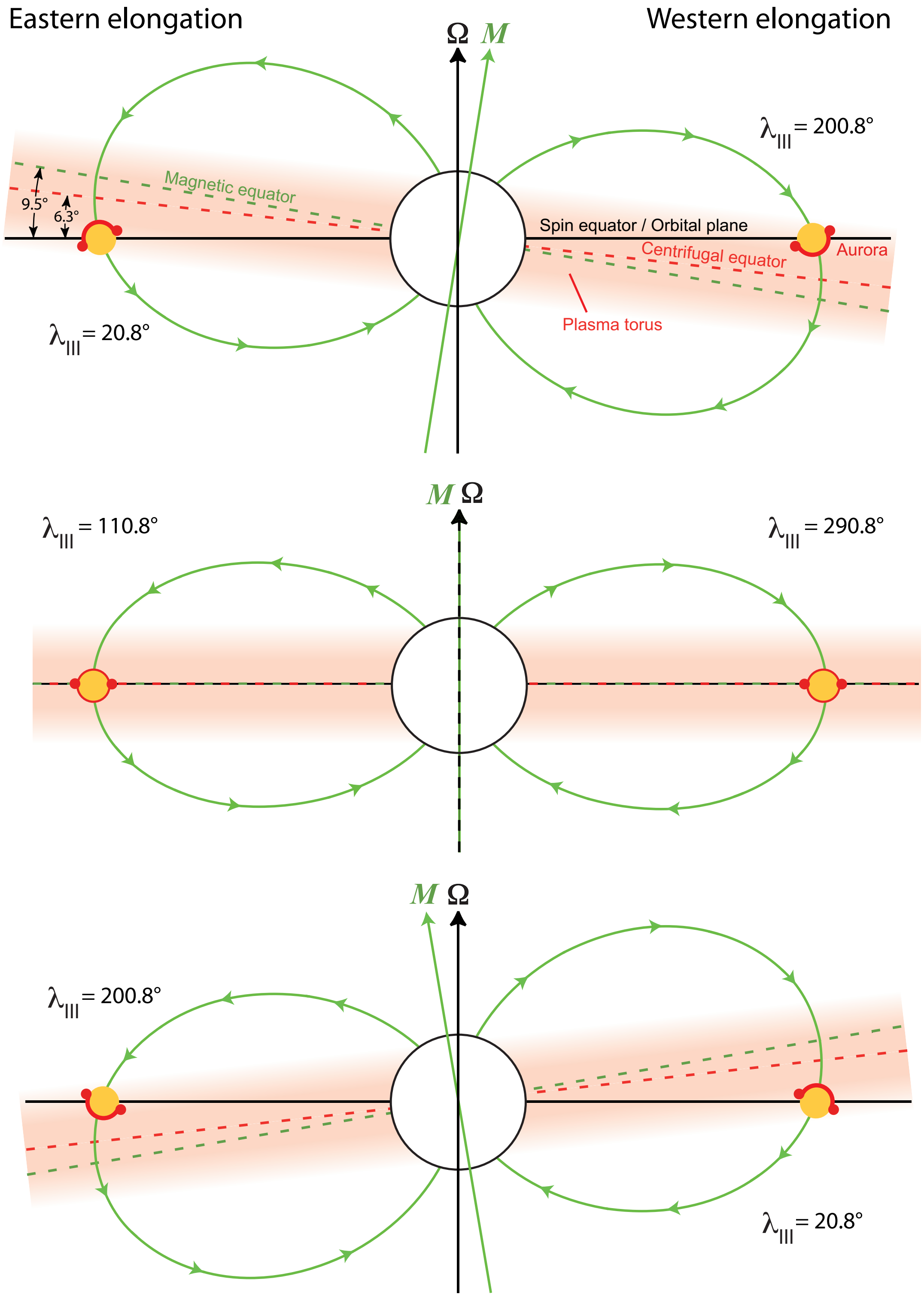

Figure 4.5: *Sketch of the Jovian magnetosphere, plasma torus and Io's aurora features. The varying locations of the equatorial aurora spots and limb glow when Io is at eastern and western elongation are depicted for different System III longitudes. Due to the tilt of the magnetic moment with respect to the rotation axis and the resulting tilt of the centrifugal equator the aurora features vary periodically during a synodic rotation period of Jupiter.*

$\varphi_{obs} = 0°/180°$), the longitudinal extension of the spots becomes visible, see Figure 4.4. As estimated by *Saur et al.* (2000) the electron energy of flux tubes is used up slowly on the flanks, which leads to continuous emission in narrow regions close to the equator on the sub-/anti-Jovian hemisphere. The longitudinal extension of the flank emission together with the line of sight effect lead to the strong intensity of the spots in the observations at eastern and western elongation. In contrast, for images taken some time after eastern elongation (orbit sector E2 in Figure 4.4) the equatorial spots are hardly brighter than the radiation emitted all over Io's disk. This may be partially due to the fact, that the anti-Jovian spot, which is *on* the disk in those images, is always displaced towards the generally darker hemisphere. Thus, one hemisphere reveals a bright limb glow and the opposite side radiates through the spot resulting in an evenly bright emission pattern. In several images, only one equatorial spot is clearly detectable, where the opposite flank emission is obstructed by Io.

Taken together, the observed variability of the aurora morphology appears to originate primarily from (i) Io's orbital longitude and (ii) the magnetospheric environment, i.e., the magnetic field direction and the distance from the torus equator at the time of the observation. However, contributions of, for instance, atmospheric changes to the observed variation can not be ruled out, as there are no observations taken with identical magnetospheric and orbital conditions. Additionally, a change of the total brightness of factor $\sim$3 has been measured, which will be discussed in the next section.

4.1.3 Variation of the aurora brightness

The total brightness of the emission is measured within a radius of 1.5 R_{Io} around the disk center and normalized to the disk area ($\pi R_{Io}{}^2$). The measured brightnesses of the OI] 1356 Å images is displayed in Figure 4.6 (left) as a function of Io's distance from the torus equator $z_c = d_{Jup} \sin(2/3\psi_m)$, with the distance from Jupiter d_{Jup}, and the magnetic latitude ψ_m. The right panel in Figure 4.6 shows the brightness in the chronological order of the observations. Figures 4.7 and 4.8 depict the respective OI 1304 Å and SI 1479 Å total brightnesses. The brightness in the images taken in the G140M mode is adjusted to the bandwidth covered by the G140L images. In the SI 1479 Å images taken in the G140L mode the displaced multiplet lines are only partially included within a radius of 1.5 R_{Io} (see Figure 4.1). Therefore the total inferred SI 1479 Å brightness can be altered depending on the proportion of the displaced emission that is covered in the image.

Like the equatorial spots and limb glow (*Retherford et al.* 2000, 2003), the total aurora brightness tends to decrease with increasing distance to the torus equator. Assuming a constant atmospheric density, the brightness after Equation (4.4) depends on the latitudinal variation of the available electron energy supply, i.e., the ambient electron density and temperature. *Retherford et al.* (2000) and *Wolven et al.* (2001) proposed the variation of the local electron density as probable source of the brightness variation in the STIS observations. An analytical approximation for the latitudinal density distribution in the torus is given by (*Hill and Michel* 1976)

$$n(z_c) = n_0 \exp\left[-(z_c/H_c)^2\right] \quad , \tag{4.6}$$

with the distance from the centrifugal equator z_c and the latitudinal torus scale height H_c. The electron temperature on the other hand increases with latitude ψ_m, i.e., with increasing z_c. Analyzing *Ulysses* plasma data *Meyer-Vernet et al.* (1995) derive an approximate temperature profile given

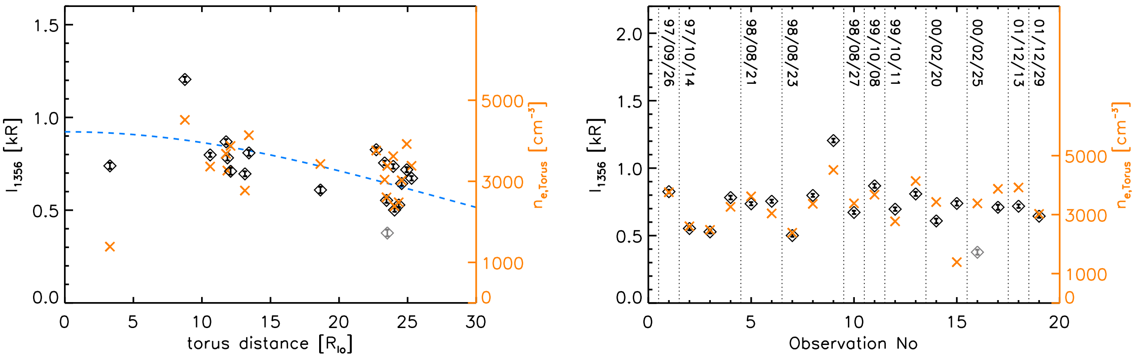

Figure 4.6: *(Left) Auroral brightness and torus electron density as a function of Io’s distance from the torus center. The black diamonds (grey for eclipse image) show the measured OI] 1356 Å brightness with error bars. The blue dashed line shows the fitted profile (4.7) after the latitudinal torus density distribution of Hill and Michel (1976). The values calculated by the torus density model of Smyth et al. (2011) is shown by the orange crosses with the corresponding orange density scale axis. (Right) OI] 1356 Å brightness and torus density of Smyth et al. (2011) for the observations in chronological order.*

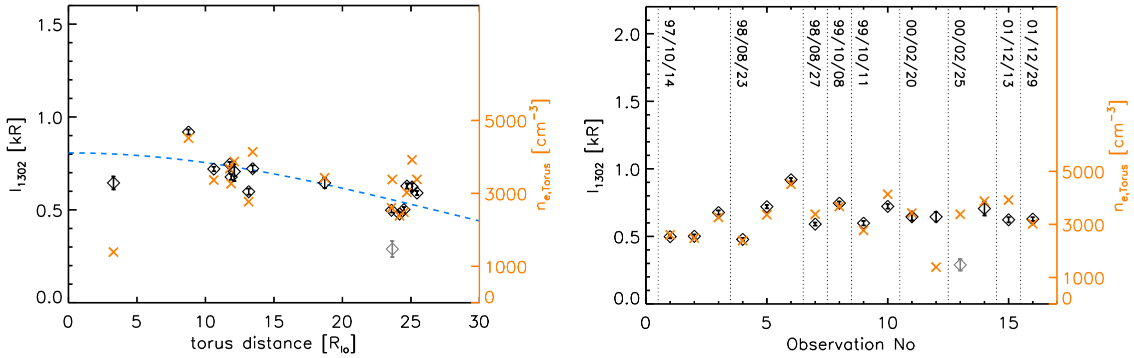

Figure 4.7: *Same as Figure 4.6, but for OI 1304 Å.*

by $T_e(z_c) \propto n_e(z_c)^{-1/2}$. Due to the nearly infinite heat conductivity along the field lines the local temperature differences can be compensated by heat exchange within a flux tube during the interaction with Io and are thus neglected here. Instead we assume that the emission is proportional to the local electron density after (4.6) (referred to as *Hill* model) and fit a theoretical intensity as a function of the torus distance z_c

$$I_{theo}(z_c) = I_0 \exp\left[-(z_c/H_c)^2\right] \quad , \tag{4.7}$$

to the measured brightnesses. The fitting coefficients in (4.7) are the maximum brightness I_0 in the torus center and the torus scale height H_c. The eclipse observation is excluded as the aurora is likely to be affected by an atmospheric collapse. The fitted profiles are shown in Figures 4.6, 4.7 and 4.8, the fitted parameters for OI] 1356 Å, OI 1304 Å and SI 1479 Å are listed in Table 4.3.

The brightness profiles of OI] 1356 Å, OI 1304 Å as well as SI 1479 Å all yield fitted torus scale heights of $H_c = 0.8 - 1.0\,\mathrm{R_J}$. Reported scale heights for the latitudinal density decrease by *Bagenal* (1994) and *Bagenal and Delamere* (2011, their Equation 6) are $H_c \approx 1$ $\mathrm{R_J}$ and $H_c \approx 0.75$ $\mathrm{R_J}$,

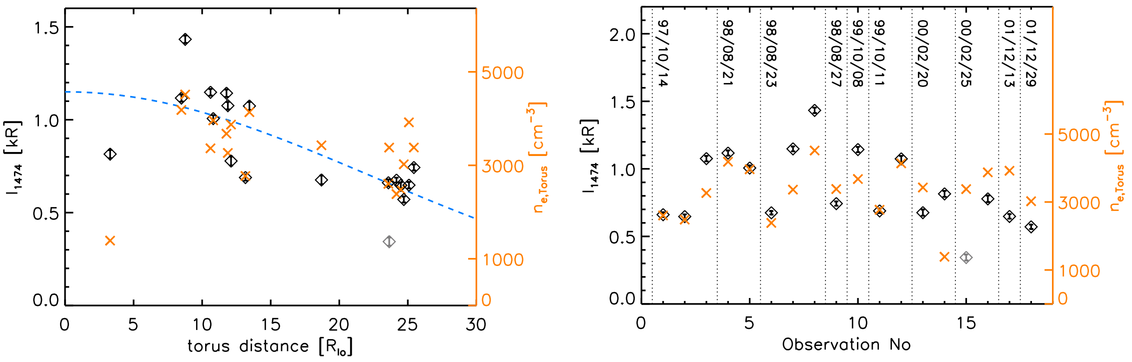

Figure 4.8: *Same as Figure 4.6, but for SI 1479 Å.*

Table 4.3: *Comparison of auroral brightness and torus density*

Multiplet	*Hill* density model			*Smyth* density model		
	I_0[a]	H_c[a]	s_I[b]	c_{conv}[c]	s_I[b]	ρ_{cor}
	[kR]	[R$_J$]	[kR]	[kR/(10^3 cm^{-3})]	[kR]	
OI] 1356 Å	0.89	1.0	0.15	0.219	0.09	0.80
OI 1304 Å	0.81	1.0	0.11	0.196	0.06	0.88
SI 1479 Å	1.14	0.8	0.18	0.255	0.19	0.68
SI] 1900 Å[d]	-	-	-	0.40	-	-

[a] Fitted parameters of Eq. (4.6).
[b] Standard deviations.
[c] Fitted conversion factor of Eq. (4.8).
[d] The derived conversion factor is based only on two G230M images.

respectively, which matches almost exactly our derived values. However, the standard deviation s between the measures brightnesses and our fitted profile is relatively large and much larger than the observation errors. Hence, there seems to be a general correlation of the torus density and the aurora brightness, although the brightness variation can not be explained by a simple density profile like (4.6).

Recently, *Smyth et al.* (2011) presented a sophisticated four dimensional (three spatial dimensions and local time) empirical model for the plasma torus. Analyzing the Galileo Plasma Wave System (PWS) measurements during flyby J0 in 1995, they derive the absolute electron density in Io's orbit as a function of System III longitude and the Io heliocentric phase angle, which is equivalent to the sub-solar longitude φ_{sun} (see Figure 17c in *Smyth et al.* 2011). The density values $n_{e,Symth}$ inferred from the *Smyth* torus model are clearly correlated with the measured aurora brightnesses of the OI 1304 Å and OI] 1356 Å emission, see Figures 4.6 and 4.7. A linear fit for

$$I_{theo}(\lambda_{III}, \varphi_{sun}) = c_{conv}\, n_{e,Smyth}(\lambda_{III}, \varphi_{sun}) \tag{4.8}$$

yields a conversion coefficient c_{conv} from ambient torus density to aurora brightness in Rayleigh for OI] 1356 Å, OI 1304 Å and SI 1479 Å as well as for SI] 1900 Å (based on only two SI] 1900 Å observation images). The standard deviation between measured and fitted brightness is considerably lower for OI] 1356 Å and OI 1304 Å than for the fitted intensity for the *Hill* density profile, and similar for SI 1479 Å, see Table 4.3. In the extracted 3 $R_{Io} \times 3$ R_{Io} images centered on the brightest lines the SI 1479 Å brightness is hard to determine as features of the weaker emission lines are only partly included. Therefore, the measured OI] 1356 Å and OI 1304 Å brightnesses, which are resembled better by the *Smyth* model, are more reliable references for a comparison to the torus density. Furthermore, the *Smyth* model predicts a relatively low density and thus brightness for the observations taken when Io was closest to the torus equator (o5h909030-40 with $z_c = -3.3\mathrm{R_{Io}}$, Obs No 15 in Figure 4.6, right), where the expected brightness after the *Hill* profile is expected to be highest. However, the *Smyth* model seems to even underestimate the electron density in this region as the deviation is the largest.

To check whether the assumption of a linear correlation between the torus density and the aurora brightness is justified, we calculate the sample correlation coefficient (*Bevington and Robinson* 2003)

$$\rho_{cor} = \frac{\sum_{i=1}^{N}(I_i - \bar{I})(n_{e,i} - \bar{n}_e)}{\sqrt{\sum_{i=1}^{N}(I_i - \bar{I})^2}\sqrt{\sum_{i=1}^{N}(n_{e,i} - \bar{n}_e)^2}} \quad , \tag{4.9}$$

where I_i is the observed brightness and $n_{e,i}$ the corresponding electron density after the *Smyth* model with mean values of all observations $\bar{I}$ and $\bar{n}_e$. As for observation o5h909030-40 the model density appears to be significantly underestimated for all multiplets and as the density gradient in the *Smyth* model is large around the parameters λ_{III} and φ_{obs}, this data point is excluded for the calculation of the correlation coefficient. The eclipse observation is also discarded here. The derived ρ_{cor} values for OI] 1356 Å and OI 1304 Å of 0.80 and 0.88 clearly indicate a primarily linear dependence of the total aurora emission on the torus density considering the uncertainties of the torus model and the time variability of the torus (*Delamere and Bagenal* 2003, *Smyth et al.* 2011). The lower correlation coefficient for SI 1479 Å (see Table 4.3) could be due to the difficulties determining the absolute brightness in the spatial SI 1479 Å images mentioned above. The OI] 1356 Å, OI 1304 Å and SI 1479 Å brightness in the STIS eclipse observation appears to be exceptionally low and significantly lower than expected from the ambient torus density for all three multiplets, see grey diamonds in Figures 4.6 to 4.8. The eclipse observations are analyzed in detail in Section 4.2.5.

4.2 Phenomenological model for the aurora distribution

The detailed analysis of the morphology and brightness variations in the STIS images revealed a primarily systematic variability of Io's UV aurora. The position of the equatorial spots and the north/south limb glow ratio as well as the overall brightness appear to be controlled predominantly by the magnetospheric environment. Neglecting possible atmospheric changes and other than the periodic magnetospheric variations, the local emission distribution is thus only a function of Io's System III longitude λ_{III} at the time of the observation. It has been shown that the brightness is almost linearly correlated to the torus density, which is also a function of λ_{III}, but also depends on the sub-solar longitude φ_{sun}. Assuming that the atmosphere is optically thin, the observed aurora pattern is then determined by integrating the local emission rate along the line of sight (*los*) corresponding to the viewing geometry of an observer given by the sub-observer longitude φ_{obs} (and an Io-centric sub-observer latitude if the observer is above or below the Jovian equatorial plane).

With these assumptions, we now develop a phenomenological model for the three-dimensional distribution of the local UV emission based on the observed aurora features at the different viewing angles and magnetospheric conditions. The idea is to find an analytical formula for the local emission rate i, which reproduces the main aurora features, in particular the equatorial spots and limb glow, when integrated along the *los*, for a given System III longitude λ_{III}, sub-solar longitude φ_{sun}, and sub-observer longitude φ_{obs}:

$$I_{mod}(\lambda_{III}, \varphi_{sun}, \varphi_{obs}) = \int_{los} i_{mod}(\lambda_{III}, \varphi_{sun}) \, \mathrm{d}s(\varphi_{obs}) \quad . \tag{4.10}$$

In the next section a functional form for the spatial emission distribution is set up, which is estimated to reproduce the spatial and temporal aurora characteristics as derived from the observations in this work and previous studies (e.g., *Roesler et al.* 1999, *Retherford et al.* 2000, 2003). The model function depends on several parameters representing quantitative properties of the aurora.

4.2.1 Functional description

The relatively bright limb glow appearance is likely to be an effect of the cumulative radiation seen along the limb of the disk, originating from a global emission all over Io's surface. The flank emission clearly exceeds the global radiation both in brightness and radial extension. Therefore the near-surface aurora is described by two separate functions accounting for: (i) a globally emitting atmosphere and (ii) enhanced emission along the sub- and anti-Jovian flanks of Io due to the high input of electron energy into the atmosphere in this region. All fitting parameters in the model functions are indicated with a star (*).

To set up the phenomenological distribution functions, we first assume that the flank emission is symmetric with respect to the equator ($z = 0$). The equatorial plane also separates the northern and southern hemisphere in the description. Hence, we assume that the magnetic background field points exactly southward, i.e., in the negative z-direction ($B_x = B_y = 0$). In this case, the magnetic equator is equivalent to the planetographic equator. The local emission will be given as a function of Io-centric spherical coordinates r, ϑ, φ, where φ refers to the west longitude on Io with $\cos\varphi = \frac{y}{\sqrt{(x^2+y^2)}}$ and $\sin\varphi = \frac{x}{\sqrt{(x^2+y^2)}}$. ϑ is the *Io-graphic* latitude with $\sin\vartheta = \frac{z}{r}$ ranging from $\vartheta = -90°$ at the south pole to $\vartheta = 90°$ at the north pole. x, y, z refer to the Cartesian IPhiO coordinate system, see Section 4.1.2.

Global emission

We assume a global contribution to the aurora from Io's atmosphere given by the local volume emission rate

$$i_{\mathrm{glob}}(r, \vartheta) = i^*_{0,\mathrm{glob}} \exp\left(-\frac{r - \mathrm{R_{Io}}}{H^*_r}\right) \left[1 - \mathrm{erf}\left(\frac{z_c}{H^*_c}\right) \tanh\left(\frac{\vartheta}{20°}\right)\right] \quad . \tag{4.11}$$

The first two terms on the right hand side describe a symmetric global distribution. The emission intensity decreases exponentially with height above the surface $h = r - \mathrm{R_{Io}}$ according to a scale height H^*_r, with a maximum intensity at the surface ($r = \mathrm{R_{Io}}$) given by $i^*_{0,\mathrm{glob}}$. For $r < \mathrm{R_{Io}}$, the emission is naturally zero. This profile resembles the radial density profile of an ideal isothermal atmosphere

$$n_n(h) = n_0 \exp\left(-\frac{h}{H_{\mathrm{atmo}}}\right) \quad , \tag{4.12}$$

with the atmospheric scale height H_{atmo} given by

$$H_{\text{atmo}} = \frac{k_B T}{Mg} \quad . \tag{4.13}$$

k_B is the Boltzmann constant, T the atmospheric temperature, M the mean molecular mass, and g Io's gravitational acceleration. For an isothermal atmosphere the auroral emission would also decrease exponentially with h, if the electron density and temperature were homogeneous in Io's environment (and assuming g to be constant). All these assumptions are not valid for Io (e.g., *Strobel et al.* 1994, *Saur et al.* 1999), the radial emission profile is chosen as a mathematical form describing the expected profile very roughly, rather than as a physical description.

Additionally, a hemispheric asymmetry is implemented by the last term of (4.11) in square brackets. The brightness of the global emission on the northern or southern hemisphere is related to Io's position with respect to the torus equator given by z_c via the Gauß error function defined by

$$\text{erf}(x) = \frac{2}{\sqrt{\pi}} \int_0^x \exp(-x^2)\mathrm{d}x \quad . \tag{4.14}$$

Using this z_c dependence, H_c^* in Equation (4.11) can be related to the torus scale height in the torus density profile (Eq. 4.6) after *Hill and Michel* (1976). The total amount of electrons in the flux tube above Io's north hemisphere after Equation (4.6) is given by an integration along the field line ($\mathrm{d}z_B$):

$$N_e^N(z_c) = \int_{z_c}^{Z_{up}} n_{e,0} \exp\left[-(z_B/H_c)^2\right] \mathrm{d}z_B \quad . \tag{4.15}$$

As the local electron density becomes negligibly small for $z_B \gg H_c$, the upper boundary of the flux tube Z_{up} can be set to infinity to yield

$$N_e^N(z_c) = \int_{z_c}^{\infty} n_{e,0} \exp\left[-(z_B/H_c)^2\right] \mathrm{d}z_B = n_{e,0} H_c \frac{\sqrt{\pi}}{2} \left[1 - \text{erf}\left(\frac{z_c}{H_c}\right)\right] \quad . \tag{4.16}$$

With the flux tube content above Io's south pole

$$N_e^S(z_c) = \int_{-\infty}^{z_c} n_{e,0} \exp\left[-(z_B/H_c)^2\right] \mathrm{d}z_B = n_{e,0} H_c \frac{\sqrt{\pi}}{2} \left[1 + \text{erf}\left(\frac{z_c}{H_c}\right)\right] \quad , \tag{4.17}$$

we can derive a ratio of the flux tube contents of

$$r_{N/S}(z_c) = \frac{N_e^N}{N_e^S} = \frac{\left[1 - \text{erf}\left(\frac{z_c}{H_c}\right)\right]}{\left[1 + \text{erf}\left(\frac{z_c}{H_c}\right)\right]} \quad . \tag{4.18}$$

Together with the dependence on the Io-centric latitude ϑ in Equation (4.11) given through

$$\tanh\left(\frac{\vartheta}{20^\circ}\right) \quad , \tag{4.19}$$

which is positive in the north ($\vartheta > 0$) and negative in the south ($\vartheta < 0$) hemisphere, the implemented asymmetry in (4.11) resembles the brightness ratio of the northern and southern hemispheres expected after Equation (4.18). The latitudinal profile of Equation (4.19) is chosen to obtain a smooth, continuous transition between the hemispheres and is a purely phenomenological description. The denominator in (4.19) determines the slope of the north/south transition and is set to 20°. With this value the intensity ratio at $\vartheta = 20°/45°$ corresponds to $75\%/97\%$ of the maximum intensity ratio at the poles.

The actual north/south brightness variation depends on the electron energy transfer along the flux tubes during the convection of the magnetic field across Io, i.e., the field aligned motion of the electrons and the parallel heat conduction compared to the time scale of the flux tube convection. Latitudinal temperature variations in the Jovian magnetosphere (*Meyer-Vernet et al.* 1995) might also alter the effectiveness of energy transfer into northern and southern atmosphere. Although the functional description of the hemispheric asymmetry is a rough approximation, we show in the next section that the implemented dependency reproduces the relative limb glow brightnesses.

The fitting parameters in (4.11) are the surface intensity i_0^*, the radial scale height H_r^*, and H_c^*, which is related to the scale height of the Io torus.

Flank emission

To describe the distribution of the bright emissions on the sub- and anti-Jovian flanks we use a functional form for the volume emission rate given by

$$i_{\text{spot}}(r, \vartheta, \varphi) = i_{0,\text{spot}}^* \left(\frac{r}{\text{R}_{\text{Io}}}\right)^{-\kappa^*} \exp\left[-\left(\frac{\vartheta}{\Theta^*}\right)^2 - \left(\frac{\varphi - \varphi_0^*}{\Phi^*}\right)^2\right] \quad , \tag{4.20}$$

for each of the two sides (sub-/anti-Jovian). $i_{0,\text{spot}}^*$ is the maximum emission rate in the spot center. We assume a Gaussian profile for the longitudinal and latitudinal expansion of the emission with a peak density at the equator. The maximum in the longitudinal direction is specified by φ_0^* and is expected to be shifted from the sub-/anti-Jovian points ($\varphi = 0°/180°$) towards the downstream hemisphere, i.e., towards $\varphi = 90°$. The width of the two dimensional Gaussian profile is determined by Θ^* and Φ^*, respectively.

Measurements of the spot center yield a height above the surface of approximately 100 km, although large uncertainties are connected with the value due to the two-dimensional projection in the images (*Retherford et al.* 2000). For the model, the radial profile of the spots was first estimated by a Gaussian distribution

$$i(r) \propto \exp\left[-\left(\frac{h - h_0}{H_{\text{spot}}}\right)^2\right] \quad , \tag{4.21}$$

with height $h = r - \text{R}_{\text{Io}}$, an offset from the surface to the spot center h_0, and a radial width H_{spot}. Fitting the model parameters h_0 and H_{spot} to reproduce the observation images, as explained in Section 4.2.2, yielded a negative radial offset h_0, with $|h_0|$ being even larger than the width H_{spot}. This means the maximum flank emission was found at the surface of Io. Since $|h_0| > H_{\text{spot}}$, the peak of the Gaussian profile was far below the surface, where the emission is naturally zero, and only the tail represented the emission distribution above the surface. This profile can be well resembled by the power law

$$i(r) \propto \left(\frac{r}{\text{R}_{\text{Io}}}\right)^{-\kappa^*} \quad , \tag{4.22}$$

with index $\kappa^* > 0$, implemented in (4.20).

The fitting parameters in (4.20) are the local emission rate in the spot center $i_{0,\text{spot}}^*$, the power law index for the radial decay κ^*, the latitudinal and longitudinal width Θ^* and Φ^* as well as the longitude of the spot center φ_0^*. The parameters of each spot (anti-/sub-Jovian) are fitted both combined with one parameter value and separately in order to investigate possible differences between the spots.

The total local volume emission rate is then calculated by adding the global contribution and the emission at the sub- and anti-Jovian flanks

$$i_{\text{loc}}(r,\vartheta,\varphi) = i_{\text{glob}}(r,\vartheta) + i_{\text{anti-J spot}}(r,\vartheta,\varphi) + i_{\text{sub-J spot}}(r,\vartheta,\varphi) \quad . \tag{4.23}$$

Adjustment to the background field and line-of-sight integration

The equatorial spots have been observed to rock up and down according to the varying orientation of the background field. Rather than symmetric with respect to Io's planetographic equator, they presumably form around the magnetic equator, which is tilted by β_0 against the equator after (4.5). Similarly, the symmetry plane for the north/south limb glow asymmetry is supposably represented by the magnetic equator, as the assumed differences originate from the electron energy transport along the magnetic field. The distribution of the local emission i_{loc} given by (4.23) was derived for a southward directed magnetic field $\mathbf{B} = B_z$. Due to the tilt of Jupiter's magnetic moment, either of the magnetic field components B_x and B_y is non-zero in Io's orbit at all times. The emission distribution is therefore adjusted to the orientation of the Jovian magnetic field at the time of the observation.

Therefore, the polar axis of the coordinate system of the local emission distribution is rotated from the spin axis towards the negative magnetic field direction. The local emission coordinates are then given by

$$\begin{pmatrix} r' \\ \vartheta' \\ \varphi' \end{pmatrix} = \mathbf{R}_\alpha \begin{pmatrix} r \\ \vartheta \\ \varphi \end{pmatrix} \quad , \tag{4.24}$$

with (r,ϑ,φ) referring to the spherical coordinates of the IPhiO system explained above. $\mathbf{R}_\alpha$ is the rotation matrix with the rotation angle α is given by

$$\alpha = \zeta^* \beta_0 = \zeta^* \arctan\left(\frac{\sqrt{B_x^2 + B_y^2}}{|B_z|}\right) \quad , \tag{4.25}$$

with the inclination angle β_0 given by (4.5). B_x, B_y, and B_z are the components of the undisturbed homogeneous background field in the IPhiO coordinate system. The radius vector is naturally unchanged, i.e., $r' = r$.

The magnetospheric **B** field in Io's orbit is dominated by the intrinsic field of Jupiter. Contributions of the magnetic field arising from magnetospheric currents or Chapman-Ferraro currents at the magnetopause are more than an order of magnitude lower and therefore neglected here (*Khurana et al.* 2004). The magnetic field direction during the observations is calculated as function of the System III longitude λ_{III} using the VIP4 model of *Connerney et al.* (1998). For $\zeta^* = 1$ the flank emission is symmetric around the magnetic equator, which is then also the plane separating the northern and southern global emission. Like the parameters in Equations (4.11) and (4.20), the parameter ζ^* is fitted to the observations.

To compute the two-dimensional projection of the local near-surface emission as seen by an observer, we integrate along the line of sight (*los*) over the local emission distribution:

$$I_{\mathrm{loc}} = \int_{los} i_{\mathrm{loc}} \, \mathrm{d}s \quad . \tag{4.26}$$

The *los* is determined by the sub-observer longitude φ_{obs}.

Extended emission

Wolven et al. (2001) analyzed the sulfur and oxygen emissions in the STIS G140L images along the spatial detector axis finding an extended coronal emission reaching out to more than 5 $\mathrm{R_{Io}}$ above the surface. To account for the contribution of the coronal emission, we add a constant background emission, I_{ext}, to the computed two-dimensional pattern (4.26). The total modeled brightness is calculated as

$$I_{mod} = I_{\mathrm{ext}} + I_{\mathrm{loc}} \quad . \tag{4.27}$$

For simplicity, we thereby assume the coronal emission to be spatially homogeneous with an extension substantially larger than the radius of the analyzed emission (1.5 $\mathrm{R_{Io}}$). In this case of a homogeneously radiation space, half of the coronal radiation is obstructed by the disk of Io. Hence, the background radiation is given by

$$\begin{aligned} I_{\mathrm{ext}} &= 0.5\, I^*_{0,\mathrm{ext}} && \text{on the disk} \\ I_{\mathrm{ext}} &= I^*_{0,\mathrm{ext}} && \text{above the limb} \quad . \end{aligned} \tag{4.28}$$

The value $I^*_{0,\mathrm{ext}}$ accounting for the extended emission is another fitting parameter.

Overview of the model functions

The phenomenological description of the two-dimensional aurora morphology as seen from an observer is given by the sum of the local and extended two-dimensional radiation patterns after Equation (4.27). The extended emission is assumed to be constant and is given by Equation (4.28). The local emission is calculated by an integration along the line of sight (depending on φ_{obs})

$$I_{\mathrm{loc}} = \int_{los(\varphi_{obs})} \left[i_{\mathrm{glob}}(r', \vartheta') + i_{\text{anti-J spot}}(r', \vartheta', \varphi') + i_{\text{sub-J spot}}(r', \vartheta', \varphi') \right] \, \mathrm{d}s \tag{4.29}$$

over the local emission distribution as a function of the rotated coordinate system $(r', \vartheta', \varphi')$. The rotation angle depends on the parameter ζ^* and the direction of the background field $\mathbf{B}(\lambda_{III})$. The local volume emission rate is given by the flank emission (or spot emission)

$$i_{\mathrm{spot}}(r', \vartheta', \varphi') = i^*_{0,\mathrm{spot}} \left(\frac{r'}{\mathrm{R_{Io}}} \right)^{-\kappa^*} \exp \left[- \left(\frac{\vartheta'}{\Theta^*} \right)^2 - \left(\frac{\varphi' - \varphi^*_0}{\Phi^*} \right)^2 \right] \quad , \tag{4.30}$$

for each of the two spots and a global emission

$$i_{\mathrm{glob}}(r', \vartheta') = i^*_{0,\mathrm{glob}} \exp \left(- \frac{r' - \mathrm{R_{Io}}}{H^*_r} \right) \left[1 - \mathrm{erf} \left(\frac{z_c}{H^*_c} \right) \tanh \left(\frac{\vartheta'}{20^\circ} \right) \right] \tag{4.31}$$

with a hemispheric asymmetry. The model parameters **p** are summarized in Table 4.4. The parameters describing the flank emission are analyzed individually for each spot investigating possible differences between the anti-Jovian and sub-Jovian flank.

Table 4.4: *Description of the parameters of the aurora model equations (4.27 to 4.31)*

No	Parameter	Description
1	$I^*_{0,\mathrm{ext}}$	Constant background brightness
		Global emission
2	$i^*_{0,\mathrm{glob}}$	Volume emission rate at surface
3	H^*_r	Scale height of global emission
4	H^*_c	Scale height for hemispheric asymmetry
		Flank emission
5	$i^*_{0,\mathrm{spot}}$	Volume emission rate in the spot center
6	κ^*	Power law index for radial decay
7	Θ^*	Latitudinal extension (width)
8	Φ^*	Longitudinal extension (width)
9	φ^*_0	West longitude of the spot center
10	ζ^*	Proportional inclination of the local emission

Additionally, the total photon emission rate of the global aurora and the combined flank emissions can be calculated by integrating over the entire space around Io. Thereby, we use 1.5 $\mathrm{R_{Io}}$ as outer radial boundary to include only the local emission. Assuming $z_c = 0$ without loss of generality, the total photon rate of the global emission is

$$\varepsilon_{\mathrm{glob}} = \int_{\mathrm{R_{Io}}}^{1.5\,\mathrm{R_{Io}}} \int_{-\pi/2}^{\pi/2} \int_0^{2\pi} i^*_{0,\mathrm{glob}} \exp\left(-\frac{r' - \mathrm{R_{Io}}}{H^*_r}\right) r'^2 \cos\vartheta'\, \mathrm{d}\varphi' \mathrm{d}\vartheta' \mathrm{d}r' \quad . \tag{4.32}$$

Similarly, the total photon emission rate of both spots is given by

$$\varepsilon_{\mathrm{spots}} = \int_{\mathrm{R_{Io}}}^{1.5\,\mathrm{R_{Io}}} \int_{-\pi/2}^{\pi/2} \int_0^{2\pi} \left[i^*_{0,\text{sub-J}}(r', \vartheta', \varphi') + i^*_{0,\text{anti-J}}(r', \vartheta', \varphi')\right] r'^2 \cos\vartheta'\, \mathrm{d}\varphi' \mathrm{d}\vartheta' \mathrm{d}r' \quad . \tag{4.33}$$

4.2.2 Fitting of the model

The derived phenomenological description (Equations 4.27 – 4.31) depends on the observational parameters φ_{obs}, λ_{III}, and z_c, which is a function of λ_{III}. φ_{obs} determines the *los* integration, λ_{III} the rotation of the local emission, and z_c the hemispheric asymmetry. Corresponding to the observational parameters (Table 4.2) a model image is generated for each of the STIS observation images. By adjusting the model parameters to fit the observed emission, quantitative properties of the aurora are inferred.

For each spectral line of the multiplets OI 1304 Å, OI] 1356 Å, and SI 1479 Å a two-dimensional model image is generated separately and adjusted to the relative observed (OI] 1356 Å, SI 1479 Å) or theoretical (OI 1304 Å) intensities after Table 4.1. The adjusted images of each spectral line are superposed with a spatial offset in (x'_d, y'_d) according to the rotated displacement on the detector dispersion axis x_d in the respective STIS observation. The modeled two-dimensional emission I_{mod}

is spatially binned according to the spatial resolution of the observations. The modeled emission is then given as a function of detector pixels $I_{mod}(x'_d, y'_d)$ of the rotated axis x'_d and y'_d, with y'_d pointing towards Jovian North. We will drop the accents and use x_d and y_d for the pixel values in the rotated images from now on. In the STIS images the resolution varies between 18.7 pixels and 25.6 pixels per $\mathrm{R_{Io}}$ depending on the observation mode and the distance of Io from HST. To account for the scattering in the telescope system the modeled images are convolved with the STIS point spread function.The PSF is simulated with the *Tiny Tim* tool for the respective observing mode and rotated according to the image rotation as described in Appendix A.5. The binned, PSF-convolved, and superposed images can be compared directly to the STIS observation images, pixel by pixel.

By minimizing the chi-squared value after (3.8) of the measured and modeled brightness of all pixels in an image

$$\chi^2_{img}(\mathbf{p}) = \sum_{x_d,y_d} \left[\frac{I_{obs}(x_d,y_d) - I_{mod}(x_d,y_d,\mathbf{p})}{\sigma_I(x_d,y_d)} \right]^2 \quad , \tag{4.34}$$

the most probable values for the model parameters $\mathbf{p}$ are inferred. $\sigma_I(x_d,y_d)$ is the propagated statistical pixel error after (3.4). The sum in (4.34) includes all pixels within a radius of 1.5 $\mathrm{R_{Io}}$ around the center of the disk. By choosing this relatively small region, distortions from nearby spectral lines are minimized, whereas the near-surface bright emission is almost entirely covered. Depending on the spatial resolution, the total number of pixels in the images within 1.5 $\mathrm{R_{Io}}$ ranges from 2472 pixels up to 4644 pixels, see Table 4.2.

The development of the phenomenological model was based on the assumption, that the observed aurora morphology and intensity only depend on the magnetospheric environment and the observing geometry. The two-dimensional morphology in an individual observation image can be explained by various three-dimensional distributions projected on the observation plane. However, a simultaneous fitting of all observation images obtained at different viewing perspectives yields much more rigorous constraints on the local emission distribution. Due to the different perspectives in the images, a three-dimensional distribution can be actually constraint. We will therefore derive a universal best-fit parameter set by minimizing the average squared deviations of all pixels in all acquired images of an emission multiplet. The reduced total chi-squared is given by the sum over all images

$$\chi^2_{\mathrm{tot}}(\mathbf{p}) = \frac{1}{N_{img}} \sum_{img} \frac{1}{N_{pix}} \sum_{x_d,y_d} \left[\frac{I_{obs}(x_d,y_d) - I_{mod}(x_d,y_d,\mathbf{p})}{\sigma_I(x_d,y_d)} \right]^2 \quad , \tag{4.35}$$

with the number of all images obtained for the particular emission multiplet N_{img}, and the number of pixels in the respective image N_{pix}. The number of the parameters M is neglected here, since $M \ll N$. Through the division by N_{pix} we make sure, that the images are weighed equally, i.e., independently of the number of pixels.

If all images are fitted simultaneously, brightness variations that are independent of the observing geometry, must be taken into account in the model. The total brightness has been shown to be correlated to the local torus electron density. An approximate brightness can be inferred using (4.8) with the derived conversion factors c_{conv} (Table 4.3) from the torus density after *Smyth et al.* (2011) for a given λ_{III} and φ_{sun}. However, the dependence on the torus density is presumably not exactly linear. Additionally, the uncertainties in the modeled torus densities are not known. Instead of scaling the brightness of our modeled images with the ambient torus density, we therefore multiply each model image with a factor given by the total brightness $I_{obs,tot}$ of the respective observation image divided by the average brightness in all images $\langle I_{obs,tot} \rangle$. By adjusting the intensity in the model images to the observed total brightness with

$$I_{mod}^{adj}(x_d,y_d) = I_{mod}(x_d,y_d)\,\frac{I_{obs,tot}}{\langle I_{obs,tot}\rangle} \quad , \tag{4.36}$$

we can derive average emission intensities for all images simultaneously by minimizing (4.35) for $I_{mod}^{adj}(x_d,y_d)$. The effect of the observing geometry on the visibility of the aurora features and thus the observable total emission is thereby neglected. According to our results for the emission distribution, the brightness variations due to the viewing geometry are $< 8\%$ of the average observed brightness and therefore significantly smaller than the variations due to the changing torus density (up to 80%). The derived volume emission rates and background radiation then apply to the average observation brightness of the STIS images.

To search the parameter space for an optimized $\chi^2_{\mathrm{tot}}(\mathbf{p})$, the down-simplex method by *Nelder and Mead* (1965) is used. The advantages and disadvantages of the minimization method are discussed in Section 3.5.3. The total number of data points, i.e., the number of all pixels in all images, is 60724 for OI 1304 Å, 69784 for OI] 1356 Å 67060 for SI 1479 Å, and 5352 for SI] 1900 Å, whereas the dimension of the parameter space is on the order of 10. As explained in Section 3.5.3, a shallow profile is expected for $\chi^2_{\mathrm{tot}}(\mathbf{p})$. Since $\sigma_I(x_d,y_d) \approx I(x_d,y_d)$, the reduced chi-squared $\chi^2_{\mathrm{tot}}(\mathbf{p})$ is also expected to be below 1 for almost any random parameter set.

To check, whether the inferred three-dimensional distribution adequately resembles the observations, we quantitatively analyze the total radiation of distinct larger regions and compare the deviation between modeled and observed intensity weighted with the propagated statistical errors. In particular, we analyze the brightness of the northern and southern limb (I^N_{limb}, I^S_{limb}) and of the equatorial spots ($I_{\text{anti-J spot}}$, $I_{\text{sub-J spot}}$) as well as the total brightness I_{tot} and the disk brightness I_{disk}. I_{tot} always refers to the total intensity of all pixels within 1.5 R_{Io} of the disk center, which is normalized to the disk area. The disk brightness I_{disk} accounts for the summed brightness of all pixels within 1.0 R_{Io} of the disk center.

The analyzed areas include $\gtrsim$100 pixels, i.e., the errors are reduced by a factor of $\gtrsim$10. For instance, the signal to noise ratio for the measured total brightness in the images is $SNR(I_{tot}) \approx 50$, on average. Furthermore, the analysis of the relative brightness of certain areas allows a comparison of the modeled and observed morphology independently of the absolute intensities. By calculating the reduced chi-squared for the values inferred from the modeled images Y_{mod} and from the observation images Y_{obs} weighted with the respective propagated error $\sigma_{Y_{obs}}$

$$\chi^2_Y = \frac{1}{N_{img}} \sum_{img} \left[\frac{Y_{obs} - Y_{mod}}{\sigma_{Y_{obs}}}\right]^2 \quad , \tag{4.37}$$

we can determine the difference quantitatively. The number of degrees of freedom is set to the number of analyzed image pairs N_{img}, as the model parameters are assumed to be fixed in this case (and thus do not reduce the degrees of freedom).

4.2.3 Distribution of the OI] 1356 Å aurora

As the OI] 1356 Å aurora has been shown to be the clearest of all emissions imaged, we first derive a parameter set in best agreement with the OI] 1356 Å images. Thereafter, the inferred distribution is compared with and adapted to the observed OI 1304 Å, SI 1479 Å, and SI] 1900 Å emission patterns in Section 4.2.4. Particularly, the OI 1304 Å and SI 1479 Å aurora are potentially not optically thin. Nonetheless, the fitted aurora model yields reasonable agreement with the observations.

After testing various initial parameters and variation length scales, a parameter set minimizing the chi-squared value for all STIS OI] 1356 Å images has been obtained. Due to the high pixel uncertainty the resulting chi-squared value after (4.35) is very low with $\chi^2_{tot}(1356) = 0.25$. This means that the mean deviation of the modeled pixel intensity to the observed value corresponds to one fourth of the propagated statistical uncertainty. The best-fit parameters are listed in Table 4.5. The listed minimum and maximum for each parameter refer to the values, where the resulting chi-squared is 2% larger than the best-fit chi-squared, if the parameter is varied individually. This small variation boundary is chosen due to the shallow χ^2 profile, see Section 3.5.3. Note that the minimum and maximum values, therefore, do *not* determine an absolute uncertainty of the parameters, but specify the relative sensitivity of the model to the respective parameter.

In Figures 4.9 and 4.11 the OI] 1356 Å observations are displayed ordered after the sub-observer longitude. Figures 4.10 and 4.12 show the respective model images. At first glance, the model images seem to resemble the main features of the observations, i.e., the approximate spot position and brightness as well as the limb glow appearance. The noticeable small scale features in the observations can be attributed to statistical random noise to major parts due to the mentioned low count rate and high pixel uncertainty. The total brightness of the fitted model images is ∼5% lower than the observed total brightness. As discussed in Section 3.5.3, this is likely to be an effect of the fitting technique, since we assume a Gaussian probability distribution for the pixel counts, which are principally Poisson distributed. We will now quantitatively examine the accordance of the image pairs, discuss the derived parameter values and elaborate on their relevance and physical meaning. The parameter values for the emission intensities, $I^*_{0,\mathrm{ext}}$, $i^*_{0,\mathrm{glob}}$ and $i^*_{0,\mathrm{spot}}$ are scaled to an ambient torus density of $n_e = 3000$ cm^{-3}. Other possible parameter values explaining the observations will be reflected.

Extended emission

The derived average coronal brightness of $I_{0,\mathrm{ext}} = 0.09$ kR is slightly lower than the measured coronal brightness 1 $\mathrm{R_{Io}}$ above the surface of ~ 0.10 kR by *Wolven et al.* (2001). The small difference can at least in part be attributed due to the differing methods of subtracting the background emission along the slit. Principally, the inferred value is on the order of the observed coronal OI] 1356 Å brightness.

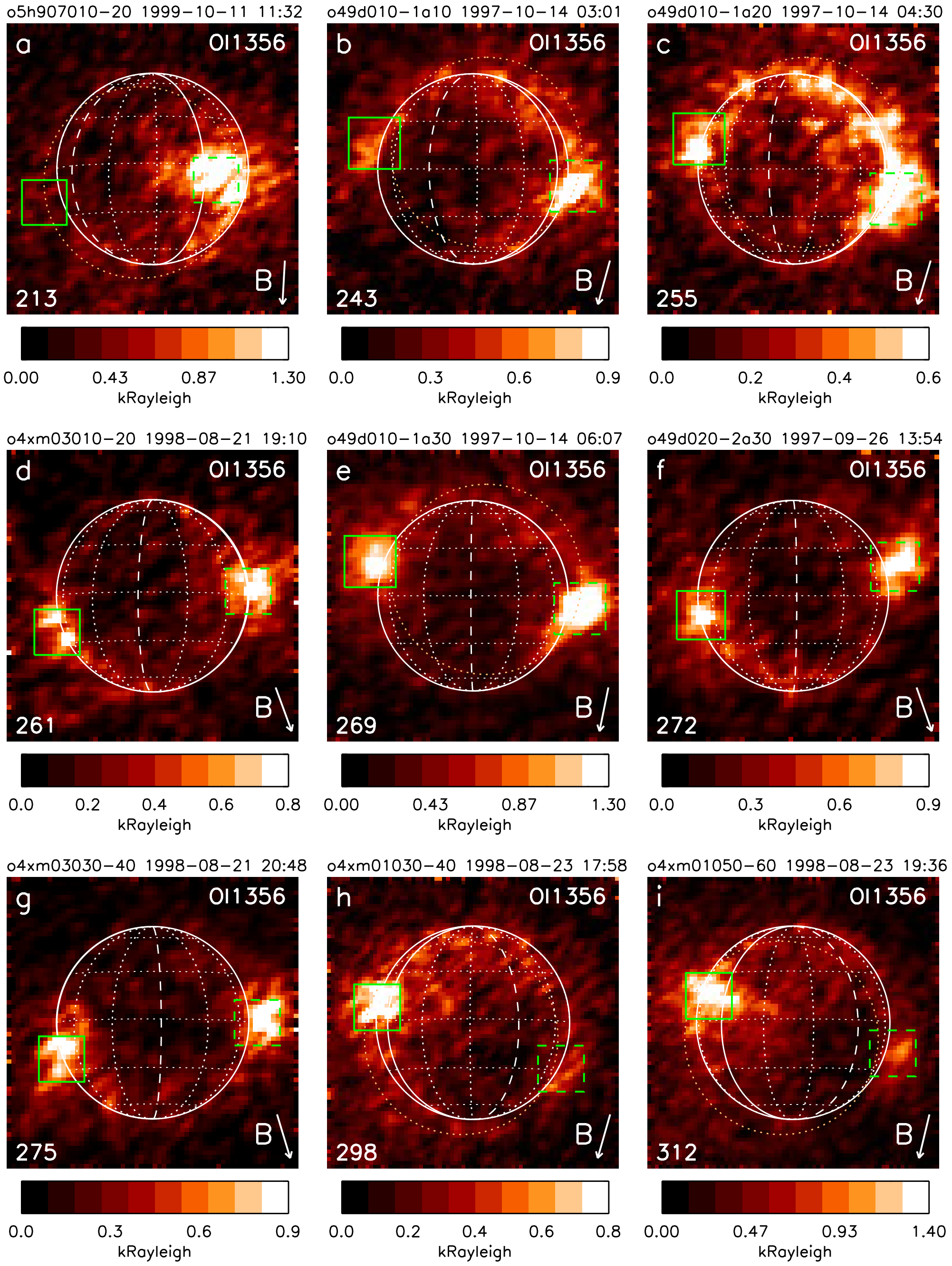

Figure 4.9: *STIS images of the OI] 1356 Å aurora ordered by sub-observer longitudes from* $\varphi_{obs} = 213^\circ$ *(a) to* $\varphi_{obs} = 312^\circ$ *(i) (around western elongation). The sub-observer longitude of the observation is specified in the lower left corner, the arrow in the lower right corner shows the direction of the background magnetic field. The green boxes indicate the sub-Jovian (solid) and anti-Jovian (dashed) equatorial spots. For further explanations see Figure 4.1. The observation parameters are listed in Table 4.2.*

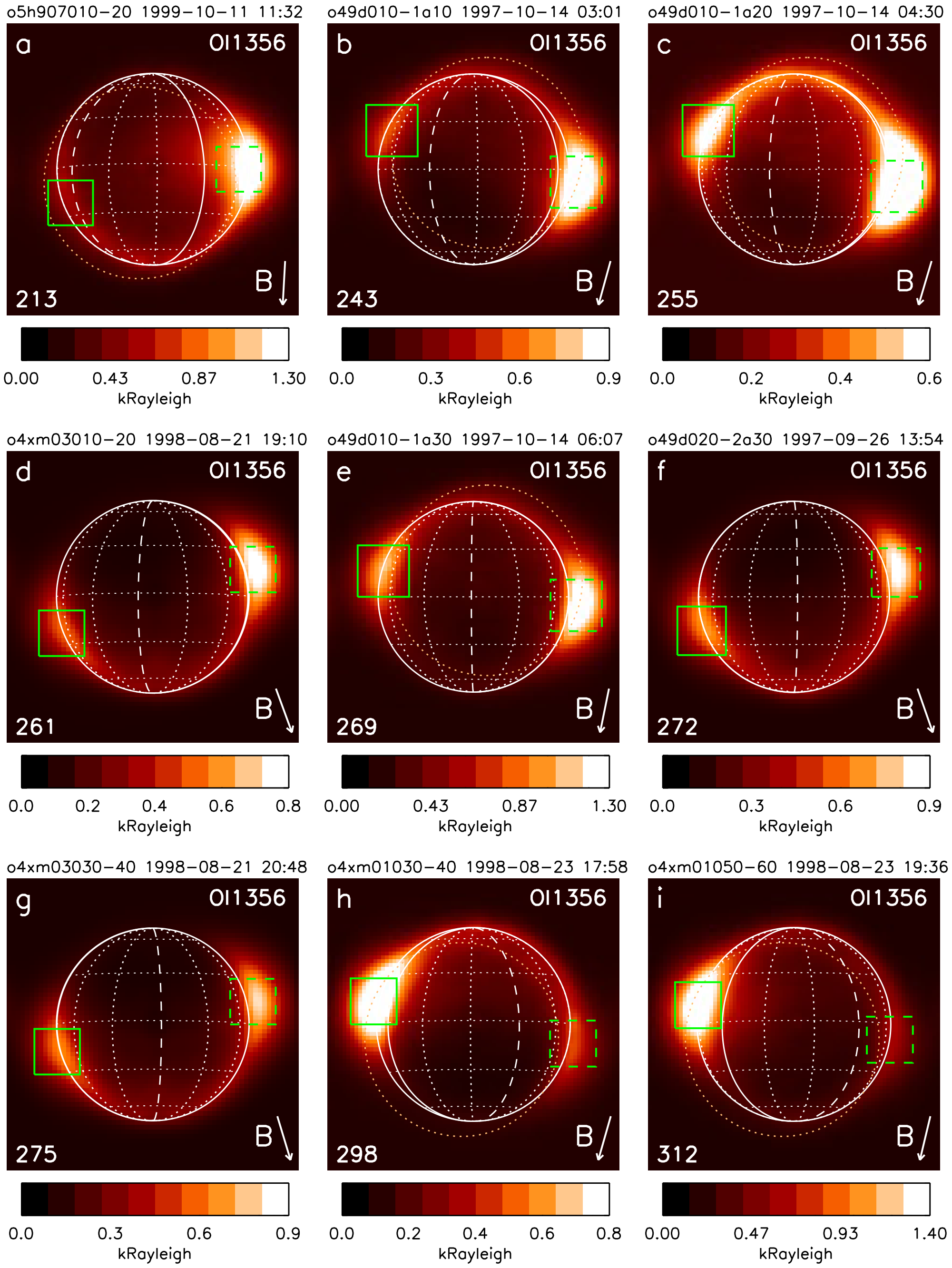

Figure 4.10: *Modeled images of the OI] 1356 Å aurora corresponding to the observations of Figure 4.9. For the model parameters see Table 4.5.*

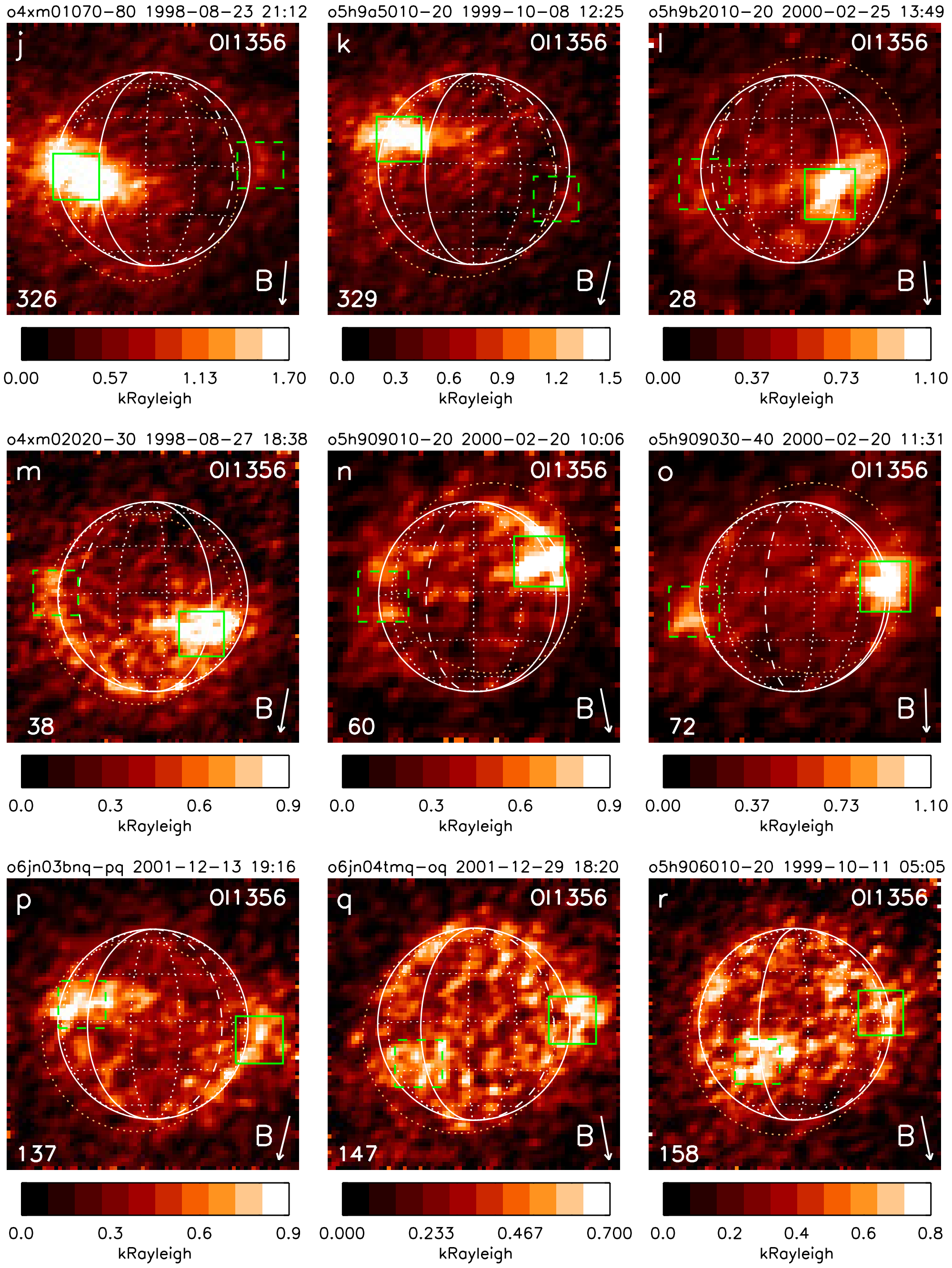

Figure 4.11: *STIS images of the OI] 1356 Å aurora ordered by sub-observer longitudes from* $\varphi_{obs} = 326°$ *(j),* $\varphi_{obs} = 329°$ *(k) (before eclipse), and* $\varphi_{obs} = 28°$ *(l) to* $\varphi_{obs} = 157°$ *(r) (after eclipse and around eastern elongation). For further explanations see Figures 4.9 and 4.1.*

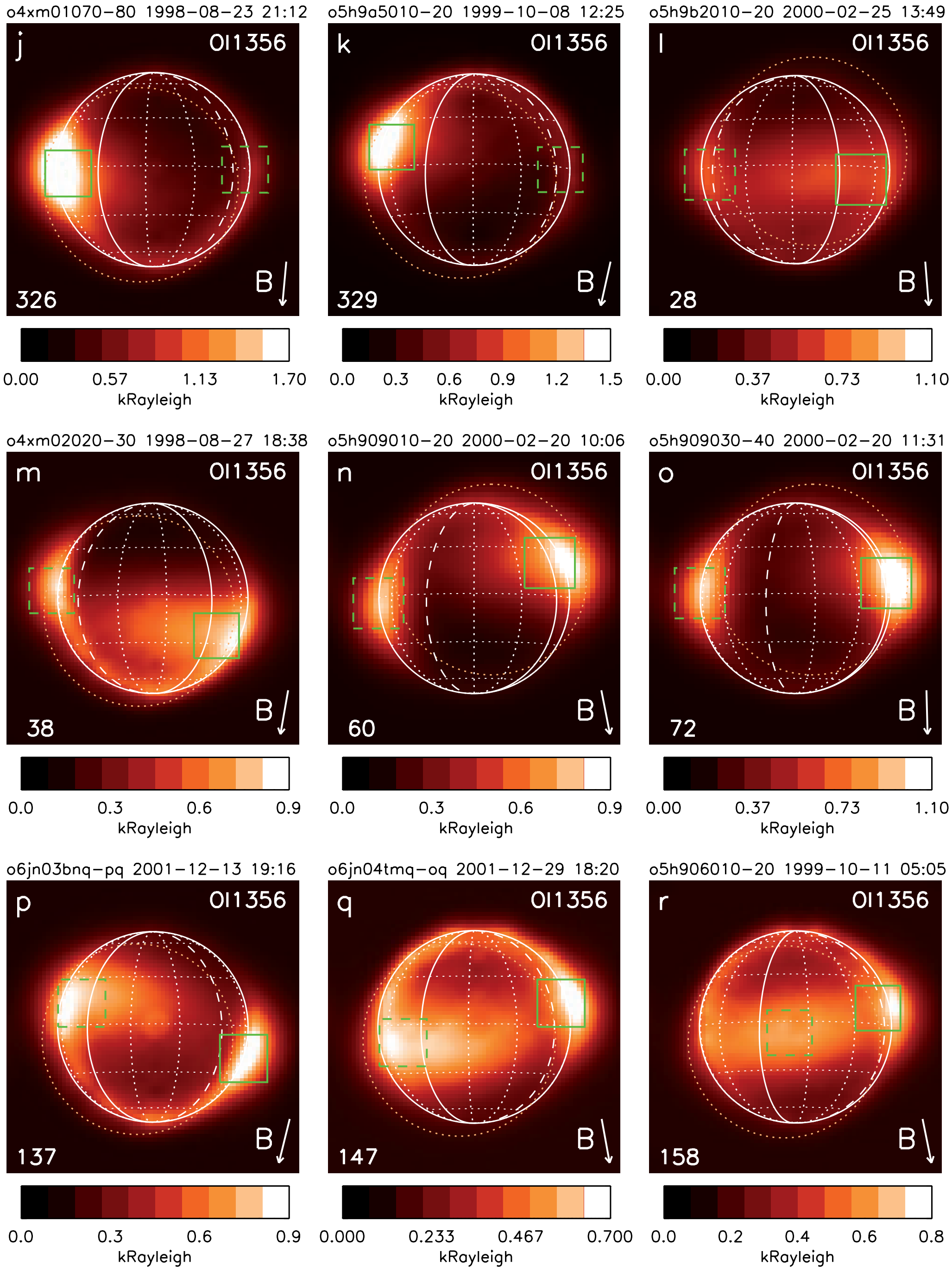

Figure 4.12: *Modeled images of the OI] 1356 Å aurora corresponding to the observations of Figure 4.11. For the model parameters see Table 4.5.*

Table 4.5: *Best-fit parameters and total photon emission rates for the OI] 1356 Å aurora.*

No	Parameter	Unit	**Best-fit value**[a]	Min[b]	Max[b]
1	$I^{*}_{0,\mathrm{ext}}$[c]	[kR]	**0.09**	0.07	0.11
		Global emission			
2	$i^{*}_{0,\mathrm{glob}}$[c]	$[\mathrm{cm}^{-3}\mathrm{s}^{-1}]$	**82.4**	65.6	95.4
3	H^{*}_{r}	[km]	**9.8**	7.8	11.2
4	H^{*}_{c}	$[\mathrm{R_J}]$	**1.1**	0.6	2.1
		Flank emission			
5a	$i^{*}_{0,\mathrm{spot}}$[c] (day)	$[\mathrm{cm}^{-3}\mathrm{s}^{-1}]$	**12.5**	10.2	14.4
5b	$i^{*}_{0,\mathrm{spot}}$[c] (night)	$[\mathrm{cm}^{-3}\mathrm{s}^{-1}]$	**7.6**	4.7	10.0
6	κ^{*}		**6.4**	5.4	7.3
7	Θ^{*}	[°]	**23**	20	27
8	Φ^{*}	[°]	**48**	40	56
9	φ^{*}_{0}	[°]	**20**	12	28
10	ζ^{*}		**0.79**	0.53	1.04
		Total photon emission rates			
	$\varepsilon_{\mathrm{glob}}$[c,d]	$[\mathrm{s}^{-1}]$	$\mathbf{3.5 \times 10^{25}}$		
	$\varepsilon_{\mathrm{spots}}$[c,d]	$[\mathrm{s}^{-1}]$	$\mathbf{2.9 \times 10^{25}}$		

[a] Best-fit values with $\chi^2_{\text{best-fit}} = 0.25$.

[b] Minimum and maximum for an individual variation of the parameter resulting in a chi-squared of $\chi^2 \leq 1.02\,\chi^2_{\text{best-fit}}$.

[c] The given intensities correspond to a torus density of $n_e = 3000\ \mathrm{cm}^{-3}$

[d] Total photon emission rates of the global emission and the combined flank emission after (4.32) and (4.33), respectively.

Global emission and limb glow

The fit yields a maximum OI] 1356 Å volume emission rate at the surface of $8.24 \times 10^{-2}\ \mathrm{cm}^{-3}\,\mathrm{s}^{-1}$ and a scale height of 9.8 km. Neglecting the hemispheric asymmetry, this corresponds to a minimum brightness on the disk of

$$I_{\mathrm{glob,disk}} = 10^{-9} \int_{los} i^{*}_{glob}(r)\,\mathrm{d}r = 10^{-9}\ i^{*}_{0,\mathrm{glob}} H^{*}_{r} = 0.08\ \mathrm{kR} \tag{4.38}$$

at the sub-observer point, where the *los* through the local emission is shortest. The factor 10^{-9} accounts for the conversion to kilorayleighs [kR]. With the contribution from the coronal emission of $0.5\,I_{0,\mathrm{ext}} \approx 0.05$ kR, the average minimum brightness on the disk center becomes $\sim$0.13 kR in agreement with the measured values of the observations at western elongation, where no contributions from the flank emission are expected near the disk center. The total photon emission rate of the global aurora after (4.32) is $\varepsilon_{\mathrm{glob}} = 3.5 \times 10^{25}\ \mathrm{s}^{-1}$.

The obtained scale height of $H^{*}_{r} = 9.8$ km is considerably lower than the spatial resolution in the STIS images of $\Delta x \geq 70$ km. A rough estimation of the atmospheric scale height using (4.13) for the SO_2 atmosphere with a near-surface temperature of $T \approx 120$ K (*Strobel et al.* 1994, *Wong and Smyth* 2000) yields $H_{\mathrm{atmo}}(SO_2) = 9$ km. This indicates that the radial profile of the global emission might be controlled by the neutral gas abundance and not by the distribution of the electron energy. The scale heights of purely O_2 and O atmospheres are higher by a factor of 2 and 4, respectively. However, models of Io's atmosphere indicate that the near-surface ($h < 100$ km) SO_2 abundance is considerably higher than the O and O_2 abundance by at least two orders of magnitude (*Summers and Strobel* 1996, *Wong and Smyth* 2000). Hence, despite the very low SO_2 emission rates at the presumably low electron temperatures ($k_B T_e \leq 5$ eV), the global emission might in part originate from SO_2. On the other hand, for near-surface emission the optical depth might become $\tau \approx 1$ due to the high SO_2 absorption cross sections, see Section 4.1. Therefore, it is not clear, how this near-surface emission is generated.

In the STIS observations the limb glow appears to be broader than expected for $H_r^* = 9.8$ km, see e.g., the bright northern limb in Figure 4.9c. Two effects primarily influence the broadening: First, the displacement of the 1358.5 Å emission with respect to the 1355.6 Å line smears the narrow limb glow. The 1358.5 Å disk is indicated by the dotted orange circle in the displayed images. Additionally, spreading in the telescope assembly contributes to the broadening. Although in the respective model image (Figure 4.10c) the northern limb glow appears narrower, it still extends over several pixels due to the two effects, which are taken into account in the model. The inferred small scale height is also in agreement with other observations. For instance, high-resolution images taken during eclipse by the NH LORRI (*Spencer et al.* 2007a) also reveal a very narrow limb glow at visible wavelengths, see Figure 5.2 in Chapter 5. However, as structures on spatial scales below 70 km can not be properly resolved in the STIS images, the derived scale height must be interpreted with caution.

To determine the emission around the northern and southern limb we follow *Retherford et al.* (2003) and compute the average brightness of all pixels within two arcs with angular ranges of 90° centered at Io north and Io south, and with inner and outer radii of 0.75 and 1.25 R_{Io}, see Figure 2.9. They argue that these sections exclude contributions from the bright flank emission, but include the brightest limb glow. Our derived values of the limb glows are in agreement with the values listed in Table 2 of *Retherford et al.* (2003). The maximal observed ratio between the northern limb glow I_{limb}^N and southern limb glow I_{limb}^S is ∼2 as stated by *Retherford et al.* (2003). The brighter limb is found on the hemisphere facing the torus center. Figure 4.13 compares the limb glow ratio

$$r_{N/S} = I_{\mathrm{limb}}^N / I_{\mathrm{limb}}^S \tag{4.39}$$

for the observation and model images as a function of Io's distance to the torus equator z_c. The uncertainty of the observed limb glow $\sigma_{I_{\mathrm{limb}}}$ is given by the brightness variation, when the disk is shifted by two pixels in each direction according to the uncertainty of the disk location. The uncertainty of the disk location produces larger limb glow errors than the propagated statistical errors of the pixels within the limb glow regions. Calculating the chi-squared for the limb glow ratio after (4.37) yields $\chi^2_{r_{N/S}} = 0.81$, i.e., the model reproduces the limb glow ratio within the statistical uncertainty. The fitted scale height H_c for the hemispheric asymmetry is 1.1 R_J. Due to the implemented dependence on the distance to the torus equator z_c in (4.31), we can compare H_c^* to the torus scale heights of 1 R_J and 0.75 R_J reported by *Bagenal* (1994) and *Bagenal and Delamere* (2011), respectively. The reasonable agreement indicates that the hemispheric asymmetry is in fact directly coupled to the relative electron energy supply in the flux tubes above and below Io.

A comparison with the theoretical brightness ratio $r_{N/S}$ after (4.18) with the $H_c^* = 1.1$ R_J (blue dashed line in Figure 4.13) reveals that the limb glow ratio as measured in the images is affected by the background emission and/or the flank emission. The theoretical profile (4.18) predicts an essentially larger ratio for $z_c > 20$ R_{Io} than inferred from both the model and observation images. As for $z_c = 20$ the measured limb glow on the hemisphere opposite to the torus is decreased down to ∼0.12 kR, the average coronal (or extended) emission in the limb sections of ∼0.07 kR (the

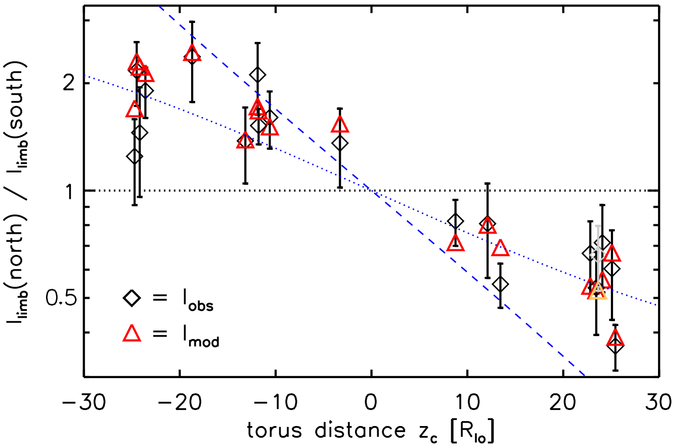

Figure 4.13: *Ratio of the limb glow brightness after (4.39) as measured in the OI] 1356 Å observations (black diamonds with error bars) and in the modeled images (red triangles) versus Io's distance to the torus equator. The values for the image taken in eclipse are displayed in grey and orange, respectively. The blue lines show theoretically predicted limb glow ratios for a torus scale height of* $H_c = 1.1\ R_J$. *The dashed line shows the profile for the ratio of the global emission only (Eq. 4.18), the dotted line indicates the actual expected ratio when the coronal emission is taken into account (Eq. 4.40).*

limb section is partially on the disk) contributes significantly to the radiation as measured around the limb in the images. The average modeled global emission within the limb glow regions is $\sim$0.09 kR not counting the background emission. There is no hemispheric asymmetry expected in the coronal emission, because the flux tubes are not intersected by Io. The measured ratio thus results from the relative global emission in the hemispheres plus a constant background emission

$$r_{N/S}(z_c) = \frac{0.07 + 0.09\left[1 - \mathrm{erf}\left(\frac{z_c}{H_c}\right)\right]}{0.07 + 0.09\left[1 + \mathrm{erf}\left(\frac{z_c}{H_c}\right)\right]} \approx \frac{\left[1.8 - \mathrm{erf}\left(\frac{z_c}{H_c}\right)\right]}{\left[1.8 + \mathrm{erf}\left(\frac{z_c}{H_c}\right)\right]} \quad . \tag{4.40}$$

The corrected limb glow ratio profile is shown by the blue dotted line in Figure 4.13 in good agreement with the inferred ratio of most images. Deviations from the theoretical profile could be due to e.g., contributions from the flank emission to the measured brightness in the limb glow areas. An analysis of the proportion of both limb emissions to the total brightness $\left(I^N_{\mathrm{limb}} + I^S_{\mathrm{limb}}\right)/I_{\mathrm{tot}}$ reveals, that the limbs become brighter for $z_c > 20\ \mathrm{R_{Io}}$. Since large z_c imply a stronger tilt of the ambient magnetic field, the spot locations are shifted to higher latitudes and thus affect the limb glow.

In their analysis of the relative north and south limb glow, *Retherford et al.* (2003) find a larger torus scale height $H_c \approx 2$ for the simple Gaussian torus density profile of *Hill and Michel* (1976). Since they do not consider contributions from a roughly symmetric and constant coronal emission, the larger scale height is necessary to explain the lower slope, particularly for $z_c > 20\ \mathrm{R_{Io}}$. Because their inferred torus scale height turns out to be larger than expected (after e.g., *Bagenal* 1994), they derive a Kappa distribution for the torus density explaining the measured limb ratios. According to our analysis, the actual limb glow is yet in agreement with a Gaussian torus profile with a scale height of $\sim 1\ \mathrm{R_J}$, similar to previously reported scale height values.

Flank emission and equatorial spots

Neglecting possible asymmetries between the sub-Jovian and anti-Jovian flanks due to e.g., atmospheric asymmetries (e.g., *Spencer et al.* 2005) or the ionospheric Hall effect (*Saur et al.* 2000), the flank emission parameters (parameters 5–9 of Table 4.4) are first set equal for the anti-Jovian and sub-Jovian side. Thereafter, asymmetries between the spots are investigated.

For the latitudinal extension the fit yields a width of $\Theta^* = 23^\circ$ or $\Delta y_d \approx \mathrm{R_{Io}} \tan(\Theta^*) = 0.4\ \mathrm{R_{Io}}$. This means that the spot brightness at a latitude of $\vartheta = 45^\circ$ is $\sim$0.15 of the maximum brightness at $\vartheta = 0^\circ$. By comparing the latitudinal width of the spots in the observation and model images by eye, it seems that the model overestimates the latitudinal width. This is due to the probably simplified implementation of the dependence of the spot location on the background field direction. With a larger latitudinal extension, the modeled flank emission more likely coincides with the bright spots in the observations, even if the modeled tilt of the flank emission does not exactly match the tilt in the observation. Thus, the actual latitudinal width of the spot is probably smaller than 23°. The inferred longitudinal offset of the spot center of $\varphi_0^* = 20^\circ$ corresponds exactly to the mid value of the offset range of 10°–30° measured in the STIS OI] 1356 Å images by *Retherford et al.* (2000). The fitted longitudinal width of $\Phi_0^* = 48^\circ$ indicates a very elongated flank emission reaching from the upstream hemisphere far into the downstream hemisphere. For certain viewing perspectives, the downstream part of the elongated flank emission on the opposite hemisphere to the observer creates an enhanced feature above the limb, see e.g., Figure 4.11m. In previous studies, these features have been attributed to a *wake emission*, which is thought to be independent of the magnetic field topology (*Moore et al.* 2010). In fact, they can be presumably attributed to the extended equatorial spots.

An individual analysis of the parameters for the sub- and anti-Jovian flanks yields negligible differences ($< \pm 5^\circ$) in Θ^*, φ_0^*, and Φ_0^*. The power law index is fitted with one parameter for both spots yielding $\kappa^* = 6.4$. The parameter value for the volume emission rate fitted for both the spots together is $i^*_{0,\mathrm{spot}} = 11\ \mathrm{cm^{-3}\,s^{-1}}$.

To analyze the spot brightness in the images we use a method similar to the approach of *Retherford et al.* (2000). An average brightness within a square of diameter 0.5 $\mathrm{R_{Io}}$ corresponding to $10-13$ pixels is determined to include the brightest emission on the sub- and anti-Jovian hemispheres. The box size is chosen to account for most of the flank emission but minimize the influence of the asymmetric global emission. Since the derived latitudinal total width ($2\Theta^*$) implies a larger extension than 0.5 $\mathrm{R_{Io}}$, the box includes only the brighter portion of the flank emission. Regions located further away from the spot center in latitudinal direction, where the brightness of the flank emission is comparable to the global emission brightness, are thereby excluded. Within 0.5 $\mathrm{R_{Io}}$ above Io's surface the flank emission decreases to $<$0.1 of the maximum at the surface for $\kappa^* = 6.4$. Hence, most emission in the radial direction is included. The box location is set to the brightest $0.5\ \mathrm{R_{Io}} \times 0.5\ \mathrm{R_{Io}}$ area close to the limb, where the respective spot is expected. When the flank emission opposite to the observer is mostly obstructed by the disk, the limb closer to the derived longitudinal spot center is searched for the brightest area. The inferred equatorial spot locations are displayed with green boxes in Figures 4.9 to 4.12.

To compare the relative brightness of the spots, the ratio of the brightnesses within the boxes

$$r_{\mathrm{spots}} = \frac{I_{\text{anti-J spot}}}{I_{\text{sub-J spot}}} \tag{4.41}$$

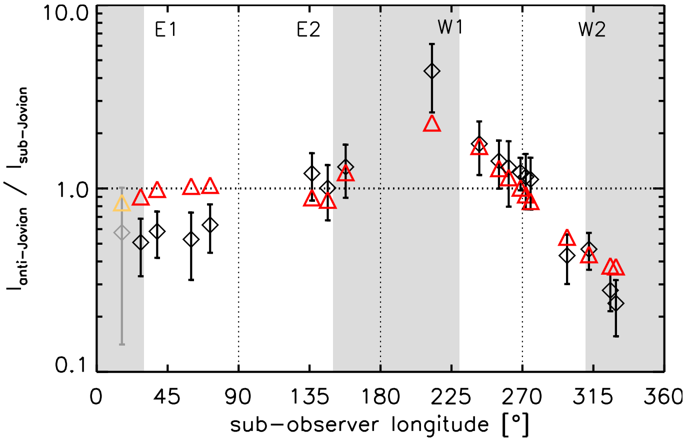

Figure 4.14: *Ratio of the spot brightnesses after (4.41) as measured in the OI] 1356 Å observations (black diamonds with error bars) and in the modeled images with equal flank emission rate* ($i^*_{0,spot} = 1.1 \times 10^{-2}\ m^{-3}\ s^{-1}$) *for both spots (red triangles) versus the sub-observer longitude. The values for the image taken in eclipse are displayed in grey and orange, respectively. E1 and E2 (W1 and W2) specify the orbit sections before and after eastern (western) elongation as illustrated in Figure 4.4. The grey shaded areas indicate the orbital period, where one spot is almost entirely obstructed by Io corresponding to the derived latitudinal extension and offset.*

as measured in the images is calculated. Figure 4.14 shows the comparison of the values inferred from the observations and from the model images, when for both spots one mutual parameter for the brightness $i_{0,\mathrm{spot}}$ is used. The numbers E1, E2, W1, and W2 at the top of the figure refer to the quarters of Io's orbit before (1) and after (2) eastern and western elongation. For a completely symmetric emission the ratio in the images around $\varphi_{obs} = 270°$, i.e., close to western elongation, would be expected to be unity. Accordingly, the brightness ratio in the modeled images is $\sim$1 for $\varphi_{obs} = 270°$, see Figure 4.14. However, in the observations around western elongation the anti-Jovian spot is clearly brighter, which has been shown before by *Retherford et al.* (2000). Towards larger orbital longitudes (Section W2), the anti-Jovian spot is fainter as it is covered by the disk of Io, whereas the sub-Jovian spot becomes brighter with the *los* crossing through almost the entire flank emission. Around eastern elongation the ratio profile is expected to be principally less steep, because the flank emission extends far in the downstream region and is thus less obstructed by the disk. The general difference between the eastern and western elongation is resembled by the model. However, the profile of the spot ratio inferred from the model images is not as steep as the observed profile in the orbit section W1 and W2. i.e., the modeled ratio is closer to 1. Similarly, the modeled ratios in orbit sections E1 and E2 turn out to be also closer to 1 than the observed brightness ratios. The chi-squared after (4.37) for the spot ratio in the observation and model images is $\chi^2_{r_{\mathrm{spots}}} = 1.6$. This means, the spot properties are not reproduced by the model within the observational uncertainty with a unified intensity parameter $i^*_{0,\mathrm{spot}}$ for both spots.

We find that an asymmetry between the day side and night side hemispheres can explain this discrepancy. Therefore, either the sub-Jovian or the anti-Jovian side is assumed to be the "night side", although the entire hemisphere that is visible to the observer almost coincides with the day side hemisphere. We consider the flank, where the sub-Jovian/anti-Jovian meridian is closer to the sub-solar longitude, to be the day side flank. The opposite hemisphere is attributed to the night side. Thereby, we assume that the visible emission above the night side hemisphere is affected by the response of the surface and atmosphere to the ceasing sunlight. In the two observations taken

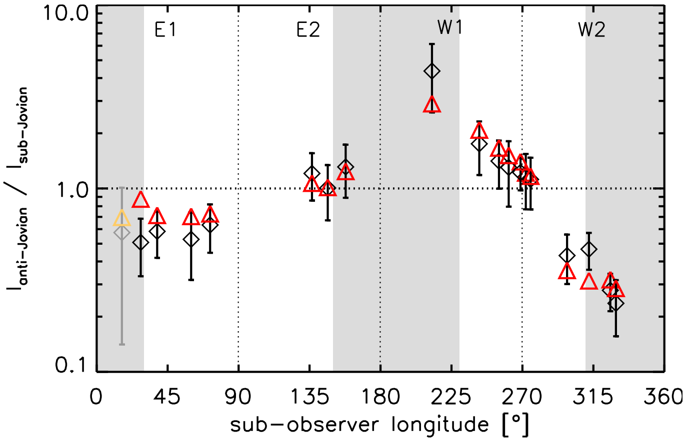

Figure 4.15: *Same as Figure 4.14, but with the flank volume emission rate $i^*_{0,spot}$ fitted individually for the day side and night side hemispheres (see Table 4.5).*

shortly after western elongation ($\varphi_{obs} \gtrsim 270°$) the anti-Jovian flank is still assigned to the day side assuming a thermal inertia of the surface and the atmosphere as inferred by *Walker et al.* (2012). The model is then fitted with two parameters accounting for the local emission rates of the day and night side flanks, separately. The resulting ratio of

$$\frac{i^*_{0,\text{spot}}(day)}{i^*_{0,\text{spot}}(night)} \approx 1.64 \tag{4.42}$$

indicates a brighter flank emission on the primarily sunlit hemisphere. The obtained emission rates are given in Table 4.2, the corresponding ratio profile is shown in Figure 4.15. Although not all modeled spot ratios agree with the observed values within the error bars, the average squared deviation is $\chi^2_{r_{\text{spots}}} = 0.77$. This means that a day/night side asymmetry is consistent with the observed spot brightness ratio.

Nonetheless, other local emission distributions might explain the measured brightness ratios as well as the assumed asymmetry. If the longitudinal extension of the flank emission is lower, i.e., the emission is more concentrated around the spot center, higher brightness ratios would be expected. Furthermore, if the longitude of spot center is changing during Io's orbit the visible brightness of the flank also varies. Therefore, we will check the agreement between the modeled and observed morphology analyzing another brightness ratio in the images.

Around eastern and western elongation the flank emission appears very bright and is located directly *above* the limb. Close to $\varphi_{obs} \approx 0°$ ($\varphi_{obs} \approx 180°$) the sub-Jovian (anti-Jovian) flank emission is mostly visible *on* the disk of Io, whereas the anti-Jovian (sub-Jovian) spot is hardly detectable. Therefore, the ratio of the total brightness to the disk brightness

$$r_{\text{tot/disk}} = \frac{I_{\text{tot}}}{I_{\text{disk}}} \tag{4.43}$$

might be used as a diagnostic to verify the inferred spot intensities and extensions, but also to check the radial profile of the global emission. The ratios inferred from the model and observation images principally follow the same expected φ_{obs} dependency, see Figure 4.16. At western elongation the strong spot emissions are located primarily above the limb. Accordingly, $r_{\text{tot/disk}}$ is high. At

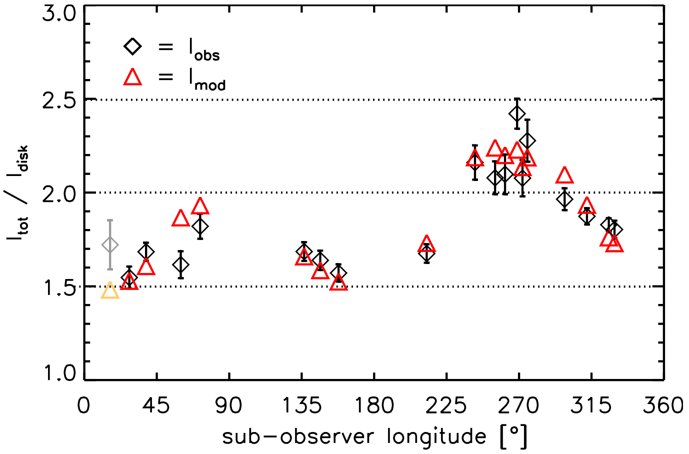

Figure 4.16: *Ratio of the total emission in the images to the emission on the disk (Eq. 4.43) as measured in the OI] 1356 Å observations (black diamonds with error bars) and in the modeled images (red triangles) versus Io's orbital longitude. The values for the image taken in eclipse are displayed in grey and orange, respectively.*

eastern elongation large parts of the flank emission contribute to I_{disk} resulting in a lower ratio. For some images the observed ratio deviates considerably from the modeled values, like at $\varphi_{obs} \approx 60°$ (Figure 4.16). These deviations appear to be due to non-periodic variations, which can not be reproduced by the model. As the uncertainty of I_{tot} and I_{disk} is low, the chi-squared (Eq. 4.37) for the $r_{\mathrm{tot/disk}}$ values is high, with $\chi^2_{r_{\mathrm{tot/disk}}} = 2.8$. However, the general trend and average ratio of all images $\langle r_{\mathrm{tot/disk}} \rangle$ are in agreement.

Other distributions of the flank emissions that were tested to explain the spot ratios yield a significantly worse agreement for $r_{\mathrm{tot/disk}}$. If the longitudinal extension of the flank emission (Φ^*) was smaller, e.g., to explain the steep r_{spots} profile, the amplitude of the $r_{\mathrm{tot/disk}}$ variation in the model as a function of φ_{obs} would be clearly larger differing significantly from the observed $r_{\mathrm{tot/disk}}$ variation. The ratio $r_{\mathrm{tot/disk}}$ might also be used as a test value to verify the radial decay of the global emission. For larger scale heights $H_r^* > 50\,\mathrm{km}$, the $r_{\mathrm{tot/disk}}$ ratio obtained from the model images is lower than the observed ratio in all 19 images, as the portion of the global emission above the limb increases with increasing scale height. Similarly, the other values for the brightness ratios of the distinct areas, like the relative brightness of both spots compared to I_{disk}, yield a reasonable agreement for the model and observation images for the derived best-fit parameters of Table 4.5.

The parameter ζ^*, specifying the proportional inclination of the local emission, is fitted to 0.79. This means that the tilt of the reference system for the flank and global emissions corresponds to 79% of the tilt of the undisturbed background field. The tilt α of the connecting line between the two spot centers (center of the box) with respect to Io's equator as measured in the images is displayed in Figure 4.17 as a function of the ambient magnetic System III longitude (λ_{III}). The chi-squared value after (4.37) for the deviation of the inferred angles (model and observations) is $\chi^2_\alpha = 2.5$. For most observations the model qualitatively resembles the tilt of the spots. There are, however, clear deviations, which appear to be of systematic rather than statistical nature. The visibility of the spots, which depends on the observing geometry, certainly influences the measured spots angles additionally. We will discuss the tilt of the equatorial spots and the correlation to the background field in more detail in Section 4.3. We will also elaborate on the calculation of the spot tilt α and the derivation of the errors of the spot positions.

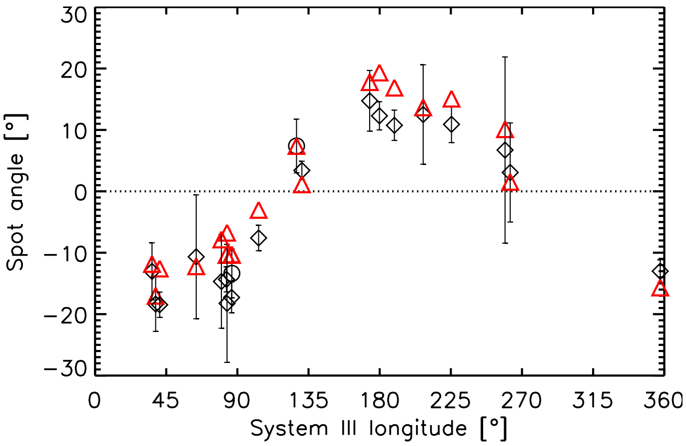

Figure 4.17: *Angle between the line connecting the two equatorial spots and Io's equator (spot angle) as measured in the OI] 1356 Å observations (black diamonds with error bars) and in the modeled images versus the System III longitude. The two spot angles derived from the SI] 1900 Å images are shown with black circles (*$\lambda_{III} \approx 90^\circ$ *and* 130°*).*

Finally, we note that the derived total photon emission rate of both spots after Equation (4.33) of $\varepsilon_{\text{spots}} = 2.9 \times 10^{25}$ s^{-1} is very similar to the total rate of the global aurora $\varepsilon_{\text{glob}} = 3.5 \times 10^{25}$ s^{-1}.

4.2.4 Distribution of the OI 1304 Å, SI 1479 Å, and SI] 1900 Å aurora

Generally, the OI 1304 Å, SI 1479 Å, and SI] 1900 Å emissions are expected to approximately resemble the distribution of the OI] 1356 Å aurora. As the OI 1304 Å and SI 1479 Å emission include allowed transitions, absorption and resonant scattering in the atmosphere is expected in addition to the emission from excited oxygen and sulfur, which might alter the observed morphology. Furthermore, the neutral gas distribution of O and S possibly differ due to the different formation processes or an influence on the sulfur abundance from direct volcanic outgassing of S_2 (e.g., *Spencer et al.* 2000a). By fitting the phenomenological aurora model to the OI 1304 Å, SI 1479 Å, and SI] 1900 Å observations, we check the universality of the aurora distribution inferred for OI] 1356 Å and investigate differences between the emission lines.

OI 1304 Å aurora

For generating the OI 1304 Å model images, the relative strength of three multiplet lines are set to the theoretical values (see Table 4.1), as there are no measurements for the line strengths available for Io. The parameters fitted to the 15 OI 1304 Å images (without eclipse observation) are listed in Table 4.6. The observation and model images are shown in Appendix B.1. The spatial resolution in the displayed images is reduced by factor 2 to enhance the visibility of the general emission pattern, as the OI 1304 Å emission appears very patchy otherwise.

The total measured brightness of OI 1304 Å aurora ranges from 0.48 kR to 0.92 kR with an average brightness corresponding to 90% of the OI] 1356 Å aurora brightness. The inferred relative brightness $I_{1356}/I_{1304} \approx 1.1$ is in between the ratios expected from solely electron impact on O_2, where $I_{1356}/I_{1304} \approx 2$, and on O, where $I_{1356}/I_{1304} \approx 0.4$.

Table 4.6: *Best-fit parameters and total photon emission rates for the OI 1304 Å aurora*

No	Parameter	Unit	**Best-fit value**[a]	Min[b]	Max[b]
1	$I^*_{0,\mathrm{ext}}$ [c]	[kR]	**0.14**	0.07	0.16
		Global emission			
2	$i^*_{0,\mathrm{glob}}$ [c]	[cm^{-3}s^{-1}]	**194**	158	233
3	H^*_r	[km]	**4.2**	3.0	7.1
4	H^*_c	[R$_\mathrm{J}$]	**1.2**	0.6	3.3
		Flank emission			
5a	$i^*_{0,\mathrm{spot}}$ [c] (day)	[cm^{-3}s^{-1}]	**3.9**	3.2	4.9
5b	$i^*_{0,\mathrm{spot}}$ [c] (night)	[cm^{-3}s^{-1}]	**2.5**	1.4	3.7
6	κ^*		**3.0**	2.1	4.3
7	Θ^*	[°]	**27**	21	33
8	Φ^*	[°]	**59**	45	80
9	φ^*_0	[°]	**25**	9	44
10	ζ^*		**0.80**	0.27	1.39
		Total photon emission rates			
	$\varepsilon_\mathrm{glob}$ [c,d]	[s^{-1}]	$\mathbf{3.4 \times 10^{25}}$		
	$\varepsilon_\mathrm{spots}$ [c,d]	[s^{-1}]	$\mathbf{2.2 \times 10^{25}}$		

[a] Best-fit values with $\chi^2_\text{best-fit} = 0.17$.

[b] Minimum and maximum of the parameter resulting in a chi-squared of $\chi^2 \leq 1.02\,\chi^2_\text{best-fit}$.

[c] The given intensities correspond to a torus density of $n_e = 3000$ cm^{-3}

[d] Total photon emission rates of the global emission and the combined flank emission after (4.32) and (4.33), respectively.

Principally, the obtained parameters are similar to the values obtained from the OI] 1356 Å observations (Table 4.5). The fitted background emission $I^*_{0,\mathrm{ext}}$ is higher by a factor of ~1.7 compared to OI] 1356 Å. The ratio I_{1356}/I_{1304} of ~0.6 implies a corona consisting of mostly atomic oxygen rather than O_2. This is consistent with the calculated corona abundances of atmosphere models (e.g., *Wong and Smyth* 2000). In the corona absorption and scattering of the SI 1479 Å emission can be neglected due to the generally low neutral gas density.

For the equatorial spots, the volume emission rates are again analyzed individually for the day side and night side hemispheres yielding a similar brightness ratio of

$$\frac{i^*_{0,\mathrm{spot}}(day)}{i^*_{0,\mathrm{spot}}(night)} \approx 1.61 \quad . \tag{4.44}$$

The corresponding chi-squared for the values inferred from the model and observation images after (4.37) is $\chi^2_{r_\mathrm{spots}} = 0.34$. This confirms the hypothesis of a day/night side asymmetry as explanation for the observed spot ratios. The brightness of the flank emission rate is noticeably lower by a factor of ~3 compared to the OI] 1356 Å flank emission for both spots. On the other hand, the extension of the flank emission (Θ^*, Φ^*) is somewhat larger (~20%) and the radial decrease lower by factor ~2. The total photon flank emission rate after (4.33) is $\varepsilon_\mathrm{spots}(1304) = 2.2 \times 10^{25}$ s^{-1}, which corresponds to 75% of the total flank emission for OI] 1356 Å. If the OI 1304 Å emission is not attenuated by absorption, the resulting brightness ratio of $I_{1356}/I_{1304} \approx 1.3$ implies that dissociative excitation of O_2 contributes to the aurora at the flanks.

The brightness of the global emission after (4.32) of $\varepsilon_{\text{glob}} = 3.4 \times 10^{25}$ s^{-1} is almost identical to the rate for OI] 1356 Å. The very low scale height implies again that the radiation is emitted very close to the surface. Resonantly scattered sunlight and atmospheric absorption probably affect the observed OI 1304 Å intensity. An estimation of the relative contributions of the oxygen species is thus not possible. The parameter controlling the limb glow asymmetry is fitted to $H_c^* = 1.2$ R_J in reasonable agreement with the OI] 1356 Å value ($H_c^* = 1.1$ R_J) and the reported torus scale heights. The chi-squared for the limb glow ratios measured in the images is $\chi^2_{r_{N/S}} = 0.88$. Hence, the OI 1304 Å limb glow ratio follows the same dependence on the flux tube contents as for the OI] 1356 Å limb emission. The deviation of the measured ratio $I_{\text{tot}}/I_{\text{disk}}$ for the model and observations is clearly larger than the observation uncertainty, thus $\chi^2_{r_{\text{tot/disk}}} = 3.9$. As for OI] 1356 Å, the general trend and average ratio of all images $\langle r_{\text{tot/disk}} \rangle$ are still in agreement.

The relative inclination inferred for OI 1304 Å is $\zeta^* = 0.80$ confirming the general dependence on the background field direction obtained from the OI] 1356 Å morphology.

Altogether, the basic morphological properties that were inferred for the OI] 1356 Å aurora apply also to the OI 1304 Å emission. The OI 1304 Å aurora is less confined to the spot centers, but more spread out leading to a smoother emission profile across the images. The more evenly distributed emission pattern is probably due to contributions from resonant scattering of the incident solar light but also of the locally emitted OI 1304 Å radiation by atomic oxygen in Io's vicinity. To exactly determine the local emission rates, scattering and absorption effects have to be taken into account.

SI 1479 Å aurora

The G140L images of the SI 1479 Å multiplet are modeled using the relative intensities of the blended lines as inferred by *Feaga et al.* (2002), see Table 4.1. For the G140M images, only the 1473.0 Å and 1474.1 Å lines are modeled, as the other weaker emission lines are clearly separated by the dispersion.

The total observed SI 1479 Å brightness varies between 0.57 kR and 1.43 kR with an average corresponding to 1.2 times the average OI] 1356 Å aurora brightness. This ratio is in agreement with the values derived from the STIS images by *Wolven et al.* (2001). The excitation rate f_{1479} for atomic sulfur at $k_B T_e = 5$ eV is an order of magnitude higher than the f_{1356} excitation rate for atomic oxygen. Although the SI 1479 Å brightness might be reduced in an optically thick atmosphere, the observed I_{1479}/I_{1356} brightness ratio indicates a surplus of oxygen abundance compared with the S abundance in Io's atmosphere in agreement with other observations and models.

Table 4.7 contains the model parameters fitted to the 17 SI 1479 Å images (without eclipse observation). The parameters describing the spatial distribution are again similar to the parameters obtained for the OI] 1356 Å images. Despite the spatial overlap of the multiplet lines the modeled images clearly resemble the main features of the observation images, see Figures B.5 to B.8 in Appendix B.2.

Although the total SI 1479 Å brightness is higher, the background emission from the corona is lower than the fitted values for OI] 1356 Å and OI 1304 Å. Absorption and scattering of the

Table 4.7: *Best-fit parameters and total photon emission rates for the SI 1479 Å aurora*

No	Parameter	Unit	**Best-fit value**[a]	Min[b]	Max[b]
1	$I^*_{0,\mathrm{ext}}$ [c]	[kR]	**0.05**	0.03	0.07
		Global emission			
2	$i^*_{0,\mathrm{glob}}$ [c]	[cm^{-3}s^{-1}]	**144**	116	170
3	H^*_r	[km]	**6**	4	8
4	H^*_c	[R$_\mathrm{J}$]	**1.2**	0.5	6.1
		Flank emission			
5a	$i^*_{0,\mathrm{spot}}$ [c] (day)	[cm^{-3}s^{-1}]	**24.8**	21.0	28.6
5b	$i^*_{0,\mathrm{spot}}$ [c] (night)	[cm^{-3}s^{-1}]	**17.6**	12.7	22.6
6	κ^*		**8.0**	7.1	9.3
7	Θ^*	[°]	**21**	18	24
8	Φ^*	[°]	**63**	52	75
9	φ^*_0	[°]	**11**	2	22
10	ζ^*		**0.81**	0.50	1.10
		Total photon emission rates			
	$\varepsilon_\mathrm{glob}$ [c,d]	[s^{-1}]	**3.4×10^{25}**		
	$\varepsilon_\mathrm{spots}$ [c,d]	[s^{-1}]	**5.4×10^{25}**		

[a] Best-fit values with $\chi^2_\text{best-fit} = 0.23$.

[b] Minimum and maximum of the parameter resulting in a chi-squared of $\chi^2 \leq 1.02\,\chi^2_\text{best-fit}$.

[c] The given intensities correspond to a torus density of $n_e = 3000$ cm^{-3}

[d] Total photon emission rates of the global emission and the combined flank emission after (4.32) and (4.33), respectively.

SI 1479 Å emission is negligible in the corona. Assuming $k_B T_e = 5$ eV in the corona, the excitation rates of atomic sulfur and oxygen are $f_{1479} = 4.0$, $f_{1356} = 0.32$. The ratio of $I^*_{0,\mathrm{ext}}(1479) : I^*_{0,\mathrm{ext}}(1356) = 1 : 1.6$ thus implies that the relative S/O abundance in Io's corona is ∼0.05.

The volume emission rate $i^*_{0,\mathrm{glob}}$ and the scale height H^*_r of the global emission are very similar to the values obtained for OI] 1356 Å and OI 1304 Å. The total photon rate for the global emission after (4.32) is $\varepsilon_\mathrm{glob} = 3.4 \times 10^{25}$ s^{-1} and matches exactly the rate for OI] 1356 Å. Like for OI 1304 Å, the surface-near atmosphere is probably optically thick for SI 1479 Å, which prevents a straightforward estimation of the abundances using the excitation rates. The hemispheric asymmetry is again best reproduced by a scale height on the order of 1 R$_\mathrm{J}$ ($H^*_c = 1.2$ R$_\mathrm{J}$). The limb glow brightness can not be directly measured in the images, because the equatorial spots of the displaced spectral lines contaminate the emission around the limb of the primary disk in the images.

The steep radial decay and the extension of the flank emission resemble the OI] 1356 Å spot profile. The obtained day/night side asymmetry of

$$\frac{i^*_{0,\mathrm{spot}}(day)}{i^*_{0,\mathrm{spot}}(night)} \approx 1.49 \tag{4.45}$$

is somewhat lower than the inferred values for the oxygen aurorae. Nevertheless, the general trend of a brighter day side spot applies also to the sulfur emission. The chi-squared (Eq. 4.37) of the measured spot ratios of the model and observation images is $\chi^2_{r_{\mathrm{spots}}} = 1.1$. The total photon rate of the both spots of $\varepsilon_{\mathrm{spots}} = 5.4 \times 10^{25}$ s^{-1} is roughly twice the OI] 1356 Å rate, indicating a higher S/O mixing ratio in the atmosphere than in the corona. However, to accurately determine the S abundance, absorption of the SI 1479 Å emission in the atmosphere has to be taken into account. The inferred proportional inclination of $\zeta^* = 0.81$ is very similar to the values for OI] 1356 Å and OI 1304 Å proving the universal dependence of the local emission on the background field.

SI] 1900 Å aurora

To fit the model to two STIS SI] 1900 Å images the number of model parameters is reduced. As the two SI] 1900 Å observations are taken shortly before western elongation the viewing geometry does not allow a determination of the longitudinal extension and offset of the equatorial spots. Therefore, Φ^* and φ_0^* are approximated by the values fitted earlier. The doublet lines are separated by more than 1.5 R$_{\mathrm{Io}}$, so we only model the brighter line at 1900.3 Å. For the fitted parameters see Table 4.8, the two model and observation images are displayed in Appendix B.3. The morphology is clearly dominated by the two bright spots, which are well resembled by the model images.

Table 4.8: *Best-fit parameters and total photon emission rates for the SI] 1900 Å aurora*

No	Parameter	Unit	Best-fit value	Min	Max
1	$I^*_{0,\mathrm{ext}}{}^{\mathrm{c}}$	[kR]	**0.09**	0.08	0.11
			Global emission		
2	$i^*_{0,\mathrm{glob}}{}^{\mathrm{c}}$	[cm^{-3}s^{-1}]	**85**	83	88
3	H_r^*	[km]	**7**	6	8
4	H_c^*	[R$_\mathrm{J}$]	**9**	1	24
			Flank emission		
5a	$i^*_{0,\mathrm{spot}}{}^{\mathrm{c}}$(day)	[cm^{-3}s^{-1}]	**27.6**	25.4	29.8
5b	$i^*_{0,\mathrm{spot}}{}^{\mathrm{c}}$(night)	[cm^{-3}s^{-1}]	**41.5**	39.9	43.2
6	κ^*		**6.8**	6.2	7.3
7	Θ^*	[°]	**16**	14	17
8	Φ^*	[°]	50	*not fitted*	
9	φ_0^*	[°]	20	*not fitted*	
10	ζ^*		**1.07**	0.95	1.12
			Total photon emission rates		
	$\varepsilon_{\mathrm{glob}}{}^{\mathrm{c,d}}$	[s^{-1}]	$\mathbf{2.5 \times 10^{25}}$		
	$\varepsilon_{\mathrm{spots}}{}^{\mathrm{c,d}}$	[s^{-1}]	$\mathbf{6.4 \times 10^{25}}$		

[a] Best-fit values with $\chi^2_{\text{best-fit}} = 0.08$.

[b] Minimum and maximum of the parameter resulting in a chi-squared of $\chi^2 \leq 1.02\,\chi^2_{\text{best-fit}}$.

[c] The given intensities correspond to a torus density of $n_e = 3000$ cm^{-3}

[d] Total photon emission rates of the global emission and the combined flank emission after (4.32) and (4.33), respectively.

The SI] 1900 Å brightness can not be compared directly to the SI 1479 Å brightness as the images are not obtained concurrently. The obtained correlation to the torus electron density c_{conv} (see Table 4.3) implies an approximate ratio of $I_{1900}/I_{1479} \approx 1.6$. Accordingly, the background brightness $I^*_{0,\mathrm{ext}}$ and total spot emission of $\varepsilon_{\mathrm{spots}} = 6.4 \times 10^{25}$ s^{-1} is slightly increased with respect to the values fitted for SI 1479 Å. The global emission of $\varepsilon_{\mathrm{glob}} = 2.5 \times 10^{25}$ s^{-1} is somewhat lower, although in the observation images the disk reflected solar light is not subtracted.

The observed relative limb glows are exactly opposed to the expected hemispheric asymmetry from Io's position with respect to the torus. Consequently, the scaling parameter H^*_c is fitted to a very large value to minimize the hemispheric asymmetry in the model images, as it is implemented to resemble to opposite ratio. The fitted day/night asymmetry of the flank emission also turns out to be opposed to the other fitted values with a brighter sub-Jovian spot (night side) by factor 1.5. Hence, there seem to be systematic differences between the SI] 1900 Å aurora and the other emission morphologies. Due to the lower throughput and higher dark rate of the used MAMA-NUV detector (*STScI* 2011) and considering possible contributions from reflected sunlight, the SI] 1900 Å emission contains a large uncertainty especially in the region of low brightness. Additionally, only two observation images have been fitted. To infer general properties of the SI] 1900 Å aurora a larger set of images is necessary.

The tilt of the auroral spots is relatively high compared to the background field tilt with $\zeta^* = 1.07$. The low latitudinal extension of the spots (clearly visible in the observation images) is also noticeably leading to a fitted width of $\Theta^* = 16°$. As the spots are very bright and clearly confined, we will investigate the spot angles in Section 4.3 together with the spot angles measured in the OI] 1356 Å images.

4.2.5 Eclipse observations

The eclipse exposures revealed the lowest intensity of all STIS observations in the OI] 1356 Å and OI 1304 Å as well as the SI 1479 Å emission, see Figures 4.6 to 4.8. The exposures were taken after about three fourths of Io's passage through Jupiter's shadow. In the analysis of the STIS eclipse observation by *Retherford* (2002) it is reported that the OI] 1356 Å aurora is by a factor of $\sim$2 dimmer than expected. Using the derived conversion coefficients c_{conv} given in Table 4.3, we can calculate an expected total brightness

$$I_{exp} = c_{conv}\, n_{e,Smyth}(\lambda_{III}, \varphi_{sun}) \tag{4.46}$$

for the eclipse observations with the values of the torus density $n_{e,Smyth}(\lambda_{III}, \varphi_{sun})$ from the *Smyth* model. The expected brightness for OI] 1356 Å is higher by a factor of 2.0 compared to the observed total intensity I_{obs} in exact agreement with the result of *Retherford* (2002). In case of the OI 1304 Å and OI] 1356 Å emission, I_{exp} is even higher by factor 2.3 and 2.5 in comparison to the observed total intensities. Although the correlation of the aurora with the electron density is probably not exactly linear, the large deviations for all three emission multiplets in eclipse indicate that the aurora is indeed significantly altered. Therefore, we fit the model to the eclipse images, individually. Instead of using the measured eclipse brightness as reference for calibrating the modeled aurora after Eq. (4.36), we apply the expected brightness I_{exp}.

The brightness ratio $r_{\mathrm{tot/disk}}$ of the eclipse observation is clearly higher than in the image modeled with the standard parameter set, see Figure 4.16 for OI] 1356 Å. This indicates a decrease of the near-surface aurora as proposed by *Retherford* (2002). Analyzing the morphology of the STIS OI] 1356 Å eclipse image, *Retherford* (2002) finds that the visible sub-Jovian spot appears to be confined to a smaller region around the magnetic equator compared to the image taken directly

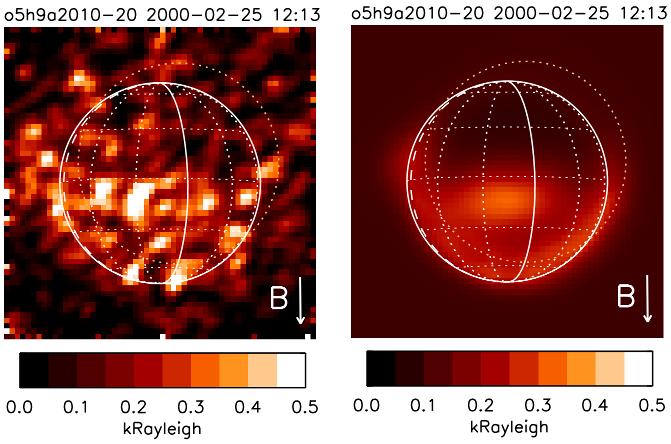

Figure 4.18: *(Left) STIS OI] 1356 Å observation taken during eclipse. The statistical fluctuations are high due to the extraordinary low emission level in eclipse. (Right) Modeled eclipse observation with decreased global and flank emission rates.*

after egress during the same visit, but has the same offset from the sub-Jovian meridian of ∼20°. The OI] 1356 Å corona is found to be not altered in the OI] 1356 Å eclipse image.

An individual fit of only the model parameters $I^*_{0,\mathrm{ext}}$, $i^*_{0,\mathrm{glob}}$, $i^*_{0,\mathrm{spot}}$ for the intensities of the three aurora parts and Θ^* and Φ^* for the extension of the spots to the OI] 1356 Å, OI 1304 Å, and SI 1479 Å eclipse image principally confirm the results of *Retherford* (2002). The other parameters are left unchanged as necessary constraints for fitting the single eclipse images. For the OI] 1356 Å and OI 1304 Å emission, the fitted extended aurora value is weaker than the standard value with $I^*_{0,\mathrm{ext}}(eclipse) \approx 0.8\, I^*_{0,\mathrm{ext}}(sunlit)$, indicating a relatively unchanged atomic oxygen corona. In case of SI 1479 Å, the extended emission is lower by 50% similar to the decrease in total brightness, which suggests that the sulfur abundance in the corona decreases in eclipse. The fitted global emission $i^*_{0,\mathrm{glob}}$ is reduced drastically for OI 1304 Å and SI 1479 Å down to less than 20% of the fitted value for the sunlit observations. Since the global emission has been found to arise at very low altitudes, the reduced brightness is consistent with a collapse of the near-surface SO_2 atmosphere in eclipse as expected (*Wong and Smyth* 2000). The drop of the global OI] 1356 Å emission by factor 2 is lower and comparable to the reduction of the total brightness. The obtained values for the latitudinal and longitudinal extension of the flank emission indeed imply a narrowing of the spots. Both Θ^* and Φ^* are lower by factor 1.5 to 2 for all emission images. The spot brightness on the other hand hardly changes compared to the sunlit observations.

A direct comparison between the observed and modeled morphology of the OI] 1356 Å aurora is shown Figure 4.18. The eclipse observations and the corresponding model images of OI 1304 Å and SI 1479 Å aurora are displayed together with the other images in Appendix B. All eclipse images suffer a high noise level due to the generally low intensity. A similarity between the modeled images and the observations is hard to see because of the patchiness of the observations. Although the fitted model parameters for the eclipse images generally resemble the expected properties for an atmospheric collapse, these results have to be interpreted with caution due to the high uncertainty in the eclipse images. However, the decrease of the total brightness in all emissions is a striking indication for an atmospheric collapse, when Io moves into Jupiter's shadow.

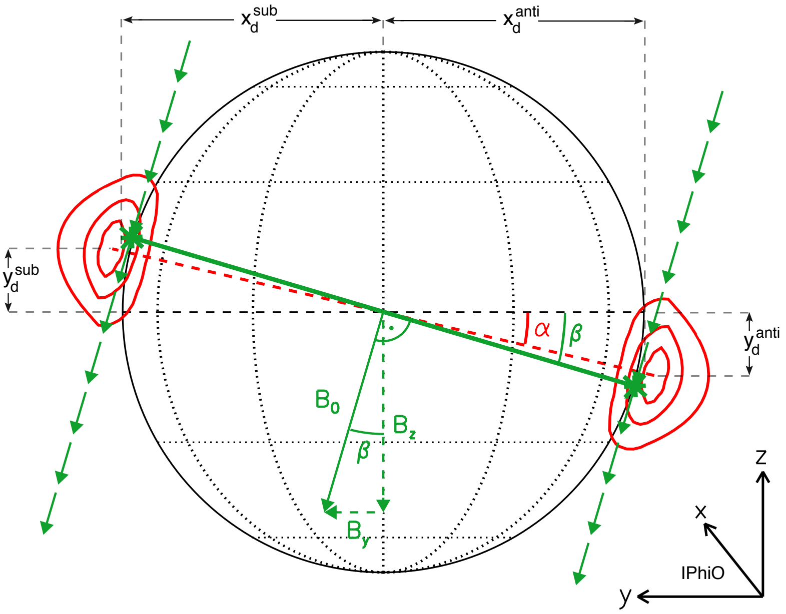

Figure 4.19: *Sketch of the spot location when Io is at western elongation and* $\lambda_{III} \approx 20.8°$ *(*$B_x \approx 0$*). The angle* β *of the connection line between the tangent points of the magnetic field is here given by Equation 4.51.*

4.3 Rocking of the equatorial spots

By fitting the phenomenological aurora model, we have obtained a proportional inclination of the near-surface aurora of ∼80% of the background field tilt, consistently for the OI] 1356 Å, and OI 1304 Å as well as SI 1479 Å images. However, as already stated by *Retherford et al.* (2000), the correlation appears to be affected by other factors than just the orientation of the background field. By comparing the inclination of the spots in the model and observation images, we have found that in some cases the tilt is overestimated, where in other cases the actual tilt is higher than the estimated inclination. After a description of the method of measuring the spots in the images, we will analyze the influence of the atmosphere, the plasma interaction and the induction signals on the spot locations.

4.3.1 The spot angle

The location of each equatorial spot is set to the center of an approximately 0.5 $R_{Io} \times$ 0.5 R_{Io}wide box that includes the brightest pixels close to the central longitude of the respective flank emission, as explained in Section 4.2.3. Figure 4.19 illustrates the determination of the spot angle α given by the tilt of the connecting line of the spot centers with respect to Io's equator. The center of a box is specified by the horizontal and vertical pixel values in the image, designated x_d and y_d, respectively. x_d and y_d are zero for the center pixel in each image. The measured horizontal offset, x_d, of the box center depends on the observation geometry. For images with $\varphi_{obs} \approx 0°/180°$ one spot is located rather on the disk than on the limb resulting in small x_d value, see e.g., Figure 4.11i. In contrast, at western elongation the spot is located above the limb yielding a large x_d. To calculate the angle α we therefore assume that the spots are located exactly on the surface, i.e., at $r = 1$ $\mathrm{R_{Io}}$, where the emitted radiation is at maximum after the derived distribution in the phenomenological model. With this assumption the angle between the connecting line of the spots and the equator is given by

$$\alpha = \arcsin\left(\frac{y_d^{\mathrm{anti}} - y_d^{\mathrm{sub}}}{2\,\mathrm{R_{Io}}}\right) \quad , \tag{4.47}$$

with the vertical offset of the spot centers from the equatorial plane for the sub-Jovian spot y_d^{sub} and anti-Jovian spot y_d^{anti}, see Figure 4.19. Using this definition, the angle does not depend on the measured horizontal position of the spots x_d, which can not be directly related to the actual spot location as explained above. Note that α is negative, when the sub-Jovian spot is displaced to the north, i.e., when Io is located below the torus equator.

To determine the uncertainty of the vertical spot position y_d^{spot}, we shift the boxes in the vertical direction (up and down). For each shift along the vertical axis, we calculate the intensity for the brightest box centered at the new y_d' allowing an offset on the horizontal axis of maximal 5 pixels from the original x_d^{spot}. When the difference between the intensity of the actual spot box, I_{spot}, and the intensity of the shifted box, I_{shift},

$$\Delta I = I_{\mathrm{spot}} - I_{\mathrm{shift}} \tag{4.48}$$

exceeds the propagated statistical error of ΔI given by

$$\sigma_{\Delta I} = \sqrt{\sigma_{\mathrm{spot}}^2 + \sigma_{\mathrm{shift}}^2 - 2\sigma_{\mathrm{common}}^2} \quad , \tag{4.49}$$

the intensities differ significantly, i.e., outside the statistical uncertainty. σ_{spot}, σ_{shift} are the combined statistical errors of all pixels within the boxes, $\sigma_{\mathrm{common}}^2$ is the covariance of the intensities of the actual and shifted spot boxes given by the combined error of the pixels that are included in *both* boxes. In other words, the uncertainty in the overlap of the boxes accounts equally for both intensities and must thus be subtracted. The error in y_d, σ_d, is then set to the value furthest away from y_d^{spot} with $\Delta I/\sigma_{\Delta I} < 1$. Figure 4.20 shows intensity difference ΔI as function of the box displacement in the vertical direction for an image with two bright aurora spots (left) and for an image where one spot box is hardly brighter than the neighboring boxes (right).

The propagated error for the spot angle α (Eq. 4.47) is then given by

$$\sigma_\alpha = \sqrt{\left(1 - \left[\frac{y_d^{\mathrm{anti}} - y_d^{\mathrm{sub}}}{2\,\mathrm{R_{Io}}}\right]^2\right)^{-1} \left(\frac{1}{2\,\mathrm{R_{Io}}}\right)^2 \left[(\sigma_d^{\mathrm{sub}})^2 + (\sigma_d^{\mathrm{anti}})^2\right]} \quad , \tag{4.50}$$

with the averaged uncertainties of the sub-Jovian σ_d^{sub} and anti-Jovian σ_d^{anti} spot position along y_d. The errors for the spot angles shown in Figure 4.17 correspond to the derived propagated uncertainty σ_α.

4.3.2 Correlation with the background magnetic field

Although the average fitted inclination of the near-surface emission in the OI] 1356 Å, OI 1304 Å, and SI 1479 Å images are almost identical, the inferred spot angles for some of the OI] 1356 Å observation and model images reveal considerable differences, see Figure 4.17. For lower System III longitudes ($\lambda_{III} < 120°$), the absolute values of the measured spot angles appear to be principally

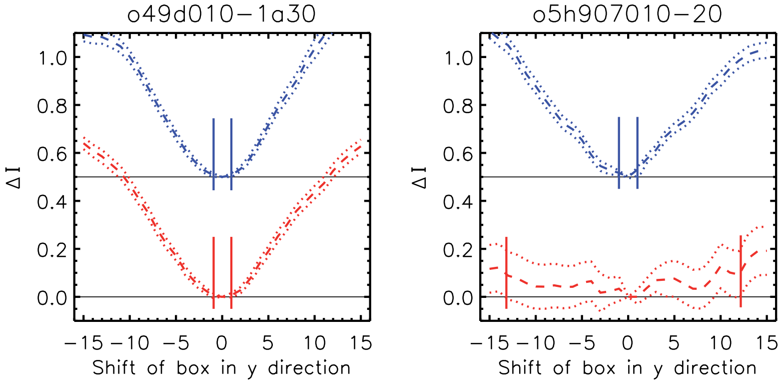

Figure 4.20: *Intensity difference* ΔI *(dashed lines) after* (4.48) *of the shifted spot boxes with respect to the brightest box as a function of the displacement in pixels for two observation images. The sub-Jovian spot is shown in red, the anti-Jovian spot in blue. The dotted lines show the error range* $\sigma_{\Delta I}$ *after* (4.49)*. The vertical lines indicate the maximum displacement within the statistical uncertainty corresponding to uncertainties of the vertical spot positions,* σ_d^{sub} / σ_d^{anti}.

larger than the angle in the modeled images, whereas for $\lambda_{III} > 120°$, the observed angle is mostly lower than the respective modeled angle. Hence, the measured angles seem to be systematically differing with a negative offset. For the analysis of the spot angles, we use the angles obtained from the 18 OI] 1356 Å images (without the eclipse image) and from the 2 SI] 1900 Å images yielding 20 data points for the measured angle α_{obs}. Due to the overlapping morphology of the lines at 1479 Å, and the flat emission pattern with weak spots at OI 1304 Å, the spot angles can not be determined with sufficient accuracy in these images.

First, we apply a method to directly estimate the correlation of the spot angles to the ambient magnetic field, which is further assumed to be the homogeneous constant background field. Therefore, we analyze the dependency of the spot angles on B_x and B_y, separately. The angle of the magnetic equator with respect to Io’s planetographic equator, β_0, is given by Equation (4.5). In case $B_x \approx 0$, the angle becomes

$$\beta_y = \arctan\left(\frac{B_y}{B_z}\right) \quad . \tag{4.51}$$

β_y then corresponds to the latitude of the tangential points of the homogeneous background field with the sub-/anti-Jovian meridian. Figure 4.19 illustrates the tangential magnetic field points for this scenario. Assuming that the spots are located at the sub-/anti-Jovian meridian, the measured spot angle α_{obs} would be equal to β_y, if the flank emission was exactly symmetric with respect to the torus equator. In this case, the model parameter ζ^* would be unity. The angle β_y is shown by the dashed blue line in Figure 4.21 for all System III longitudes. It is obvious, that the spot angle α_{obs} is correlated to β_y, even though there are clear deviations as expected from fitted inclination of $\zeta^* \approx 0.8$. The measured spot location might be displaced solely due to the longitudinal extension of the spots. Further assuming that $B_x \approx 0$, the offset of the spots from Io’s equator y_d decreases, when the spot center is displaced from the Jovian facing meridian. Graphically, each point on the magnetic equator is closer to the planetographic equator than the intersecting points with the Jovian facing meridian. For the derived longitudinal spot offset of $\varphi_0^* = 20°$, y_d is decreased by $\sim$6%. This effect results in a lowered measured spot angle α_{obs} in the images.

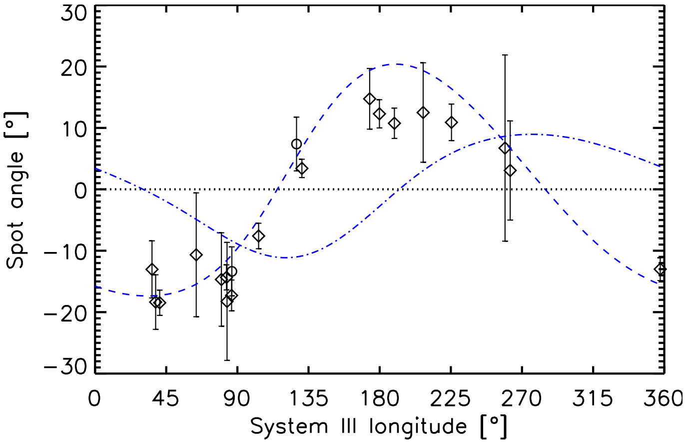

Figure 4.21: *Angle between the line connecting the two equatorial spots and Io's equator (spot angle* α_{obs}*) as measured in the OI] 1356 Å / SI] 1900 Å observations (black diamonds/circles with error bars). The dashed blue line indicates the tilt of the background field in y direction* β_y *after* (4.51)*, the dashed-dotted blue line shows* β_x *after* (4.52).

In case $B_y \approx 0$, the magnetic equator is solely rotated about the y-axis by

$$\beta_x = \arctan\left(\frac{B_x}{B_z}\right) \quad . \tag{4.52}$$

If the elongated flank emission is symmetric with respect to the tilted magnetic equator, the measured vertical position of the spots changes from upstream to downstream. For $B_x < 0$, the upstream part of the spot is found above the planetographic equator, whereas the downstream part is below. For $B_x > 0$, the behavior is exactly opposed. This means, that the measured offset y_d in the images depends on the part of the spot, that is visible for the observer. Comparing the angle β_x (dashed-dotted blue line in Figure 4.21) to the observed spot angles, the influence of the magnetic field tilt in the x-direction is unclear. Additionally, the alignment with the magnetic equator might be altered as the flow direction of the incoming plasma is directed in the x-direction with a neglecting z-component. Consequently, the spots are symmetric with respect either to the flow direction or to the magnetic equator. The bright flank emission is though to coincide with the regions of high ionospheric densities (*Saur et al.* 2000), which are presumably not aligned with the magnetic equator. Thus, the expansion of the flank emission along the direction of the flow (along x in IPhiO) can not be described by a simple approximation. Furthermore, the maximum tilt in y-direction is larger by a factor of ~2 compared to the tilt in x-direction, as the maximum B_y component is larger by ~2 than the maximum B_x. Therefore, we analyze solely the correlation of α_{obs} to the tilt of the background field in y-direction β_y, keeping in mind a possible influence of the tilt in B_x.

The chi-squared value of α_{obs} and β_y is

$$\chi^2_{\alpha\beta_y} = \frac{1}{N}\sum_{i=1}^{N}\left[\frac{\alpha_{obs,i} - \beta_{y,i}}{\sigma_{\alpha_i}}\right]^2 = 2.6 \quad , \tag{4.53}$$

where the magnetic angle $\beta_{y,i}$ is calculated for each image i corresponding to the System III longitude of the observation λ_{III}. This means the observed spot angles are resembled equally well by β_y than by the spot angles measured in the model images ($\chi^2_\alpha = 2.5$).

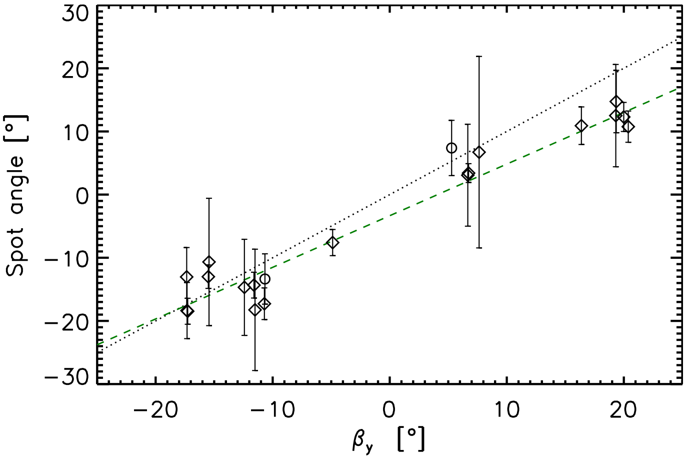

Figure 4.22: *Angle between the line connecting the two equatorial spots and Io's equator (spot angle) as measured in the OI] 1356 Å (diamonds) and SI 1479 Å (circles) observations versus the tilt β_y (Eq. 4.51) of the undisturbed background field. The dashed green line shows the fitted functional dependence* (4.54). *The dotted line shows a theoretical 1:1 correlation.*

To estimate a general trend for the deviation α_{obs} from β_y, we fit a linear function of the form

$$\alpha_\beta(\beta_y) = a_1 + a_2\,\beta_y \tag{4.54}$$

to the observed spot angles α_{obs}. The fitted coefficients are

$$\begin{aligned} a_1 &= -3.34\,(\pm 0.65)\,^\circ \\ a_2 &= 0.82\,(\pm 0.05) \quad . \end{aligned} \tag{4.55}$$

The slope coefficient (a_2) implies an attenuated inclination of the spots compared to the background field in agreement with the result for the inclination of the phenomenological model. Additionally, the fit yields an offset of -3.34° for the spot angles with respect to the background field tilt. The obtained offset reflects the systematic deviation mentioned at the beginning of the section. This offset corresponds to 18% of the maximal observed spot angle, and is thus not insignificant. Although the statistics of 20 data points is limited and not all System III longitudes are covered well by the observations, there seems to be a general trend in the correlation between α and β_y. The resulting chi-squared value of

$$\chi^2_{\alpha\alpha_\beta} = \frac{1}{N-2}\sum_{i=1}^{N}\left[\frac{\alpha_{obs,i} - \alpha_{\beta,i}}{\sigma_{\alpha_i}}\right]^2 = 0.8 \quad , \tag{4.56}$$

indicates, that the measured angles can be explained by this functional dependence on the background field within the uncertainty. In Figure 4.22 the measured spot angles α_{obs} are shown as a function of the magnetic field tilt β_y. The green dashed line illustrates the derived linear correlation. This inferred trend is confirmed by an independent analysis of *Retherford et al.* (2000) and *Retherford* (2002). Applying a slightly different method, *Retherford et al.* (2000) derive a slope of 0.8 (±0.3) for a linear correlation through zero (no offset). *Retherford* (2002) derive very similar values for the correlation between the spot inclination and the background field obtaining a slope of 0.83 (±0.25) and also a small negative offset (see Figure 3.3a of *Retherford* 2002). Thus, both the attenuation of the variation and the offset in the spot angles is measured independently of the analyzing technique.

The position of the spots can be affected by various different processes. Due to the two-dimensional projection of the emission in the images, the observing geometry and the tilt in the x-direction might cause an attenuated (lower) measured spot angle α_{obs}. Since the inclination in the phenomenological model, by which the projection effect is eliminated, was fitted to $\zeta^* \approx 0.8$ as well (except for the SI] 1900 Å images), the tilt of the spots is likely to be affected by other processes, additionally. As the combined exposure time of the analyzed images is roughly 40 minutes, the measured angles are just an average over this time period. In 40 minutes, the System III longitude at Io changes by about 19°. The averaging may lead to a small attenuation of the measured variation. The deviations of $\alpha_o bs$ from the magnetic field tilt are, however, higher than the change of β_y within 40 minutes.

We have shown, that the spots arise very close to the surface. Therefore, a direct correlation to the background field can, in fact, not be expected. The magnetic field close to Io is strongly disturbed by the interaction of the magnetospheric plasma with Io's atmosphere, see Section 2.1.3 and Figure 2.6. Induction signals from the interior of the moon might further alter the magnetic field in the close vicinity. In particular, the influence of the induced magnetic fields is maximal on the surface of Io and decreases roughly with r^{-3}. Furthermore, we have assumed a global, symmetric atmosphere. Io's atmospheric distribution, however, is thought to be highly asymmetric and possibly even patchy due to the influence of volcanic outgassing. Before we analyze the influence of the plasma interaction and of the induction signals on the magnetic field topology, we estimate the impact of an inhomogeneous atmospheric distribution in the next section.

4.3.3 Influence of the atmospheric distribution

To estimate the influence of an inhomogeneous atmosphere, the magnetic field is further assumed to be the constant homogeneous background field. With the additional assumption that the heat flux along the unperturbed magnetic field lines is equally effective from the north and from the south of the flux tube, the strongest radiation is emitted at the tangent point on Io's surface, where the neutral density peaks. We define now a *flux tube neutral column density* given by an integral over atmospheric density along the flux tube above, or north of, the tangent point p_β

$$N_{ft}^N = \int_{p_\beta}^{Z_N} \mathrm{d}z_B \, n_n(z_B) \quad , \tag{4.57}$$

and below, or south of, the tangent point p_β

$$N_{ft}^S = \int_{Z_S}^{p_\beta} \mathrm{d}z_B \, n_n(z_B) \quad . \tag{4.58}$$

The boundaries Z_N and Z_S are set to points along $\mathbf{B}$, where n_n become negligibly small. For a globally symmetric atmosphere the *flux tube neutral column densities* are equal for the flux tubes sections above and below p_β, see Figure 4.23a. Thus, the aurora brightness after (4.4) is then also completely symmetric with respect to the magnetic equator, if the electron temperature T_e and density n_e in the flux tube are spatially homogeneous.

Since Io's atmosphere is considerably denser around the equator than close to the poles, this symmetry might be broken by the inhomogeneous atmospheric distribution, and in particular by the

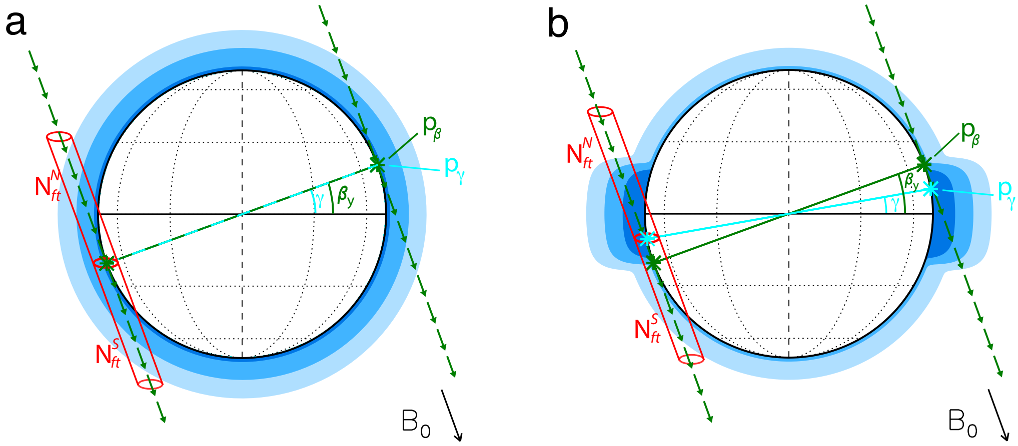

Figure 4.23: *Sketch of the tangent points of the magnetic field lines (green stars) and of the symmetry points of the flux tube neutral density (turquoise stars). The angles of the connecting lines between the points with respect to the planetographic equator are* β_y *and* γ*, respectively. The tangent magnetic field lines are indicated by the green arrows, the atmospheric distribution is sketched by the blue areas. (a) For a globally symmetric atmosphere, the symmetry points coincide with the tangent points, thus* $\gamma = \beta_y$*. (b) For a dense equatorial atmosphere confined to a narrow region, the symmetry points are displaced towards the planetographic equator, i.e.,* $\gamma < \beta_y$*.*

latitudinal dependence of the neutral density. Principally, if the atmosphere is confined to a region around the equator, the rocking of the equatorial spots might be suppressed due to the lack of neutral gas at higher latitudes. As approximation for the latitudinal profile we use the distribution

$$N_n(\vartheta) = N_0 + N_{eq}\ \exp\left[-\left(\frac{\vartheta}{\delta\vartheta}\right)^6\right] \quad , \tag{4.59}$$

inferred by *Strobel and Wolven* (2001) from the STIS Lyman-α observations. N_0 is the low polar column density, N_{eq} is the additional equatorial density, which is higher than N_0 by roughly two orders of magnitude. The latitude, where the column density drops from $N_{eq} + N_0$ to N_0, is determined by $\delta\vartheta$, which is $\sim$35° in the analysis of *Strobel and Wolven* (2001). For our analysis, we assume an exponential radial profile

$$n_n(r) \propto \exp\left(-\frac{r}{H(r)}\right) \quad , \tag{4.60}$$

with a scale height of $H(r) = 10$ km for $r \leq 20$ km, and $H(r) = 100$ km for larger r.

The electron energy supply from north and south are further assumed to be equal. However, the atmospheric column density along the flux tube is not symmetric any more with respect to the tangent point for a tilted background field and a latitudinal density profile given by (4.59). As a rough approximation for the spot position, we then use the point along the flux tube p_γ, where the *flux tube neutral column densities* above and below are equal. For homogeneous T_e and n_e in the flux tube, the total emission above and below are also equal. Even if we assume that the heat conduction along $\mathbf{B}$ is finite and the temperature along the flux tube decreases inside the atmosphere, the electron temperature will be roughly proportional to the inverse of the neutral density. Hence, the symmetry of the emission along the flux tube would still be symmetric to this point.

For a dense atmospheric ring reaching up to a latitude of $\delta\vartheta = 35°$ N/S, this symmetry point p_γ of the *flux tube neutral column density* is shifted only slightly towards the equator with respect to p_β. The angle of the connecting line between the symmetry points γ with respect to the tilt of the magnetic equator (see Figure 4.23) is $\gamma \approx 0.98\,\beta_y$. Thus, the influence of the density drop at latitudes on the tilt of the equatorial spots should be negligible.

Assuming a considerably narrower region of high density around the equator with $\delta\vartheta = 15°$ N/S, the angle of the connecting line between the symmetry points is on average $\gamma \sim 0.8\,\beta_y$, in agreement with the observed relative spot inclination of roughly 0.8 of the background field. The tangent and symmetry points for this case are sketched in Figure 4.23b. However, as the drop-off of the dense atmosphere has been found to be not closer to the equator than $\vartheta = 30°$ N/S, such a narrow atmospheric ring around the equator is highly unlikely and the attenuation of the rocking of the spots is presumably not caused by atmospheric inhomogeneities. Several observations indicate an atmospheric column density that is constantly higher than 10^{16} cm^{-2} from the equator up to north and south latitudes of $30-40°$ (*Jessup et al.* 2004, *Spencer et al.* 2005, *Feaga et al.* 2009). Therefore, a patchy or very asymmetric atmospheric distribution as explanation for the observed offset of the spot angles can also be ruled out.

Taken together, the atmospheric distribution probably influences the spot location only marginally. The spots move up and down between $\sim 20°$ N/S of the equator. Therefore the latitudinal decrease of the neutral gas abundance at higher latitude ($\vartheta > 30°$ N/S) has no measurable influence on the rocking of the spots.

4.3.4 Effects of the plasma interaction

So far, we have related the spot angle α_{obs} to the tilt of the undisturbed homogeneous background field β_y after (4.51). As already mentioned, the magnetic field is in fact considerably perturbed in Io's vicinity. The interaction between the plasma and the atmosphere induces ionospheric currents, which produce magnetic field perturbations δB_P on the order of $0.3B_0$ (e.g., *Saur et al.* 1999). *Khurana et al.* (2011) derive additional perturbing signals from induction in Io's interior with amplitudes as high as $\delta B_{ind} = 650$ nT also roughly corresponding to $0.3B_0$. In this section we will qualitatively discuss the influence of the plasma interaction, before we estimate the effect of the induction in the next section.

In Section 4.3.2, we have derived a functional correlation between α_{obs} and β_y given by a slope of 0.82 and an offset of -3.34° (Eq. 4.54). Using the definition of $\beta_y = \arctan(B_y/B_z)$, the inferred offset a_1 and slope a_2 can be related to systematic deviations of the magnetic field components B_y and B_z. While B_z is approximately constant in Io's orbit at -2000 nT, B_y varies roughly between ± 750 nT during a synodic rotation of Jupiter. On the one hand, a change of the constant B_z component is related to a change of the slope in (4.54). The offset in (4.54), on the other hand, could be due to an offset added to the variable B_y component. We, therefore assume a function for the modified tilt of the magnetic field given by

$$\beta_y^c = \arctan\left(\frac{B_y + B_y^c}{B_z + B_z^c}\right) \tag{4.61}$$

with the coefficients B_y^c and B_z^c describing a constant offset in the local magnetic field. Fitting β_y^c

to the observed spot angles α_{obs} yields for the coefficients

$$\begin{aligned} B_y^c &= 159\,(\pm 39)\ \mathrm{nT} \\ B_z^c &= -502\,(\pm 154)\ \mathrm{nT} \quad , \end{aligned} \tag{4.62}$$

with a chi-squared of

$$\chi^2 = \frac{1}{N-2}\sum_{i=1}^{N}\left[\frac{\alpha_{obs,i}-\beta_y^c}{\sigma_{\alpha_i}}\right]^2 = 0.8 \quad . \tag{4.63}$$

This means the magnetic field tilt is in agreement with the observed spot angles, when a constant magnetic field given by B_y^c and B_z^c is superposed on the varying Jovian magnetic field. β_y^c as a function of λ_{III} is displayed in Figure 4.24.

We now compare the obtained deviation from the undisturbed background field with the expected perturbation arising from the local plasma interaction. As explained above, the B_z^c offset affects the amplitude of the variation of the spot angle, which is the slope in (4.54). Since the magnetic field at Io points southward, i.e., $B_z < 0$, the derived negative offset corresponds to an increase of the magnetic field strength of ~25% resulting in a reduced slope. For $B_y \ll B_z$, the increase $B_z' = B_z + B_z^c \approx 1.25\,B_z$ matches almost the decrease of the slope

$$\beta_y' = \arctan\left(\frac{B_y}{B_z'}\right) \approx \frac{B_y}{1.25\,B_z} = 0.8\,\beta_y \quad . \tag{4.64}$$

Neglecting the Hall conductance, the ionospheric currents are principally driven from the sub-Jovian to the anti-Jovian hemisphere (see Figure 2.5). The magnetic field generated by the ionospheric currents is directed southward on the upstream side of Io leading to an enhancement of B_z, and northward on the downstream side, where B_z is thus reduced. The region of the enhanced magnetic field strength, often referred to as *pile-up* region, has been detected during Galileo flybys upstream of Io at low latitudes (*Kivelson et al.* 2001). The spots, however, are displaced from the Jovian-facing meridian towards the downstream hemisphere, where a *reduced* magnetic field is generally expected. A Galileo flyby in the wake revealed a strongly decreased field strength, but at distances of ~900 km above the surface (*Kivelson et al.* 1996). Galileo never passed through the wake close to Io. Although, it has not been measured yet, the expected reduced magnetic field in the downstream region is exactly opposed to the derived negative offset B_z^c. Only in the case the interaction region is highly asymmetric with respect to the downstream and upstream sides, for instance due to a much denser and more extended atmosphere on the downstream hemisphere, the pile-up region can be displaced towards the wake. A strong asymmetry has not been observed for Io's atmosphere. Taken together, the lower inclination of the spot angle, i.e., the reduced slope in (4.54), probably does not originate from the perturbation of the local field by the plasma interaction.

The offset in B_y can be related to the offset a_1 in (4.54). The offset of the spot angles corresponds to ~20% of the amplitude of the variation. Accordingly, the derived B_y^c corresponds to ~20% of the amplitude of the varying B_y component. A perturbation field in the y-direction arises from either the field aligned currents parallel to z or perpendicular currents in the x-direction due to the Hall conductance (see $j_\perp$ in Figure 2.5). However, the B_y perturbations generated by these currents are exactly opposed in the regions above and below the magnetic equator, which can be assumed to be the symmetry plane for the interaction. Hence, a general offset in B_y towards one direction as inferred from the spot angles is not expected from a rough estimation of the perturbations due to the plasma interaction.

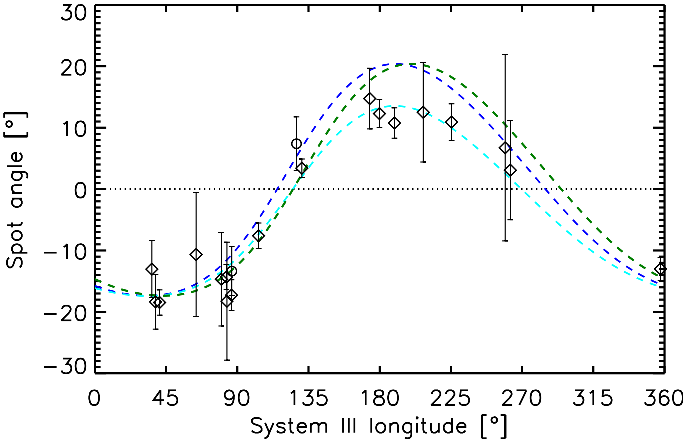

Figure 4.24: *Angle between the line connecting the two equatorial spots and Io's equator (spot angle* α_{obs}*) as measured in the OI] 1356 Å / SI] 1900 Å observations (black diamonds/circles with error bars). The dashed blue line indicates the tilt of the background field in y-direction* β_y *after* (4.51). *The dashed turquoise line shows magnetic field tilt* β_y^c *with constant offsets in* B_y *and* B_z *after* (4.62), *the dashed green line shows the tilt of the background field with a temporal delay of ~22 minutes, which corresponds to a shift in* λ_{III} *of 10°.*

Another effect of the plasma interaction possibly affects the magnetic field environment. As the plasma velocity is severely reduced inside the interaction region, the convection of the magnetic field is slowed accordingly. So far, we have assumed that the background field is determined by the System III longitude at the time of the observation. Due to the slowing of the convection of the flux tubes, the ambient magnetic orientation differs from the orientation of the rigidly corotating field. A test for a shift in the System III longitude λ_{III}, which is equivalent to a temporal delay of the ambient field, reveals a slightly better agreement, if β_y is calculated with the magnetic field components for $\lambda'_{III} = \lambda_{III} - 10(\pm 2)^\circ$. The chi-squared of β_y for the delayed magnetic field environment is

$$\chi^2_{\alpha\beta} = \frac{1}{N-1}\sum_{i=1}^{N}\left[\frac{\alpha_i - \beta_{y,i}(\lambda'_{III})}{\sigma_{\alpha_i}}\right]^2 = 1.9 \quad . \tag{4.65}$$

The expected tilt of the delayed Jovian background field is shown by the dashed green line in Figure 4.24. Converted to a time delay, this corresponds to the magnetic field 22 minutes before t_{obs}. If the size of the interaction region is approximated by the diameter of Io (3642 km), the convection speed turns out to be strongly reduced to ~3 km s^{-1}. Measurements by the Galileo Plasma Analyzer (PLS) during a close flyby on the anti-Jovian flank (I27) revealed a reduced flow speed of ~2 km s^{-1} (*Frank and Paterson* 2001). The agreement with the spot angles is, however, only slightly better than without considering this delay. This means the delayed ambient magnetic field orientation is certainly not the only factor influencing the spot angle variation, as it can not account for the observed reduced amplitude.

4.3.5 Influence of induced magnetic fields from the interior

Due to the tilt of Jupiter's magnetic moment with respect to the rotation axis, the planet's dipole field changes periodically in Io's orbit. In an electrically conductive layer inside the moon, the change of the ambient magnetic field induces currents, which in turn are the source of induced magnetic fields or secondary magnetic fields. *Khurana et al.* (2011) claimed that Galileo mag-

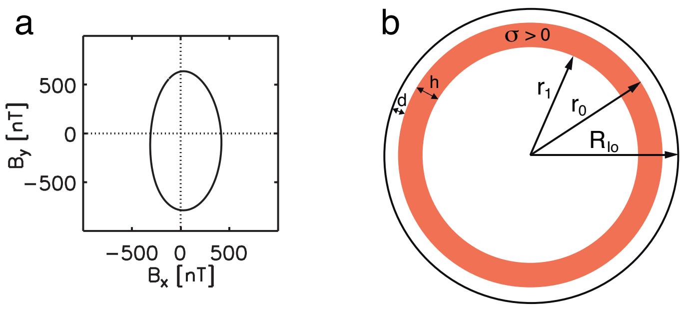

Figure 4.25: *(a)* B_y *vs.* B_x *of Jupiter's internal field in Io's orbit after the VIP4 model (Connerney et al. 1998). (b) Model of Io's interior with a conductive layer of thickness h under a non-conductive crust of thickness d. The conductivity* σ *is assumed to be zero everywhere outside the red layer.*

netometer measurements brought evidence that the measured magnetic field perturbations in Io's vicinity arise from induction in a global magma ocean under Io's crust. Therefore, we will now investigate the possible effects of induced magnetic fields from Io's interior on the location of the equatorial aurora spots.

The amplitudes of varying magnetic fields arising in the current sheet or from the currents at the magnetopause are more than an order of magnitude lower than Jupiter's field (*Seufert et al.* 2011) and are therefore neglected here. For Jupiter's internal field we further use the VIP4 model by *Connerney et al.* (1998). The variability is mostly confined to the equatorial xy-plane, B_z is approximately constant in Io's orbit. The variation of B_x and B_y during a synodic rotation of Jupiter is displayed in Figure 4.25a.

As the secondary fields are opposed to the inducing fields, the total magnetic field is principally reduced. Thus, the reduced variation of the magnetic field in the xy-plane might lead to a reduced variation of the aurora spots. However, as the variation of the secondary fields is phase shifted with the respect to the varying primary field, the exact response needs to be calculated. We therefore use a simple theoretical approach to calculate the induction response from the interior quantitatively.

Inside a shell of spatially constant conductivity σ, an induction equation of the form

$$\frac{\partial \mathbf{B}}{\partial t} = \frac{1}{\sigma\mu}\Delta\mathbf{B} \tag{4.66}$$

can be derived from Maxwell's equations and Ohm's law. The magnetic permeability μ can be assumed to be equal to the vacuum permeability μ_0 (*Saur et al.* 2010). Since the induction equation is linear in $\mathbf{B}$, the primary field can be decomposed as a superposition of the real parts of fields with individual frequencies ω_n in the form

$$\mathbf{B}(t) = \sum_n \mathbf{B}_n \mathrm{e}^{i\omega_n t} \quad . \tag{4.67}$$

The frequencies correspond to the inverse of the synodic period of Jupiter $T_{\mathrm{Jup,syn}} = 12.95$ h, and of fractions of this period. A solution for the secondary fields $\tilde{\mathbf{B}}$ outside the body as a function of the inducing or primary fields $\mathbf{B}$ has been derived by several authors for conductive layers with a spherical geometry (e.g., *Parkinson* 1983). Figure 4.25b illustrates the assumed interior model for Io with a layer of uniform conductivity σ, thickness h, outer radius r_0 and inner radius $r_1 = r_0 - h$. The induced signal from a conductive core is negligible for the analyzed periods of

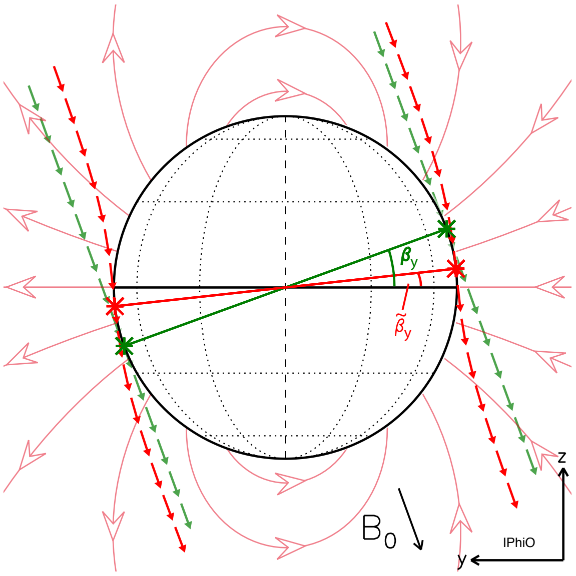

Figure 4.26: *Sketch of the effect of an induced dipole field from Io's interior on the tangent points of the magnetic field lines. The light red lines show the induced dipole, the tangent field lines of the superposed magnetic fields are depicted by the deep red arrows. The red asterisks indicate the tangent points of the superposed field, the green asterisks indicate the tangents points of the background field.*

the inducing fields (*Seufert et al.* 2011). We follow the solution presented by *Saur et al.* (2010) for the description of the induced fields. With the assumption that the primary field **B** is spatially homogeneous, the secondary field at $\mathbf{r} = (x, y, z)$ is a dipole field, which is given by

$$\tilde{\mathbf{B}}(\mathbf{r},t) = -Ae^{i\phi}\left[3(\mathbf{r}\mathbf{B}(t))\mathbf{r} - r^2\mathbf{B}(t)\right]\frac{r_0^3}{2r^5} \tag{4.68}$$

(cf. Equations (10) and (16) of *Saur et al.* 2010). The parameters A and ϕ depend on the ocean parameters and the complex wave number $k = \pm(1+i)\sqrt{\mu_0\sigma\omega/2}$ and are given by

$$Ae^{i\phi} = \frac{\xi J_{5/2}(r_0k) - J_{-5/2}(r_0k)}{\xi J_{1/2}(r_0k) - J_{-1/2}(r_0k)} \quad , \tag{4.69}$$

with

$$\xi = \frac{(r_1k)J_{-5/2}(r_1k)}{3J_{3/2}(r_1k) - (r_1k)J_{1/2}(r_1k)} \quad , \tag{4.70}$$

(cf. Equations (14) and (15) of *Saur et al.* 2010). J_m are Bessel functions of first kind and order m. A and ϕ correspond to the relative amplitude and phase of the secondary with respect to the primary field. Thus, for finite conductivity, $A < 1$ and $-\frac{\pi}{2} \leq \phi \leq 0$. The total magnetic field in Io's environment is then given as a superposition of the homogeneous background field **B** and the induced dipole field after (4.68):

$$\mathbf{B}_{tot}(\mathbf{r},t) = \mathbf{B}(t) + \tilde{\mathbf{B}}(\mathbf{r},t) \quad . \tag{4.71}$$

We continually assume that the auroral spots arise at the tangent points of the magnetic field line on Io's surface, where the neutral density is presumably highest. We now show that for the geometry of a superposed dipole and homogeneous field, the angle between the tangent points of the field line on a circle in the yz-plane is simply given by

$$\tilde{\beta}_y = \arctan\left(\frac{B_y + \tilde{B}_y^{pol}}{B_z + \tilde{B}_z^{pol}}\right) \quad , \tag{4.72}$$

with the magnetic field strength on the polar axis of the induced dipole field ($\mathbf{r} \parallel \mathbf{B}$) at distance r

$$\tilde{\mathbf{B}}^{pol}(r,t) = -Ae^{i\phi}\,\mathbf{B}(t)\frac{r_0^3}{r^3} \quad . \tag{4.73}$$

Using (4.73), Equation (4.68) becomes

$$\tilde{\mathbf{B}}(\mathbf{r},t) = \left[3(\mathbf{r}\,\tilde{\mathbf{B}}^{pol})\mathbf{r} - r^2\tilde{\mathbf{B}}^{pol}\right]\frac{1}{2r^2} \quad . \tag{4.74}$$

In the yz-plane (at the sub-Jovian and anti-Jovian meridian), $\tilde{\mathbf{B}}^{pol}$ can be expressed as

$$\tilde{\mathbf{B}}^{pol} = \tilde{B}_y^{pol}\mathbf{e}_y + \tilde{B}_z^{pol}\mathbf{e}_z \quad . \tag{4.75}$$

Using polar coordinates r and ϑ defined by $y = r\cos\vartheta$ and $z = r\sin\vartheta$ with unit vectors $\mathbf{e}_r$ and $\mathbf{e}_\vartheta$, Equation (4.74) can be written as

$$\tilde{\mathbf{B}}(\mathbf{r},t) = [\tilde{B}_y^{pol}(r)\cos\vartheta + \tilde{B}_z^{pol}(r)\sin\vartheta]\mathbf{e}_r + \frac{1}{2}[\tilde{B}_y^{pol}(r)\sin\vartheta - \tilde{B}_z^{pol}(r)\cos\vartheta]\mathbf{e}_\vartheta \quad . \tag{4.76}$$

The background field in the yz-plane $\mathbf{B} = B_y\mathbf{e}_y + B_z\mathbf{e}_z$ can be written in polar coordinates as

$$\mathbf{B} = (B_y\cos\vartheta + B_z\sin\vartheta)\mathbf{e}_r + (-B_y\sin\vartheta + B_z\cos\vartheta)\mathbf{e}_\vartheta \quad . \tag{4.77}$$

For the tangent point of the magnetic field on a circle in the yz-plane centered in the origin, the radial component of the superposed field $\mathbf{B}_{tot} = \mathbf{B} + \tilde{\mathbf{B}}$ has to be zero. Thus, the requirement that

$$B_y\cos\vartheta + B_y\sin\vartheta + \tilde{B}_y^{pol}(r)\cos\vartheta + \tilde{B}_y^{pol}(r)\sin\vartheta = 0 \tag{4.78}$$

yields for the northern or southern latitude ϑ of the tangential point

$$\tan\vartheta = \left|\frac{B_y + \tilde{B}_y^{pol}}{B_z + \tilde{B}_z^{pol}}\right| \quad . \tag{4.79}$$

By definition, the latitude of the tangential points corresponds to the angle $\tilde{\beta}_y$. Thus, we have shown that the tangential point of a magnetic field line of the superposed background and induced fields on a circle is given by Equation (4.72). Figure 4.26 illustrates the reduced magnetic field angle due to the induced dipole field, which is superposed in the background field.

By varying the conductivity σ, depth d, and thickness h of the subsurface layer, we now fit the tilt of the tangent points $\tilde{\beta}_y$ after (4.72) to the observed angles of the spots α_{obs}. Thereby, we assume that the equatorial spots are located on the surface, i.e., $r = \mathrm{R_{Io}}$. It turns out, that there is no set of parameters for the ocean yielding a better agreement between $\tilde{\beta}_y$ and α_{obs} than for either $\sigma = 0$ or $h = 0$, i.e., without conductive layer. At first glance, this is surprising, as with a simultaneous variation of the thickness and depth as well as the conductivity, almost all possible amplitudes and phase shifts are tested. However, although the induction signal leads to an attenuation of the total

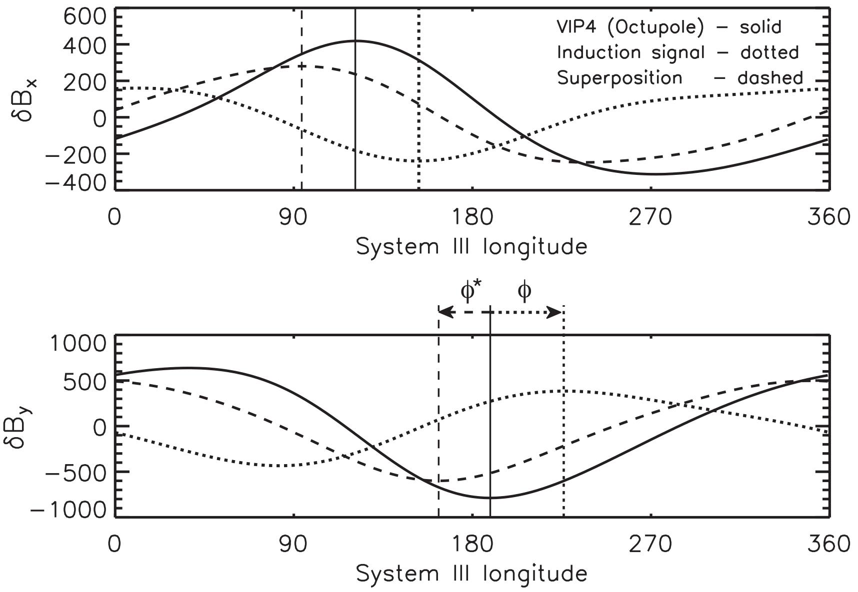

Figure 4.27: *The variation of* B_x *(top panel) and* B_y *(bottom panel) in Io's orbit during a synodic rotation of Jupiter. The primary field is shown as solid black line, the amplitude of the secondary (induced) field is depicted by the dotted line, the dashed line is the superposition of both fields. The vertical lines indicate the maximum of the absolute field strength during the orbit of the primary, secondary and superposed fields. The relative shift of the lines illustrates the delay* ϕ *of the phase shifted induced field and the "lead" of the superposed field by* ϕ^**. The ocean parameters for this case are* $d = 50$ *km,* $h = 200$ *km, and* $\sigma = 0.05\ S\,m^{-1}$.

amplitude of B_y, the phase shift leads to a shift of the angle $\tilde{\beta}_y$ with respect β_y, that is opposed to the deviation of the measured spots α_{obs} from β_y.

Figure 4.27 illustrates the shift of the secondary and of the superposed fields with respect to the background field variation. The induced signal naturally lags behind the inducing signal. The amplitude and phase A and ϕ of the response depend on the frequency ω of the inducing signal. An average phase shift ϕ for the total signal can be estimated by the shift of the maximum amplitude of the secondary to the primary field, which is marked with the vertical lines in Figure 4.27. As the delayed induced signal attenuates the primary field, the maximum of the superposed fields is shifted towards lower System III longitudes λ_{III} as indicated by ϕ^* in Figure 4.27. This means the total field is "ahead" in time with respect to the primary field. In the previous section, we have shown that the spot angles is in better agreement with the magnetic field tilt, if the ambient field is delayed by $\lambda_{III} \approx 10°$ or 22 minutes. Hence, the shift of the induced fields is exactly opposite to the observed deviation.

For a relatively low conductance of $(\sigma h) \approx 3 \times 10^3$ S, the amplitude of the induced field for the main frequency $\omega = 1/T_{\mathrm{Jup,syn}}$ is $A \approx 0.2$. This implies a reduction of the variation of B_y and therefore of β_y to 80% for a zero phase shift. However, in that case the phase shift is $\phi \approx -60°$ resulting in a strongly shifted, but only slightly attenuated total signal. The pink dashed line in Figure 4.28 shows $\tilde{\beta}_y$ for an ocean with $d = h = 50$ km and $\sigma = 0.05\,\mathrm{S\,m^{-1}}$.

The thickness and depth comply with the minimum thickness and maximum depth as derived for a conductive global magma layer by *Khurana et al.* (2011) from the Galileo measurements.

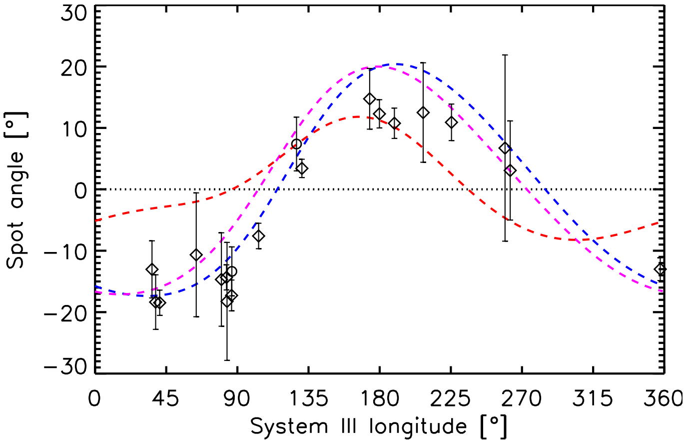

Figure 4.28: *Same as Figure 4.24, but with dashed lines for angles of the magnetic field for an ocean with* $d = h = 50$ *km and conductivities of* $\sigma = 0.05\ S\,m^{-1}$ *(pink dashed line), and* $\sigma = 0.43\ S\,m^{-1}$ *(red dashed line). The latter conductivity and the extension of the ocean resemble the parameters of the derived magma layer by Khurana et al. (2011).*

For the conductivity, *Khurana et al.* derive a value of $\sigma = 0.43$ assuming a magma layer with a melt fraction of 20%. Using these parameters, the amplitudes of the induced fields are $A \approx 0.8$ and the phase shift $\phi \approx -25°$ (i.e., the signal is only slightly shifted). The high amplitude and low phase shift lead to very effective shielding of the magnetic field variation close to the surface. The resulting variation of $\tilde{\beta}_y$ during a rotation period is shown by the red dashed line in Figure 4.28. Such a strong induction clearly contradicts the high spot angles observed between $60° < \lambda_{III} < 100°$. The resulting chi-squared value for the deviation of $\tilde{\beta}_y$ to α_{obs} of $\chi^2_{\tilde{\beta}_y} = 14$ quantitatively determines the essential disagreement of the angles.

Hence, weaker induction signals imply relatively high phase angle yielding a magnetic field angle $\tilde{\beta}_y$ that is "shifted away" from the observed spot angles. For a highly conductive ocean, the phase shift is lower, even though still in the "wrong" direction, but the high induced amplitudes lead to a complete shielding of the magnetic field variation from the surface. Since we have shown that the spots arise at very low altitudes, the rocking would be strongly attenuated by this shielding, and much stronger than the derived attenuation of ~80%. Taken together, the observed spot angles is inconsistent with the existence of a conductive magma layer just below Io's surface according to our approximation.

4.4 Implications of the derived aurora properties

We have shown that the STIS aurora observations obtained over a period of five years can be reproduced by the derived phenomenological model for the emission in the vicinity of Io. In addition, by correlating the derived spot angles to the ambient magnetic field, we have investigated the local magnetic field topology. In this section, the implications of the observed intensities and the inferred spatial distribution of the emission for the atmosphere and the plasma environment as well as the results for the ambient magnetic field will be discussed.

4.4.1 Energy supply and plasma interaction strength

The total brightness has been shown to be almost linearly proportional to the torus electron density upstream of Io. One the one hand, this implies that the effectiveness of the transfer of the electron energy into the atmosphere is controlled by the local density of the electrons. It means, on the other hand, that the energy stored in the flux tubes is not completely depleted. If the electron energy supply of the flux tubes was completely used up due to the collisions in Io's atmosphere, the yield of emitted radiation would be independent of local properties. Contributions to the aurora from excitation by energetic electron beams observed in the wake of Io (*Michael and Bhardwaj* 2000, *Frank and Paterson* 1999) are also ruled out due to the clear dependence on the density of the thermal plasma.

Furthermore, the nearly 1:1 correlation to the upstream torus density suggests that the local interaction strength is relatively constant. To demonstrate the influence of the interaction on the aurora brightness, we can apply the interaction parameter α_{Io} given in Equation (2.16). As explained in Section 2.1.3, the factor α_{Io} principally determines the fraction of the upstream flux tubes that are not deflected around the body and can thus enter Io's atmosphere. The obtained correlation suggests that α_{Io} does not undergo large variations due to the changing upstream torus density. This is also consistent with the result, that the distribution of flank emission does not vary strongly apart from the variations connected to the magnetic field orientation. For instance, in the case of drastic changes of the interaction strength and thus α_{Io}, the equatorial spots would be expected to arise at different altitudes depending on the deflection of the plasma (*Saur et al.* 2000). However, conclusions on the interaction strength are limited, as a wide range of processes has to be taken into account including effects of the ionospheric currents on the atmosphere due to, for instance, Joule heating (*Saur et al.* 1999).

The total photon emission rates inferred from the phenomenological model for the global emission is on the same order of magnitude as the flank emission for all multiplets. This means, that the electron energy is sufficient to globally excite the near-surface atmosphere despite the generally strong deflection of the incoming plasma. The direct correlation of the limb glow brightness to the flux tube contents above the hemispheres indeed implies a very effective energy transport along the field lines. The field-parallel thermal conductivity of the electrons in the torus plasma is extremely high. Deeper in the atmosphere collisions with the neutrals reduce the thermal conductivity. At very low altitudes the neutral density presumably exceeds the plasma density by several orders of magnitude. However, according to our analysis, the auroral emission, which creates the limb glow, originates almost entirely from regions very close to the surface at altitudes of $h < 100\,\mathrm{km}$. Consequently, the electron energy transport has to be effective even at high neutral density.

An approximation of the effective electron thermal conductivity in a partially ionized plasma is given by *Banks and Kockarts* (1973)

$$\kappa_{hc} = \frac{7.7 \times 10^5 \, T_e^{5/2}}{1 + 3.22 \times 10^4 \, T_e^2 \, \sigma_{en} n_n / n_e} \quad [\mathrm{eV\,cm^{-1} s^{-1} K^{-1}}] \tag{4.80}$$

(cf. their Equation 22.116). k_B is the Boltzmann constant and n_e and n_n the local density of the electrons and the neutrals, respectively. The momentum transfer cross section σ_{en} of elastic electron scattering from sulfur dioxide is $\sim 10^{-15}$ cm^2 (*Gulley and Buckman* 1994). At a given electron temperature T_e, the conductivity thus depends on the relative weight of the two terms of the sum in the denominator of (4.80). Figure 4.29 (left) illustrates the dependency of κ_{hc} on

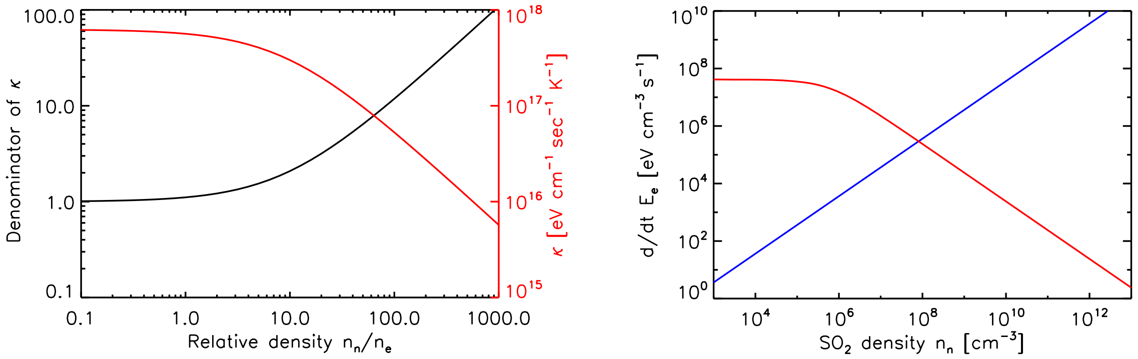

Figure 4.29: *(Left) Effective electron thermal conductivity as a function of the relative neutral density to electron density ($k_BT_e = 5$ eV). The denominator of the RHS of Equation* (4.80) *is shown in black, the total thermal conductivity κ_{hc} after Equation* (4.80) *is depicted in red. (Right) Magnitude of the two terms on the RHS of Equation* (4.81) *as a function of the SO_2 gas abundance. The blue curve shows the collisional cooling, the red curve demonstrates the effectiveness of the heat conduction along the flux tubes.*

the mixing ratio of neutrals to electrons for $k_BT_e = 5$ eV. As long as $n_n \lesssim n_e$, the second term in the denominator is lower than 1 and the conductivity is thus constantly high. Where $n_n \gg n_e$, κ_{hc} decreases by several orders of magnitude. We can now estimate the effectiveness of the heat conduction by using a simple approximation for the temperature balance in a flux tube inside Io's atmosphere:

$$\frac{3}{2}k_Bn_e\frac{\mathrm{d}T_e}{\mathrm{d}t} = -\left(\mathfrak{L}_c(T_e) + \frac{3}{2}k_BT_ef_{ion}(T_e)\right)n_en_n - \frac{\partial}{\partial z_B}Q_{flux} \quad . \tag{4.81}$$

The first term on the RHS accounts for the energy loss due to inelastic collisions $\mathfrak{L}_c(T_e)$ and heating of newly ionized electrons, where f_{ion} is the ionization rate. The inelastic collision term

$$\mathfrak{L}_c(T_e) = \varepsilon_{ion}f_{ion}(T_e) + \varepsilon_{dis}f_{dis}(T_e) + \varepsilon_{rot}f_{rot}(T_e) + \varepsilon_{vib}f_{vib}(T_e) \tag{4.82}$$

includes ionization, dissociation, and rotational and vibrational excitation of neutral SO_2 with rates f and energy ε (see also Equations (13) and (14) of *Saur et al.* 1999). The energy loss has to be compensated through heat conduction along the flux tubes given by the derivative of the heat flux density along the magnetic field. The heat flux can be approximated by the thermal conductivity and the temperature gradient along the flux tube z_B:

$$Q_{flux} = -\kappa_{hc}\frac{\partial}{\partial z_B}T_e \quad . \tag{4.83}$$

We now assume, that in one step the electron energy inside the atmosphere is depleted through the collisions, and in a next step the heat conduction transfers energy along the flux tube into the atmosphere. The heat flux is then approximated by

$$\langle Q_{flux}\rangle = \langle\kappa_{hc}\rangle\frac{\Delta T_e}{H_{hc}} \quad , \tag{4.84}$$

where ΔT_e is the temperature decrease and H_{hc} a typical distance for the heat transport, which is assumed to be roughly the scale height of the atmosphere (100 km). The heat flux term in (4.81) can then be expressed as

$$\frac{\partial}{\partial z_B} Q_{flux} \approx \frac{1}{H_{hc}} \langle \kappa_{hc} \rangle \frac{\Delta T_e}{H_{hc}} \quad . \tag{4.85}$$

Assuming that the electron density is given by the torus density of $n_e = 3000\ \mathrm{cm}^{-3}$ and further assuming an electron temperature drop of $k_B \Delta T_e = 1$ eV, we can estimate the magnitude of both terms on the RHS of (4.81) as a function of the neutral gas abundance n_n. Figure 4.29 (right) illustrates that for a sulfur dioxide abundance of $n_n \gtrsim 10^8\ \mathrm{cm}^{-3}$, the energy supply via heat conduction drops below the estimated energy consumption in the atmosphere.

Close to the surface, the SO_2 density is expected to increase up to $\sim 10^{12}\ \mathrm{cm}^{-3}$ (e.g., *Summers and Strobel* 1996, *Wong and Smyth* 2000). The electron density, on the other hand, is increased only by a factor $\sim$10 with respect to the ambient torus electron density in Io's ionosphere (*Saur et al.* 1999, *Frank and Paterson* 2001) and thus $n_{e,\mathrm{max}} \approx 5 \times 10^5\ \mathrm{cm}^{-3}$. Additionally, the peak ionospheric densities are found several tens of km above the surface. Hence, according to our approximation the energy supply via heat conduction is not effective enough to prevent the electrons from cooling deep inside the atmosphere. Nonetheless, the inferred radial profile of the global emission contradicts this approximation as most radiation is emitted within 100 km above the surface suggesting that the heat conductivity is large enough close to preserve the electron from cooling.

4.4.2 Atmospheric abundances

By using the inferred total photons emission rates, we are able to estimate a lower boundary for the mixing ratios of the atmospheric species. *Saur et al.* (2003) derive an analytical approximation for the total radiation rate produced by electron impact in the atmosphere of Io:

$$\varepsilon_{\mathrm{theo}} = \varepsilon_{\mathrm{sheet}} \frac{D_{\mathrm{interact}}}{db_0} \alpha_{Io} \tag{4.86}$$

(see Appendix B of *Saur et al.* 2003). $\varepsilon_{\mathrm{sheet}}$ refers to the radiation in a *sheet of plasma* corresponding to the area, which is spanned by a flux tube of width db perpendicular to the flow direction and magnetic field moving through the interaction region. Thus, $\varepsilon_{\mathrm{sheet}}$ is related to the part of the electron energy of a flux tube that is deposited in the atmosphere. $\frac{D_{\mathrm{interact}}}{db_0}$ specifies the number of flux tubes across the interaction region of width D_{interact}, where db_0 is the width of the undistorted flux tube, and α_{Io} is the parameter for the electrodynamic interaction strength as defined in Equation (2.16). An expression for $\varepsilon_{\mathrm{sheet}}$ as a function of the upstream electron temperature $T_{e,0}$ and the reduced electron temperature after the flux tubes passed Io T_e, is given by Equation (9) of *Saur et al.* (2003)

$$\begin{aligned} \varepsilon_{\mathrm{sheet}} =& \gamma v_{e,0}\, db_0 \int_{\text{flux tube}} n_e(z_B)\, \mathrm{d}z_B \int_{T_{e,0}}^{T_e} \left[\frac{\frac{3}{2} k_B f_\lambda(T_e')}{-\left(\mathfrak{L}_c(T_e') + \frac{3}{2} k_B T_e'\right)} \right. \\ & \left. \times \exp\left(\int_{T_{e,0}}^{T_e'} \frac{\frac{3}{2} k_B f_{ion}(T_e'')}{-\left(\mathfrak{L}_c(T_e'') + \frac{3}{2} k_B T_e''\right)} \mathrm{d}T_e'' \right) \right] \mathrm{d}T_e' \quad . \end{aligned} \tag{4.87}$$

γ is the mixing ratio of the excited species and $v_{e,0}$ the undisturbed velocity of the plasma flow. The terms with the temperature integrals in (4.87) estimate the yield of radiation compared to the energy loss through elastic and inelastic collisions depending of the overall temperature decrease

$\Delta T = T_{e,0} - T_e$ in the atmosphere. f_λ is the excitation rate, f_{ion} the ionization rate and $\mathfrak{L}_c$ accounts for cooling by inelastic collisions and is given by Equation (4.82).

Using Equation (4.86) together with Equation (4.87) and assuming that the electron energy in the flux tubes is completely depleted, i.e., $T_e = 0$, the maximum total emission rate $\varepsilon_{\text{theo,max}}$ for a given mixing ratio of the excited species can be estimated. For an optically thin atmosphere the estimated total rate $\varepsilon_{\text{theo,max}}$ must be higher than or equal to the inferred photon emission rates of the near-surface aurora $\varepsilon_{\text{glob}} + \varepsilon_{\text{spots}}$. Thus, we can derive minimum mixing ratios for the excited species, so that $\varepsilon_{\text{theo,max}} \geq \varepsilon_{\text{glob}} + \varepsilon_{\text{spots}}$. Following *Saur et al.* (2003), we use $\alpha_{Io} = 0.1$ and $D_{\text{interact}} = 3\ \text{R}_{\text{Io}}$, which is in agreement with the outer aurora boundary of our calculations of $\varepsilon_{\text{glob}}$ and $\varepsilon_{\text{spots}}$. As the OI] 1356 Å and SI] 1900 Å emissions involve only spin-forbidden transitions, they can widely be assumed optically thin and will be used for estimating the oxygen and sulfur mixing ratios.

When taking into account solely excitation of atomic oxygen to produce OI] 1356 Å, we find a minimum O/SO$_2$ mixing ratio of $\gamma_{\text{O}} = 0.13$ in order to yield the total photon emission rate of $\varepsilon_{\text{glob}} + \varepsilon_{\text{spots}} = 6.4 \times 10^{25}\ \text{s}^{-1}$. Contributions from dissociative excitation of O$_2$ and SO$_2$ with mixing ratios of $\gamma_{\text{O}_2} = 0.1$ and $\gamma_{\text{SO}_2} = 1$ are roughly $6 \times 10^{24}\ \text{s}^{-1}$ and $2 \times 10^{24}\ \text{s}^{-1}$ and thus an order of magnitude lower. Similarly, for SI] 1900 Å we obtain a minimum S/SO$_2$ mixing ratio of $\gamma_{\text{S}} = 0.02$ to produce the inferred total photon emission rate of $\varepsilon_{\text{glob}} + \varepsilon_{\text{spots}} = 8.9 \times 10^{25}\ \text{s}^{-1}$. As for oxygen, dissociative excitation of SO$_2$ produces about 2×10^{24} photons per second, which is also an order of magnitude lower than the yield of excitation of atomic sulfur. The derived lower boundaries for the mixing ratios of 0.13 and 0.02 for atomic oxygen and sulfur to SO$_2$, respectively, imply a relative abundance of S/O of ~0.2, which is in agreement with previous observations (e.g., *Feaga et al.* 2004). Using the same mixing ratios, the estimated photon emission rates $\varepsilon_{\text{theo,max}}$ for OI 1304 Å and SI 1479 Å are higher by roughly a factor of 2 with respect to the values inferred from the phenomenological model. This suggests that the emissions are considerably attenuated due to absorption in the atmosphere.

Note that we have assumed that the entire flux tube energy is deposited in the atmosphere for this estimation. However, the correlation of the brightness to the local electron density implies, that the electron energy of the flux tubes is, in fact, *not* entirely depleted. Consequently, even higher mixing ratios are needed to produce the observed intensities.

4.4.3 Sublimation versus volcanic outgassing

We have shown that the variations of the morphology and brightness of Io's UV aurora observed over a period of five years primarily depend on the magnetospheric properties, which are determined by one parameter, λ_{III}. Apart from that the aurora does not undergo large variations, but appears to be rather constant. This constancy implies, that the influence of possible atmospheric changes on the UV emission is very low. If the atmosphere was to major parts supplied by direct volcanic outgassing, large temporal variations of the density would be expected due to transient volcanic activity, see Section 2.1.1. Thus, the inferred constancy of the UV aurora suggests a certain atmospheric temporal and spatial uniformity, which is consistent with a sublimation-driven atmosphere.

The model results also show that the day side flank emission is consistently brighter by a factor of $1.4 - 1.6$ than the emission on the hemisphere, which is primarily on the night side. The only exception are the two SI] 1900 Å images, which, however, suffer a high noise level. The higher day side brightness could be due to an enhanced neutral gas abundance, since the atmosphere is assumed to partially collapse on the night side. However, a higher neutral density leads to higher local ionospheric conductivities, that shield the incoming electrons from that region. In other words, the interaction parameter α_{Io} is decreased, possibly eliminating the effect of the increased neutral density on the day side. *Saur et al.* (2000) simulated this feedback effect by implementing a higher density on the sub-Jovian flank in their plasma model and find that the radiated emission is only slightly increased for a twice higher density. According to their results, the Hall effect, which rotates the flow towards Jupiter (see Section 2.1.3), plays clearly the dominant role for the relative brightness of the flank emission. *Saur and Strobel* (2004) investigated the effect of the global shielding by the interaction on the total radiation yield. In case the global atmospheric column density drops from 1.5×10^{16} cm^{-2} in sunlight down to 2×10^{14} cm^{-2}, when Io moves into Jupiter's shadow, they find that the total emission is reduced by $\sim$50% (see Figure 5 of *Saur and Strobel* 2004). This means that the atmospheric collapse is not balanced any more by the weaker shielding in this density range. Therefore, a similar collapse of the night side atmosphere by roughly two orders of magnitude might result in a similar reduction of the radiation in agreement with our findings. The Hall effect is likely to affect the asymmetry additionally, even though our results suggest that the atmospheric collapse primarily controls the anti-sub-Jovian brightness difference.

The analysis of the brightness in eclipse also indicates a drastic drop of neutral gas abundance. The near-surface global emission in eclipse has been shown to be reduced down to 20–50% of the inferred values for the observations in sunlight. According to the results of *Saur and Strobel* (2004), this again implies that the atmospheric column density is reduced by two orders of magnitude. Our results also show that the reduction of the flank and coronal aurora is lower than that of the global emission. This is in agreement with the expected collapse of the near-surface SO_2 atmosphere due to the lack of sublimation support in shadow.

Taken together, the constancy of the UV aurora, the day-night side asymmetry and the low eclipse brightness are consistent with an atmospheric collapse of two orders of magnitude. According to these results, sublimation of SO_2 frost deposits plays the dominant role in sustaining the atmosphere, whereas contributions of direct volcanic outgassing, which is independent of sunlight, are on the order of 1% at maximum.

4.4.4 Local magnetic field topology

The main factor controlling the location of the equatorial spots is the orientation of the background field, although a systematic deviation of the measured spot angles from the orientation of the undisturbed background field indicate that other factors influence the location, additionally. We have shown that a direct influence of an inhomogeneous neutral gas abundance is negligible. The local perturbations of the magnetic field, on the other hand, most likely affect the spot location.

With the very simplified assumption that the location of the auroral spots is represented by the tangent points of the magnetic field lines on the surface, it turned out that the estimated magnetic field perturbation due to both the plasma interaction and the induced magnetic fields in Io's interior are not in accordance with the observed spot angles. However, we have only qualitatively reflected the influence of the plasma interaction. Thus, local atmospheric inhomogeneities could easily alter this global picture leading to asymmetries of the ionospheric conductivity and thus the generated magnetic field. The inferred temporal delay of the ambient magnetic field is consistent with the expected deceleration of the plasma at Io, but cannot account for the attenuation of the rocking of the spots.

To estimate the influence of induction signals, we derived an approximation for the magnetic field topology given by the superposition of the background field and an induced dipole field from the interior. According to this approximation the measured spot angles are inconsistent with any kind of induction signal from an interior conductive layer. In particular, with the parameters of the putative magma ocean derived by *Khurana et al.* (2011) the induction would largely shield the variations of the background field from the surface leading to a strong suppression of the rocking of the spots, which appears to incompatible with the observations. Galileo magnetometer measurements obtained during several flybys at Io, on the other hand, revealed perturbation features that are consistent with induction signals (*Khurana et al.* 2011, *Dols* 2011). The distance of Galileo at the closest approach of the flybys at Io is not smaller than 200 km. The auroral spots, in contrast, are located very close to the surface ($h < 100$ km), where the strength of the induced field is considerably larger. Thus, the aurora observations are in principal a powerful tool to investigate the induced fields. However, further analysis of the observed aurora morphology is needed including a calculation of the exact correlation between the spot locations and the magnetic field topology. Furthermore, the plasma interaction and induction very likely exert considerable influence on each other. Such mutual effects have only been simulated for Europa so far by *Schilling et al.* (2008), where the authors find that the induced magnetic fields cause time varying asymmetries in the current density and the plasma density in the vicinity of the moon. Therefore, effects of an inhomogeneous atmosphere or the induction could possibly modify the geometry of the plasma interaction.

4.5 Preliminary conclusion

In the present chapter, a universal analytical expression for the spatial distribution of the UV emission in the vicinity of Io has been derived. Thereby, we have demonstrated the principal dependencies of the aurora formation on the magnetospheric and atmospheric configuration. Our model for the UV aurora is able to reproduce the main features of the observed morphology for all STIS images taken over a period of five years. Therefore, the model can even be applied to predict the brightness and morphology of future observations. Moreover, the model results imply considerable differences of the atmosphere on the day side and on the night side. Accordingly, a drastic collapse of the neutral density in eclipse has been inferred. In the case of the spot variations, we have found that the rocking is not consistent with magnetic induction in a highly conductive interior layer, even though the exact correlation of the spot locations to the magnetic field environment remains unclear. However, to infer quantitative properties for densities and mixing ratios in the atmosphere as well as to elucidate the role of the magnetic field for the formation of the auroral spots, all discussed effects must be modeled self-consistently. Thereby, both the important chemical and physical reactions in the atmosphere and the electrodynamical processes in the interior and the vicinity of the moon have to be taken into account. So far, such a comprehensive model has not been developed.

The *Saur* interaction model (see Section 2.1.3 and *Saur et al.* 1999) calculates, self-consistently, the plasma density, the velocity and the temperature of the ions and electrons, and the electric field for a given neutral SO_2 atmosphere. It has been successfully applied to explain several features of Io's plasma interaction. However, it lacks the self-consistent calculation of the magnetic field perturbation, since it is based on the assumption of a constant homogeneous field. Provided that Io's atmosphere at least partially collapses during eclipse, the local plasma interaction and thus the magnetic field perturbations are weaker than in the case of a sunlit atmosphere, i.e., the assumption of a homogeneous field is more justified. As mentioned earlier, magnetic field perturbation of more than $\frac{\Delta B}{B} = 0.3$ are expected in a dense atmosphere in sunlight. For the interaction in eclipse with an increased atmospheric density, results of the *Saur* model indicate that the perturbation of the magnetic field is lower by a factor of 2, thus $\frac{\Delta B}{B} \approx 0.15$.

The model also accounts for the heat conduction along the constant magnetic field lines, even though the conductivity is simplified and parametrized. Due to the expected collapse of the near-surface atmosphere in eclipse, the SO_2 abundance might be reduced by more than two orders of magnitude. This means, the thermal conductivity in the atmosphere is presumably higher in eclipse. Therefore, the simplified calculation of the field aligned heat conduction in the model is suitable. Moreover, due to the decreased atmospheric density, most emissions can be assumed optically thin.

In the following chapter, we will slightly modify and adapt the model of *Saur et al.* (1999) to the case when Io is in eclipse to simulate the plasma interaction and formation of Io's aurora self-consistently. We will compare our results to recently obtained observations of the UV aurora in eclipse by the Hubble Space Telescope and the New Horizons spacecraft. These observations provide good constraints for the morphology and brightness, and have a lower noise level than the STIS eclipse observations. The model does not simulate induction effects from the interior and does not account for small scale features in the atmosphere. However, it provides good constraints for the local electron density and temperature in Io's environment allowing to infer relative and absolute atmospheric abundances by comparing the model results and the observations.

5 Simulation of Io's visible and UV aurora in eclipse

In this chapter we study the morphology of Io's aurora in eclipse by comparing simulation results of a three-dimensional two-fluid plasma model to observations by the high-resolution Long-Range Reconnaissance Imager (LORRI) on-board the New Horizons (NH) spacecraft and by the Hubble Space Telescope Advanced Camera for Surveys (HST ACS). Most parts of this study have been published in *Roth et al.* (2011).

5.1 LORRI and ACS images of the visible and UV aurora in eclipse

The observing geometry for Earth-bound observations of Jupiter's satellites is generally constrained to low solar phase angles, i.e., the sub-solar point is always close to the sub-observer point on the surface. Hence, when Io is in Jupiter's shadow, the HST always monitors the sub-Jovian hemisphere like in the STIS and ACS eclipse images. In contrast, spacecraft imaging of Io in eclipse is not bound to distinct observing angles, but allows an observation of the anti-Jovian hemisphere as monitored by the LORRI during Ieclipse04. The geometry of the observations is depicted in Figure 5.1. The observational and magnetospheric parameters during the eclipse occasions are given in Table 5.1.

Besides the advantage of observing the anti-Jovian hemisphere, the LORRI eclipse observations contain the highest spatial resolution obtained so far of Io's auroral emission revealing numerous

Table 5.1: *Eclipse occasions of LORRI and HST ACS observations.*

Event	Date	Moment	UTC	φ_{HST}[a] [°]	φ_{NH}[b] [°]	λ_{III}[c] [°]	ψ_m[d] [°]	B_x[d] [nT]	B_y[d] [nT]	B_z[d] [nT]
Ieclipse03	2007-02-27	Ingress	14:21	344	310	154	6.5	308	-580	-2145
		Mid-eclipse	15:24			183	9.0	79	-788	-2141
		Egress	16:27			212	9.5	-142	-715	-2108
Ieclipse04	2007-03-01	Ingress	08:50	–	240	255	5.8	-300	-321	-2022
		Mid-eclipse	09:53			284	1.5	-308	-11	-1966
		Egress	10:56			313	−3.4	-261	264	-1938

[a] Sub-observer longitude of the HST ACS observation.

[b] Sub-spacecraft longitude of the NH LORRI images. Note that this does not correspond to Io's orbital position as for the Earth-bound HST images.

[c] Longitude (λ_{III}) and latitude (ψ_m) of the Jovian System III.

[d] Background magnetic field calculated with the magnetic field model of *Connerney et al.* (1998) for the internal field of Jupiter.

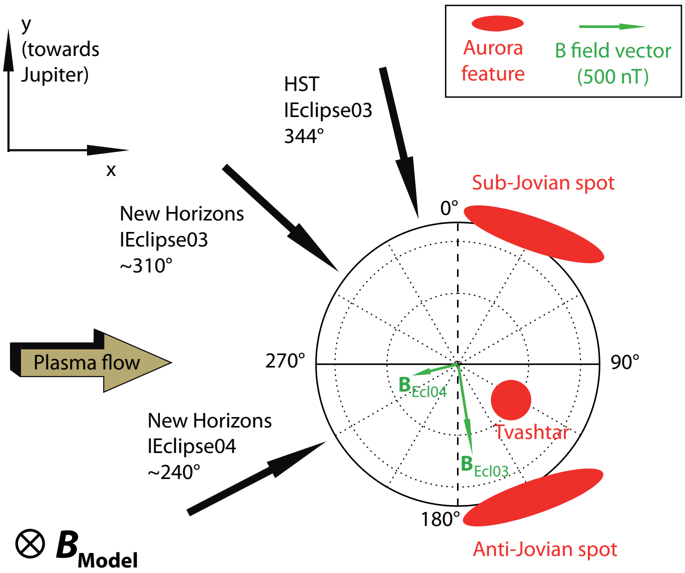

Figure 5.1: *Geometry of the Ieclipse03 and Ieclipse04 observations in the IPhiO coordinate system. The black arrows point out the viewing angle of the New Horizons probe and the Hubble Space Telescope. The Jovian background field vectors in the xy-plane at mid-eclipse are shown with green arrows. Up to the right a magnetic field vector of 500 nT is displayed for comparison ($B_z \approx 2000$ nT). The undisturbed plasma flow is directed in positive x-direction. The background field in the simulation model is assumed constant in negative z direction (perpendicular to the displayed xy-plane). The expected key features of the aurora are sketched by the red areas.*

small scale aurora features. The composed LORRI and ACS exposures during the two eclipse events are displayed in Figure 5.2. The technical characteristics of the LORRI and ACS images are explained in Section 3.4. We now describe and assign the essential features in the images.

As explained in Section 3.4, in the LORRI observations emissions from a broad wavelength range between 3500 and 8500 Å are imaged. The observed diffuse emissions in the LORRI images originate from excitation of SO_2 and S_2 emission bands as well as from excited atomic oxygen, atomic sodium and potassium. Contributions of excitation of atomic sulfur are low. During Ieclipse03 (Figure 5.2 b), the sub-spacecraft coordinates are $\varphi_{obs} \approx 310\,^{\circ}$W (west longitude) and $\vartheta_{obs} \approx 7\,^{\circ}$S. Hence, the sub-Jovian upstream quadrant is visible during the observation. The brightest small spots on the disk appear to be thermal emission. The measured intensity corresponds to a black body temperature of approximately 1200 K (*Spencer et al.* 2007a). Fainter small spots are low-altitude gas emissions. On the upstream side, which correspond to the right-hand limb in the image, enhanced radiation is visible only within a relatively small region, which has been attributed to a volcanic hot spot located east of the Girru paterae and therefore named *East Girru* (*Spencer et al.* 2007a). Considering the geometry of the background magnetic field during Ieclipse03, the observed emission maximum around East Girru could also result from the magnetic field tilt and represent a shifted anti-Jovian equatorial spot. The main part of the anti-Jovian spot is probably obstructed by the disk. However, the East Girru emission appears to consist of one low and one high altitude emission part. Assuming that the plasma parameters do not vary discontinuously, the puzzling two part emission could originate from two different atmospheric species, as for example emission from SO_2 close to the surface and from atomic oxygen at higher altitudes. As the images do not provide a spectral resolution, the double-structure feature cannot be analyzed for different emission lines. Around the downstream (left-hand) disk edge there is a diffuse emission region of approximately 500 × 1000 km^2, which corresponds to the sub-Jovian equatorial spot. Apart from the equatorial band there is small enhanced emission just above the limb close to the north pole. The bright area can undoubtedly be assigned to the huge Tvashtar plume (see also Figure 2.1). Unlike most of Io's volcanoes, Tvashtar is located at a high latitudes. Since the neutral gas abundance at the poles is expected to be two orders of magnitude lower than at the equator, Tvashtar creates a locally enhanced neutral atmosphere.

In the Ieclipse04 image (Figure 5.2 a), the Tvashtar plume is clearly evident above the limb. The bright area is similar to the plume size derived from sunlit observations with a height of about 350 km and full width of 1100 km (*Spencer et al.* 2007a). The geometry of this image with sub-observer longitude $\varphi_{obs} \approx 240\,^{\circ}$W and latitude $\vartheta_{obs} \approx 3\,^{\circ}$S allows an observation of both equatorial spots. While the sub-Jovian spot is restricted to a small area, the anti-Jovian spot extends further on the disk. Emission originating from excitation of the volcanic plume gas possibly contributes also to the several confined thermal hot spots. For Ieclipse04 the viewing angle is just $\sim$30° offset from the upstream view at 270° W, where both spots are expected to be clearly visible and similar in brightness. Note that in the case of Ieclipse03, the deviation from the upstream view is only $\sim$10° more, but there is no clear anti-Jovian spot observable.

In the ACS image (Figure 5.2c), most of the observed radiation originates from the OI 1304 Å, OI] 1356 Å and SI 1479 Å emissions. The viewing angle from HST is $\varphi_{obs} \approx 344\,^{\circ}$W and $\vartheta_{obs} \approx 0\,^{\circ}$. Thus the sub-Jovian hemisphere is monitored, the plasma flow is directed from right (upstream) to left (downstream) in the image. The morphology is dominated by three features. The brightest area on the disk corresponds to the sub-Jovian equatorial spot. The emission above the downstream limb (left) in the wake probably reflects parts of the extended anti-Jovian spot as inferred in the previous chapter from the STIS images. And third, similar to the LORRI observation, the emission on the upstream side is considerably enhanced only above the East Girru region. Again, this enhancement can not definitely be assigned to a volcanic region, but might also originate from a smooth, continuous atmosphere and an inhomogeneous electron environment. In addition to the LORRI images, the NH Alice spectrograph measured the total intensity of the OI 1304 Å and OI 1304 Å oxygen multiplets and the SI 1479 Å sulfur multiplet during four eclipse events between February 25 and March 3, 2007 (*Retherford et al.* 2007a). The measured UV intensities are listed in Table 5.2 together with the values derived from the STIS images and measured brightnesses of the visible aurora.

An eclipse passage takes about two hours, which is approximately one sixth of the synodic period of Jupiter. Since the observation images (Figures 5.2 a-c) are combinations of several co-aligned exposures during one eclipse event, the plasma environment and magnetic field vary between the exposures. Therefore, we can not identify an exact observation geometry. Nonetheless, we now describe the plasma conditions during the LORRI and ACS observations referring to the midway time of the respective eclipse passage. As for the STIS images, the three components of **B** listed in Table 5.1 are calculated with the VIP4 model and given in the Io-centric IPhiO system described in Section 2.1.3.

During Ieclipse03, Io is above the plasma torus and reaches the maximum distance to the torus center shortly before egress. The y-component of the magnetic field vector is relatively large. The component in the direction of the orbital movement (B_x) in turn is low. The angle β_0 after Equation (4.5) between the magnetic field and the polar axis varies between $\sim$16° and $\sim$19°. During Ieclipse04 Io passes through the torus center from north to south. Accordingly, the y-

Table 5.2: *Observed and simulated total intensities of the investigated emission lines. The variation of the simulated intensity results from changes in the viewing geometry as well as various upstream electron densities.*

Emission	STIS images I_{tot} [kR]	Other observations I_{tot} [kR]	Eclipse observations $I_{tot,ecl}$ [kR]	Eclipse simulation $I_{sim,ecl}$ [kR]
OI] 1356 Å	0.50 – 1.21	0.48 – 0.88 [a]	0.38 – 0.80 [a]	0.4 – 0.7
SI 1479 Å	0.57 – 1.43	0.60 – 1.17 [a]	0.43 – 1.20 [a]	0.6 – 1.1
SI] 1900 Å	1.1 – 2.1	1.68 – 2.33 [d]	–	0.5 – 0.9
NaI 5890 Å	–	–	4 [b]/ 6.9 [c]	3.4 – 6.6
OI 6300/6364 Å	–	–	6.8 [f]/14.2 [b]/23.7 [c]	6.2 – 11.8
KI 7670 Å	–	–	$<$ 10.35 [e]	2.2 – 4.3

[a] NH ALICE, *Retherford et al.* (2007a)
[b] HST STIS, *Retherford* (2002)
[c] Galileo SSI, *Bouchez et al.* (2000)
[d] IUE, *Ballester et al.* (1987)
[e] Cassini ISS, *Geissler et al.* (2004)
[f] Galileo SSI, *Geissler et al.* (1999)

component of **B** is lower and the B_x component somewhat larger. β_0 is roughly 10°. Furthermore, the ambient plasma density presumably is higher during Ieclipse04 in the torus center than during Ieclipse03, when Io is far away from the center. The field vectors in the *xy*-plane during mid-eclipse are shown in Figure 5.1. The direction of the magnetic field for the observing geometry at mid-eclipse is displayed in the lower right corner in Figures 5.2 a-c.

In all observations five areas are highlighted with green frames, which will be separately analyzed. The two areas around the equatorial spots span a region of $\sim 9.2 \times 10^5$ km^2 or roughly 0.6 R_{Io} × 0.46 R_{Io}, comparable in size to the equatorial boxes applied in the analysis of the STIS images. However, due to the geometric constraints in the simulation setup the modeled auroral emission is not tilted. Therefore, the boxes are located at a fixed position at the equator of Io and have a slightly larger extension in the vertical direction to adequately cover the spots in the observations as well. Additionally, the brightness in a $\sim 6.4 \times 10^5$ km^2 sized region centered at the calculated position of the Tvashtar plume is investigated to compare the observed and simulated emission intensities originating from the volcano. The large boxes on the upper and lower edge of Io cover an area of $\sim 3.8 \times 10^6$ km^2 around the poles, similar to the limb glow areas in Section 4.2. The total emission within the boxes is integrated and normalized to the covered area to investigate the auroral morphology quantitatively.

Previous studies (e.g., *Saur et al.* 2000) and our analysis of the STIS images have demonstrated that the formation of the auroral emission is controlled by the interaction of the plasma with the atmosphere. The density and distribution of the atmospheric gas influence this interaction, i.e., the neutral gas controls the flow pattern and the temperature and density profiles of the electrons. Since the electrons generate the auroral emission, electron temperature and density are, in addition to the atmospheric density, the essential parameters for calculating the aurora. On the other hand, the distribution and local density of emitting gas particles is directly reflected by the intensity and morphology of the aurora. To calculate both effects self-consistently, we use the *Saur* plasma model, which is explained in detail in Section 2.1.3. In Section 4.5, we have shown that the assumption of the model are particularly justified for the eclipse case, where a collapse of the atmosphere is expected. In the following section, the essential modifications and the setup of the model is described in detail.

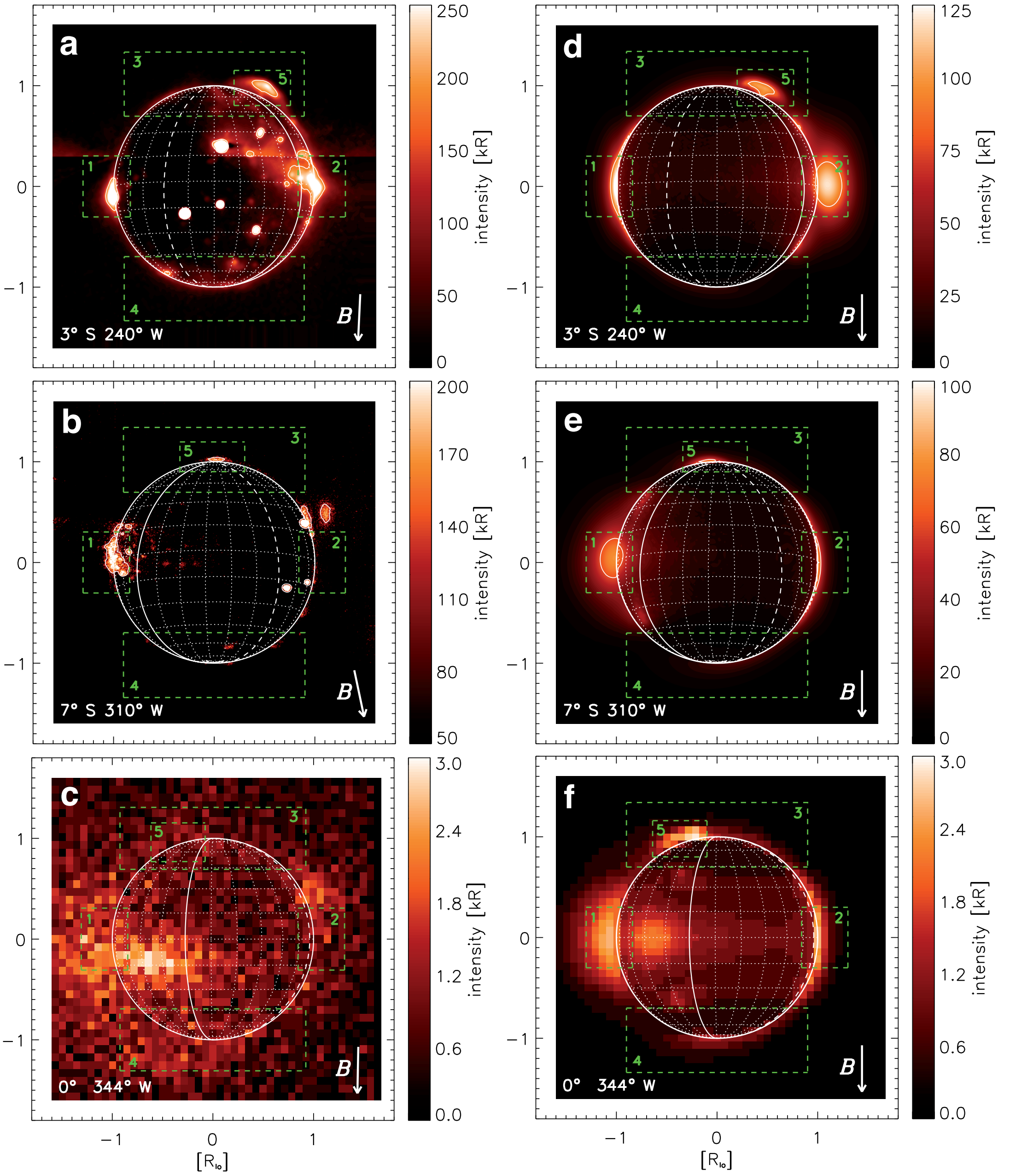

Figure 5.2: Aurora observations and the respective simulated emission patterns. Technical characteristics of the New Horizons LORRI observations of Ieclipse04 (a) and Ieclipse03 (b) and the HST ACS Ieclipse03 image (c) are listed in Table 3.3 in Section 3.4. The displayed LORRI images have undergone some corrections to remove blemish emission. The corresponding simulated emission morphologies (d, e and f) are displayed with the respective viewing geometry. The color scale and the contour lines differ by a factor of 2 between observation and simulation for the LORRI images. Contours are 150 kR (a), 100 kR (b), 75 kR (d) and 50 kR (e). Note that the HST ACS observation (c) covers wavelengths from 1250 – 1900 Å, whereas the corresponding simulation (f) takes into account only emission from OI] 1356 Å and SI 1479 Å. The orbital trailing (270°) longitudes are indicated with dashed meridians, the sub-Jovian (0°) and anti-Jovian (180°) meridians are displayed in plain bold. The emission within the green framed areas is investigated quantitatively. The total and relative intensities of the boxes are shown in Table 5.4.

5.2 Numerical simulation

5.2.1 Plasma model

The coordinate system of the simulation corresponds principally to the IPhiO system, i.e., the plasma flow v_0 is parallel to x and y points towards Jupiter. The magnetic field, however, is constant and always anti-parallel to the z-axis. Thus, we do not take into account the inclination and rocking of the magnetic field due to the tilt of the Jovian dipole field axis with respect to the rotation axis. The model geometry is depicted at the left edge of Figure 5.1.

The general simulation approach and the basics equations of the model are described in Section 2.1.3. In the following section we explain the treatment of the two plasma parameters, which are essential for aurora simulation: the density and temperature of the electrons. The equations of the temperature and density evolution are adapted from Equations (4) and (16) of *Saur et al.* (1999), but slightly modified. The evolution of the electron density n_e is described by the following continuity equation:

$$\frac{d}{dt}n_e = f_{ion}\, n_e n_{SO_2} + k_{hee}\, n_{SO_2} - \alpha n_e^2 \quad . \tag{5.1}$$

The first term on the right hand side describes single ionization by electron impact on neutral gas n_{SO_2} due to thermal electrons with the temperature dependent collisional ionization rate f_{ion}. With the second term we account for ionization by kappa-distributed energetic bidirectional electrons (k_{hee}) observed in Io's vicinity (e.g., *Williams et al.* 1999). The electron energies in the beams span the range from keV to hundreds of keV (*Williams et al.* 1996, *Frank and Paterson* 2002). According to the simulated electron beam morphology by *Jacobsen et al.* (2010) and the observations during various Galileo flybys (*Williams and Thorne* 2003, *Frank and Paterson* 2002) we assume a spatial distribution of the high energetic electrons given by

$$f_{hee} = f_{hee,0}\left[\tanh(3x+1)+1\right]\exp\left(-10y^6\right)c(x,y) \tag{5.2}$$

with

$$\begin{aligned} c &= 1 \quad \text{for} \quad x^2+y^2 > 1\,\mathrm{R_{Io}} \\ c &= 0.5 \quad \text{for} \quad x^2+y^2 \leq 1\,\mathrm{R_{Io}} \quad . \end{aligned} \tag{5.3}$$

Thus, the beams are assumed to be relatively narrow (width in y-direction: ~1.4 R_{Io}) but to extend far into the wake. However, outside the atmosphere (e.g., in the far wake), where the neutral density vanishes, no ionization can take place anyway. Using the geometrical factor $c(x,y)$ we take into account that directly above (below) Io the electron beam from the south (north) is shielded by the satellite. For the energy flux we use the derived value by *Saur et al.* (2002). We note that Expression (5.2) is derived from observations and models for a dense sunlit atmosphere. The formation of the beams possibly changes in eclipse, but has not been observed yet. The third term on the RHS of equation (5.1) describes the loss due to recombination with a rate α. For the adopted parameter values we refer the reader to *Saur et al.* (1999, 2002). The photo-ionization terms of Equation (4) of *Saur et al.* (1999) are omitted in eclipse.

As the electron velocity in the *Saur* model (Equation 2.12) is simply given by the $\mathbf{E}\times\mathbf{B}$-drift, there is no plasma movement along $\mathbf{B}$ included. But, in fact plasma transport along $\mathbf{B}$ does occur, particularly in the wake of Io. The only electron source in the wake is the newly ionized population through the electron beams. For a low density atmosphere as expected in eclipse the ionization by electron beams is mainly confined to the region close to the equator, where the atmosphere is densest. Altogether, the wake region will be rather void, if movement along **B** is neglected. However, parallel movement due to the pressure gradient in the wake of Io possibly fills the relatively void regions in the downstream area and might thus enhance the aurora in the downstream region. To account for the parallel movement, we modified the model assuming that the plasma particles move along **B** with thermal velocity v_{th}.

The total time derivative on the left hand side of (5.1) can be written as the partial time derivative and the convective term $\mathbf{v}_e \nabla n_e$. By separating the flow in the xy-plane from the movement along z,

$$\mathbf{v}_e \nabla n_e = \mathbf{v}_\perp \nabla_\perp n_e + \mathbf{v}_z \frac{\partial}{\partial z} n_e \quad , \tag{5.4}$$

we rewrite the continuity equation as

$$\mathbf{v}_e(x,y) \nabla_\perp n_e = f_{ion}\, n_e n_{SO_2} + k_{hee}\, n_{SO_2} - \alpha n_e^2 - v_{th} \frac{\partial}{\partial z} n_e \quad , \tag{5.5}$$

$\mathbf{v}_\perp$ is the electron flow $\mathbf{v}_e(x,y)$ and the parallel flow along z is approximated by the thermal velocity v_{th}. Thus, following the 2D electron flow $\mathbf{v}_e(x,y)$ a parallel flow as loss or production term depending on the density gradient along z is calculated. Numerically, we consider the net flow from or to both the grid cell above and below the current position. The flow direction is determined by the sign of the respective electron density gradient between the cells. This description is somewhat similar to a diffusive process. The thermal parallel velocity v_{th} is assumed to be the ion sound speed, as the inertia of the ions mainly determines the movement of the plasma. The ion sound speed is approximately half of the undisturbed relative flow velocity of the plasma, so the flow fills the wake at an angle of approximately $\arcsin\left[v_{th}/v_e(x,y)\right] \geq 30^\circ$. The propagation along $\mathbf{B}_0$ enables the plasma to fill the wake of Io, which is important to explain the observed auroral emission in the downstream region. Expanding into low density regions such as Io's wake the plasma can be accelerated to velocities higher than the thermal velocity (*Samir et al.* 1983). By the assumption of a parallel movement with v_{th}, the propagation speed into the wake might thus be underestimated.

The second important plasma quantity for aurora simulation is the thermal energy or temperature of the electrons, T_e. The temperature evolution in our model is given by

$$\frac{3}{2} k_B n_e \frac{dT_e}{dt} = -\left(\mathfrak{L}_c(T_e) + \frac{3}{2} k_B T_e f_{ion}(T_e) \right) n_e n_{SO_2} - \frac{3}{2} k_B T_e k_{hee}\, n_{SO_2} - \frac{\partial}{\partial z_B} Q_{flux} \quad . \tag{5.6}$$

$\mathfrak{L}_c(T_e)$ accounts for cooling by inelastic collisions between the magnetospheric electrons and the atmosphere, including ionization, dissociation, and rotational and vibrational excitation of neutral SO_2, see Equation (4.82). The newly added electrons resulting from impact ionization by the thermal electrons as well as by the electron beams with ionization frequency k_{hee} are assumed to be cold. The adjustment to magnetospheric bulk temperature of these cold electrons leads to a decrease in temperature of the hot (magnetospheric) electrons. The heat flux Q_{flux} is parametrized as described in the following paragraph.

Taking advantage of the anisotropy of the thermal conductivity we assume no heat flow perpendicular to **B**. The parallel conductivity is parametrized based on the approximation derived in Section 4.4.1. We consider the electrons in a flux tube along **B** outside the atmosphere to adjust to one common temperature T_e^{out} instantaneously. When the flux tube passes through the atmosphere, we

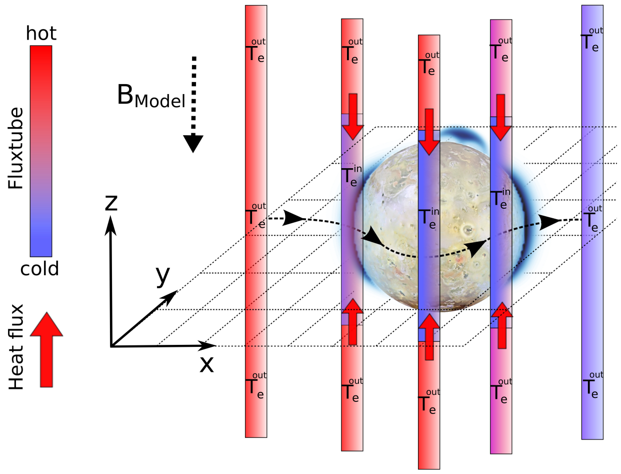

Figure 5.3: *Evolution of the electron temperature in the simulation model. The flux tubes are convected through the Io's interaction region given by the 2D electron flow profile in the xy-plane. The heat conduction perpendicular to* **B** *is neglected, the heat conduction parallel to* **B** *is infinite outside the atmosphere. Inside the atmosphere the plasma cools down to* T_e^{in} *and the heat flow from outside (*T_e^{out}*) is limited due to a finite heat conductivity along* **B**. *The heat flow from the outer tube part to the inner is parametrized and depends on the temperature gradient between the two parts (*$\sim (T_e^{out} - T_e^{in})/H_{hc}$*).*

divide it in three parts, two outer parts with temperature $T_e^{out}$and an inner part with temperature T_e^{in} as illustrated in Figure 5.3. The inner part uniformly cools down due to the various collision processes described in equation 5.6. For a temperature difference between the inner and outer parts $\Delta T_e = T_e^{out} - T_e^{in}$ a typical heat flow is calculated using Equation (4.84). As described, the average heat transport is controlled by a typical distance H_{hc}, which is set to the scale height of the atmosphere of 100 km. The heat conductivity κ_{hc} is given in Equation (4.80) depending on the local temperature T_e^{in}, and the quotient of the electron and neutral density. The temperature in the outer part T_e^{out} decreases due to the heat flow to the cooler inner part, i.e., the outer parts serve as finite heat reservoirs and the energy of the entire flux tube is depleted. The heat flow from the hotter outer part to the inner part Q_{flux} is sketched in Figure 5.3.

5.2.2 Atmosphere model

Based on the distribution given in Equation (4.59), we assume a dense atmospheric ring ranging from the equator to approximately 35° north and south. At higher latitude a low density background n_{bg} is assumed, with a ratio of $n_{bg}/n_{eq} = 0.02$ for SO_2. Additionally, we want to investigate longitudinal asymmetries, such as the observed difference between sub- and anti-Jovian hemispheres (e.g., *Spencer et al.* 2005) as well as a denser downstream atmosphere as inferred by *Saur et al.* (2002). The surface density n_s for the neutral species s is thus modeled by

$$n_s(\vartheta, \varphi) = n_{bg} + \left(n_{eq} - n_{bg}\right)\left(1 + \beta \cos(\varphi - \gamma)\right) \exp\left[-\left(\frac{\vartheta}{35^\circ}\right)^6\right] \quad , \qquad (5.7)$$

with the latitude ϑ and west longitude φ. n_{eq} is the surface density at the equator, β and γ specify the strength and orientation of the longitudinal inhomogeneity and are fitted to the observations. The density declines exponentially with increasing altitude. The vertical structure is determined by the scale height H_s. We assume the scale height to vary with φ according to the longitudinal variation of the surface density:

$$H_s(\varphi) = H_{s,0}\left(1 + \beta\cos(\varphi - \gamma)\right). \tag{5.8}$$

The simultaneous variation of scale height and surface temperature allows an implementation of a larger difference in column density between two hemispheres with smaller local gradients than choosing a strongly varying surface density at a constant scale height. When the local density gradients are too large, the numerical simulation becomes unstable.

For modeling the plasma interaction, we assume the atmosphere to consist solely of SO_2. The surface scale height $H_{s,0}$ in Equation (5.8) for SO_2 is set to 100 km. As discussed in Chapter 4.2, the actual scale height of SO_2 is expected to be significantly lower with values of $\sim$10 km at the surface. However, since the perturbed electric field is calculated with the integrated conductivities (see Section 2.1.3), the interaction strength depends rather on the total neutral gas abundance than on the exact distribution of the atmosphere. At high altitudes, the implemented scale height is roughly in agreement with actual values. Thus, a scale height of 100 km represents an average scale height for Io's atmosphere and the interaction strength still constraints the global column density, since the crucial parameter for the interaction is the total atmospheric gas content.

The longitudinal distribution of the equatorial atmosphere in eclipse, which is modeled here, does not necessarily correspond to the longitudinal distribution at daytime seen around a full Io orbit. The fractional atmospheric collapse might vary with longitude due to different atmosphere and surface conditions or the position of the observer and the sun. For instance, the atmosphere may respond differently on the sub-Jupiter hemisphere, which is sunlit before eclipse ingress, than on the anti-Jovian hemisphere, which is at night for several hours already before eclipse.

As the LORRI observations revealed a bright volcanic plume close to the north pole, we additionally implement a plume shaped density enhancement located at the Tvashtar paterae at 62°N and 122°W. The neutral gas distribution of the plume is given by

$$\begin{aligned} n_{plume}(h,d) = & n_{plume,0}\left\{ \exp\left(-\left[\left(\frac{h}{H_V}\right)^2 + \left(\frac{d}{D_V}\right)^2 \right]^3 \right) \right. \\ & - \exp\left(-\left[\left(\frac{h}{0.4H_V}\right)^2 + \left(\frac{d-d_0}{0.4D_V}\right)^{\frac{3}{2}} \right]^3 \right) \\ & \left. + 30\exp\left(-\left[\left(\frac{h}{0.1H_V}\right)^2 + \left(\frac{d}{0.05D_V}\right)^2 \right]^3 \right) \right\} \quad , \end{aligned} \tag{5.9}$$

where $n_{plume,0}$ is the density in the center of Tvashtar, h the vertical distance from surface and d the horizontal distance on the surface to the plume center. The height and width are set to $H_V = 360$ km and $D_V = 550$ km according to the estimated plume extent (*Spencer et al.* 2007a). The subtracted exponential function in the second line of (5.9) roughly describes the expected low density region within the plume after *Zhang et al.* (2003). We also include a high density region above the vent by adding the term in third line of (5.9). The plume model of *Zhang et al.* (2003)

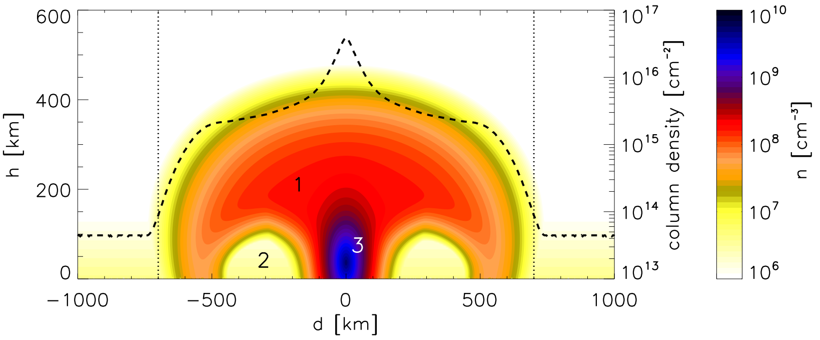

Figure 5.4: *The density distribution model for the Tvashtar plume for the derived number density* $n_{plume,0}$ *displayed in a vertical plane through the center. The local neutral gas density is color-coded, the dashed line represents the derived vertical column density above the plume. The plume density is given by Equation* (5.9) *and consists of three components: (1) the main plume, (2) a low density ring as found by ballistic models and (3) a high density region above the crater. The shape replicates roughly the modeled Pele-like plume by Zhang et al. (2003) with a peak column density over the plume center and a shallow decrease of the column density from ∼200 to ∼500 km distance from the center. The plume-averaged column density is determined within a distance to the plume center of <700 km (dotted vertical lines).*

also indicates the formation of a canopy shock, which we do not account for in our simulation. $n_{plume,0}$ is the only free parameter of the plume. The three plume regions are marked in Figure 5.4, where a cross section through the volcano density and the column density above the plume are shown.

While for the interaction simulation only collisions with SO_2 are taken into account, the auroral emission is modeled individually for O, S, Na and K using the simulated electron temperature and density. Thereby, we derive mixing ratios n_{comp}/n_{total} for these atmospheric components. For the simulation of the LORRI images the mixing ratio of the species is assumed to be identical in the equatorial atmosphere and in the plume. For atomic sulfur and oxygen the radial decrease is smaller than for SO_2 (e.g., *Summers and Strobel* 1996). The Cassini observations of *Geissler et al.* (2004) revealed O assigned emission at higher surface distances than the emission assigned to SO_2, see Figure 2.11(right). This indicates a shallower decrease of O compared to SO_2. For atomic sodium, HST observations of the NaI 5890 Å line revealed a very shallow drop-off with increasing height (*Retherford* 2002). Therefore, we assume a slightly larger scale height for these constituents of $H_{s,0}(\mathrm{X}) > H_{s,0}(\mathrm{SO_2})$ (see Table 5.3). Moreover, we assume a higher n_{bg}/n_{eq} ratio for atomic species, as the Cassini observations (*Geissler et al.* 2004) reveal considerably stronger northern and southern limb glow for the emission that is attributed to excitation of atomic species.

5.2.3 Emission simulation

Assuming equilibrium, the local intensity of the stimulated emission of an atmospheric gas is calculated by Equation (3.14). In case of Na and K, re-absorption in the atmosphere is taken into account. All other emission lines are assumed to be optically thin for a reduced atmospheric density in eclipse, i.e., the brightness is just given by an integration along the line of sight over the local emission. Due to the long lifetime or small radiative decay rate of $k_d = 0.00681\ \mathrm{s}^{-1}$ of the $\mathrm{O}(^1D)$ state, we include collisional quenching at low altitudes for the OI 6300/6364 Å emission.

The lowered intensity I is calculated with the Stern-Vollmer relationship

$$I = I_0 \frac{k_d}{k_d + k_q} \tag{5.10}$$

where k_q is the quenching rate and I_0 the intensity without quenching. For k_q we use the estimated value of 1×10^{-10} cm^{3}s^{-1} from *Geissler et al.* (2004). Quenching and radiative decay are equally probable when the SO_2 number density is 6.8×10^7 cm^{-3}.

The LORRI observations cover wavelengths from 3500 to 8500 Å (see Section 3.4) . Within this range emission from SO_2 bands and S_2 bands as well as from atomic oxygen (5577 Å, 6300 Å, 6364 Å, 7774 Å and 8446 Å), atomic sulfur (7725 Å), atomic sodium (5889/5896 Å) and potassium (7670 Å) are expected. The OI 7774 Å and OI 8446 Å lines contribute less than 1% to the total emission (*Geissler et al.* 2004) and are neglected. The electron impact excitation cross sections for OI 5577 Å and OI 6300/6364 Å are based on the laboratory measurements of *Doering and Gulcicek* (1989a,b) and *Doering* (1992). The cross sections for the sodium and potassium D lines were adopted from theoretical calculations by *Kim* (2001). For further details on the cross sections and the associated rates see *Geissler et al.* (2004) and references therein. Cross sections for electron excitation of S_2 are not measured, so we can only estimate the contribution of S_2 emission roughly.

A large number of emission lines can be found in the pass-band of the HST ACS (1250 – 1900 Å) observation, such as emission from atomic oxygen and sulfur as well as from sulfur ions (*Ballester et al.* 1987, *Roesler et al.* 1999) and also chlorine emission (*Feaga et al.* 2004). Since cross sections are not available for all of the lines, we solely analyze the oxygen multiplet at 1356 Å and the sulfur multiplet at 1479 Å, which presumably contribute most. Neglecting all the lower emissions in the pass-band, we can not compare the emission quantitatively with the ACS observation. A quantitative comparison also would necessitate an accurate analysis of optical depth of various lines (see Section 4.1 and *Feaga et al.* 2002). However, by simulating the OI] 1356 Å and SI 1479 Å emission we are able to compare the model results to the ACS observation regarding the morphology and the relative intensities of the individually analyzed areas, since oxygen and sulfur generally are by far the main contributors in the observed wavelength range. For the used oxygen and sulfur excitation rates in the UV range see Section 4.1.

5.2.4 Simulation setup

A constant magnetic field is the basic assumption of the theoretical approach, it is not possible to fully consider the varying plasma conditions in the simulation. Moreover, the model is symmetric with respect to the xy-plane at $z = 0$. For the implementation of the volcanic plume on the north pole, we run simulations with and without plume and combine the results. The influence of the plume on the aurora in the equator region turns out to be negligible ($< 1\%$). Note, the asymmetry of Io's atmosphere due to Tvashtar near Io's north pole generates also a small asymmetry in Io's plasma interaction. However, due to the small spatial extend of the plume compared to Io's diameter and the relative amount of the plume gas compared to the total gas of Io's atmosphere, the asymmetry in the plasma interaction is negligible.

The actual plasma environment varies during a synodic rotation of Jupiter. The angle between the undisturbed plasma flow and the plane perpendicular to $\mathbf{B}_0$ varies only within -3° and 3°, which is negligible. The tilt of the magnetic field with respect to the polar axis of Io is sometimes as large

Table 5.3: *Best-fit parameters of the model atmosphere.*

Atmosp. Species	Equ. surface mixing ratio	*Geissler et al.*, 2004	Sc.height H (km)	backgr. n_{bg}/n_{eq}	Long.asym. γ , β	Vert. col. dens.(cm^{-2}) upstream	downstr.	Tang.col.dens. (cm^{-2})
All	100 %	-	-	-	90° , 1/3	1.0×10^{15}	4.0×10^{15}	1.8×10^{16}
SO_2	80 %	82 %	100	0.02	90° , 1/3	8.0×10^{14}	3.3×10^{15}	1.5×10^{16}
O	12 %	5 %	150	0.15	90° , 1/3	1.8×10^{14}	7.3×10^{14}	3.2×10^{15}
S	1.5−3.0 %	2.5 %	150	0.15	90° , 1/3	1.9×10^{13}	7.8×10^{13}	4.1×10^{14}
Na	0.12 %	0.12 %	150	0.5	90° , 1/3	1.8×10^{12}	7.3×10^{12}	6.5×10^{13}
K	0.04 %	0.036 %	150	0.5	90° , 1/3	6.0×10^{11}	2.4×10^{12}	1.1×10^{13}
S_2,O_2,SO	∼5%	∼10%						
	Height h (km)		Width σ (km)		Av. col. dens. (cm^{-2})		Max. col. dens. (cm^{-2})	
Tvashtar	360		1100		5×10^{15}		3×10^{16}	

as 20° during a rotation period. Due to the symmetry of the model with respect to the equatorial plane, which is always assumed to be perpendicular to the background field, we are not able to investigate a tilt between the atmospheric ring and the orbital plane. To minimize the effect of the simplified model geometry, we compare the simulated aurora intensities in larger areas around the equatorial spots and the Tvashtar region with the observed intensities. The variation of the torus electron density in the upstream plasma is, nonetheless, included. For the Ieclipse03 simulation, where Io is far from the torus center we assume a lower density of $n_e = 1900$ cm^{-3}, while during Ieclipse04, where Io crosses the torus center, the electron density is presumably higher and we use $n_e = 3600$ cm^{-3}. The electron temperature of the upstream plasma is $k_B T_{e,0} = 5$ eV. For the initial velocity we assume the relative azimuthal velocity of the rotating plasma $v_0 = 57$ km s^{-1}, the background field is set to $B_0 = 2050$ nT.

5.3 Results of the aurora simulation

By varying the equatorial SO_2 surface density, we first derive the total gas content of the atmosphere and its distribution. Thereafter, we fit the mixing ratios and spatial distributions of atomic oxygen and sulfur as well as the trace elements sodium and potassium to the previously observed intensities as well as the morphology in the LORRI and ACS images. Both, emission from the excited atomic species and from excitation of SO_2 contribute to the intensity and morphology of the LORRI simulations, so the derivation of the abundances for SO_2 and those of the minor components are correlated to each other. Therefore, we obtain the best-fit atmosphere results from an iterative variation of both the total gas content and the mixing ratios of the minor species. Finally, we constrain the gas content of the Tvashtar plume.

5.3.1 Equatorial atmosphere

The main benchmark for constraining the density of the atmospheric ring is the morphology and location of the equatorial spots. We assume the same longitudinal variations for SO_2 and the minor components. First, we analyze the brightness of the equatorial spots in the LORRI observations. In the LORRI Ieclipse04 observation (Figure 5.2 a) the ratio of the anti-Jovian to the sub-Jovian spot brightness is $I_{anti}/I_{sub} = 1.8$. For LORRI Ieclipse03 (Figure 5.2 b) the anti-Jovian spot can not be identified clearly. The spot might be displaced towards the East Girru feature. The ratio for the equator boxes is $I_{anti}/I_{sub} = 0.2$. The morphology is in best agreement with both observations for a model atmosphere with an average equatorial column density of $N_{eq,av} = 2.3\times10^{15}$ cm^{-2}.

Table 5.4: *Comparison between the emission intensities of the observations (Figures 5.2 a-c) and the simulation results (Figures 5.2 d-f) . Absolute intensities are given in kR. The measured and calculated intensities of the framed regions are all normalized to the box areas, the total intensity is normalized to the area of Io's disk. The numbers in parentheses (1-5) refer to the green box numbers.*

	Figure	Total	Equ. spots		Ratio	North		South		Tvashtar	
		I_{tot}	$I_{sub}(1)$	$I_{anti}(2)$	I_{anti}/I_{sub}	$I_N(3)$	I_N/I_{tot}	$I_S(4)$	I_S/I_{tot}	$I_t(5)$	I_T/I_{tot}
Observation											
LORRI Iecl04	5.2 a	62.6	53.6	97.3	**1.8**	21.3	**0.3**	20.5	**0.3**	62.6	**1.0**
LORRI Iecl03	5.2 b	40.9	70.6	22.2	**0.3**	6.5	**0.2**	11.2	**0.3**	12.1	**0.3**
HST ACS Iecl03	5.2c	1.8	0.7[a]	1.6[a]	**0.4**	0.58[a]	**0.4**	0.7[a]	**0.4**	0.7[a]	**0.4**
Simulation											
LORRI Iecl04	5.2 d	29.0	29.3	60.4	**2.1**	9.1	**0.3**	5.2	**0.2**	23.6	**0.9**
LORRI Iecl03	5.2 e	17.1	38.2	13.7	**0.4**	4.0	**0.2**	3.1	**0.1**	8.9	**0.5**
HST ACS Iecl03	5.2 f	1.4	0.9[a]	1.9[a]	**0.5**	0.4[a]	**0.3**	0.3[a]	**0.2**	1.1[a]	**0.8**

[a] Direct comparison of absolute intensities of the HST ACS observations with the simulation is limited, since the simulation does not take into account all emission lines in the observed wavelength range. The SI 1479 Å emission is assumed to be optically thin, although the line strengths clearly indicate re-absorption (*Feaga et al.* 2002).

The asymmetry parameters are fitted to $\beta = \frac{1}{3}$ and $\gamma = 90°$ (Eq. 5.7 and 5.8) indicating a longitudinal asymmetry in favor of the downstream side. The column density on the upstream side is thus $N_{eq,up} = 1.0 \times 10^{15}$ cm^{-2}, the downstream column density is $N_{eq,down} = 4.0 \times 10^{15}$ cm^{-2}. The simulated aurora morphologies corresponding to the LORRI images are displayed in Figures 5.2 d and 5.2 e, where the brightness ratios are $I_{anti}/I_{sub} = 2.1$ (Ieclipse04) and $I_{anti}/I_{sub} = 0.4$ (Ieclipse03). The derived atmospheric distribution also yields a morphology that is in good agreement with the HST Ieclipse03 observation on the sub-Jovian side. The derived eclipse column density corresponds to $\sim 10\%$ of the column density for a sunlit atmosphere of $N_{sun} = (1\text{–}5) \times 10^{16}$ cm^{-2} reported in the review paper of *Lellouch et al.* (2007). This day-side column density also coincides with the column densities derived by *Saur et al.* (2000) and *Saur et al.* (2002), where the same simulation model for a sunlit atmosphere interaction is applied. The parameters of the best-fit atmosphere are listed in Table 5.3. The resulting absolute simulated and measured intensities of the marked areas are listed in Table 5.4 for comparison. The relative intensities refer to the absolute values divided by the total intensity. Like in the previous chapter, the total intensity I_{tot} corresponds to the total measured emission in the images normalized to the area of Io's disk.

In order to illustrate the formation of the aurora morphology, we show results of the plasma interaction simulation for Ieclipse03 in Figure 5.5: the atmospheric electron temperature in the flux tubes (Figure 5.5 a), the electron density in the equatorial plane (Figure 5.5 b) and the electric current in the northern Alfvén wing (Figure 5.5 c). Due to the relatively low density in the equatorial atmosphere the energy stored in the flux tubes is sufficient to keep the electron temperature in most regions between 4 and 5 eV, and above 1 eV everywhere in the interaction region. The lowest temperature is found on the flanks, where the electron density is highest, see Figure 5.5 a. These high density regions in the anti- and sub-Jovian equatorial region (Figure 5.5 b) mainly control the position of the equatorial spots. The overall interaction strength is strongly decreased compared to the model results for a denser atmosphere (*Saur et al.* 1999). The average Pedersen conductance is on the order of only $\Sigma_P \approx 10$, whereas the Hall conductance is even lower $\Sigma_H \approx 1$. The interaction parameter is therefore considerably higher at $\alpha_{Io} = 0.5 - 0.7$, i.e., more than five times higher than for a dense atmosphere. Hence, the deflection of the plasma is clearly lower and the plasma flow almost symmetric with respect to the x-axis. The low atmospheric density and the gas plume around Tvashtar also cause a complex current pattern in the Alfvén wing, see Figure 5.5 c.

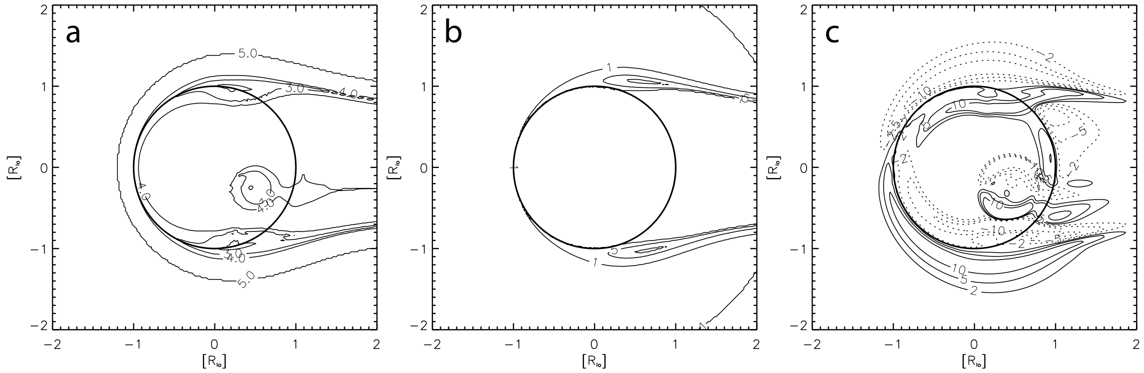

Figure 5.5: Results of the plasma interaction simulation: (a) Electron temperature profile within the atmosphere (xy-plane). Isolines for 1 to 5 eV. (b) Electron density in units of torus density (1900 cm^{-3}) in the xy-plane at $z = 0$. (c) Isolines of electric currents in 10^{-7} A m^{-2} in the northern Alfvén wing.

In addition to the usual current system in the northern wing, i.e., sub-Jovian downward and anti-Jovian upward currents, contrarily oriented currents evolve on both sides within the outer usual system. Because of the low neutral density around the poles and the overall low atmospheric density, only on the flanks a dense ionosphere forms. Consequently, the current system is inhomogeneously short-circuited in the atmosphere. Two separate current systems form on the anti- and sub-Jovian hemisphere, respectively. Furthermore, a small *winglet* is generated around the plume of the Tvashtar volcano, which we further discuss in Section 5.3.3. Simulation results for a similar model setup but a dense global atmosphere with a neutral column density of $N = 6 \times 10^{16}$ cm^{-3} can be found in *Saur et al.* (1999).

Assuming a longitudinal asymmetry with a higher and denser atmosphere on the anti-Jovian hemisphere, as inferred for the day-side atmosphere (*Jessup et al.* 2004, *Spencer et al.* 2005, *Feaga et al.* 2009), yields a much stronger anti-Jovian spot. This would imply clear visibility of the spot during Ieclipse03 in Figure 5.2 b, where no emission on the anti-Jovian limb is detected except for the East Girru region. Furthermore, during Ieclipse04 the anti-Jovian spot would be brighter and at a considerably higher altitude above the surface than the sub-Jovian in the LORRI observation (Figure5.2 a). As the anti-Jovian emission maximum is only slightly higher and very close to the limb, there is no indication for an atmospheric anti-sub-Jovian asymmetry in eclipse. The non-appearance of an atmospheric bulge on the anti-Jupiter side could be explained by the fact that it is nighttime on the anti-Jovian hemisphere before eclipse ingress. The response of the atmosphere to a 21-h night compared to a 2-h eclipse event is likely to be different and the anti-Jovian atmospheric bulge might be reduced due to that.

Instead, the simulation results imply a longitudinal asymmetry of the atmosphere with increasing scale height and surface density from upstream to downstream. Compared to a longitudinally symmetric distribution, the emission is shifted downstream, which leads to a lower intensity on the upstream hemisphere and increasing intensity in the wake. The simulation still predicts more radiation to be emitted on the upstream than on the downstream side, although the downstream emission is more located and thus peaks higher. The observing geometry of the LORRI observations does not allow a separation of emission from the two hemispheres, but the emission appears to be brighter in the downstream region. However, larger datasets containing a range of exposures observing both upstream and downstream generally confirm a higher emission on the upstream hemisphere (*Oliversen et al.* 2001) in agreement with our simulation results.

The simulated ACS aurora image (Figure 5.2 f) is adjusted to the spatial resolution of the observation and convolved with the ACS PSF, see Appendix A.5. In the ACS observation (Figure 5.2 c) on the upstream hemisphere (right limb) aurora is observable only around East Girru, the corresponding simulation yields clear emission on the limb of the upstream equatorial side. In this region the fluid approach and the assumption of a constant background field might not describe the behavior of the electrons in the upstream region with the required accuracy. A highly distorted and piled up magnetic field in this region may hinder the electrons to move along **B** into the atmosphere near the equator. The electrons with pitch angles close to 90° are reflected when the magnetic field increases and they do not reach thicker atmosphere layers. *Moore et al.* (2010) obtained this effect in their particle simulation. However, flux tubes with large **B** due to the upstream pile up have a smaller cross section close to Io. As these flux tubes are connected to a larger cross section further away from Io, a smaller area is linked to a larger energy reservoir. The combination of the both effects require further investigation with kinetic models. In the downstream region, the large cavity behind Io may lead to a faster filling of the wake than we assumed. This would cause higher emission in the wake. Nonetheless, the position and size of the sub-Jovian spot and the wake feature are in good agreement for the simulation and the HST ACS observation (Figures 5.2 c and 5.2 f). The so-called wake feature is composed of two constituents. First, the tail of the spots can contribute to what is observed as wake emission, depending on the exact viewing geometry. Additionally, emission that is stimulated by electrons, which emerge from ionization by highly energetic beams directly behind Io. In our simulation the contribution from the flanks is stronger in agreement with the results from the phenomenological aurora model.

Choosing a hypothetical viewing geometry, where the observer is located above the north pole, we can measure the height of the maximum emission on the flanks above the limb in our simulated aurora distribution. Depending on the emitting species and the density of the upstream electrons, the local emission peaks at altitudes between ∼150 km and ∼300 km with our best-fit atmosphere. The results of the phenomenological model indicate that the spots in fact arise very close to surface. The obtained simulated altitudes are likely to be an effect of the implemented atmospheric scale height of 100 km, which overestimates the actual scale height at the surface by factor of 10.

The observed overall aurora brightness is $I_{tot} = 40.9$ kR in the LORRI Ieclipse03 image and $I_{tot} = 62.6$ kR during Ieclipse04. The varying intensity is in agreement with the changes of the upstream torus density. The intensity ratio of the simulated emission of the LORRI images is similar. In both cases the modeled intensity differs from the observed one by a factor of ∼2, i.e., $I_{obs}/I_{sim} \approx 2$. Some of the measured and calculated excitation cross sections are subject to large uncertainties (*Darrell Strobel, personal communication*) leading to a large uncertainty in the calculated total intensity. Another possible reason for the discrepancy of simulation and observation are additional emitters in the wavelength range of the LORRI pass-band, which we do not account for in the simulation. Emission from S_2 is expected at near-UV and blue visible wavelengths (*Geissler et al.* 2004), but not simulated due to the lack of exact electron impact cross sections. In recent HST observations *Trafton et al.* (2012) detected unidentified emissions between 4100 Å and 5700 Å, which they attribute to vibronic bands of SO_2 or other molecules. These emissions are also not included in the simulation. In the Ieclipse03 LORRI image thermal emission around volcanic hot spots clearly contributes to the observed radiation, but is not simulated. Besides from these physical reasons, systematic uncertainties in the LORRI images might be large due to difficulties when compiling several exposures. Systematic errors such as copious instrument scattered light might also lead to an under- or overestimation of the brightness.

5.3.2 Minor atmospheric constituents

Since the LORRI observations do not spectrally resolve the emission, we compare our simulation results with a range of spectral observations of various emission lines resulting from oxygen, sulfur, sodium and potassium to constrain the abundance of these species. We are aware of the limitations of using observations made by different telescopes or cameras at different times, as for example long term variations and differing signal-to-noise ratios. But still, the measured intensities of the various observations differ not more than by a factor of 5 and are thus still a good way to derive abundances and check the derived atmospheric distribution.

We find that for a O/SO_2 mixing ratio of 12% at the surface and a surface scale height of 150 km, the simulated intensity and morphology of the oxygen multiplets OI] 1356 Å and OI 6300 Å are in good agreement with the observations (*Retherford et al.* 2007a, *Retherford* 2002, *Bouchez et al.* 2000, *Geissler et al.* 1999, *Moore et al.* 2010). A comparison of the intensities for the analyzed emission lines can be found in Table 5.2. To derive a sulfur mixing ratio we use the most recent eclipse observation of the SI 1479 Å multiplet taken by the NH Alice spectrograph in 2007 as benchmark. The measurements revealed a varying total intensity during three eclipse events of $I = 0.4 - 1.2$ kR. Assuming a sulfur mixing ratio of 1.5% at the surface the model calculates a total intensity $I = 0.6 - 1.1$ kR. The intensity range in the model results is due to the varying upstream electron density and the variation of the viewing perspective. Although there have been no SI] 1900 Å observations in eclipse, a comparison of the sulfur intensities in sunlight indicates that a two times higher sulfur mixing ratio is needed to explain the SI] 1900 Å brightness. In case of the sodium emission we use the observed intensities in eclipse by *Retherford* (2002) and *Bouchez et al.* (2000) as reference. Compared to optically thin intensities the abundance of both Na and K need to be corrected by a factor of 3.5 and 3, respectively (*Geissler et al.* 2004). To achieve emission comparable to the observed intensities in the simulated sodium aurora an abundance of sodium bearing species of 0.12 % (at the surface) has to be implemented, assuming a surface scale height of 150 km. For potassium there are no direct measurements of K assigned emission lines in the close vicinity ($d < 1\,R_{io}$) of Io. Using the Na/K ratio of 3.3 derived from infrared filter observations at 6700 – 8500 Å by *Geissler et al.* (2004), which implies a K mixing ratio of 0.04%, the total intensity of the simulated KI 7670 Å emission line is $I = 2.2 - 4.3$ kR. This is clearly lower than the total intensity of the infrared filter observations (*Geissler et al.* 2004), which provide an upper limit of 10.7 kR.

All derived atmosphere parameters and the resulting equatorial column densities are summarized in Table 5.3. The higher scale height of atomic species is in agreement with atmospheric models (e.g., *Summers and Strobel* 1996). The higher polar mixing ratios for O, S, Na and K is derived from the observed limb glow and polar emission for the respective emitter. The compared total intensities for all four analyzed constituents are listed in Table 5.2.

5.3.3 Tvashtar plume

To constrain the plume density we analyze both the morphology and the intensity of the radiation inside the framed Tvashtar regions (Box 5) in Figure 5.2. During Ieclipse04 the whole plume of Tvashtar was in the field of view of LORRI. The plume is radiating rather uniformly with a maximum intensity in the plume center ~220 km above the limb. The simulated absolute flux inside the framed volcano region, $I_{Tvashtar}$, is half of the observed flux from this region. Since for Ieclipse04 the simulated total intensity I_{tot} also differs approximately by factor of 2 from the observation, we compared the ratio $I_{Tvashtar}/I_{tot}$ with our simulation results. For Ieclipse04 the averaged emission intensity inside the Tvashtar region is almost equal to the disk-averaged total intensity, i.e., the ratio is $I_{Tvashtar}/I_{tot} = 1.0$. Assuming a gas density of $n_{plume,0} = 1.7 \times 10^8$ cm^{-3} in the main plume or an average column density of $N_{plume} = 5 \times 10^{15}$ cm^{-2} over the plume region the modeled plume aurora is in good agreement with the measurements, where $I_{Tvashtar}/I_{tot} = 0.9$, see also Table 5.4. In the LORRI Ieclipse03 observation the upper edge of the glowing plume is visible just above the limb. The emission in the observation and simulated aurora match very well regarding the morphology and relative strength.

Interestingly, a small Alfvén wing is generated above Tvashtar due to the increased neutral and thus plasma density in the region. The upward and downward current are displayed in Figure 5.5 c. Nonetheless, with the derived plume density, the electrons are still able to excite emission all over the plume (Figure 5.2 d), since the plasma flow is deflected only moderately. The intensity maximum is found to be in the radial center at a limb distance of ~180 km and the plume emission appears to be rather uniformly. For a lower plume density of $N_{plume} < 3 \times 10^{15}$ cm^{-2} the total modeled emission is too weak. For both LORRI observations the intensity ratio of plume and disk-averaged emission would be lower than the observed ratio by at least a factor of 2. In the case of a higher plume density of $N_{plume} > 7 \times 10^{15}$ cm^{-2} the current system in and above the plume becomes stronger. This leads to a stronger deflection of the electron flow around the plume region. The electrons deposit energy mostly on the upstream side of such a dense plume and the simulated aurora appears non-uniformly with a clear maximum at the upstream edge. On the other hand, the plume averaged emission intensity hardly increases with increasing plume density. The energy deposited all over the plume is almost at maximum for our best-fit plume density $N_{plume} = 5 \times 10^{15}$ cm^{-2}, i.e., in the case of denser plume the intensity can hardly increase independently of the deflection of the incoming electrons.

Although the viewing angle of the HST ACS Ieclipse03 image allows the whole plume to be visible by HST, only a very weak UV emission enhancement of $I_{tvashtar}/I_{poles} \approx 1.2$ was observed in the expected region. With the derived column density of $N_{plume} = 5 \times 10^{15}$ cm^{-2}, our simulation predicts a ~3 times higher emission inside the Tvashtar region compared to the polar area around it. The pass-band of the HST observation includes mostly oxygen and sulfur emission lines. The lack of an emission enhancement around Tvashtar could indicate a low abundance of O and S in the plume. With 3 times lower abundances of atomic sulfur (~0.5%) and oxygen (~4%) within the plume the $I_{tvashtar}/I_{poles}$ ratio matches approximately the HST ACS observation.

As Tvashtar is considered a Pele-type plume (see Section 2.1.1), a high S_2 abundance is expected. Observations of the Tvashtar plume in scattered light and absorption by *Jessup and Spencer* (2008) revealed a spectral behavior that is consistent with previous observations of the Pele plume. For Pele various S_2/SO_2 ratios between ~1% and 30% have been obtained by *Jessup et al.* (2007). If dissociation of SO_2 and S_2 happens on time scales much larger than the average time of flight for the plume gas, the abundance of atomic sulfur and atomic oxygen in the plume will be lower than in an equatorial atmosphere, which is not solely of volcanic origin. *Moses et al.* (2002) show that the lifetimes for photolysis of SO_2 or S_2 producing S and O is in the range of hours, while ballistic flight times are on the order of 10 minutes. Using a thermodynamic model *Fegley and Zolotov* (2000) infer mixing ratios of atomic sulfur and oxygen to SO_2 and S_2 of the order of 10^{-2} and below. This implies a low abundance of S and O and would thus explain the low intensity in the UV range.

The local density for a cut through the best-fit plume for the LORRI observations and the vertical column density as a function of the distance to the plume center (d in Eq. (5.9)) are shown in Figure 5.4. Applying the model of a volcanic system developed by *Kieffer* (1982) and later adapted by *Strobel and Wolven* (2001) to the derived average column density of $N_{plume} = 5 \times 10^{15}$ cm^{-2} and the implemented plume size, Tvashtar appears to be a high temperature, low pressure volcano. The large size of the plume indicates relatively high particles velocities and thus a high temperature at the volcanic crater, which results from a high temperature ($T_0 \approx 800$ K) reservoir in the model system of *Kieffer* (1982). Our derived average column density is low compared to common plume models (e.g., *Zhang et al.* 2003) and would imply a low mean plume pressure of 0.1 nbar and correspond to the low pressure case, which principally corresponds to a small plume size, discussed in *Strobel and Wolven* (2001).

Measurements and model calculations (e.g., *McGrath et al.* 2000, *Zhang et al.* 2003) generally yield comparatively denser plumes for volcanoes close to the equator. Thus, our derived plume density and pressure appears to be relatively low. However, our method is hardly able to determine the plume density close to the surface accurately as the observed and simulated radiation is mostly emitted at a distance >50 km from the ground. A higher localized density at very low altitudes might also not influence the plasma interaction strongly. If the density below 50 km increased exponentially over the whole plume area with an atmospheric scale height on the order of tens of km, the plume column density would go up by at least a factor of 2.

The total content of the equatorial atmosphere, which we derived in Section 5.3.1, equals ∼10 times the total content of a volcanic plume with the plume density derived for Tvashtar. In other words, if we ruled out sublimation as possible atmospheric source, about 10 active volcanoes of the size of Tvashtar would be necessary to sustain the eclipse atmosphere. Pele-type plumes, such as Tvashtar, are the largest observed plumes and not more than 16 plumes have been observed at all (*Geissler and Goldstein* 2007). Therefore it is unlikely that an atmosphere of the derived column density can be sustained solely by direct volcanic outgassing in eclipse, but there has to be an essential amount of gas species that do not condense during eclipse. The atmospheric density in sunlight is approximately ten times higher (*Lellouch et al.* 2007) than our derived equatorial atmosphere, so there would have to be ∼50–100 Tvashtar-sized active volcanoes to create such a dense atmosphere without sublimation. Hence, direct volcanic outgassing is possibly able to sustain at least parts of the eclipse atmosphere, but cannot be considered as an essential source for the sunlit atmosphere.

5.4 Conclusions and comparison to the phenomenological model

We have modeled the auroral emissions from the atmosphere while Io is in eclipse of Jupiter and investigated the effect of various atmospheric distributions on the intensity and morphology of the aurora. Our model results imply an atmospheric column density of $N_{eclipse} = (1-4) \times 10^{15}$ cm^{-2}. This means, when Io moves into Jupiter's shadow, its atmospheric density decreases down to approximately 10% of the day side sunlit atmosphere, where column density is estimated to be $N_{sun} = (1-5) \times 10^{16}$ cm^{-2}. Despite the density decrease, the atmosphere presumably covers most of the surface around the equator up to ∼35 °N/S latitude. With a smooth atmospheric ring and a low density of 2% of the equatorial density at high latitudes we were able to reproduce the main features of the observed auroral emission. Independently of the exact location of active volcanoes, sub-Jovian and anti-Jovian bright spots arise due to the diverted plasma flow. The various observed spot morphologies primarily result from the respective viewing geometry of the

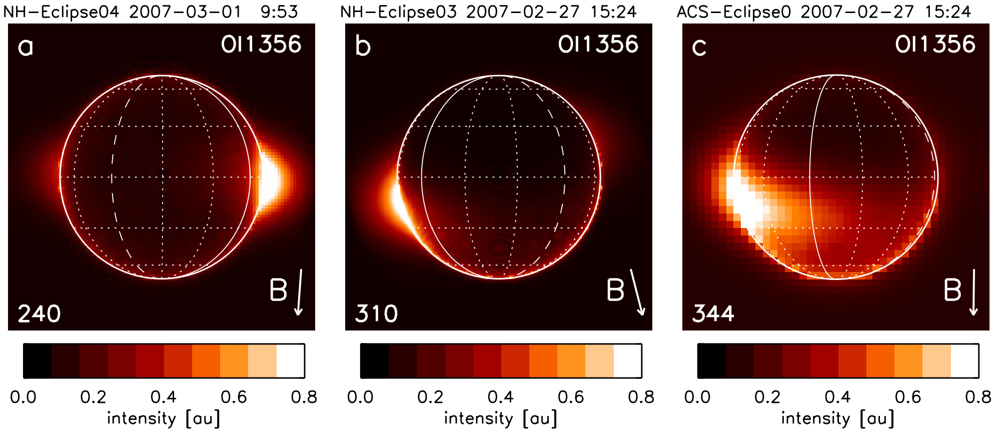

Figure 5.6: *Expected OI] 1356 Å morphology after the phenomenological model presented in Chapter 4 for the LORRI Ieclipse04 (a) and Ieclipse03 (b) observations and the ACS observation (c). The intensity is normalized, i.e., the intensity of the brightest pixel is 1. For visibility the maximum of the color-coded intensity is set to 0.8.*

observer and the resulting visibility of the aurora features, as demonstrated in Chapter 4. For the Tvashtar plume we find a column density of $N_{plume} = 5 \times 10^{15}$ cm^{-2}. This relatively low plume content also supports the idea of an atmosphere that is sustained almost solely by sublimation. If a larger number of plumes of the Tvashtar size were active in the last decades, they likely would have been observed already. So far, 16 mostly smaller plumes have been observed (*Geissler and Goldstein* 2007) and thus volcanic outgassing probably is not able to sustain a dense atmosphere as measured in sunlight. Compared to detailed atmospheric models (e.g., *Walker et al.* 2010), the inferred neutral distribution appears to be simplified. However, since the advantage of our model is the inclusion of the influence of a chosen atmospheric distribution on the plasma interaction and thus the deflection of the magnetospheric electrons, we did not consider the small scale variations of the equatorial atmosphere for numerical reasons but focused on the global structure.

Analyzing various spectrally resolved observations we derived mixing ratios for minor constituents in the atmosphere: 12% atomic oxygen, 1.5−3% atomic sulfur and 0.12% sodium. The derived mixing ratios and the resulting column densities are in general agreement with previous observations and model results (*Geissler et al.* 2004, *Wong and Smyth* 2000, *Summers and Strobel* 1996). The values for oxygen and sulfur are similar to the minimum mixing ratios estimated in Chapter 4. The S/O ratio is roughly 0.1−0.2 in agreement with the previously estimated abundances and the results of *Feaga et al.* (2004).

The simulation results are in principle in agreement with the outcome of the phenomenological aurora model implying a mainly sublimation-driven atmosphere. Even though the STIS eclipse images indicate a more drastic collapse of up to 99% of the atmosphere in shadow, the general decrease of neutral gas abundance is necessary to explain the STIS eclipse observations as well as to reproduce the observed morphology in the LORRI images. To compare the three dimensional distribution derived in Chapter 4 to the morphology in the LORRI and ACS observations, we have calculated the OI] 1356 Å emission pattern expected for the sunlit atmosphere with the phenomenological model. As for the STIS images, the spatial resolution is thereby adjusted to the observations and the modeled ACS image is convolved with the ACS PSF, see Appendix A.5. Figure 5.6 shows the modeled morphology of the OI] 1356 Å emission for the two LORRI images (a,b) and the ACS image (c). The relative brightness of the equatorial spots roughly agree with the observed ratios in the LORRI images, compare Figures 5.6 (a,b) and 5.2 (a,b). The spots in the observations are, however, clearly less extended, which is consistent with the estimated behavior for a lower atmospheric density. The difference in the spot extension might also originate from the differing emitting species. While the phenomenological model is based on the UV oxygen emission, the LORRI images mostly show emission of excited SO_2. The emission on the upstream (right-hand) limb of the LORRI IEclipse03 image is notable. In the modeled image (Figure 5.6 b) the anti-Jovian spot reproduces the near-surface feature of the observed emission in the East Girru region, see Figure 5.2 b. The second observed small feature in the East Girru region appears to be indeed detached from the surface and is therefore likely to originate from excited plume gas. The simulation also confirms that the emission observed in the wake of Io can be attributed to the flank emission extending far downstream, see Figures 5.6 (c) and 5.2 (c).

In the STIS images, the morphology has been shown to be hardly affected by volcanic activity at all. In the LORRI images, however, the emission from the Tvashtar plume is very prominent. As discussed in the previous section, the lack of atomic gas in the plume might causes a differing brightness in the visible (LORRI) and UV (STIS) wavelength range. In addition, for a dense sunlight atmosphere, the stronger interaction more effectively shields the incoming plasma. Due to effictive shielding the brightness of the Tvashtar plume might be decreased in sunlight and therefore significantly less prominent than in eclipse even at visible wavelengths.

The principal similarity of the morphology in the images created with the phenomenological model and the high-resolution images eclipse images implies that the aurora morphology is controlled by the plasma interaction also in eclipse and not by the exact distribution of the atmospheric gas or the locations of volcanoes. Even though a clear intensity decrease and some changes in the emission distribution have been detected, the general aurora morphology dominated by the bright equatorial spots is preserved in eclipse. Considering the inferred constancy of the UV aurora within the five years of STIS observations, the relatively unchanged morphology in eclipse confirms the general stability of the aurora in terms of its morphology.

6 Europa's UV aurora

In this chapter the brightness and morphology of the oxygen emissions in the STIS observations obtained in October 1999 are analyzed in detail. We will investigate the correlation with the magnetospheric properties and analyze possible atmospheric abundances explaining the observed intensities.

6.1 Overview of the STIS images

The processing of the STIS G140L observations of Europa is performed as described in Section 3.3.2. In the first place, we will analyze the two oxygen multiplets OI] 1356 Å and OI 1304 Å. The spectral lines of the oxygen multiplets and the offset of the respective disks in the images are explained in Section 4.1. For Europa, the disk of the OI 1304 Å aurora is centered at the averaged wavelength of the multiplet at 1303.5 Å. Additionally, we will examine the Lyman-α radiation, HI 1216 Å, and briefly discuss the surface reflected CII 1335 Å emission, although the CII 1335 Å signal is low and probably affected by the oxygen emission. The exposures taken during one orbit are again combined to decrease the noise level. We thus extract five images for each emission, where the image obtained during orbit 2 consists of only one exposure.

The observations have been analyzed previously by *McGrath et al.* (2004, 2009) and *Cassidy et al.* (2007), see Section 2.2.3. However, in the previous studies the individual images for each of the five orbits have been hardly investigated separately. Instead, the authors analyze primarily the superposed images. As the synodic rotation of Jupiter at Europa is $T_{\mathrm{Jup,syn}} = 11.25$ h, the magnetospheric properties change considerably during the 7-h duration of the observation campaign. The System III longitude and the corresponding magnetic latitude for the five HST orbits is displayed in Figure 6.1. During four orbits, Europa is located below the magnetic and centrifugal equator passing through the center from south to north right before the last orbit. *McGrath et al.* (2009) show the five images of the OI] 1356 Å emission (their Figure 5) and briefly mention a variability of the location of the brightest emission. They do not see a correlation of the emission to the background field like observed at Io. We will analyze, for the first time, the five individual images of both the OI] 1356 Å and OI 1304 Å aurora together with the Lyman-α radiation and relate the observed features to the ambient plasma density and magnetic field as well as to the atmospheric neutral gas abundances.

The surface reflected CII 1335 Å radiation spatially overlaps with the OI] 1356 Å emission in the images, see Figures 6.3 and 6.5. The CII 1335 Å intensity is about a factor of 2 lower than the oxygen emissions from Europa's atmosphere. In the previous evaluations of the Europa STIS images by *McGrath et al.* (2004, 2009) and *Cassidy et al.* (2007) the reflected sunlight has not been

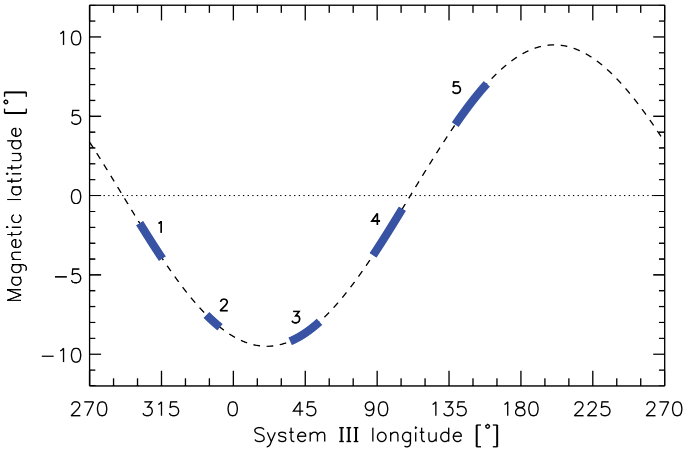

Figure 6.1: *Magnetic latitude vs. System III longitude during a synodic rotation of Jupiter at Europa (dashed line). The blue bars indicate the parameter interval during the combined exposures of the five HST orbits. The numbers refer to the orbits as listed in Table 6.1. As one exposure failed in the second orbit, the second blue bar is shorter.*

subtracted leading to a constant surplus of emission in the upper right corner of the images. We have assumed a constant albedo all over the surface for the calculation of the surface reflected light. In case the albedo is spatially variable, the subtracted CII 1335 Å intensity in the overlap region might be over- or underestimated. Nonetheless, the average calculated CII 1335 Å intensity should be in agreement with the actual surface reflected radiation and the uncertainty of the subtracted sunlight from each pixel is included in the error analysis.

As for Io, most of the observed oxygen emission is produced by electron impact excitation of Europa's neutral atmosphere. The density of the plasma torus in Europa's orbit is lower, whereas the temperature increases with larger distances to Jupiter. The torus density is roughly 30−50 cm^{-3}, the temperature of the thermal electrons has been found to be 15−25 eV (*Sittler and Strobel* 1987, *Bagenal and Delamere* 2011). Additionally, hot electrons have been detected at a temperature of ~250 eV with an approximate mixing ratio of 5% (*Sittler and Strobel* 1987). For comparability, we adopt the values used by *Hall et al.* (1995) for the analysis of the GHRS observations of $n_e(20\,\text{eV}) = 38\ \text{cm}^{-3}$ and $n_e(250\,\text{eV}) = 2\ \text{cm}^{-3}$. The main atmospheric constituent of Europa's atmosphere is molecular oyxgen O_2 with smaller mixing ratios of atomic oxygen O and water H_2O. In Figure 6.2 the relevant excitation rates for electron impact on O, O_2 and H_2O producing the oxygen and Lyman-α (H_2O only) emission are shown. The rates are calculated after Equation (4.2). For the excitation of oxygen they are identical to the values for Io. For the electron impact cross sections on water producing OI 1304 Å and HI 1216 Å we use the measured values of *Makarov et al.* (2004). Emission of OI] 1356 Å upon electron impact on H_2O was not detected. The main argument for O_2 to be the main constituent are the relative excitation rates of atomic and molecular oxygen (*Hall et al.* 1995). Whereas the excitation of O implies a relative brightness of $I_{1356}/I_{1304} < 0.5$ over a wide range of electron temperatures, the O_2 rates are in agreement with the ratio inferred in the previous observations of $I_{1356}/I_{1304} \approx 2$. As the global abundance of H_2O is commonly expected to be low, contributions of dissociative excitation of water molecules to produce OI 1304 Å are negligible on the global scale.

Depending on the density of atomic oxygen, resonant scattering of solar radiation by O atoms might be non-negligible. The brightness due to resonantly scattered OI 1304 Å can be estimated

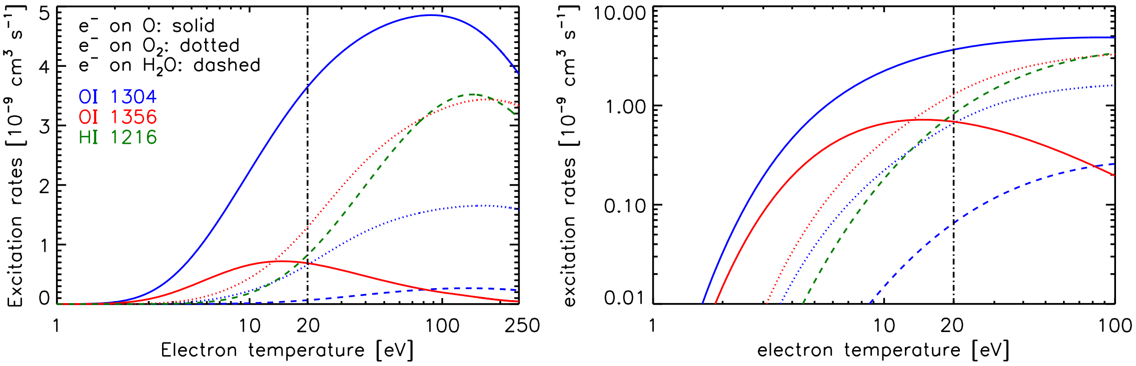

__Figure 6.2:__ Direct and dissociative excitation rates for O, O_2 and H_2O producing OI 1304 Å, OI] 1356 Å and HI 1216 Å emission. The right plot is an enlargement of the left plot on a double logarithmic scale. The vertical line indicates the temperature of the thermal torus electrons at Europa of 20 eV.

by the resonant scattering probability, the optical depth of the atmosphere and an effective resonant scattering albedo, see Equation (4) of *Hall et al.* (1995). The intensity of resonantly scattered solar OI 1304 Å can be approximated for the expected O column densities of $N_O \approx 10^{13} - 10^{14}$ cm^{-2} by

$$I_{\rm scat} = 1.5\,\left(N_O[\mathrm{cm}^{-2}]\times 10^{-12}\right)^{0.55} \quad [R] \tag{6.1}$$

(*Darrell Strobel, personal communication*). The scattered OI 1304 Å intensity is thus on the order of 10−20 R.

H_2O absorbs solar Lyman-α radiation with a cross section of $\sim 1.5\times10^{-17}$ cm^2 (*Chan et al.* 1993) similar to the absorption cross section of SO_2 at 1216 Å. The global H_2O column density on Europa is, however, about three orders of magnitude lower than the SO_2 column density at Io (e.g., *Plainaki et al.* 2012, *Feaga et al.* 2009). Therefore, by far most Lyman-α radiation can reach the surface and is reflected without absorption by H_2O. Due to the low H_2O abundance, Lyman-α emission from dissociative excitation of H_2O is also presumably negligible with respect to the high intensity of the reflected solar Lyman-α of more than 1000 R.

The five OI] 1356 Å and OI 1304 Å observations are shown in Figure 6.3 and 6.4, respectively, together with a superposition of all exposures. The superposition of the observed Lyman-α and CII 1335 Å emission patterns is displayed in Figure 6.5. The spatial resolution is reduced by factor 2, i.e, 2×2 pixels are binned together in the displayed images. In the images of the oxygen emission the average signal to noise ratio of a single pixel of ~0.1 is extremely low. The uncertainty of the binned pixels is only slightly decreased. In our analysis we will primarily investigate larger areas in the images taking into consideration the propagated combined errors. The signal to noise ratios for the total brightness are 19 and 12 on average for the OI] 1356 Å and OI 1304 Å images, respectively. In case of the Lyman-α and CII 1335 Å emission only the superposed images will be analyzed. Here, the SNR for the total brightness are roughly 40 and 15, respectively.

In Figures 6.3(a-e) and 6.4(a-e), the yellow circle in the northern, anti-Jovian quadrant of the disk indicates an area, where a surplus of OI 1304 Å emission is observed. This feature will be discussed in detail in Section 6.4. The observations were obtained shortly before western elongation (see Table 6.1), i.e., the upstream or trailing hemisphere is visible to the observer. As the sub-observed longitude changes from the first exposure ($\varphi_{obs} = 245.8°$) to the last exposure

($\varphi_{obs} = 272.3^\circ$), the pixels that are superposed in the combined image do not refer to exactly the same points on the surface. The images taken during HST orbits 1 to 5 will be simply designated image 1 to image 5 in the following. Table 6.1 lists all observational parameters for the five orbits.

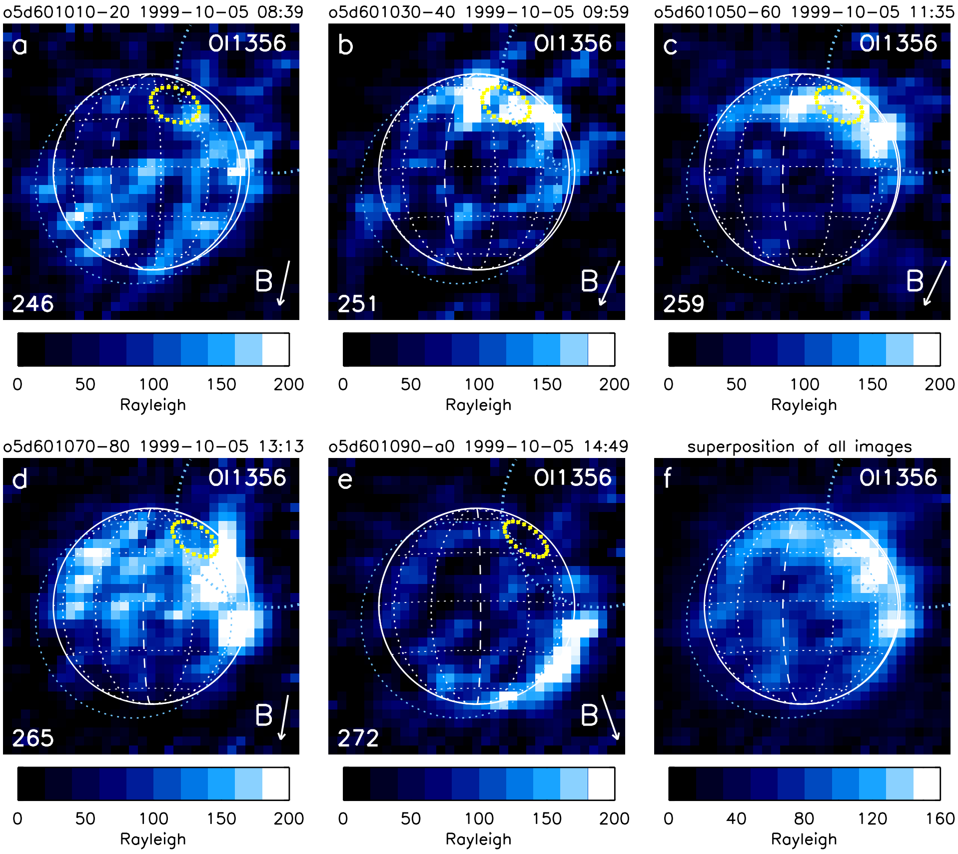

Figure 6.3: *STIS observations of Europa’s OI] 1356 Å aurora. (a)-(e) Images obtained during HST orbits 1 to 5. (f) Superposition of the five images. The yellow circle shows the area, where a surplus of OI 1304 Å emission is observed (230 °W 45 °N). The disk of the brightest line is shown in white with dotted longitudes and latitudes. The dashed longitude indicates the upstream/downstream meridian (270°/90° west longitude), the sub-Jovian/anti-Jovian meridian (0°/180° west longitude) is shown as solid line. The dispersed disk location of the additional line of the multiplet (1358.5 Å) is shown by the dotted circle in light blue that is slightly displaced from the main disk. The widely displaced dotted circle indicates the disk of the surface reflected CII 1335 Å radiation, which is subtracted in the images. The sub-observer longitude is specified in the lower left corner, the arrow in the lower right corner shows the direction of the background magnetic field. Europa is located below the torus equator, when the magnetic field points towards Jupiter (left). The observational parameters are listed in Table 6.1.*

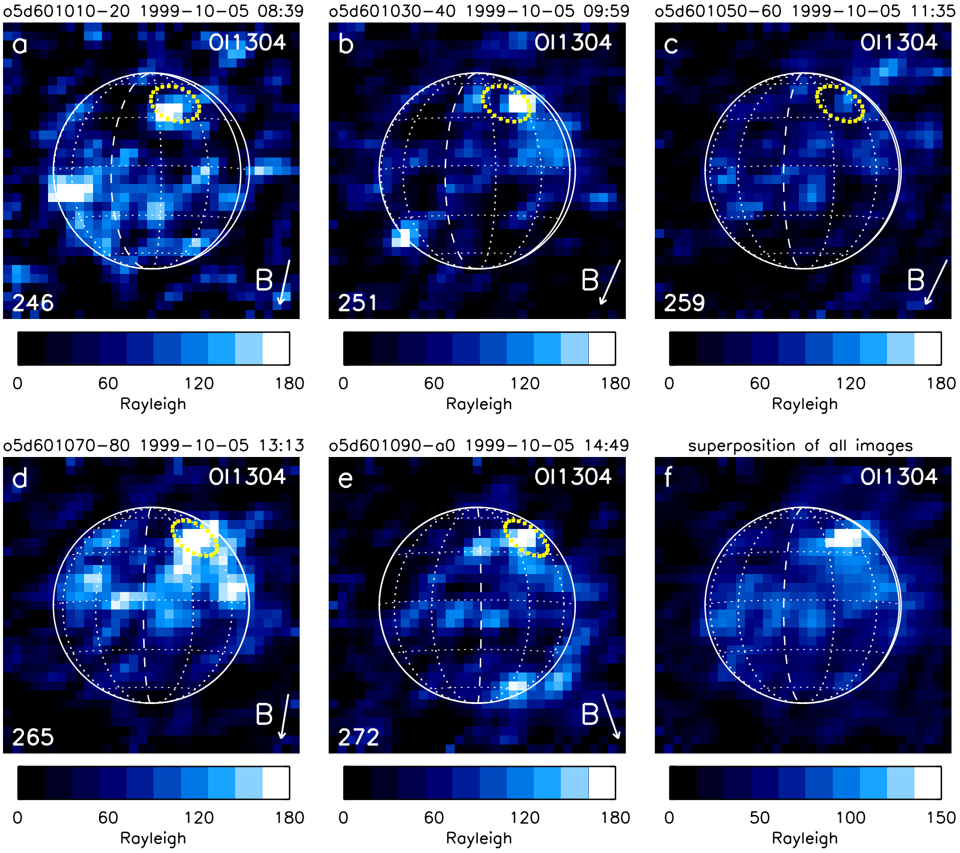

__Figure 6.4:__ STIS observations of Europa's OI 1304 Å aurora. (a)-(e) Images obtained during HST orbits 1 to 5. (f) Superposition of the five images. The yellow circle shows the area, where a surplus of emission is observed in four of the five images (230 °W 45 °N). The observation parameters are listed in Table 6.1. For further explanations see also Figure 6.3.

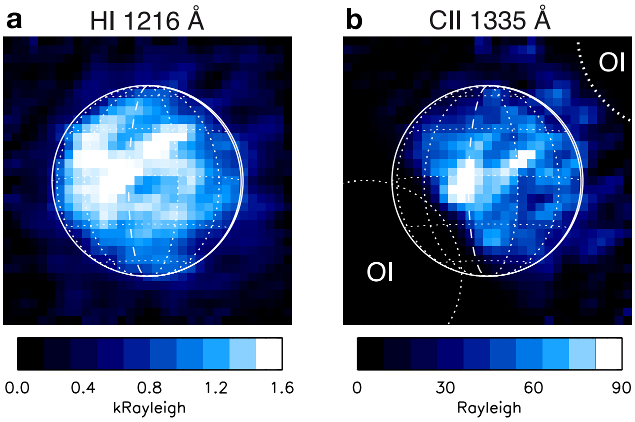

__Figure 6.5:__ Superposition of all exposures obtained during the five HST orbits of the Lyman-α (HI 1216 Å) radiation (a) and the surface reflected CII 1335 Å (b). The CII 1335 Å emission is affected by the oxygen emission through the dispersion in the observations. The disks of the OI] 1356 Å emission (bottom left) and OI 1304 Å emission (top right) are shown with dotted white circles in (b). The overlap area is blackened. Note that the Lyman-α intensity is given in kR.

Table 6.1: *Observational parameters of the STIS Europa images.*

No[a]	Dataset	R_E[b]	d_{obs}[c]	d_{sun}[c]	φ_{obs}[d]	φ_{sun}[d]	λ_{III}[e]	ψ_m[e]	z_c[e]	B_x[f]	B_y[f]	B_z[f]
		[pixel]	[AU]	[AU]	[°]	[°]	[°]	[°]	[R_J]	[nT]	[nT]	[nT]
1	o5d601010-20	21.8	4.01	4.95	245.8	249.8	308.4	-2.9	-0.31	-53	67	-379
2	o5d601030-40	21.8	4.01	4.95	250.9	255.0	347.4	-7.9	-0.86	-31	167	-383
3	o5d601050-60	21.8	4.01	4.96	258.5	262.6	44.7	-8.7	-0.94	18	198	-396
4	o5d601070-80	21.8	4.01	4.96	265.4	269.4	96.6	-2.3	-0.25	69	71	-404
5	o5d601090-a0	21.8	4.01	4.96	272.3	276.3	148.8	5.8	0.63	61	-146	-412

[a] Number of the image, corresponding to the orbit number in Table 3.2.

[b] Radius of Europa in pixels.

[c] Distance between Europa and the observer (d_{obs}) / the Sun (d_{sun}).

[d] Europa-centric sub-observer longitude/orbital longitude as seen from HST (φ_{obs}) and the Sun (φ_{sun}), see also Appendix A.1. The difference between φ_{obs} and φ_{sun} is the solar phase angle.

[e] Longitude of the Jovian System III λ_{III}, magnetic latitude ψ_m, and the distance between Europa and the torus equator z_c.

[f] Background magnetic field given by the superposition of the internal field of Jupiter calculated with the VIP4 model (*Connerney et al.* 1998) and the current sheet field after *Khurana* (1997)

6.2 Brightness of the oxygen aurora

In comparison to the morphology of Io's aurora observed at western elongation, where most emission is concentrated in the bright equatorial spots above the limb, the morphology of Europa's oxygen emission differs significantly. Roughly 70% of the OI] 1356 Å and OI 1304 Å emission emerges on the disk and not above the limb. The total brightness I_{tot} within 1.5 R_E around the disk center normalized to the disk area varies between 125 R and 169 R for OI] 1356 Å and 76 R and 121 R for OI 1304 Å. The total brightness, I_{tot}, as well as the brightness of all pixels on the disk, I_{disk}, are listed in Table 6.2. The inferred total intensities are slightly higher than the fluxes of approximately 70−90 R (OI] 1356 Å) and 40−65 R (OI 1304 Å) observed by the GHRS also on the upstream hemisphere (*Hall et al.* 1998). If we only take into account the emission from the disk of Europa, our values are reduced by ~30% and in reasonable agreement with the previous observations. Figure 6.6 shows the OI] 1356 Å and OI 1304 Å brightness and the combined intensity of each image as a function of the distance of Europa to the torus center.

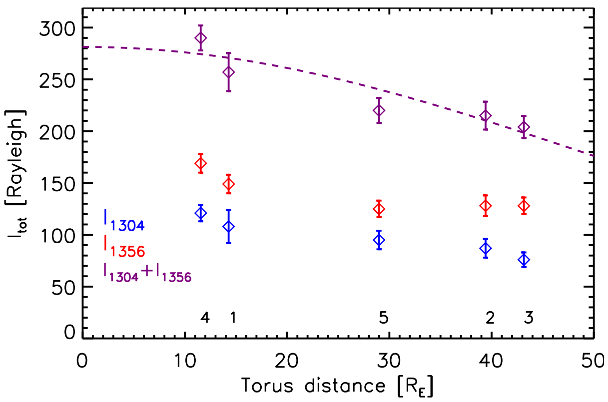

Figure 6.6: *Total brightnesses within 1.5 R_E of the disk center with error bars for the OI] 1356 Å aurora (red), OI 1304 Å aurora (blue) and the combined brightness of both oxygen emissions (violet). The dashed line shows the fitted profile of Equation* (4.7) *with $H_c = 1.7\ R_J$. The numbers at the bottom refer to the HST orbits.*

Table 6.2: *Observed absolute and relative intensities of the OI] 1356 Å, OI 1304 Å, HI 1216 Å and CII 1335 Å emission.*

Orbit[a]	Dataset	I_{tot}[b] [R]	I_{disk} [R]	I_{circle}[c] [R]	I_{circle} / I_{disk}	I_{circle} / $I_{\text{anti-J,north}}$
OI] 1356 Å						
1	o5d601010-20	149 ± 9	100 ± 7	53 ± 29	0.53 ± 0.34	0.49 ± 0.32
2	o5d601030-40	128 ± 10	94 ± 8	183 ± 55	1.95 ± 0.68	1.21 ± 0.44
3	o5d601050-60	128 ± 8	88 ± 6	190 ± 39	2.16 ± 0.54	1.26 ± 0.33
4	o5d601070-80	169 ± 9	132 ± 7	97 ± 35	0.73 ± 0.32	0.57 ± 0.25
5	o5d601090-a0	125 ± 8	73 ± 6	40 ± 34	0.55 ± 0.54	0.58 ± 0.58
	Average[d]	**140 ± 4**	**97 ± 3**	**113 ± 20**	**1.16 ± 0.22**	**0.87 ± 0.17**
OI 1304 Å						
1	o5d601010-20	108 ± 16	75 ± 11	128 ± 61	1.71 ± 0.98	2.00 ± 1.32
2	o5d601030-40	87 ± 9	52 ± 7	70 ± 43	1.35 ± 0.90	0.75 ± 0.51
3	o5d601050-60	76 ± 7	49 ± 5	81 ± 29	1.65 ± 0.75	1.25 ± 0.60
4	o5d601070-80	121 ± 8	91 ± 6	278 ± 45	3.05 ± 0.64	1.94 ± 0.43
5	o5d601090-a0	95 ± 9	65 ± 6	224 ± 50	3.45 ± 0.95	2.46 ± 0.74
	Average[d]	**97 ± 5**	**66 ± 3**	**159 ± 19**	**2.36 ± 0.39**	**1.74 ± 0.30**
HI 1216 Å						
	Average[d]	1614 ± 40	1215 ± 27	949 ± 190	0.78 ± 0.16	0.82 ± 0.17
CII 1335 Å						
	Average[d]	–	∼50	52 ± 18	–	0.83 ± 0.31

[a] Number of the images, corresponding to the orbit number in Table 3.2.

[b] Total emission with 1.5 R_E around the center normalized to the area of the disk.

[c] Brightness of the area with radius 350 km around 230° W and 45° N. The number of pixel varies between 34 and 46 depending on the viewing angle (yellow circle in Figures 6.3 and 6.4).

[d] The average brightness refers to the sum of the brightnesses in the individual images divided by the number of images. Note that for the values of the encircled area this does not correspond to the brightness in the encircled area in the superposed images. The relative brightnesses are the ratios of the averaged absolute brightnesses.

As expected, the observed intensity is higher, when Europa is closer to the torus center, where the electron density is presumably largest. This correlation has also been observed in the ACS observations by *Saur et al.* (2011). We can again compare the aurora brightness to the analytical approximation for the latitudinal density distribution in the torus by *Hill and Michel* (1976) given in Equation (4.6). As for Io, we therefore fit the coefficients I_0 and H_c of the theoretical intensity profile given in Equation (4.7) to the combined total brightness of the OI] 1356 Å and OI 1304 Å aurora. The best agreement is obtained for a torus scale height of $H_c = 1.6\,(\pm 0.2)$ R_J and a maximum brightness of $I_0(1304+1356) = 283$ R in the center. The scale height is in suitable agreement with the estimated torus scale height at Europa's orbit of $H_c = 1.7$ R_J by *Bagenal and Delamere* (2011, their Equation 6). Although the fit is based on only five data points, the total brightness seems to be principally controlled by the ambient electron density.

The relative total brightness of the two oxygen aurorae is $I_{1356}/I_{1304} = 1.45 \pm 0.09$, which is in between the values obtained by *Hall et al.* (1998) of 1.3 and 2.2. Using the approximation of *Hall et al.* (1998) that the electron density and temperature are spatially homogeneous and constant and that the atmosphere is confined to the geometric cross section of the disk, a column density for O and O_2 can be derived. As stated above, a temperature of 20 eV for the cold electrons with a 5% mixing ratio of hot electrons (250 eV) and a total density of $n_e = 40$ cm^{-3} is assumed. The theoretical total brightness is then given by

$$I_{\lambda,\text{emis}} = \sum_n N_n f_\lambda(T_e)\, n_e \quad , \tag{6.2}$$

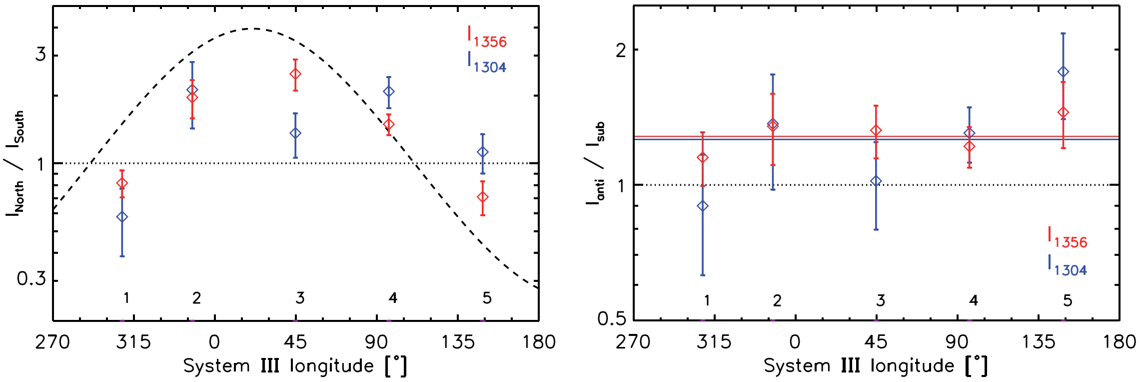

Figure 6.7: *(Left) Ratio of the total disk brightness of the northern hemisphere and the southern hemisphere for the five OI] 1356 Å (red diamonds with error bars) and OI 1304 Å (blue diamonds) images. The bold dashed line shows the ratio of the flux tube contents above and below Europa after Equation 4.18 with* $H_c = 1.7\ R_\mathrm{J}$. *(Right) Ratio of the total disk brightness of the anti-Jovian hemisphere and the sub-Jovian hemispheres. The thin lines show the average ratios for OI] 1356 Å (red) and OI 1304 Å (blue). The numbers at the bottom refer to the HST orbits.*

with the neutral column densities N_n and the excitation rate coefficients f_λ. The sum over n includes all excited neutral species that contribute to the respective emission. For OI 1304 Å contributions from resonantly scattered sunlight after (6.1) are additionally taken into account.

Fitting the theoretical brightness after Equations (6.2) and (6.1) as a function of N_n to the average I_{disk} values, we find that the OI] 1356 Å and OI 1304 Å emissions are best reproduced by atmospheric column densities of $N_{\mathrm{O_2}} = (1.7 \pm 0.1) \times 10^{15}$ cm^{-2} and $N_\mathrm{O} = (3.9 \pm 1.2) \times 10^{13}$ cm^{-2}. The mixing ratio O/O$_2$ is thus roughly 2%. As already explained, the plasma properties are in fact strongly altered by the interaction with the atmosphere. The assumptions applied for the derivation of the atmospheric abundances will be discussed in Section 6.5.

6.3 Morphology of the oxygen aurora

Since most emission is emitted on the disk rather than above the limb, we will focus on the distribution of the radiation over the disk, respectively over the surface. Therefore, the emission on the northern and southern hemispheres as well as the emission on the sub-Jovian and anti-Jovian hemisphere is analyzed separately.

In the OI] 1356 Å images 2 to 4 (Figure 6.3b-d), the northern hemisphere is clearly brighter than the southern hemisphere. In the first image, the OI] 1356 Å emission appears more diffuse with a small surplus on the southern hemisphere. In image 5 the brightest emission is found in the southern hemisphere close to the limb on the anti-Jovian side. Similar to the relative limb glow brightness at Io, the relative brightness of the southern and northern hemisphere is in approximate agreement with the flux tube contents north and south of Europa. Figure 6.7 (left) shows the ratio of the intensity in the northern and southern hemispheres I_{North}/I_{South} as a function of the System III longitude. The ratio of the flux tube contents after Equation (4.18) with the torus scale height at Europa of $H_c = 1.7$ R$_\mathrm{J}$ (*Bagenal and Delamere* 2011) is shown as dashed line. With the exception of the first image, the hemisphere facing the torus center is brighter than the opposite hemisphere. The measured ratios are generally lower than the ratio of the flux tube contents.

Additionally, the OI] 1356 Å brightness ratios appear to be shifted to higher λ_{III} values. As for Io, a shift to higher λ_{III} indicates a temporal delay of the magnetospheric environment. Whether the relative hemispheric brightness is indeed delayed with respect to the ambient torus properties due to an inert response of the auroral emission, can not be inferred from the images due to the large scattering of the data points and the involved uncertainty.

The relative hemispheric brightness in the OI 1304 Å images roughly resembles the behavior in the OI] 1356 Å images. The morphology appears, however, patchier than the OI] 1356 Å emission. In the images 2, 4 and 5, the brightest radiation is emitted in a confined area in the northern, anti-Jovian quadrant. In image 1, the intensity in this area is also high, although the emission pattern is very patchy due to a high noise level resulting from an exceptionally strong terrestrial background emission during the observation. The morphology of image 5 (Figure 6.4e) is especially noticeable. Europa is located north of the torus center, i.e., the southern hemisphere is expected to be brighter, which it is in the case of OI] 1356 Å. The OI 1304 Å morphology, however, is still dominated by the bright spot in the northern, anti-Jovian quadrant leading to an opposed hemispheric brightness ratio, see Figure 6.7 (left). The bright area is located at approximately 230 °W and 45 °N in planetographic coordinates of Europa. The yellow circle in Figures 6.3 and 6.4 indicates an area of 350 km radius around this point on the surface. The brightness within this region will be analyzed in detail in the following Section 6.4.

Figure 6.7 (right) shows the relative brightness of the anti-Jovian to the sub-Jovian hemisphere in the OI] 1356 Å and OI 1304 Å images. In case of the OI] 1356 Å emission, the anti-Jovian hemisphere is consistently brighter in all images. The horizontal red line shows the average ratio of OI] 1356 Å which is $I_{anti-Jovian}/I_{sub-Jovian}(1356) = 1.30 \pm 0.09$, i.e., the anti-Jovian hemisphere is 30% brighter than the sub-Jovian hemisphere. The average ratio of OI 1304 Å (blue line) of $I_{anti-Jovian}/I_{sub-Jovian}(1304) = 1.27 \pm 0.15$ also indicates a brighter anti-Jovian hemisphere, but the individual values reveal a larger scattering about the mean. The strong OI 1304 Å emission from the confined area in the north contributes significantly to the total brightness of the anti-Jovian hemisphere.

Overall, the OI] 1356 Å morphology appears to undergo relatively systematic variations in correlation with Europa's position with respect to the torus center. As Europa is located below the torus center during four orbits the averaged emission is brighter in the north as already stated in *McGrath et al.* (2004, 2009). The OI 1304 Å aurora, however, is dominated by a bright confined spot in the northern, anti-Jovian quadrant, which does not follow the expected north-south variations, in contrast to the OI] 1356 Å emission. In the superposed image, the emission in this confined spot is also by far the brightest (c.f. also Figure 4 in *McGrath et al.* 2009). In the next section, the brightness of this presumably anomalous area is analyzed in the oxygen images as well as in the Lyman-α and CII 1335 Å observations.

6.4 Anomaly in the OI 1304 Å emission

The area of the unusually bright OI 1304 Å emission corresponds to roughly 40 pixels in the raw images. The signal to noise ratio of the combined pixels is in some images as low as 2. Therefore, we first verify the statistical significance of the detected anomaly, before we discuss possible effects causing the enhanced OI 1304 Å emission.

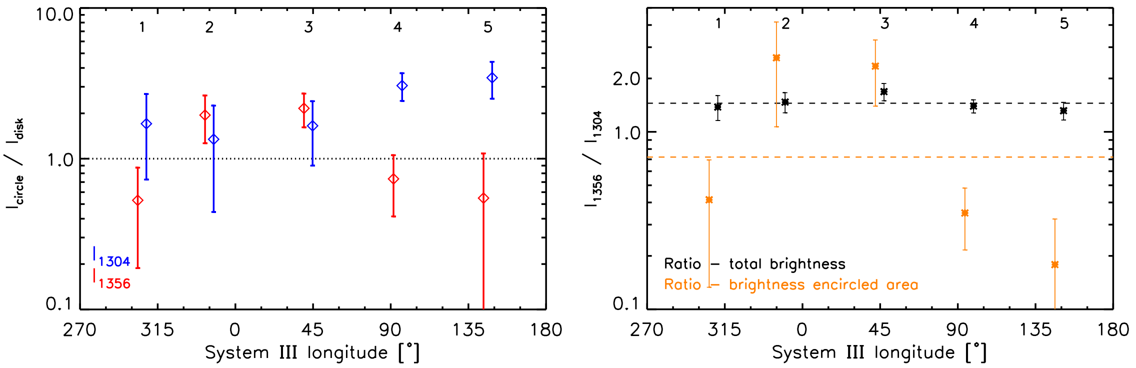

Figure 6.8: *(Left) Ratio of the average pixel intensity within the encircled region I_{circle} and the average disk brightness I_{disk} for the five OI] 1356 Å (red diamonds with error bars) and OI 1304 Å (blue diamonds) images. (Right) The ratio of the OI] 1356 Å to OI 1304 Å emission for the total observed brightness (black asterisks) and for the measured intensity in the encircled area (orange asterisks). Particularly in the images of orbit 4 and 5, the two oxygen emissions reveal remarkable differences. The numbers at the top refer to the HST orbits. (The symbols are shifted on the horizontal axis by ±3° to separate them for better visibility.)*

6.4.1 Statistical significance

For our analysis, we relate the area of the bright OI 1304 Å spot to a circular region on the surface with radius 350 km centered at 230 °W and 45 °N. Due to the varying observing angle the size of the surface area projected to the observation plane changes, see Figure 6.4 (a) to (e). The measured intensities of the encircled area, I_{circle}, are listed in Table 6.2. Figure 6.8 (left) shows the ratios I_{circle}/I_{disk} versus the System III longitude.

In case of the OI] 1356 Å aurora, the relative brightness is consistent with the inferred north-south variability. In images 2 and 3, where Europa is south of the torus and far from the center, the northern hemisphere and thus the encircled area are brighter than the disk average (Figure 6.3b,c). In the other images, where Europa is closer to the torus equator, the emission in the encircled area is similar to the averaged emission all over the disk. The OI 1304 Å ratio, in contrast, is constantly above 1, i.e., the emission in the encircled area is constantly higher than the disk average. Particularly in images 4 and 5, where Europa is slightly below and above the torus center, the ratio is exceptionally high with $I_{circle}/I_{disk} > 3$. In images 1 to 3, I_{circle}/I_{disk} is roughly 1.5 and consistent with a 1:1 ratio within error bars. The ratio of the average brightness within the circle by the average disk brightness of 2.36 ± 0.39 is, however, clearly higher than unity for OI 1304 Å. In case of OI] 1356 Å, the brightness in the encircled area approximately matches the disk brightness on average.

To eliminate the effects of the north-south variability, we have additionally compared the emission inside the circle to the emission outside the circle in the northern, anti-Jovian quadrant, see values in Table 6.2. The comparison yields similar results. The ratio I_{circle} / $I_{\text{anti-J,north}}$ is consistent with a 1:1 correlation for OI] 1356 Å, whereas for OI 1304 Å, the emission inside the circle is clearly larger with a difference beyond the uncertainty.

Hence, the OI] 1356 Å aurora does not reveal any anomalous behavior in the circled area, whereas the OI 1304 Å emission has a notable surplus. On the other hand, the OI 1304 Å emission pattern appears to be generally patchier than the OI] 1356 Å emission. We therefore test the statistical

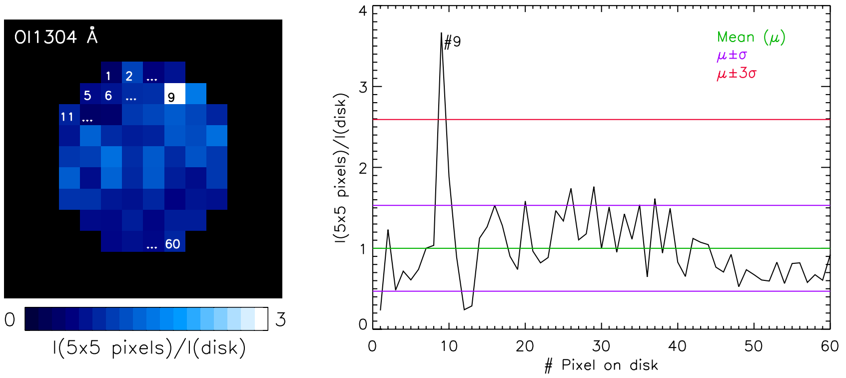

Figure 6.9: *(Left) Superposed OI 1304 Å image (Figure 6.4f) with 5×5 pixels binned together. The pixels outside the disk are blackened, the pixels on the disk are numbered consecutively. (Right) Intensity of each binned pixel. The intensity of pixel #9 deviates from the mean by more than three times the standard variation across the disk.*

significance of the local emission surplus in the northern, anti-Jovian quadrant with regard to the observed brightness variations across the disk. Therefore, we bin the flux of 5×5 pixels together for all pixels on the disk and normalize the averaged fluxes to I_{disk}. The signal to noise ratio for the binned pixels is ~1 for the individual images, and ~2.5 for the superposed image. The binned superposed observation image is shown in Figure 6.9 (left), where the binned pixels are numbered consecutively from top left (#1) to bottom right (#60). Figure 6.9 (right) illustrates the brightness variation for all 60 binned disk pixels. The flux of pixel #9, which is located at the anomalous region, is larger by more than three times the standard deviation compared to the mean flux across the disk. In the individual images 2, 4 and 5 the deviation of the brightness of the binned pixel number 9 also exceeds the 3-σ boundary. This implies that in at least three images the particular surplus of OI 1304 Å emission is not a random variation across the disk. The OI] 1356 Å as well as the Lyman-α emission pattern are clearly smoother and do not reveal deviation from the mean across the disk higher than 2 σ.

6.4.2 Possible causes for the anomaly

As the solar reflected light is higher by a factor of ~3 for OI 1304 Å than for OI] 1356 Å, the bright local emission might be explained by a local anomaly of the surface reflectivity. The surface reflected OI 1304 Å intensity, which has been subtracted from the observations, is ~30 R. To explain the emission surplus in the encircled area of up to 150 R, the local albedo must be increased by factor 5. However, such a local reflectivity inhomogeneity should also affect the Lyman-α and CII 1335 Å emission patterns, which are displayed in Figure 6.5. Although the CII 1335 Å radiation overlaps with the oxygen emissions on the dispersion axis in the STIS images, fortunately the signal in the northern, anti-Jovian quadrant is not affected by either the OI] 1356 Å or OI 1304 Å aurora. Both emission patterns, Lyman-α and CII 1335 Å, do not reveal any striking brightness enhancements in the northern, anti-Jovian quadrant. The brightness ratio $I_{circle}/I_{\text{anti-J,north}}$ is even below 1 for both the Lyman-α and CII 1335 Å emission (see Table 6.2), even though the uncertainty of the low CII 1335 Å radiation is high. Atmospheric processes influence the Lyman-α radiation additionally, but in the case of CII 1335 Å, the radiation is not affected by atmospheric processes and it is therefore a secure diagnostic for the albedo. The local enhancement seen in the

OI 1304 Å aurora is clearly not detected at CII 1335 Å and HI 1216 Å, and is therefore likely of atmospheric origin rather than caused by the surface properties.

Figure 6.8 (right) shows the relative intensity of the OI] 1356 Å to the OI 1304 Å aurora for the disk average and in the encircled area. The ratio for the disk brightnesses stays constantly close to the mean value of 1.45 ± 0.09. The brightness ratio at the anomaly, in contrast, undergoes drastic changes with an average of $I_{circle}(1356)/I_{circle}(1304) = 0.71 \pm 0.18$. This intensity ratio and the general surplus of OI 1304 Å emission possibly originates from excitation of atomic oxygen or dissociative excitation of H_2O. The cross sections of atomic oxygen imply a OI] 1356 Å to OI 1304 Å ratio of ≤ 0.5. Emission of OI] 1356 Å after dissociative excitation of H_2O could not be detected by *Makarov et al.* (2004), but the cross sections are estimated to be at least an order of magnitude lower than OI 1304 Å cross sections. Both processes therefore clearly favor emission of OI 1304 Å over OI] 1356 Å. To explain the anomalous OI 1304 Å intensity of 159 R solely by excitation of atomic oxygen, the O abundance would have to be roughly an order of magnitude higher than the inferred global abundance. However, such a local enhancement is unlikely as atomic oxygen has a small sticking coefficient at the surface and thus a relatively long resident time in the atmosphere of ~1 day (*Smyth and Marconi* 2006). Besides, a local O enhancement would likely to be coupled to an increased O_2 abundance, which, in turn, would imply a measurable anomaly in the OI] 1356 Å aurora.

H_2O on the other hand, freezes at the estimated surface temperatures of $\sim 90-130$ K. The estimated life time is on the order of tens of minutes (*Smyth and Marconi* 2006). Therefore, a surplus of H_2O abundance in a confined region is possible, if a local source producing water vapor is present. As mentioned in Section 2.1.4, *Saur et al.* (2011) developed the idea of a localized water abundance arising from shear heating as explanation for the observed enhanced oxygen emission on the downstream hemisphere. Recently, localized water plumes have been observed by Cassini at the south pole of Saturn's satellite Enceladus (*Porco et al.* 2006). The water gas ejections from rifts in the ice shell are thought to be triggered by tidal shear stresses (*Nimmo et al.* 2007). As similar shear heating is expected at Europa's surface lineaments (*Nimmo and Gaidos* 2002), we examine the consistency of the observed OI] 1356 Å, OI 1304 Å and Lyman-α intensities in the anomalous region with local surplus of water vapor.

To calculate the Lyman-α intensity for an H_2O column density of $>10 \times 10^{15}$ cm^{-2}, both absorption of solar Lyman-α radiation and dissociative excitation of H_2O and subsequent Lyman-α emission have to be taken into account. Assuming a solar zenith angle of ~0°, the attenuation of the solar Lyman-α radiation through absorption by H_2O is given by

$$I(h) = I_0 \exp\left[-\tau(h)\right] \quad , \tag{6.3}$$

where I_0 is the intensity of the incident solar Lyman-α at Europa and

$$\tau(h) = \sigma_a \int_h^\infty n_n(h')\mathrm{d}h \tag{6.4}$$

is the optical depth with the total absorption cross section σ_a and the neutral density $n_n(h)$ (*Chamberlain and Hunten* 1987). At the surface ($h = 0$) the optical depth is $\tau = \sigma_a N_n$ with the vertical atmospheric column density N_n. Assuming a homogeneous reflection from the surface, the attenuated surface reflected solar Lyman-α is then given as a function of the column density by

$$I_{\mathrm{refl}}(N_n) = I_0\, p \exp\left[-2\sigma_a N_n\right] \quad , \tag{6.5}$$

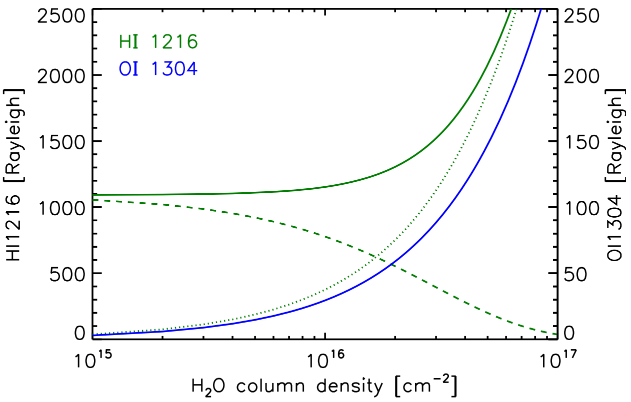

Figure 6.10: *Estimated Lyman-α (HI 1216 Å) and OI 1304 Å intensity as a function of the H_2O column density. The green dashed lines show the profile of the attenuated surface reflected Lyman-α solar radiation, the dotted line indicates the contribution from dissociative excitation of H_2O. The solid green line is the sum of the dashed and dotted line indicating the expected total Lyman-α intensity. The OI 1304 Å intensity is shown by the blue line.*

with the surface albedo $p = 0.014$ (see Section 3.3).

The Lyman-α radiation that is locally produced by electron impact is also attenuated by re-absorption in the atmosphere. Assuming that the atmospheric density decreases exponentially with height h

$$n_n \propto \exp(-h/H) \quad , \tag{6.6}$$

the proportion of the photons that are locally emitted at a height h above the surface leaving the atmosphere is given by

$$i_{esc} = i(h) \exp\left[-\sigma_a N_n \exp(-h/H)\right] \quad . \tag{6.7}$$

We further assume that the local emission follows the radial profile of the atmospheric density, i.e., $i(h) = i_0 \exp(-h/H)$ with $i_0 = I_{0,\mathrm{emis}}/H$. The observed locally produced Lyman-α radiation over the entire atmosphere can then be expressed as

$$I_{\mathrm{emis}}(N_n) = \int_0^\infty i_0 \exp(-h/H) \exp\left[-\sigma_a N_n \exp(-h/H)\right] \mathrm{d}h \tag{6.8}$$

$$\Rightarrow \quad I_{\mathrm{emis}}(N_n) = I_{0,\mathrm{emis}}(N_n) \left[\frac{1-\exp(-\sigma_a N_n)}{\sigma_a N_n}\right] \quad . \tag{6.9}$$

Thus I_{emis} depends only on N_n, if we further assume a constant, homogeneous electron density and temperature. $I_{0,\mathrm{emis}}$ is here the total Lyman-α emission for $\tau = 0$ given by Equation (6.2).

Figure 6.10 shows the contributions of attenuated surface reflected sunlight after Equation (6.5) and emission after Equation (6.9) to the total Lyman-α intensity together with the OI] 1356 Å emission originating from excited H_2O. Note that for H_2O abundances, where the absorption becomes effective, the locally produced emission contributes significantly. Below a column density of $N_{H_2O} \approx 2 \times 10^{16}$ cm^{-2} the effects thus eliminate each other resulting in an unchanged total intensity. For higher column densities the emission outweighs the reduction due to absorption.

The measured OI 1304 Å emission in the anomalous region is ~100 R higher than the disk average brightness, which requires a column density of $N_{H_2O} \approx 3 \times 10^{16}$ cm^{-2}. For this column density, the Lyman-α intensity is expected to be slightly increased as well. In the observations the

Lyman-α radiation in the anomalous region is depressed with respect to the disk average brightness opposed to the estimated behavior. However, the two competitive processes influencing the Lyman-α emission, absorption and local emission are of the same order of magnitude according to our calculations. The approximation has shown, that a locally enhanced H_2O abundance can cause a surplus of OI 1304 Å emission without affecting the Lyman-α intensity essentially.

For a column density of $N_{\mathrm{H_2O}} = 2.6 \times 10^{16}$ cm^{-2} and an equal increase of the O and O_2 abundances by 13% with respect to the derived global column densities, the resulting calculated intensities are $I_{circle}(1356) = 116$ R, $I_{circle}(1304) = 149$ R and $I_{circle}(\text{Lyman-}\alpha) = 1148$ R. A comparison with the averaged observed intensities in the anomalous region (see Table 6.2) shows that the calculated oxygen emissions are in agreement with the observation within the uncertainty. The calculated Lyman-α radiation is only slightly higher than observed. Hence, the OI 1304 Å anomaly in the confined area in the northern, anti-Jovian quadrant could possibly originate from a local abundance of water vapor.

6.5 Discussion

The total brightness has been shown to correlate to the ambient torus plasma density similar to the aurora brightness at Io. Likewise, this implies that the effectiveness of the energy transport is controlled by the amount of local electrons that collide with the atmosphere. The derived global column density of $N_{\mathrm{O_2}} = (1.7 \pm 0.1) \times 10^{15}$ cm^{-2} and $N_{\mathrm{O}} = (3.9 \pm 1.2) \times 10^{13}$ cm^{-2} are in agreement with the previously inferred abundances by, e.g, *Hall et al.* (1995) and *Cassidy et al.* (2007). By applying constant electron parameters to estimate the atmospheric abundances, we assume, that the effects of the cooling of the electrons is roughly balanced by the heat conduction along the field lines. We furthermore neglect the deflection of the plasma around the satellite, but at the same time, we do not consider the contributions from heated ionospheric electrons to excite the emission. However, *Saur et al.* (1998) derive a similar O_2 column density of $N_{\mathrm{O_2}} = 5 \times 10^{14}$ cm^{-2} from the results of their plasma interaction model, when they use the intensity of the oxygen emission as constraint. This implies that the assumption of constant electron parameters yields a reasonable approximation of the abundances. The inferred O/O_2 ratio of $\sim$0.02 is in agreement with the findings of *Hansen et al.* (2005).

Although the OI] 1356 Å aurora correlates to the ambient plasma parameters, the morphology of Europa's oxygen aurora differs significantly from the observed emission pattern at Io. At the tangential points of the background magnetic field there is clearly no increase of auroral emission in four of the five OI] 1356 Å images. The brightest emission is found on the disk rather than above the limb as in the images of Io's aurora at western elongation. *Saur et al.* (1998) derive an interaction parameter for Europa of $\alpha_{Eur} \approx 0.2$ for their best-fit atmospheric column density. The deflection of the incoming plasma around the satellite is thus roughly an order of magnitude weaker than at Io, where $\alpha_{Io} \approx 0.1$ (*Saur et al.* 1999). The incoming electrons might therefore reach the denser atmospheric layers already on the upstream hemisphere leading to the bright emission there. The electron energy in the flux tubes could then be partially depleted before they reach the flanks of Europa. However, there are several arguments against the depletion of the energy in the upstream hemisphere. First, the correlation of the auroral intensity to the local torus density implies that enough energy is available to enhance the emission, when more collisions take place. And second, the intensities observed in the wake side of $130-230$ R (OI] 1356 Å and OI 1304 Å combined, *Hall et al.* 1998, *Saur et al.* 2011) are principally on the same order of magnitude, i.e., the electrons are still hot enough to excite the atmosphere on the downstream hemisphere. Due to the effect of a considerably longer line of sight through the atmosphere at the limbs of the disk, the model of *Saur et al.* (1998) calculates a bright limb glow. This would be generally expected for a globally symmetric emission across the surface. Nonetheless, in most of the STIS observations the emission is clearly not enhanced at the limb. Results of the atmosphere model of *Plainaki et al.* (2012) suggest that the O_2 column density is more than two times higher at the sub-solar point than on the opposite side, see their Table 2. As the sub-solar point nearly coincides with the sub-observer point for Earth-bound observations, the highest O_2 abundance is always found roughly in the center of the disk in the HST images. As the auroral emission is presumably correlated to the O_2 abundance, this atmospheric asymmetry with an increasing O_2 abundance towards the sub-solar point possibly explains the observed morphology as well as the bright emission measured on the leading hemisphere in the GHRS and ACS observations.

We have also found that the anti-Jovian hemisphere is consistently brighter than the sub-Jovian hemisphere. *Saur et al.* (2000) have shown that such an asymmetry in the auroral brightness in favor of the anti-Jovian hemisphere can principally be explained by the ionospheric Hall effect. In case of Io, the Hall effect causes the anti-Jovian auroral spot to be roughly 40% brighter according to their model. For Europa, the asymmetry of the plasma flow pattern is presumably lower, as the Pedersen conductivity dominates the Hall conductivity due to the lower atmospheric densities. The estimated twist angle of the electron flow after Equation (2.15) is $\theta_{twist} = 14^\circ$ for Europa and is again roughly a factor of 2 lower than for Io. Results of the plasma model of *Saur et al.* (1998) indicate that the asymmetry is only slightly disturbed for an atmospheric column density of $N_{O_2} = 5 \times 10^{14}$ cm^{-2}. Although our analysis yields a somewhat higher O_2 column density, the Hall effect probably contributes to the observed asymmetry, but might not be the only reason. Another possible explanation is naturally an atmospheric asymmetry. Before western elongation, the sub-solar point and thus the maximum O_2 abundance after *Plainaki et al.* (2012) is found on the anti-Jovian hemisphere. If the point of the peak O_2 density lags behind the sub-solar point due to a thermal inertia of the atmosphere, a higher column density on the anti-Jovian hemisphere is indicated. However, such a sub-anti-Jovian asymmetry has neither been observed nor predicted by atmosphere models yet.

For an atmosphere consisting of solely molecular and atomic oxygen, the morphology of the OI] 1356 Å emission should be identical to the OI 1304 Å morphology. The long sticking coefficients and long travel times of the oxygen molecules principally imply a relatively even distribution across the surface. The observations, however, revealed striking differences between the emission patterns. In four of the five images, the OI 1304 Å morphology is marked by a bright spot that constantly stays in the northern, anti-Jovian quadrant. The bright emission is approximately located at 230 °W and 45 °N. It has been shown that the intensity is considerably enhanced with respect to the disk average brightness and that the spot clearly exceeds the normal variations across the surface.

An examination of a surplus of H_2O abundance has revealed that the observed OI] 1356 Å, OI 1304 Å and Lyman-α intensities in an area around the anomaly are principally in agreement with the existence of a local plume of water vapor. Although water plumes have never been detected at Europa, the shear stresses that presumably trigger the recently discovered plumes at Enceladus, should also be present at Europa (*Saur et al.* 2011). Based on the approach of *Nimmo et al.* (2007), *Saur et al.* (2011) calculated the mean resolved shear stress as proxy for a shear-heating rate on mapped lineaments on Europa for their analysis of ACS observations of Europa's aurora. After their calculations a peak in water vapor production is expected at exactly the plane-

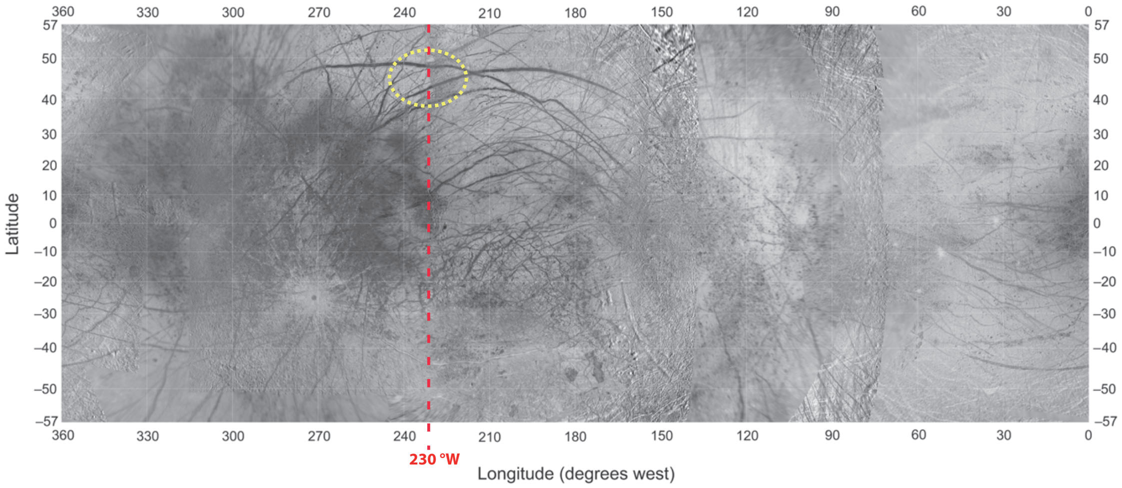

Figure 6.11: *Global mosaic of Europa's surface, in Mercator projection, based on Voyager and Galileo images (Kattenhorn and Hurford 2009, their Figure 1). The red line indicates the longitude where water vapor production is expected due to shear heating at the lineae after the calculations of Saur et al. (2011). The yellow circle shows the region around 230 °W and 45°N, where the surplus of OI 1304 Å emission is observed in the STIS images.*

tographic longitude of 230 °W, where the anomaly is observed. Figure 6.11 shows a global map of Europa's surface. The red dashed red line indicates the meridian, of the maximum shear stresses after *Saur et al.* (2011). *Greenberg et al.* (1998) calculate the tidal stresses on the surface due to a non-synchronous rotation of Europa's cryosphere, which is thought to be decoupled from the interior by the sub-surface liquid layer. Their calculations reveal a strong north-south tension centered at almost exactly the same longitude (225 °W). At the inferred latitude of the anomaly of 45 °N, two long prominent lineae, named *Minos Linea* and *Cadmus Linea*, run across Europa's surface. The two dark lineae form a cross at 210 °W, called the *Cadmus-Minos intersection region*, see Figure 6.11. Analyzing high-resolution images of Europa's surface obtained by Galileo *Geissler et al.* (1998) find that "Cadmus Linea" is among the youngest surface cracks in the area.

The striking agreement of the location of the OI 1304 Å anomaly, indicated by the yellow circe in Figure 6.11, with these findings indicates that a local ejection of water vapor might indeed be present in this area. However, the observed anomaly and the rough approximation of the H_2O abundance can not be seen as a proof for the existence of a water plume, since several inconsistencies and uncertainties have to be investigated in more detail.

The OI 1304 Å brightness in the area undergoes considerable variations between the first and last orbit. The variability could naturally be caused by a variability of the local water vapor production. A process causing such variations on time scales of hours is, however, not known. Moreover, a general hemispheric brightness asymmetry in both the OI] 1356 Å and OI 1304 Å aurora has been detected, which could not be finally explained. The ionospheric Hall effect probably disturbs the symmetry of the electron energy distribution in the atmosphere. As the anomaly is constantly located on the anti-Jovian hemisphere, such effects can not be separated in the STIS images. In addition to the bright spot in the northern, anti-Jovian quadrant, the OI 1304 Å morphology contains several other confined local intensity peaks. The reason for this general patchiness of the emission pattern is also unclear.

Furthermore, a highly increased atmospheric density in a locally confined area does not necessarily lead to increase of auroral intensity like assumed in the estimation of the H_2O abundance. In Chapter 5, we have shown that such a localized neutral gas cloud leads to a generation of a small extra Alfvén wing above the area in the case of the large Tvashtar volcano at Io's north pole, see Figure 5.5. The localized ionospheric peak leads to a deflection of the ambient plasma around the plume decreasing the emitted auroral emission. The estimated column density of the localized water plume of $\sim 10^{16}$ cm^{-2} is on the same order as the derived column density of the Tvashtar volcano and will therefore also affect the flow of the ambient plasma.

Taken together, the observed global brightness of the auroral emissions from Europa's atmosphere is consistent with the expected neutral gas abundance and local plasma parameters. The morphology of the OI] 1356 Å and OI 1304 Å aurora, in contrast, reveals several features, which are not in agreement with the expected distribution of the electron energy and neutral gas abundance. As for Io, a comprehensive model that takes into account the response of the plasma interaction to the atmospheric distribution around Europa is needed to simulate the effects self-consistently. The plasma and magnetic field environment might be even more complex than at Io due to the mutual effects of induction in Europa's putative sub-surface ocean and the ionospheric interaction with the magnetospheric plasma. The only model taking into account both effects was developed by a *Schilling et al.* (2007, 2008). The model, however, does not self-consistently calculate the temperature of the electrons, which has been shown to be essential for a correct description of the aurora generation.

7 Summary

In this thesis we present a detailed analysis of observations by the Hubble Space Telescope and by the New Horizons spacecraft of the auroral emissions emanating from the tenuous atmospheres of the Galilean moons Io and Europa. In Io's SO_2 dominated atmosphere, electron impact excitation of various atmospheric constituents leads to auroral emissions in the visible to far-ultraviolet wavelength range. Excitation of Europa's gas envelope with the main atmospheric constituent O_2 primarily produces FUV oxygen emissions. By studying the intensity and distribution of these auroral emissions, we are able to draw conclusions about the properties of the satellites' atmosphere and interior as well as the magnetospheric environment. In the case of Io, we analyze the full set of spatially resolved observations of Io's oxygen and sulfur UV aurora taken by the HST Space Telescope Imaging Spectrograph. Further, we analyze high-resolution images of Io's visible aurora taken by the NH Long-Range Reconnaissance Imager in combination with a simultaneous FUV observation by the HST Advanced Camera for Surveys. In the case of Europa, we investigate the spatially resolved HST STIS observations of the FUV oxygen emissions obtained in 1999.

The data processing of the HST STIS observations is explained step-by-step from the initial record of the 1024×1024-pixel detector to the extracted quasi-monochromatic images of the emissions from the near vicinity of the satellites. By adjusting the solar spectrum to the reflected continuum emissions we find a relatively constant, low FUV surface reflectivity of 1.7% and 1.4% for Io and Europa, respectively. The values are in agreement with previous results (*Hall et al.* 1998, *Feldman et al.* 2000). While the sulfur and oxygen emissions from Io's atmosphere are more than an order of magnitude higher compared to the surface reflected solar light, we show that for the analysis of Europa's atmospheric oxygen emission it is essential to take the reflected sunlight into account, which is of the same order of magnitude.

Io's auroral emissions have been analyzed frequently by various studies. However, in this thesis a comprehensive picture of Io's OI] 1356 Å, OI 1304 Å, SI 1479 Å, and SI] 1900 Å UV aurora is established based on the HST STIS observations taken between 1997 and 2001. We show that the variations of the observed emission pattern can be solely explained by the changes of the plasma environment and by the viewing perspective. Furthermore, the variations in brightness are strongly correlated with periodic variations of the ambient electron density. Based on these findings, we develop a phenomenological model for the spatial distribution of the oxygen and sulfur emissions in Io's vicinity. Taking into account Io's position with respect to the plasma torus, the orientation of the magnetic field and the viewing perspective of the observation, the model calculates the morphology and brightness of the auroral emission. By fitting the model parameters to the full set of STIS observations taken over five years, we find that the model is able to reproduce the main features in all OI] 1356 Å images with one parameter set. Even though the OI] 1356 Å, OI 1304 Å, SI 1479 Å, and SI] 1900 Å emissions reveal some differences, the spatial distribution turns out to be very similar for all four multiplets. The model allows us to infer the three-dimensional distribution of the aurora from the two-dimensional images. Additionally, we are able to separate variations caused by the viewing geometry and the influence of the changing magnetospheric conditions from actual temporal and spatial variations across the surface. Since the model for the UV aurora is able to reproduce the main features of the observed morphology by taking into account the variations of the magnetospheric parameters, it can even be applied to predict the emission of future UV aurora observations for a given time and observer.

Moreover, we infer quantitative properties for the distribution and total brightness of the oxygen and sulfur multiplets of Io's aurora. In contrast to previous investigations, the model results reveal that the majority of the radiation is emitted within 100 km above the surface. This includes the equatorial flank emission, which turns out to be brightest very close to the surface. The spots are shifted downstream and extend far into the wake region explaining observed features in the downstream region previously denoted *wake emission*. The asymmetric limb glow reveals a nearly 1:1 correlation with the electron energy stored in the flux tubes above and below Io, when the near-surface emission is analyzed separated from the background. The derived spatial distribution and the differences in the STIS eclipse observation clearly suggests a sublimation dominated atmosphere. The relative brightness of the equatorial spots is best explained by our model, if a difference of the flank emission intensities on the night and day side hemispheres is implemented. The evident brightness decrease in all emission multiplets observed during eclipse supports the idea of a wide collapse of the atmosphere in shadow. Additionally, the constancy of the aurora distribution over five years is consistent with a continuous neutral gas source like the sublimation of SO_2 frost, which is abundant all over Io's surface. If the atmosphere was directly supplied by volcanic outgassing, considerable spatial and temporal variations of the neutral gas abundance would be expected. A direct influence of local volcanic activity on the morphology has not been detected in the STIS observations.

In addition, we study the morphology of Io's aurora in eclipse by comparing simulation results of a three-dimensional two-fluid plasma simulation model (*Saur et al.* 1999) to high-resolution images by the NH LORRI and a simultaneous observation by the HST ACS. The simulation self-consistently calculates the plasma density, velocity, and temperature of the electrons and one ion species for a given atmospheric distribution. By using the simulated profiles for the electron properties in the vicinity of Io to calculate the auroral emissions, we include effects of the ionospheric current system on the electron flow in Io's vicinity. The simulation results are in suitable agreement with the observed morphology for an equatorial column density of $N_{eclipse} = (1-4) \times 10^{15}$ cm^{-2} corresponding to roughly 10% of the commonly assumed column density of the sunlit atmosphere. The LORRI images also reveal a huge glowing plume at the Tvashtar paterae close to the north pole. The emission from the excited plume particles enables us to constrain the plume gas content for the first time. The derived mean column density of $N_{plume} = 5 \times 10^{15}$ cm^{-2} indicates that Tvashtar is a high temperature, low pressure volcano. The total gas content of the huge plume corresponds to $\sim$10% of the gas in the equatorial atmosphere in eclipse supporting the idea of an atmosphere that is sustained almost solely by sublimation even in shadow. Despite the partial collapse of the atmosphere, the appearance of the aurora in eclipse is principally similar to the aurora in sunlight. The morphology is still dominated by the bright equatorial spots, even though they appear to be more localized in eclipse. This means that although the interaction strength is considerably lower, the electrons are still deflected around Io depositing their energy preferably on the flanks.

We infer mixing ratios of atomic oxygen and sulfur to SO_2 on the order of 10% and 2%, respectively, in the surface-near atmosphere. The resulting relative abundance of S/O is $\sim$0.2, which is in agreement with previous observations. According to the intensities of the extended emission in the STIS images, the relative sulfur to oxygen abundance is even lower in Io's corona as predicted by atmospheric models (*Summers and Strobel* 1996, *Wong and Smyth* 2000). The derived sodium mixing ratio of 0.12% is also in agreement with the previously inferred abundance of *Geissler et al.* (2004).

Furthermore, we address another interesting phenomenon: The rocking of Io's bright equatorial spots has been observed to follow the variation of the orientation of the Jovian magnetic field with an amplitude that is attenuated by roughly 20% (*Retherford et al.* 2000). The tilt of the spots in the phenomenological model was also fitted to 80% of the tilt of the background field. Measuring the angle of the tilted spot locations with respect to Io's equator shows that the tilt is subject to a negative offset in addition to the attenuated amplitude. We demonstrate that atmospheric inhomogeneities can be ruled out as cause for these deviations. A rough estimation of the field perturbations due to the ionospheric currents is not in agreement with the observed deviation of the spot angle from the background field tilt. However, due to the deceleration of the plasma by the collisions with the atmospheric gas, the ambient magnetic field is presumably delayed with respect to the fully corotating magnetosphere. The orientation of the delayed magnetic field yields a slightly better agreement with the measured tilt of the spots, but it still can not explain the observed variation. We also calculate the effects of an induced magnetic field in a putative conductive magma layer under Io's rigid crust, which has been suggested by various studies (e.g., *Keszthelyi et al.* 2004). Although the variation of the background field is attenuated close to Io due to the induction signals, which is in agreement with the attenuated amplitude of the spot rocking, the phase shift of the induced magnetic field causes a shift in the magnetic field variation that is exactly opposed to the detected temporal delay of the spot tilt. For a highly conductive layer, the induction completely shields the variation of the background field close to the surface leading to strongly attenuated rocking of the aurora spots. Hence, a magma layer with conductivities on the order of $0.5\,\mathrm{S\,m^{-1}}$ as proposed by *Khurana et al.* (2011) is not consistent with observed spot variations according to our approximation. However, to accurately determine the magnetic field topology, all effects, i.e., the plasma interaction, induction and atmospheric inhomogeneities have to be incorporated self-consistently. Further, there are numerous additional observations providing the possibility to measure and investigate the rocking of the equatorial spots, as Io's auroral emission in eclipse has been observed many times by the Galileo and Cassini spacecrafts (*Geissler et al.* 1999, 2001, 2004).

The spatial distribution of Europa's weak oxygen aurora has been scarcely investigated so far. In this thesis we carry out the first detailed analysis of the morphology and brightness of the OI 1304 Å and OI] 1356 Å emissions in the STIS images obtained during five HST orbits in 1999. The emission pattern of both oxygen multiplets differs considerably from the morphology of Io's aurora. Roughly 70% of the radiation is emitted within the cross section of Europa's disk. We demonstrate that the OI] 1356 Å emission pattern is clearly correlated to Europa's position with respect to the plasma torus. Moreover, a constant hemispheric asymmetry is detected with a higher intensity on the anti-Jovian side for both multiplets. Recent modeling results by *Plainaki et al.* (2012) indicate that the O_2 abundance is roughly two times higher on the sub-solar hemisphere. This asymmetry possibly explains that most emission is seen on the disk as the day side hemisphere almost coincides with the visible hemisphere for an Earth-bound observer.

In the OI 1304 Å emission an exceptionally high intensity is detected in a confined region in the northern, anti-Jovian quadrant of Europa's disk. The OI] 1356 Å emission as well as the surface reflected Lyman-α and CII 1335 Å are, in contrast, not enhanced in this region with respect to the ambient intensity. Furthermore, the OI 1304 Å anomaly does not follow the expected north-south variations due to Europa's changing location in the plasma torus. According to calculations of the shear heating on Europa's lineae by *Saur et al.* (2011), a peak in water vapor production is predicted at exactly the observed longitude of the OI 1304 Å anomaly. A rough approximation of the expected OI] 1356 Å, OI 1304 Å and Lyman-α brightnesses reveals that the anomaly is consistent with a locally confined abundance of water vapor with a column density of $N_{\mathrm{H_2O}} = 2.6 \times 10^{16}$ cm^{-2}. However, for the estimated atmospheric abundances we neglected the interaction of the magnetospheric plasma with Europa's atmosphere. Again, to accurately determine the effects of an asymmetric O_2 atmosphere and the influence of a local water plume, the plasma interaction has to be taken into account.

Although we shed light on some of the key issues regarding the aurorae of Io and Europa, we have also brought up interesting questions, which could not be definitely answered in this thesis. The rocking of Io's bright equatorial spots appears to be inconsistent with the expected perturbations of the magnetic field. Still, the investigation of the auroral spots possibly allows a remote sensing of the magnetic field topology in regions very close to Io's surface, which are not accessible for flyby in-situ measurements of spacecrafts. The anomalously bright spot of Europa's OI 1304 Å aurora raises the exciting question, whether gaseous water is ejected through cracks of Europa's surface similar to the geysers found on Enceladus' south pole. In November or December this year, the Space Telescope Imaging Spectrograph will monitor Europa's FUV emission for a second time during ten HST orbits. These observations will potentially provide evidence for the abundance of liquid water on Europa.

A Data processing

A.1 Observational parameters

All orbital parameters of the spacecrafts, telescopes and satellites including the distance and phase angles of the Sun and Earth, and the magnetospheric parameters of the Jovian System III are computed using the SPICE toolkit provided by the Navigation and Ancillary Information Facility (NAIF). The computed coordinates refer to the given observation time minus the light travel time from Jupiter to the Earth of approximately 35−45 minutes. In the case of the LORRI and ACS eclipse observations the mid-eclipse time is used as reference time. A description of the SPICE system and data can be found in *Acton* (1996). The software is available for download at http://naif.jpl.nasa.gov/naif/.

The definition of the orbital longitude (OLG) as seen from HST, designated φ_{obs}, or the sun, designated φ_{sun}, is depicted in Figure A.1. With this definition, the orbital longitude corresponds to the sub-observer and sub-solar central meridian west longitude in the satellite-centered coordinate system due to the synchronous rotation of Io and Europa with their orbital periods. All longitude values φ in this thesis refer to the *west* longitude, where $\varphi = 0$ corresponds to the longitude of the Jovian facing meridian on Io and Europa, respectively.

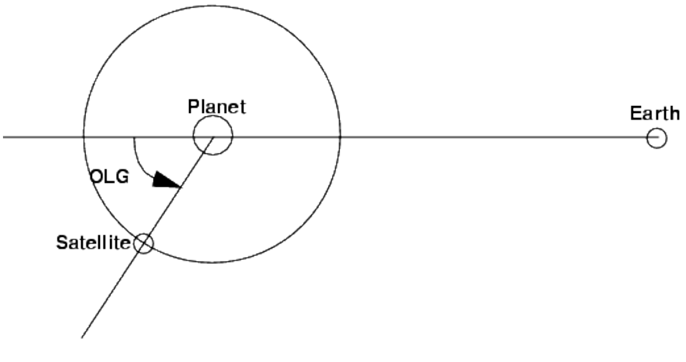

Figure A.1: *Definition of orbital longitude (OLG) of a satellite as seen from Earth (or Sun).*

The Jovian System III, which is based on the rotation of Jupiter's magnetic field, was first defined by *Seidelmann and Divine* (1977). The magnetic latitude can be approximated by

$$\psi_m = \theta^M \cos\left(\lambda_{III} - \lambda_{III}^M\right) \tag{A.1}$$

(*Dessler* 1983), where λ_{III}^M is the System III longitude of Jupiter's magnetic south pole, and θ^M

the tilt between the magnetic and polar axes. For the VIP4 model of Jupiter's magnetic field, $\lambda_{III}^{M} = 200.8$ and $\theta^{M} = 9.5°$ (*Weiss* 2004). With this definition, ψ_m is positive, when the magnetic equator is below the satellites. The distance of the satellites to the centrifugal equator is given by

$$z_c = d_{Jup} \tan(\psi_c) \tag{A.2}$$

with the distance of the satellite to the center of Jupiter d_{Jup} and the centrifugal latitude $\psi_c = \frac{2}{3}\psi_m$.

A.2 STIS Geometry

The STIS coordinate frames in the plane perpendicular to the line of sight (V_1-axis) are depicted in Figure A.2. Due to a slight tilt between the aperture and detector axes, the slit is not perfectly aligned with the y_d-axis in the images. In the *flt* data files, there is an additional small tilt between the dispersion axis and the x_d-axis of the detector, which is corrected for the *x2d* files used in this work. All analyzed STIS images are rotated into the Jovian coordinate system, i.e., the vertical axis is parallel to the rotation axis of Jupiter. The angle between the vertical axis of the detector coordinate system in the images and Celestial North is given in the file header ("ORIENTAT"). The coordinate transformation from the Celestial to the Jovian system is computed with SPICE.

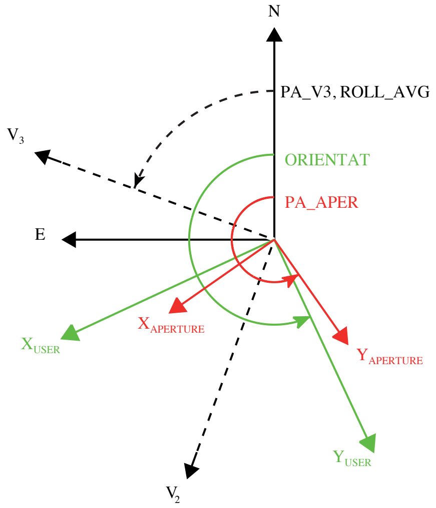

Figure A.2: *STIS coordinate systems. The orientation of the aperture (slit) is shown in red, where the long slit axis is parallel to $Y_{APERTURE}$. The orientation of the detector has a small tilt with respect to the aperture of $\lesssim 1.5°$. The detector or user axes (green, X_{USER}, Y_{USER}) represent the dispersion (designatd x_d in this work) and cross-dispersion directions (y_d in this work). V_2 and V_3 specify the general HST coordinate system, which is completed by the V_1 pointing towards the object.*

The physical location of a pixel is set to the lower left corner. Using this definition each pixel is clearly assigned if the image is subdivided through the origin, e.g., for a separate analysis of the left and right or northern and southern hemispheres.

A.3 Throughput correction (STIS)

The wavelength dependent throughput determines the percentage of the incoming photons passing through the system. Thus, the total throughput for the used optical elements converts the amount of photons reaching the telescope to the amount of detector counts. The processing of the *x2d* files includes a flux conversion, which takes into account the system throughput assuming a continuum point source. Within the extracted emission images the radiation is assumed to be monochromatic (or consisting of few discrete lines of a multiplet), i.e., the wavelength dependency along the dispersion axis of the extracted images has to be eliminated.

Throughput curves for the used grating and aperture are obtained from the calibration files, which are specified in the header of the data files. The integrated system throughput for spectroscopic images obtained with the G140L grating is shown in Figure A.3. The dashed lines indicate the analyzed emission lines and the shaded areas represent the width of the extracted emission images along the dispersion axis (corresponding 3 $R_{\mathrm{Io/Eur}}$). For each pixel in the image the intensity $I_0(x_d, y_d)$ is corrected by

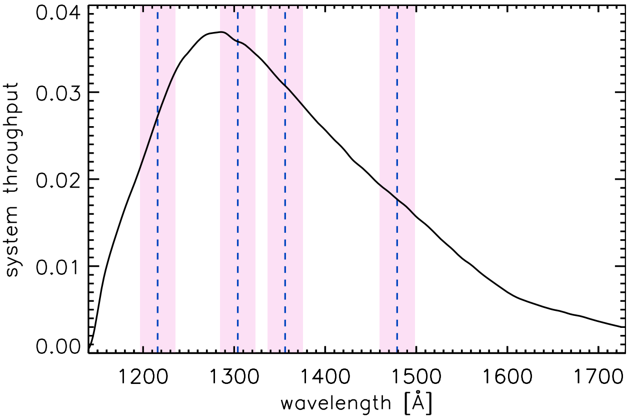

Figure A.3: *Wavelength dependent system throughput for G140L grating (solid black). The dashed blue lines with the shaded areas show the central wavelength and the approximate width (3 $R_{\mathrm{Io/Eur}}$) along the dispersion axis of the extracted HI 1216 Å, OI 1304 Å, OI] 1356 Å und SI 1479 Å images.*

$$I_{cor}(x_d, y_d) = \frac{I_0(x_d, y_d)}{T(\lambda_d)} \cdot T(\lambda_{emis}), \tag{A.3}$$

with the wavelength dependent throughput $T(\lambda_d)$, the wavelength of the pixel on the dispersion axis λ_d and the central wavelength of the emission multiplet λ_{emis} (e.g., 1356 Å). The system throughput curves for the G140M and G230M observations are not shown here. For G140M, $T \approx 0.02$ at OI] 1356 Å and $T \approx 0.01$ at SI 1479 Å, for G230M the throughput is an order of magnitude lower with $T(\lambda = 1900\,\text{Å}) \approx 0.004$. The wavelength dependent throughput of the 52"×2" aperture, which varies between 0.96 and 0.98, is corrected accordingly.

A.4 Unit conversions (STIS)

A.4.1 Solar radiation

The processing of the STIS observations includes a subtraction of the reflected solar radiation for each pixel. The solar spectral irradiance $F_{\text{refl-sun}}$ in [W m^{-3}] or in [erg cm^{-2} s^{-1} Å^{-1}] in the cgs system is converted to spectral radiance of a pixel in [erg cm^{-2} s^{-1} Å^{-1} arcsec^{-2}] as given in the *x2d* files. Therefore, $F_{\text{refl-sun}}$ is divided by the pixel plate scales:

$$L_{\text{refl-sun}}[\text{erg cm}^{-2}\,\text{s}^{-1}\,\text{Å}^{-1}\,\text{arcsec}^{-2}] = \frac{F_{\text{refl-sun}}[\text{erg cm}^{-2}\,\text{s}^{-1}\,\text{Å}^{-1}]}{m_{x_d}[\text{arcsec}]\cdot m_{y_d}[\text{arcsec}]}\,. \tag{A.4}$$

The place scale is the range that each pixel of the detector spans in one direction. For the G140L grating m_{x_d} and m_{y_d} are 0.0246 arcsec, for the medium resolution gratings G140M and G230M the plate scales are ∼0.030 arcsec .

A.4.2 Flux conversion

The conversion of the spectral flux $L(\lambda_d)$ of a pixel in [erg cm^{-2} s^{-1} Å^{-1} arcsec^{-2}] as given in the *x2d* files to brightness I in Rayleigh [R] is calculated via

$$I\,[\text{R}] = L(\lambda_d)\cdot\frac{\lambda_d}{hc}\cdot\Delta\lambda\cdot W\cdot\left(\frac{3600\cdot 360}{2\pi}\right)^2\cdot\frac{4\pi}{10^6}\,. \tag{A.5}$$

The division through $\frac{hc}{\lambda_d}$ [erg] eliminates the wavelengths dependent energy with the wavelength of the pixel λ_d, Planck's constant h and the speed of light c. $\Delta\lambda$ is the dispersion of the grating in [Å pixel^{-1}], W is the slit width in [pixel]. The last two terms account for the conversion from [arcsec^2] to steradian [sr] and the definition of the unit Rayleigh:

$$1[\text{R}] = \frac{10^6}{4\pi}\,[\text{cm}^{-2}\,\text{s}^{-1}\,\text{sr}^{-1}]\,. \tag{A.6}$$

A.4.3 Background emission error

The pixel error values σ_0 stored in the second file extension of the *x2d* files have been converted to spectral flux according to the conversion of the measured signal. The error of the detected background emission I_{bg} in [erg cm^{-2} s^{-1} Å^{-1} arcsec^{-2}] is the square root of the Poisson distributed background counts multiplied with the conversion factor from counts to spectral flux c_{flux}:

$$\sigma_{bg} = c_{flux}\cdot\sqrt{I_{bg}/c_{flux}}\quad . \tag{A.7}$$

The propagated total error for the intensity

$$I_{tot} = I_0 - I_{bg} - I_{sun} \tag{A.8}$$

with the measured flux I_0 and the reflected sunlight I_{sun} (with error σ_{sun}) is given by

$$\sigma_{tot}\,[\mathrm{erg\,cm^{-2}\,s^{-1}\,\mathring{A}^{-1}\,arcsec^{-2}}] = \sqrt{\sigma_0^2 + \sigma_{bg}^2 + \sigma_{sun}^2}\,. \tag{A.9}$$

A.5 HST point spread functions

To simulate observational telescope data it is necessary to account for the light scattering and diffraction in the optical system of the telescope. The scattering and diffraction properties are usually described by the point spread function (PSF). The *Tiny Tim* simulation software package is the standard software for modeling HST point spread functions (*Krist* 1995, *Krist et al.* 2011). The software package is available for download or can be used directly online via a web-based interface (tinytim.stsci.edu). The PSF modeling takes into account camera obscurations, aberrations, pointing errors as well as the system wavelength response. For a detailed description of the tool the reader if referred to *Krist et al.* (2011).

In our analysis, the STIS PSF is used to correctly model the disk reflected solar radiation and to generate two-dimensional images from the phenomenological aurora distribution model that are directly comparable to the observation images. Therefore, PSF for the STIS FUV-MAMA and NUV-MAMA detectors are modeled with the *Tiny Tim* tool (Version 7.4). The modeled PSF depend on the wavelength and thus vary slightly within the observed wavelength bands. Figure A.4 a-c shows STIS FUV PSF for a pixel resolution of 0.0246" (plate scale of G140L) at 1216 Å (Lyman-α), 1425 Å (central wavelength of G140L) and 1650 Å. The diameter of the modeled PSF is set to $\sim$1", which correpsonds to 40 pixels for G140L images and 33 pixels for the G140M/G230M observations. Within this diameter the PSF decreases down to $\lesssim 10^{-4}$ of the maximum value in the center, i.e., all spreading further than 1" from the center can be neglected.

To validate the modeled spreading, a STIS FUV-MAMA spectrum of star BD +75 325 obtained with the G140L grating is used (HST Proposal ID 10040). The star trace along the dispersion axis is shown in Figure A.4 d. To check the PSF properties, the observed spread signal is reduced to a line spectrum by setting the maximum pixel along y_d to the total of the y_d column for each x_d along the dispersion axis, see Figure A.4 e. The trace is not exactly aligned with the x_d-axis as the *flt* data is used to avoid further distortion of the original signal due to processing of the *x2d* data. The line spectrum is convolved with the modeled PSF for the central wavelength (1425 Å) and compared to the observed spectrum (Figure A.4 f). Figure A.5 (right) shows profiles along y_d of the observed and modeled spectra integrated along the dispersion axis from $\lambda_d = 1325$ Å to 1525 Å. The modeled spreading is in good agreement with the observed profile considering the uncertainties of the simplified reduction of the line spectrum and the possible influences of the wavelength dependency of the PSF. There are, however, slight deviations, particularly at pixels 4 and 5 in Figure A.5 (right). The deviation possibly originates from the discretized PSF, since the point source is smaller than the used pixel plate scale. Similar differences between modeled flux profiles using the *Tiny Tim* tool and STIS observations of star BD +75 325 could also not been explained by *Harper and Brown* (2006).

To calculate the scattering of the reflected sunlight, the PSF for the respective analyzed emission wavelength (e.g., PSF(λ=1356 Å) for OI] 1356 Å) is modeled and convolved with the 2-D array of the disk reflected continuum.

To account for the telescope scattering in the images generated with the phenomenological aurora model (Section 4.2) , oversampled PSF are computed with a four times higher spatial resolution (or four times lower pixel plate scale). The modeled PSF is rotated to the Jovian system (vertical axis is aligned with the Jovian rotation axis) according to the rotation of the respective observation image and resized to the actual pixel plate scale of the used grating. Rotating the oversampled PSF maintains spatial scattering information, as the spatial resolution of the *Tiny Tim* PSF simulation is higher than the detector resolution (*Krist et al.* 2011). Although the scattering in the telescope is continuous rather than spatially discrete like the detector array, the convolution of the modeled emission pattern and the PSF is carried out after the binning both arrays to the resolution of the STIS images. A higher spatial resolution for the convolution would increase the computing for fitting the model images to the observations ($\sim 6 \times 10^4$ data points) time significantly, but hardly improve the accuracy considering the uncertainty of the modeled PSF.

For the analysis of the ACS SBC F125LP filter observation in Chapter 5, the simulated emission patterns are convolved with the point spread function. Therefore, the PSF with a diameter of 1" and with the spatial resolution of the ACS MAMA detector is modeled using the *Tiny Tim* tool.

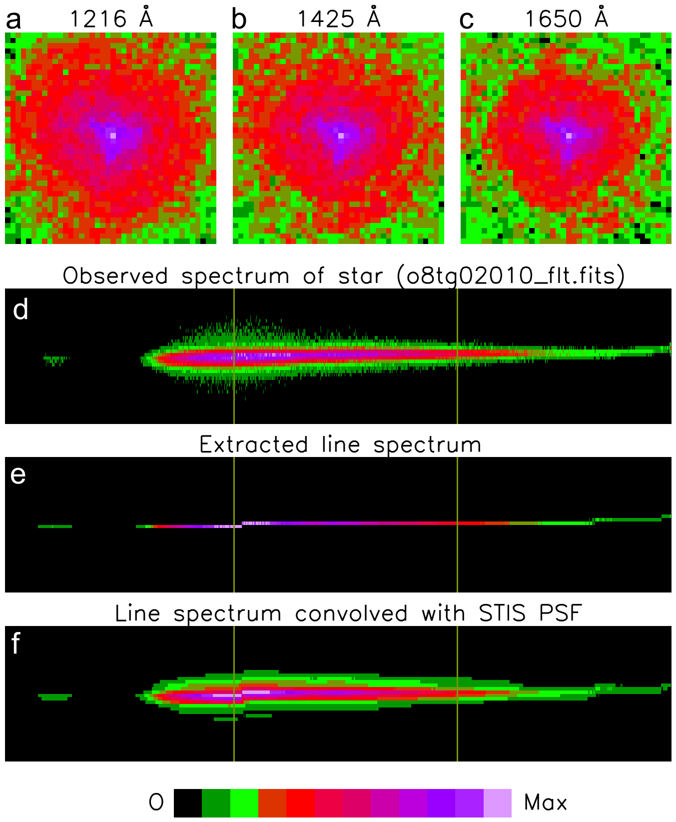

Figure A.4: *(a-c) Modeled STIS PSF for 1216 Å (red), 1425 Å and 1650 Å. The color scales of (a-c) are logarithmic. (d) Observed star spectrum. (e) Extracted line spectrum (trace). (f) Convolution of line spectrum (e) with modeled 1425 Å PSF (b). The color scales of (d-f) are linear.*

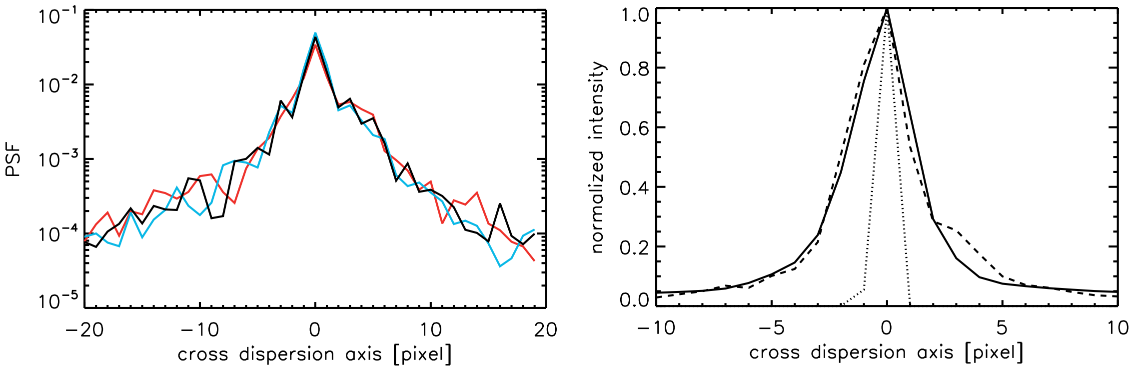

Figure A.5: *(Left) STIS PSF for 1216 Å (red), 1425 Å (black) and 1650 Å (blue) along cross dispersion axis. The scattering slightly increases towards shorter wavelengths. (Right) Observed (solid) and modeled (dashed) star spectrum integrated along the dispersion axis from 1325 Å to 1525 Å. The star point source (dotted) is distributed over 2 pixels as the trace is not fully aligned with the x_d-axis, see Figure A.4 e.*

B STIS observations and model images

B.1 O I 1304 Å

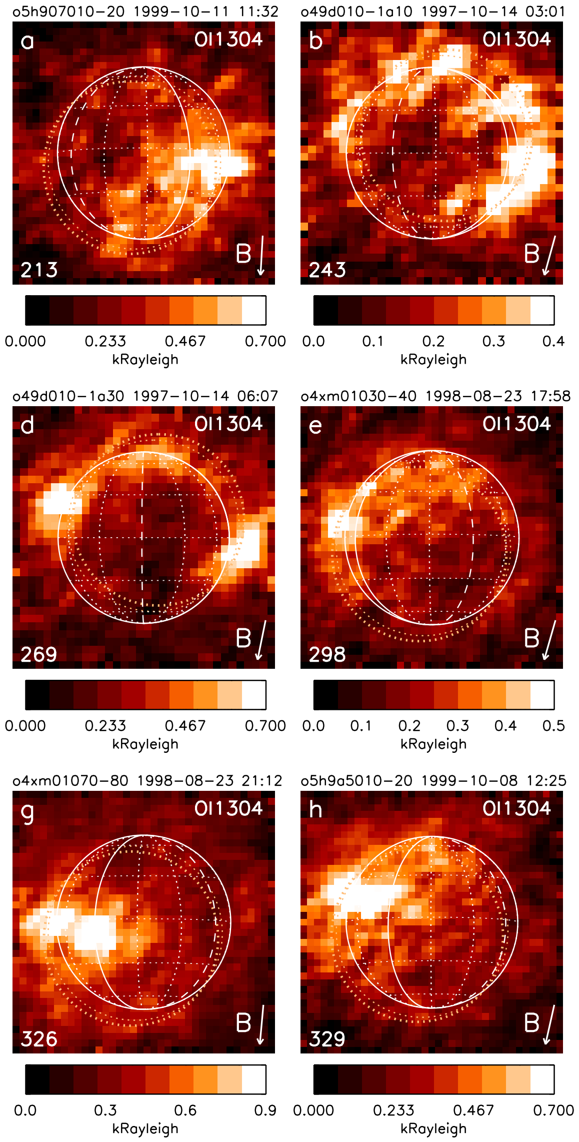

Figure B.1: *STIS images of the OI 1304 Å aurora ordered by sub-observer longitudes from* $\varphi_{obs} = 213°$ *(a) to* $\varphi_{obs} = 329°$ *(h) (around western elongation). The sub-observer longitude is specified in the lower left corner, the arrow in the lower right corner shows the direction of the background magnetic field. For further explanations see Figure 4.1. The observation parameters are listed in Table 4.2.*

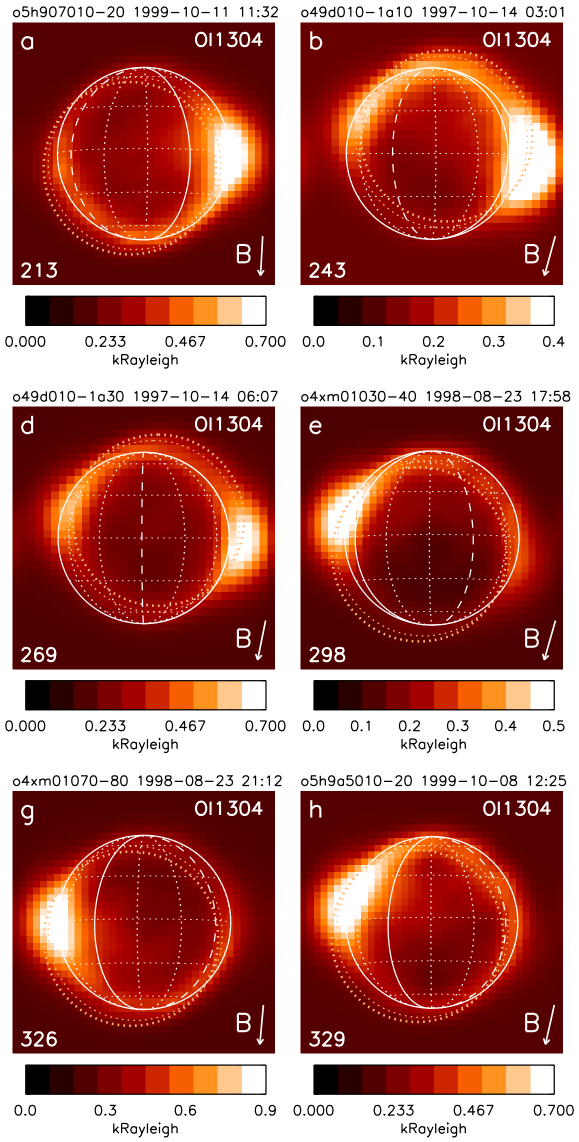

Figure B.2: *Modeled images of the OI 1304 Å aurora corresponding to the observations of Figure B.1. For the model parameters see Table 4.6.*

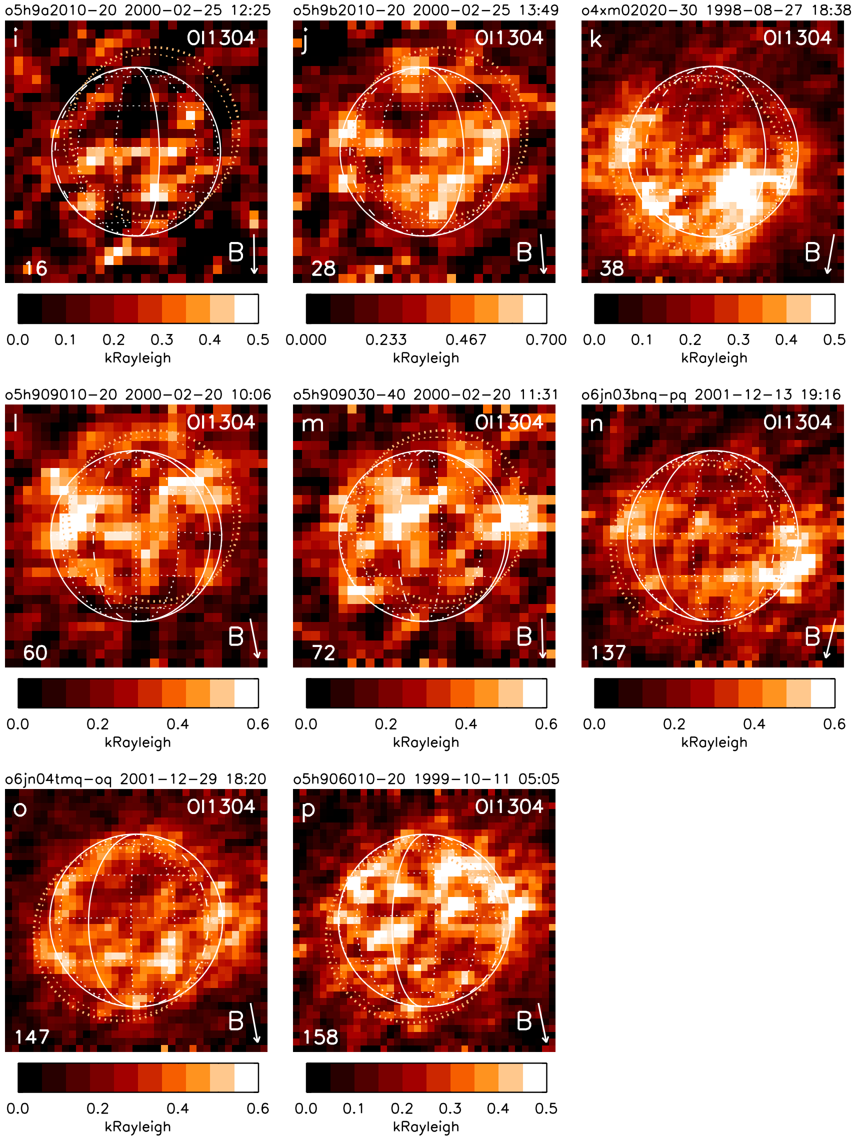

Figure B.3: *STIS images of the OI 1304 Å aurora ordered by sub-observer longitudes from* $\varphi_{obs} = 16^\circ$ *(i, eclipse) to* $\varphi_{obs} = 158^\circ$ *(p) (after eclipse / around eastern elongation). For further explanations see Figure 4.1.*

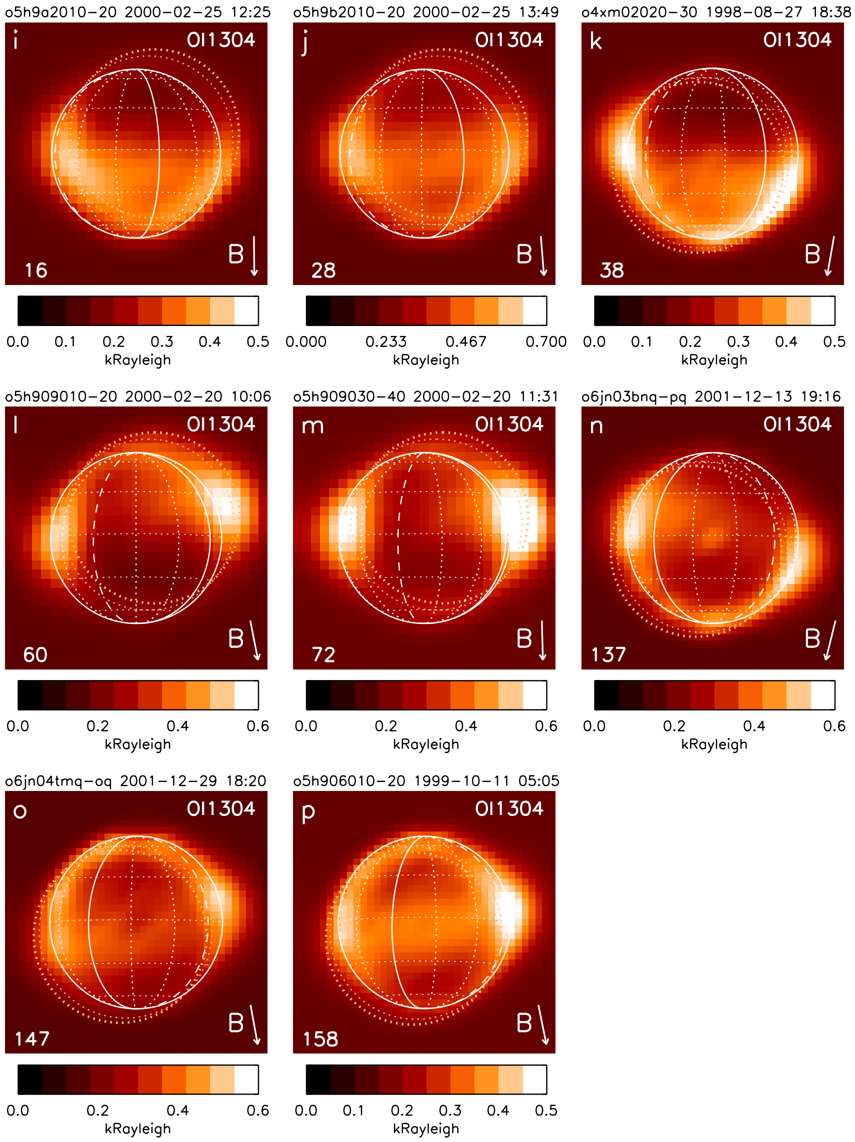

Figure B.4: *Modeled images of the OI 1304 Å aurora corresponding to the observations of Figure B.3. For the model parameters see Table 4.6.*

B.2 SI 1479 Å

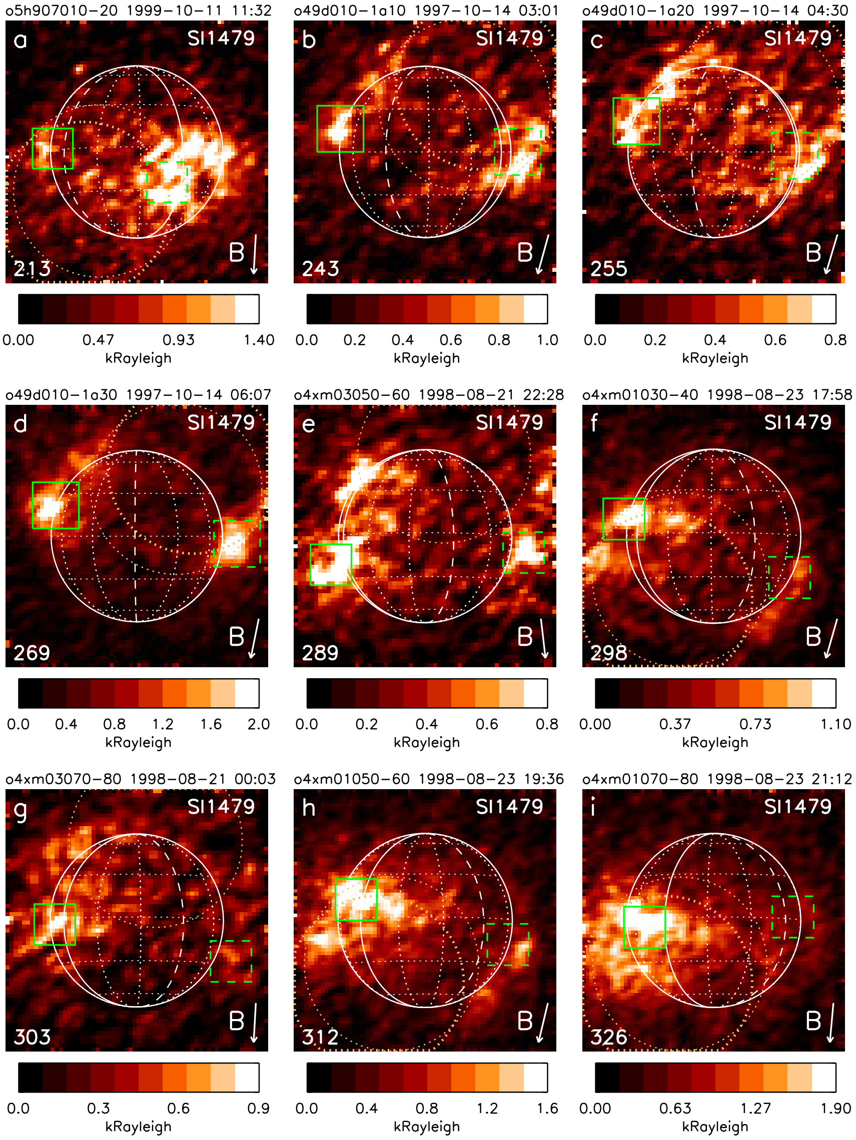

Figure B.5: *STIS images of the SI 1479 Å aurora ordered by sub-observer longitudes from* $\varphi_{obs} = 213^\circ$ *(a) to* $\varphi_{obs} = 326^\circ$ *(i) (around western elongation). The sub-observer longitude is specified in the lower left corner, the arrow in the lower right corner shows the direction of the background magnetic field. The green boxes indicate the sub-Jovian (solid) and anti-Jovian (dashed) equatorial spots. The spot locations are not included in our analysis, as the determination is hampered by the multiplet lines. For further explanations see Figure 4.1. The observation parameters are listed in Table 4.2.*

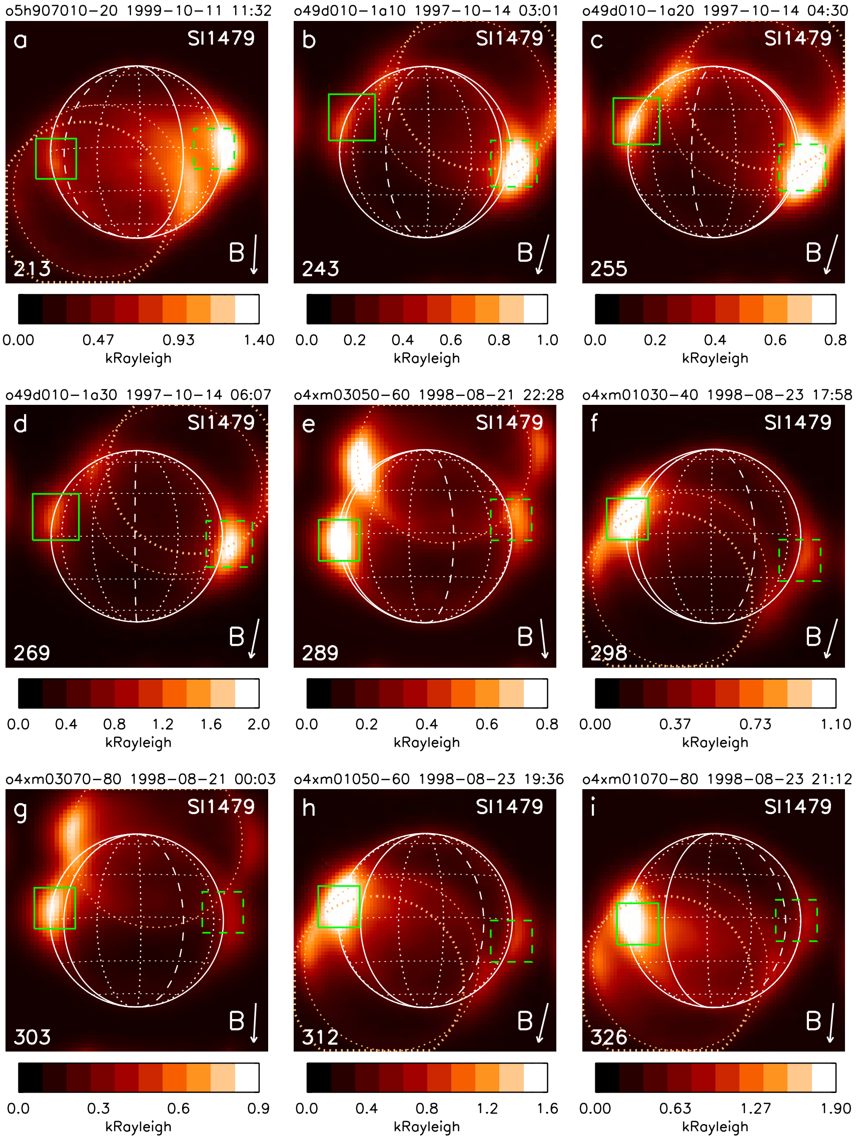

Figure B.6: *Modeled images of the SI 1479 Å aurora corresponding to the observations of Figure B.5. For the model parameters see Table 4.7.*

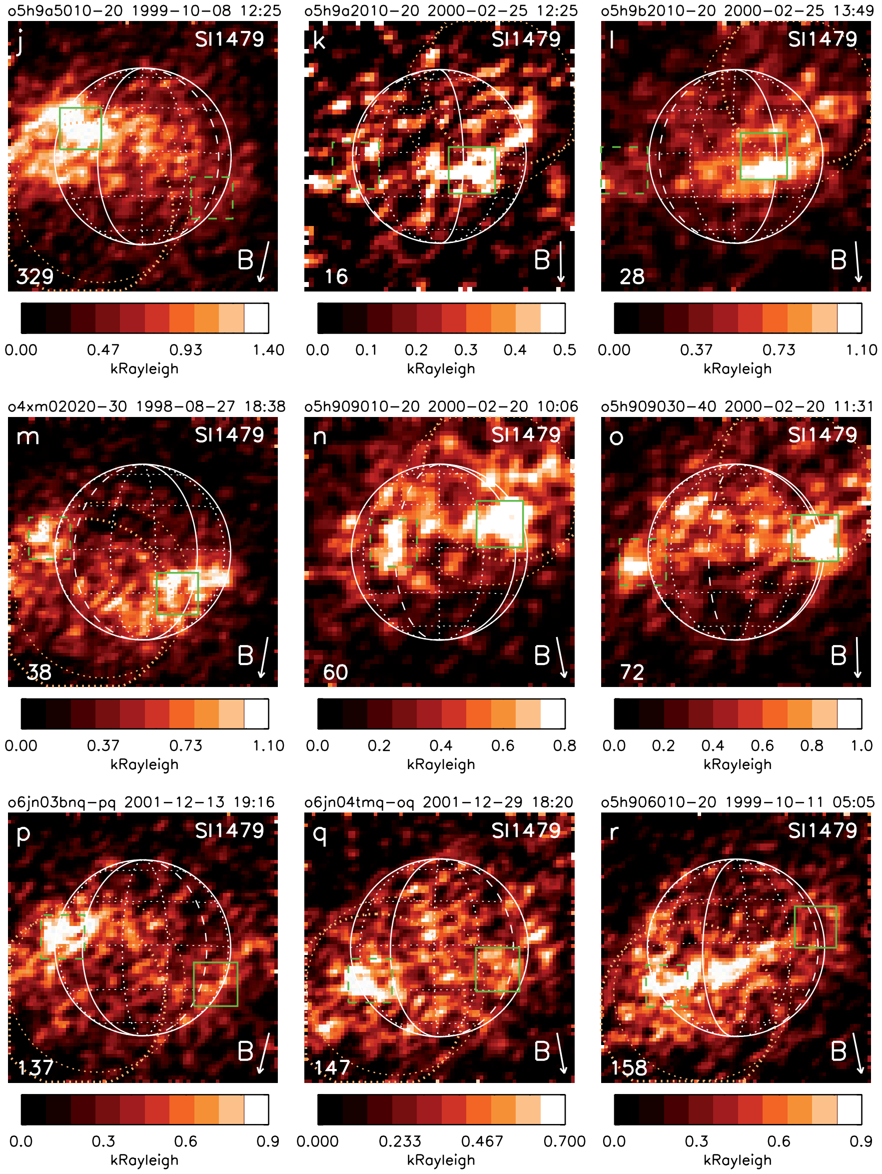

Figure B.7: *STIS images of the SI 1479 Å aurora ordered by sub-observer longitudes from* $\varphi_{obs} = 329^\circ$ *(j, before eclipse),* $\varphi_{obs} = 16^\circ$ *(k, eclipse), and* $\varphi_{obs} = 28^\circ$ *(l) to* $\varphi_{obs} = 158^\circ$ *(i) (around eastern elongation). For further explanations see Figures B.5 and 4.1.*

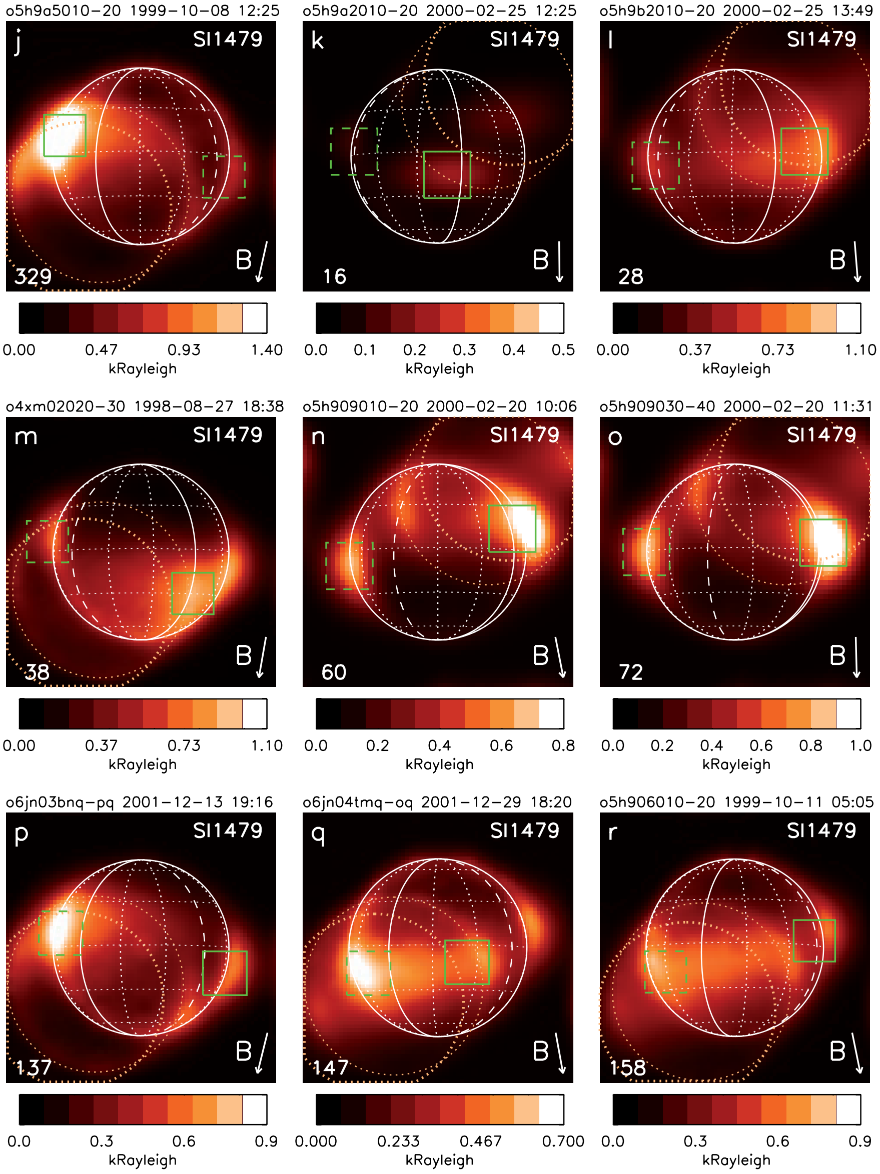

Figure B.8: *Modeled images of the SI 1479 Å aurora corresponding to the observations of Figure B.7. For the model parameters see Table 4.7.*

B.3 SI] 1900 Å

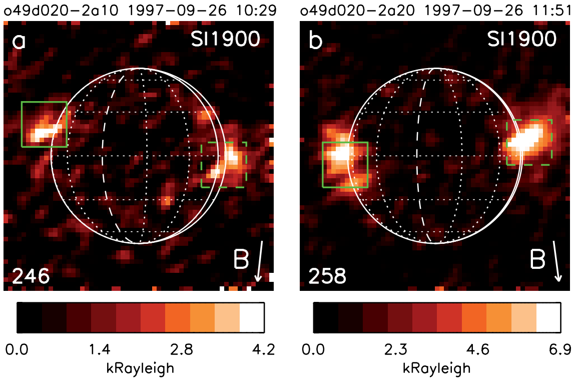

Figure B.9: *STIS images of the SI] 1900 Å aurora. The green boxes indicate the sub-Jovian (solid) and anti-Jovian (dashed) equatorial spots. The spot locations are included in our analysis in Section 4.3. The sub-observer longitude is specified in the lower left corner, the arrow in the lower right corner shows the direction of the background magnetic field. For further explanations see Figure 4.1. The observation parameters are listed in Table 4.2.*

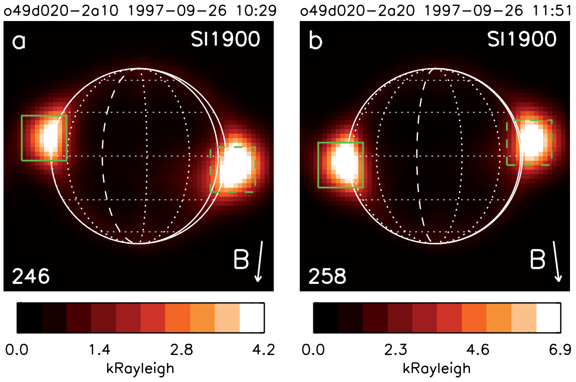

Figure B.10: *Modeled images of the SI 1479 Å aurora corresponding to the observations of Figure B.9. For the model parameters see Table 4.8.*

Bibliography

Acton, C. H., Ancillary data services of NASA's Navigation and Ancillary Information Facility, *Planet. Space Sci.*, *44*, 65–70, 1996.

Ajello, J. M., G. K. James, I. Kanik, and B. O. Franklin, The complete UV spectrum of SO2 by electron impact. I - The vacuum ultraviolet spectrum, *J. Geophys. Res.*, *97*, 10,473–10,500, 1992.

Ajello, J. M., W. R. Pryor, C. A. Barth, C. W. Hord, A. I. F. Stewart, K. E. Simmons, and D. T. Hall, Observations of interplanetary Lyman-alpha with the Galileo Ultraviolet Spectrometer: Multiple scattering effects at solar maximum, *Astronomy and Astrophysics*, *289*, 283–303, 1994.

Anderson, J. D., G. Schubert, R. A. Jacobson, E. L. Lau, W. B. Moore, and W. L. Sjogren, Europa's differentiated internal structure: Inferences from four Galileo encounters, *Science*, *281*, 2019–2022, 1998.

Austin, J. V., and D. B. Goldstein, Rarefied Gas Model of Io's Sublimation-Driven Atmosphere, *Icarus*, *148*, 370–383, 2000.

Bagenal, F., Empirical model of the Io plasma torus: Voyager measurements, *J. Geophys. Res.*, *99*(A6), 11,043–11,062, 1994.

Bagenal, F., and P. A. Delamere, Flow of mass and energy in the magnetospheres of Jupiter and Saturn, *J. Geophys. Res.*, *116*, A05209, 2011.

Ballester, G. E., H. W. Moos, P. D. Feldman, D. F. Strobel, M. E. Summers, J. Bertaux, T. E. Skinner, M. C. Festou, and J. H. Lieske, Detection of neutral oxygen and sulfur emissions near Io using IUE, *Astrophys. J.*, *319*, L33–L38, 1987.

Ballester, G. E., D. F. Strobel, H. W. Moos, and P. D. Feldman, The atmospheric abundance of SO_2 on Io, *Icarus*, *88*, 1–23, 1990.

Ballester, G. E., M. A. McGrath, D. F. Stobel, X. Zhu, P. D. Feldman, and H. W. Moos, Detection of the SO_2 atmosphere on Io with the Hubble Space Telescope, *Icarus*, *111*, 2–17, 1994.

Banks, P. M., and G. Kockarts, *Aeronomy*, vol. B, Academic Press, San Diego, Calif., 1973.

Bellucci, G., et al., Cassini/VIMS observation of an Io post-eclipse brightening event, *Icarus*, *172*, 141–148, 2004.

Bevington, P. R., and D. K. Robinson, *Data reduction and error analysis for the physical sciences*, McGraw-Hill, 2003.

Bierhaus, E. B., K. Zahnle, and C. R. Chapman, Europa's Crater Distributions and Surface Ages, in *Europa*, edited by R. T. Pappalardo, W. B. McKinnon, and K. K. Khurana, p. 161, University of Arizona Press, 2009.

Binder, A. B., and D. P. Cruikshank, Evidence for an Atmosphere on Io, *Icarus*, *3*, 299, 1964.

Bouchez, A. H., M. E. Brown, and N. M. Schneider, Eclipse Spectroscopy of Io's Atmosphere, *Icarus*, *148*, 316–319, 2000.

Broadfoot, A. L., et al., Extreme ultraviolet observations from Voyager 1 encounter with Jupiter, *Science*, *204*, 979–982, 1979.

Brown, M. E., Potassium in Europa's Atmosphere, *Icarus*, *151*, 190–195, 2001.

Brown, M. E., and R. E. Hill, Discovery of an extended sodium atmosphere around Europa, *Nature*, *380*, 229–231, 1996.

Brown, R. A., and F. H. Chaffee, Jr., High-Resolution Spectra of Sodium Emission from Io, *Astrophys. J.*, *187*, L125, 1974.

Brown, W. L., W. M. Augustyniak, E. Simmons, K. J. Marcantonio, L. J. Lnazerotti, R. E. Johnson, C. T. Reimann, G. Foti, and V. Pirronello, Erosion and molecular formation in condensed gas films by electronic energy loss of fast ions, *Nuclear Instruments and Methods in Physics Research A*, *198*, 1–8, 1982.

Carlson, R. W., J. S. Kargel, S. Douté, L. A. Soderblom, and J. B. Dalton, Io's surface composition, in *Io After Galileo: A New View of Jupiter's Volcanic Moon*, edited by R. M. C. Lopes and J. R. Spencer, p. 193, Springer Praxis Books / Geophysical Sciences, 2007.

Carr, M. H., et al., Evidence for a subsurface ocean on Europa, *Nature*, *391*, 363, 1998.

Cassen, P., R. T. Reynolds, and S. J. Peale, Is there liquid water on Europa, *Geophys. Res. Lett.*, *6*, 731–734, 1979.

Cassidy, T. A., R. E. Johnson, M. A. McGrath, M. C. Wong, and J. F. Cooper, The spatial morphology of Europa's near-surface O_2 atmosphere, *Icarus*, *191*, 755–764, 2007.

Chamberlain, J. W., and D. M. Hunten, *Theory of planetary atmospheres. An introduction to their physics and chemistry.*, *International Geophysics Series*, vol. 36, Academic Press Inc., Orlando, FL, USA, 1987.

Chan, W., G. Cooper, and C. E. Brion, The electronic spectrum of water in the discrete and continuum regions. Absolute optical oscillator strengths for photoabsorption (6 200 eV), *Chemical Physics*, *178*, 387–400, 1993.

Cheng, A. F., et al., Long-Range Reconnaissance Imager on New Horizons, *Space Science Reviews*, *140*, 189–215, 2008.

Clarke, J. T., J. Ajello, J. Luhmann, N. Schneider, and I. Kanik, Hubble Space Telescope UV spectral observations of Io passing into eclipse, *J. Geophys. Res.*, *99*, 8387–8402, 1994.

Clarke, J. T., D. Grodent, S. W. H. Cowley, E. J. Bunce, P. Zarka, J. E. P. Connerney, and T. Satoh, Jupiter's aurora, in *Jupiter. The Planet, Satellites and Magnetosphere*, edited by F. Bagenal, T. E. Dowling, and W. B. McKinnon, pp. 639–670, Cambridge University Press, 2004.

Clarke, J. T., et al., Ultraviolet emissions from the magnetic footprints of Io, Ganymede and Europa on Jupiter, *Nature*, *415*, 997–1000, 2002.

Combi, M. R., K. Kabin, T. I. Gombosi, D. L. DeZeeuw, and K. G. Powell, Io's plasma environment during the Galileo flyby: Global three-dimensional MHD modeling with adaptive mesh refinement, *J. Geophys. Res.*, *103*, 9071–9082, 1998.

Connerney, J. E. P., M. H. Acuña, N. F. Ness, and T. Satoh, New models of Jupiter's magnetic field constrained by the Io flux tube footprint, *J. Geophys. Res.*, *103*, 11,929–11,940, 1998.

Delamere, P. A., and F. Bagenal, Modeling variability of plasma conditions in the Io torus, *J. Geophys. Res.*, *108*, 1276, 2003.

Dessler, A. J., *Physics of the Jovian Magnetosphere*, Cambridge Univ. Press, 1983.

Doering, J. P., Absolute differential and integral electron excitation cross sections for atomic oxygen. IX - Improved cross section for the ^{3}P-^{1}D transition from 4.0 to 30 eV, *J. Geophys. Res.*, *97*, 19,531–19,534, 1992.

Doering, J. P., and E. E. Gulcicek, Absolute differential and integral electron excitation cross sections for atomic oxygen. VII - The ^{3}P-^{1}D and ^{3}P-^{1}S transitions from 4.0 to 30 eV, *J. Geophys. Res.*, *94*, 1541–1546, 1989a.

Doering, J. P., and E. E. Gulcicek, Absolute differential and integral electron excitation cross sections for atomic oxygen. VIII - The ^{3}P-^{5}S^0 transition (1356 Å) from 13.9 to 30 eV, *J. Geophys. Res.*, *94*, 2733–2736, 1989b.

Doggett, T., R. Greeley, P. Figueredo, and K. Tanaka, Geologic Stratigraphy and Evolution of Europa's Surface, in *Europa*, edited by R. T. Pappalardo, W. B. McKinnon, and K. K. Khurana, p. 137, University of Arizona Press, 2009.

Dols, V., Io's interaction with Jupiter's magnetosphere, Ph.D. thesis, Universite de Liège, 2011.

Douté, S., B. Schmitt, R. Lopes-Gautier, R. Carlson, L. Soderblom, J. Shirley, and Galileo NIMS Team, Mapping SO_2 Frost on Io by the Modeling of NIMS Hyperspectral Images, *Icarus*, *149*, 107–132, 2001.

Eather, R. H., *Majestic lights. The aurora in science, history, and the arts.*, American Geophysical Union, 1980.

Feaga, L. M., M. A. McGrath, and P. D. Feldman, The Abundance of Atomic Sulfur in the Atmosphere of Io, *Astrophys. J.*, *570*, 439–446, 2002.

Feaga, L. M., M. A. McGrath, P. D. Feldman, and D. F. Strobel, Detection of Atomic Chlorine in Io's Atmosphere with the Hubble Space Telescope GHRS, *Astrophys. J.*, *610*, 1191–1198, 2004.

Feaga, L. M., M. McGrath, and P. D. Feldman, Io's dayside SO_2 atmosphere, *Icarus*, *201*, 570–584, 2009.

Fegley, B., and M. Y. Zolotov, Chemistry of Sodium, Potassium, and Chlorine in Volcanic Gases on Io, *Icarus*, *148*, 193–210, 2000.

Feldman, P. D., M. A. McGrath, D. F. Strobel, H. W. Moos, K. D. Retherford, and B. C. Wolven, HST/STIS Ultraviolet Imaging of Polar Aurora on Ganymede, *Astrophys. J.*, *535*, 1085–1090, 2000.

Feldman, P. D., et al., Lyman-Alpha Imaging of the SO_2 Distribution on Io, *Geophys. Res. Lett.*, *27*, 1787–1790, 2000.

Frank, L. A., and W. R. Paterson, Intense electron beams observed at Io with the Galileo spacecraft, *J. Geophys. Res.*, *104*, 28,657–28,670, 1999.

Frank, L. A., and W. R. Paterson, Passage through Io's ionospheric plasmas by the Galileo spacecraft, *J. Geophys. Res.*, *106*, 26,209–26,224, 2001.

Frank, L. A., and W. R. Paterson, Plasmas observed with the Galileo spacecraft during its flyby over Io's northern polar region, *J. Geophys. Res. (Space Physics)*, *107*, 1220–1238, 2002.

Geissler, P., A. McEwen, C. Porco, D. Strobel, J. Saur, J. Ajello, and R. West, Cassini observations of Io's visible aurorae, *Icarus*, *172*, 127–140, 2004.

Geissler, P. E., and D. B. Goldstein, Plumes and their deposits, in *Io After Galileo: A New View of Jupiter's Volcanic Moon*, pp. 163–192, Springer Praxis Books / Geophysical Sciences, 2007.

Geissler, P. E., A. S. McEwen, W. Ip, M. J. S. Belton, T. V. Johnson, W. H. Smyth, and A. P. Ingersoll, Galileo Imaging of Atmospheric Emissions from Io, *Science*, *285*, 870–874, 1999.

Geissler, P. E., et al., Evolution of Lineaments on Europa: Clues from Galileo Multispectral Imaging Observations, *Icarus*, *135*, 107–126, 1998.

Geissler, P. E., et al., Morphology and time variability of Io's visible aurora, *J. Geophys. Res.*, *106*, 26,137–26,146, 2001.

Greenberg, R., et al., Tectonic Processes on Europa: Tidal Stresses, Mechanical Response, and Visible Features, *Icarus*, *135*, 64–78, 1998.

Gulley, R. J., and S. J. Buckman, Elastic scattering of low energy electrons from sulphur dioxide, *Journal of Physics B: Atomic, Molecular and Optical Physics*, *27*(9), 1833, 1994.

Hall, D. T., D. F. Strobel, P. D. Feldman, M. A. McGrath, and H. A. Weaver, Detection of an oxygen atmosphere on Jupiter's moon Europa, *Nature*, *373*(6516), 677–679, 1995.

Hall, D. T., P. D. Feldman, M. A. McGrath, and D. F. Strobel, The far-ultraviolet oxygen airglow of Europa and Ganymede, *Astrophys. J.*, *499*(5), 475–481, 1998.

Hand, K. P., and C. F. Chyba, Empirical constraints on the salinity of the europan ocean and implications for a thin ice shell, *Icarus*, *189*, 424–438, 2007.

Hansen, C. J., D. E. Shemansky, and A. R. Hendrix, Cassini UVIS observations of Europa's oxygen atmosphere and torus, *Icarus*, *176*(2), 305–315, 2005.

Harper, G. M., and A. Brown, Electron Density and Turbulence Gradients within the Extended Atmosphere of the M Supergiant Betelgeuse (α Orionis), *Astrophys. J.*, *646*, 1179–1202, 2006.

Hendrix, A. R., C. A. Barth, and C. W. Hord, Io's patchy SO_2 atmosphere as measured by the Galileo ultraviolet spectrometer, *J. Geophys. Res.*, *104*, 11,817–11,826, 1999.

Hill, T. W., Inertial limit on corotation, *J. Geophys. Res.*, *84*, 6554–6558, 1979.

Hill, T. W., The Jovian auroral oval, *J. Geophys. Res.*, *106*, 8101–8108, 2001.

Hill, T. W., and F. C. Michel, Heavy ions from the Galilean satellites and the centrifugal distortion of the Jovian magnetosphere, *J. Geophys. Res.*, *81*, 4561–4565, 1976.

Ingersoll, A. P., Io meteorology - How atmospheric pressure is controlled locally by volcanos and surface frosts, *Icarus*, *81*, 298–313, 1989.

Jacobsen, S., Three-Dimensional Magnetohydrodynamic Simulations of Io's Non-Linear Interaction with the Jovian Magnetosphere, Ph.D. thesis, Institut für Geophysik und Meteorologie der Universität zu Köln, 2011.

Jacobsen, S., J. Saur, F. M. Neubauer, B. Bonfond, J. Gérard, and D. Grodent, Location and spatial shape of electron beams in Io's wake, *J. Geophys. Res. (Space Physics)*, *115*(A14), 4205–4214, 2010.

Jessup, K., and J. R. Spencer, Detailed Analysis of the Tvashtar Plume Spectral Behavior, in *Lunar and Planetary Institute Science Conference Abstracts*, *Lunar and Planetary Inst. Technical Report*, vol. 39, 2008.

Jessup, K. L., and J. R. Spencer, Characterizing Io's Pele, Tvashtar and Pillan plumes: Lessons learned from Hubble, *Icarus*, *218*, 378–405, 2012.

Jessup, K. L., J. R. Spencer, G. E. Ballester, R. R. Howell, F. Roesler, M. Vigel, and R. Yelle, The atmospheric signature of Io's Prometheus plume and anti-jovian hemisphere: evidence for a sublimation atmosphere, *Icarus*, *169*, 197–215, 2004.

Jessup, K. L., J. Spencer, and R. Yelle, Sulfur volcanism on Io, *Icarus*, *192*, 24–40, 2007.

Johnson, R. E., R. W. Carlson, J. F. Cooper, C. Paranicas, M. H. Moore, and M. C. Wong, Radiation effects on the surfaces of the Galilean satellites, in *Jupiter. The Planet, Satellites and Magnetosphere*, edited by F. Bagenal, T. E. Dowling, and W. B. McKinnon, pp. 485–512, Cambridge University Press, 2004.

Johnson, R. E., M. H. Burger, T. A. Cassidy, F. Leblanc, M. Marconi, and W. H. Smyth, Composition and Detection of Europa's Sputter-induced Atmosphere, in *Europa*, edited by R. T. Pappalardo, W. B. McKinnon, and K. K. Khurana, p. 507, University of Arizona Press, 2009.

Kabin, K., M. R. Combi, T. I. Gombosi, D. L. DeZeeuw, K. C. Hansen, and K. G. Powell, Io's magnetospheric interaction: an MHD model with day-night asymmetry, *Planetary and Space Science*, *49*, 337–344, 2001.

Kanik, I., C. Noren, O. P. Makarov, P. Vattipalle, J. M. Ajello, and D. E. Shemansky, Electron impact dissociative excitation of O_2: 2. Absolute emission cross sections of the OI(130.4 nm) and OI(135.6 nm) lines, *J. Geophys. Res.*, *108*, 5126, 2003.

Kattenhorn, S. A., and T. Hurford, Tectonics of Europa, in *Europa*, edited by R. T. Pappalardo, W. B. McKinnon, and K. K. Khurana, p. 199, University of Arizona Press, 2009.

Keszthelyi, L., W. L. Jaeger, E. P. Turtle, M. Milazzo, and J. Radebaugh, A post-Galileo view of Io's interior, *Icarus*, *169*, 271–286, 2004.

Keszthelyi, L., W. Jaeger, M. Milazzo, J. Radebaugh, A. G. Davies, and K. L. Mitchell, New estimates for Io eruption temperatures: Implications for the interior, *Icarus*, *192*, 491–502, 2007.

Khurana, K. K., Euler potential models of Jupiter's magnetospheric field, *J. Geophys. Res.*, *102*, 11,295–11,306, 1997.

Khurana, K. K., M. G. Kivelson, D. J. Stevenson, G. Schubert, C. T. Russell, R. J. Walker, and C. Polanskey, Induced magnetic fields as evidence for subsurface oceans in Europa and Callisto, *Nature*, *395*, 777–780, 1998.

Khurana, K. K., M. G. Kivelson, V. M. Vasyliunas, N. Krupp, J. Woch, A. Lagg, B. H. Mauk, and W. S. Kurth, The configuration of Jupiter's magnetosphere, in *Jupiter. The Planet, Satellites and Magnetosphere*, edited by Bagenal, F., Dowling, T. E., & McKinnon, W. B., pp. 593–616, Cambridge University Press, 2004.

Khurana, K. K., X. Jia, M. G. Kivelson, F. Nimmo, G. Schubert, and C. T. Russell, Evidence of a Global Magma Ocean in Io's Interior, *Science*, *332*, 1186, 2011.

Kieffer, S. W., Dynamics and thermodynamics of volcanic eruptions - Implications for the plumes on Io, in *Satellites of Jupiter*, edited by D. Morrison, pp. 647–723, 1982.

Kim, Y., Scaling of plane-wave Born cross sections for electron-impact excitation of neutral atoms, *Physical Review A*, *64*(3), 2001.

Kivelson, M. G., K. K. Khurana, R. J. Walker, J. Warnecke, C. T. Russell, J. A. Linker, D. J. Southwood, and C. Polanskey, Io's Interaction with the Plasma Torus: Galileo Magnetometer Report, *Science*, *274*, 396–398, 1996.

Kivelson, M. G., K. K. Khurana, C. T. Russell, M. Volwerk, R. J. Walker, and C. Zimmer, Galileo magnetometer measurements: A Stronger case for a subsurface ocean at Europa, *Science*, *289*, 1340–1343, 2000.

Kivelson, M. G., K. K. Khurana, C. T. Russell, S. P. Joy, M. Volwerk, R. J. Walker, C. Zimmer, and J. A. Linker, Magnetized or unmagnetized: Ambiguity persists following Galileo's encounters with Io in 1999 and 2000, *J. Geophys. Res.*, *106*, 26,121–26,136, 2001.

Kivelson, M. G., F. Bagenal, W. S. Kurth, F. M. Neubauer, C. Paranicas, and J. Saur, Magnetospheric interactions with satellites, in *Jupiter. The Planet, Satellites and Magnetosphere*, edited by Bagenal, F., Dowling, T. E., & McKinnon, W. B., chap. 21, pp. 513–536, Cambridge University Press, 2004.

Kliore, A. J., D. P. Hinson, F. M. Flasar, A. F. Nagy, and T. E. Cravens, The ionosphere of Europa from Galileo radio occultations, *Science*, *277*(5324), 355–358, 1997.

Krist, J., Simulation of HST PSFs using Tiny Tim, in *Astronomical Data Analysis Software and Systems IV, Astronomical Society of the Pacific Conference Series*, vol. 77, edited by R. A. Shaw, H. E. Payne, & J. J. E. Hayes, p. 349, 1995.

Krist, J. E., R. N. Hook, and F. Stoehr, 20 years of Hubble Space Telescope optical modeling using Tiny Tim, in *Society of Photo-Optical Instrumentation Engineers (SPIE) Conference Series*, vol. 8127, 2011.

Leblanc, F., A. E. Potter, R. M. Killen, and R. E. Johnson, Origins of Europa Na cloud and torus, *Icarus*, *178*, 367–385, 2005.

Lellouch, E., M. Belton, I. de Pater, G. Paubert, S. Gulkis, and T. Encrenaz, The structure, stability, and global distribution of Io's atmosphere, *Icarus*, *98*, 271–295, 1992.

Lellouch, E., D. F. Strobel, M. J. S. Belton, M. E. Summers, G. Paubert, and R. Moreno, Detection of Sulfur Monoxide in Io's Atmosphere, *Astrophys. J.*, *459*, L107–L110, 1996.

Lellouch, E., M. A. McGrath, and K. L. Jessup, Io's atmosphere, in *Io After Galileo: A New View of Jupiter's Volcanic Moon*, pp. 231–264, Springer Praxis Books / Geophysical Sciences, 2007.

Linker, J. A., M. G. Kivelson, and R. J. Walker, An MHD simulation of plasma flow past Io - Alfven and slow mode perturbations, *Geophys. Res. Lett.*, *15*, 1311–1314, 1988.

Linker, J. A., M. G. Kivelson, and R. J. Walker, The effect of mass loading on the temperature of a flowing plasma, *Geophys. Res. Lett.*, *16*, 763–766, 1989.

Linker, J. A., M. G. Kivelson, and R. J. Walker, A three-dimensional MHD simulation of plasma flow past Io, *J. Geophys. Res.*, *96*, 21,037, 1991.

Linker, J. A., K. K. Khurana, M. G. Kivelson, and R. J. Walker, MHD simulations of Io's interaction with the plasma torus, *J. Geophys. Res.*, *103*, 19,867–19,878, 1998.

Lipatov, A. S., and M. R. Combi, Effects of kinetic processes in shaping Io's global plasma environment: A 3D hybrid model, *Icarus*, *180*, 412–427, 2006.

Lopes-Gautier, R., et al., Active Volcanism on Io: Global Distribution and Variations in Activity, *Icarus*, *140*, 243–264, 1999.

Makarov, O. P., J. M. Ajello, P. Vattipalle, I. Kanik, M. C. Festou, and A. Bhardwaj, Kinetic energy distributions and line profile measurements of dissociation products of water upon electron impact, *J. Geophys. Res.*, *109*(A18), A09303, 2004.

Manatt, S. L., and A. L. Lane, A compilation of the absorption cross-sections of SO_2 from 106 to 403 nm., *J. Quant. Spectrosc. Radiat. Transfer*, *50*, 267–276, 1993.

Marchis, F., R. Prangé, and T. Fusco, A survey of Io's vocanism by adaptive optics observations in the 3.8-μm thermal band (1996-1999), *J. Geophys. Res.*, *106*, 33,141–33,160, 2001.

Marchis, F., I. de Pater, A. G. Davies, H. G. Roe, T. Fusco, D. Le Mignant, P. Descamps, B. A. Macintosh, and R. Prangé, High-Resolution Keck Adaptive Optics Imaging of Violent Volcanic Activity on Io, *Icarus*, *160*, 124–131, 2002.

Marchis, F., et al., Keck AO survey of Io global volcanic activity between 2 and 5 μm, *Icarus*, *176*, 96–122, 2005.

Marquardt, D. W., An algorithm for least-squares estimation of nonlinear parameters, *SIAM Journal on Applied Mathematics*, *11*(2), 431–441, 1963.

Mauk, B. H., D. G. Mitchell, S. M. Krimigis, E. C. Roelof, and C. P. Paranicas, Energetic neutral atoms from a trans-Europa gas torus at Jupiter, *Nature*, *421*, 920–922, 2003.

McCord, T. B., et al., Salts on Europa's Surface Detected by Galileo's Near Infrared Mapping Spectrometer, *Science*, *280*, 1242, 1998.

McEwen, A. S., and L. A. Soderblom, Two classes of volcanic plumes on Io, *Icarus*, *55*, 191–217, 1983.

McEwen, A. S., et al., Active Volcanism on Io as Seen by Galileo SSI, *Icarus*, *135*, 181–219, 1998.

McGrath, M. A., M. J. S. Belton, J. R. Spencer, and P. Sartoretti, Spatially Resolved Spectroscopy of Io's Pele Plume and SO_2 Atmosphere, *Icarus*, *146*, 476–493, 2000.

McGrath, M. A., E. Lellouch, D. F. Strobel, P. D. Feldman, and R. E. Johnson, Satellite atmospheres, in *Jupiter. The Planet, Satellites and Magnetosphere*, edited by Bagenal, F., Dowling, T. E., & McKinnon, W. B., pp. 457–483, Cambridge University Press, 2004.

McGrath, M. A., C. J. Hansen, and A. R. Hendrix, Observations of Europa's Tenuous Atmosphere, in *Europa*, edited by R. T. Pappalardo, W. B. McKinnon, and K. K. Khurana, p. 485, University of Arizona Press, 2009.

Meier, R. R., Ultraviolet spectroscopy and remote sensing of the upper atmosphere, *Space Sci. Rev.*, *58*, 1–185, 1991.

Meyer-Vernet, N., M. Moncuquet, and S. Hoang, Temperature inversion in the Io plasma torus., *Icarus*, *116*, 202–213, 1995.

Michael, M., and A. Bhardwaj, FUV emissions on Io: Role of Galileo-observed field-aligned energetic electrons, *Geophys. Res. Lett.*, *27*, 3137–3140, 2000.

Moore, C., K. Miki, D. B. Goldstein, K. Stapelfeldt, P. L. Varghese, L. M. Trafton, and R. W. Evans, Monte Carlo modeling of Io's [OI] 6300 Å and [SII] 6716 Å auroral emission in eclipse, *Icarus*, *207*, 810–833, 2010.

Moore, C. H., D. B. Goldstein, P. L. Varghese, L. M. Trafton, and B. Stewart, 1-D DSMC simulation of Io's atmospheric collapse and reformation during and after eclipse, *Icarus*, *201*, 585–597, 2009.

Moore, W. B., G. Schubert, J. D. Anderson, and J. R. Spencer, The interior of Io, in *Io After Galileo: A New View of Jupiter's Volcanic Moon*, edited by R. M. C. Lopes and J. R. Spencer, p. 89, Springer Praxis Books / Geophysical Sciences, 2007.

Morabito, L. A., S. P. Synnott, P. N. Kupferman, and S. A. Collins, Discovery of currently active extraterrestrial volcanism, *Science*, *204*, 972, 1979.

Morton, D. C., Atomic data for resonance absorption lines. I - Wavelengths longward of the Lyman limit, *Astrophys. J. Suppl.*, *77*, 119–202, 1991.

Moses, J. I., M. Y. Zolotov, and B. Fegley, Alkali and Chlorine Photochemistry in a Volcanically Driven Atmosphere on Io, *Icarus*, *156*, 107–135, 2002.

Moullet, A., E. Lellouch, R. Moreno, M. A. Gurwell, and C. Moore, First disk-resolved millimeter observations of Io's surface and SO_2 atmosphere, *Astron. & Astrophys.*, *482*, 279–292, 2008.

Moullet, A., M. A. Gurwell, E. Lellouch, and R. Moreno, Simultaneous mapping of SO_2, SO, NaCl in Io's atmosphere with the Submillimeter Array, *Icarus*, *208*(1), 353–365, 2010.

Nelder, J. A., and R. Mead, A simplex method for function minimization, *"The Computer Journal"*, *7*, 308–313, 1965.

Nelson, R. M., A. L. Lane, D. L. Matson, G. J. Veeder, B. J. Buratti, and E. F. Tedesco, Spectral geometric albedos of the Galilean satellites from 0.24 to 0.34 micrometers - Observations with the International Ultraviolet Explorer, *Icarus*, *72*, 358–380, 1987.

Nelson, R. M., A. L. Lane, M. E. Morrill, B. D. Wallis, J. Gibson, W. D. Smythe, L. J. Horn, and B. J. Buratti, The brightness of Jupiter's satellite Io following emergence from eclipse - Selected observations, 1981-1989, *Icarus*, *101*, 223–233, 1993.

Neubauer, F. M., Nonlinear standing Alfven wave current system at Io - Theory, *J. Geophys. Res.*, *85*, 1171–1178, 1980.

Neubauer, F. M., The sub-Alfvénic interaction of the Galilean satellites with the Jovian magnetosphere, *J. Geophys. Res.*, *103*(E9), 19,843–19,866, 1998.

Neubauer, F. M., Alfvén wings and electromagnetic induction in the interiors: Europa and callisto, *J. Geophys. Res.*, *104*, 28,671–28,684, 1999.

Nimmo, F., and E. Gaidos, Strike-slip motion and double ridge formation on Europa, *J. Geophys. Res. (Planets)*, *107*, 5021, 2002.

Nimmo, F., J. R. Spencer, R. T. Pappalardo, and M. E. Mullen, Shear heating as the origin of the plumes and heat flux on Enceladus, *Nature*, *447*, 289–291, 2007.

Noll, K. S., H. A. Weaver, and A. M. Gonnella, The albedo spectrum of Europa from 2200 Å to 3300 Å, *J. Geophys. Res.*, *100*, 19,057–19,060, 1995.

Oliversen, R. J., F. Scherb, W. H. Smyth, M. E. Freed, R. C. J. Woodward, M. L. Marconi, K. D. Retherford, O. L. Lupie, and J. P. Morgenthaler, Sunlit Io atmospheric [OI] 6300 Å emission and the plasma torus, *J. Geophys. Res.*, *106*, 26,183–26,194, 2001.

Pappalardo, R. T., W. B. McKinnon, and K. K. Khurana, *Europa*, University of Arizona Press, 2009.

Pappalardo, R. T., et al., Geological evidence for solid-state convection in Europa's ice shell, *Nature*, *391*, 365, 1998.

Parkinson, W., *Introduction to geomagnetism*, Elsevier, 1983.

Peale, S. J., P. Cassen, and R. T. Reynolds, Melting of Io by tidal dissipation, *Science*, *203*, 892–894, 1979.

Pearl, J., R. Hanel, V. Kunde, W. Maguire, K. Fox, S. Gupta, C. Ponnamperuma, and F. Raulin, Identification of gaseous SO_2 and new upper limits for other gases on Io, *Nature*, *280*, 755–758, 1979.

Plainaki, C., A. Milillo, A. Mura, S. Orsini, S. Massetti, and T. Cassidy, The role of sputtering and radiolysis in the generation of Europa exosphere, *Icarus*, *218*, 956–966, 2012.

Porco, C. C., et al., Cassini Observes the Active South Pole of Enceladus, *Science*, *311*, 1393–1401, 2006.

Pospieszalska, M. K., and R. E. Johnson, Magnetospheric ion bombardment profiles of satellites: Europa and Dione, *Icarus*, *78*, 1–13, 1989.

Press, W. H., S. A. Teukolsky, W. T. Vetterling, and B. P. Flannery, *Numerical Recipes. The Art of Scientific Computing (3rd ed.)*, Cambridge Univ. Press, 2007.

Radebaugh, J., L. P. Keszthelyi, A. S. McEwen, E. P. Turtle, W. Jaeger, and M. Milazzo, Paterae on Io: A new type of volcanic caldera?, *J. Geophys. Res.*, *106*, 33,005–33,020, 2001.

Retherford, K. D., Io's aurora: HST/STIS observations, Ph.D. thesis, Johns Hopkins University, Baltimore, MD., 2002.

Retherford, K. D., H. W. Moos, D. F. Strobel, B. C. Wolven, and F. L. Roesler, Io's equatorial spots: Morphology of neutral UV emissions, *J. Geophys. Res.*, *105*, 27,157–27,166, 2000.

Retherford, K. D., H. W. Moos, and D. F. Strobel, Io's auroral limb glow: Hubble Space Telescope FUV observations, *J. Geophys. Res. (Space Physics)*, *108*, 1333–1341, 2003.

Retherford, K. D., et al., Io's Atmospheric Response to Eclipse: UV Aurorae Observations, *Science*, *318*, 237–240, 2007a.

Retherford, K. D., et al., Icy Galilean Satellite UV Observations by New Horizons and HST, *AGU Fall Meeting Abstracts*, p. C6, 2007b.

Roesler, F. L., et al., Far-ultraviolet imaging spectroscopy of Io's atmosphere with HST/STIS, *Science*, *283*(5400), 353–357, 1999.

Roth, L., J. Saur, K. D. Retherford, D. F. Strobel, and J. R. Spencer, Simulation of Io's auroral emission: Constraints on the atmosphere in eclipse, *Icarus*, *214*, 495–509, 2011.

Samir, U., J. K. H. Wright, and N. H. Stone, The expansion of a plasma into a vacuum: basic phenomena and processes and applications to space plasma physics., *Reviews of Geophysics and Space Physics*, *21*, 1631–1646, 1983.

Sartoretti, P., M. A. McGrath, A. S. McEwen, and J. R. Spencer, Post-Voyager brightness variations on Io, *J. Geophys. Res.*, *100*, 7523–7530, 1995.

Sartoretti, P., M. J. S. Belton, and M. A. McGrath, SO_2 Distributions on Io, *Icarus*, *122*, 273–287, 1996.

Saur, J., and D. F. Strobel, Relative contributions of sublimation and volcanoes to Io's atmosphere inferred from its plasma interaction during solar eclipse, *Icarus*, *171*, 411–420, 2004.

Saur, J., D. F. Strobel, and F. M. Neubauer, Interaction of the Jovian magnetosphere with Europa: Constraints on the neutral atmosphere, *J. Geophys. Res.*, *103*(E9), 19,947–19,962, 1998.

Saur, J., F. M. Neubauer, D. F. Strobel, and M. E. Summers, Three-dimensional plasma simulation of Io's interaction with the Io plasma torus: Asymmetric plasma flow, *J. Geophys. Res.*, *104*, 25,105–25,126, 1999.

Saur, J., F. M. Neubauer, D. F. Strobel, and M. E. Summers, Io's ultraviolet aurora: Remote sensing of Io's interaction, *Geophys. Res. Lett.*, *27*, 2893–2896, 2000.

Saur, J., F. M. Neubauer, D. F. Strobel, and M. E. Summers, Interpretation of Galileo's Io plasma and field observations: I0, I24, and I27 flybys and close polar passes, *J. Geophys. Res. (Space Physics)*, *107*, 1422–1439, 2002.

Saur, J., D. F. Strobel, F. M. Neubauer, and M. E. Summers, The ion mass loading rate at Io, *Icarus*, *163*, 456–468, 2003.

Saur, J., F. M. Neubauer, J. E. P. Connerney, P. Zarka, and M. G. Kivelson, Plasma interaction of Io with its plasma torus, in *Jupiter. The Planet, Satellites and Magnetosphere*, edited by Bagenal, F., Dowling, T. E., & McKinnon, W. B., pp. 537–560, Cambridge University Press, 2004.

Saur, J., F. M. Neubauer, and K.-H. Glassmeier, Induced Magnetic Fields in Solar System Bodies, *Space Science Reviews*, *152*, 391–421, 2010.

Saur, J., et al., Hubble Space Telescope/Advanced Camera for Surveys Observations of Europa's Atmospheric Ultraviolet Emission at Eastern Elongation, *Astrophys. J.*, *738*, 153, 2011.

Schenk, P., H. Hargitai, R. Wilson, A. McEwen, and P. Thomas, The mountains of Io: Global and geological perspectives from Voyager and Galileo, *J. Geophys. Res.*, *106*, 33,201–33,222, 2001.

Schilling, N., F. M. Neubauer, and J. Saur, Time-varying interaction of Europa with the jovian magnetosphere: Constraints on the conductivity of Europa's subsurface ocean, *Icarus*, *192*, 41–55, 2007.

Schilling, N., F. M. Neubauer, and J. Saur, Influence of the internally induced magnetic field on the plasma interaction of Europa, *J. Geophys. Res.(Space Physics)*, *113*, 2008.

Schubert, G., J. D. Anderson, T. Spohn, and W. B. McKinnon, Interior composition, structure and dynamics of the Galilean satellites, in *Jupiter. The Planet, Satellites and Magnetosphere*, edited by F. Bagenal, T. E. Dowling, and W. B. McKinnon, pp. 281–306, Cambridge University Press, 2004.

Seidelmann, P. K., and N. Divine, Evaluation of Jupiter longitudes in System III (1965), *Geophys. Res. Lett.*, *4*, 65–68, 1977.

Seufert, M., J. Saur, and F. M. Neubauer, Multi-frequency electromagnetic sounding of the Galilean moons, *Icarus*, *214*, 477–494, 2011.

Shematovich, V. I., and R. E. Johnson, Near-surface oxygen atmosphere at Europa, *Advances in Space Research*, *27*, 1881–1888, 2001.

Shematovich, V. I., R. E. Johnson, J. F. Cooper, and M. C. Wong, Surface-bounded atmosphere of Europa, *Icarus*, *173*, 480–498, 2005.

Sittler, E. C., and D. F. Strobel, Io plasma torus electrons - Voyager 1, *J. Geophys. Res.*, *92*, 5741–5762, 1987.

Smyth, W. H., and M. L. Marconi, Europa's atmosphere, gas tori, and magnetospheric implications, *Icarus*, *181*, 510–526, 2006.

Smyth, W. H., C. A. Peterson, and M. L. Marconi, A consistent understanding of the ribbon structure for the Io plasma torus at the Voyager 1, 1991 ground-based, and Galileo J0 epochs, *J. Geophys. Res.*, *116*, A07205, 2011.

Sohl, F., T. Spohn, D. Breuer, and K. Nagel, Implications from Galileo Observations on the Interior Structure and Chemistry of the Galilean Satellites, *Icarus*, *157*, 104–119, 2002.

Sparks, W. B., et al., Hubble Space Telescope observations of Europa in and out of eclipse, *International Journal of Astrobiology*, *9*, 265–271, 2010.

Spencer, J. R., K. L. Jessup, M. A. McGrath, G. E. Ballester, and R. Yelle, Discovery of Gaseous S_2 in Io's Pele Plume, *Science*, *288*, 1208–1210, 2000a.

Spencer, J. R., J. A. Rathbun, L. D. Travis, L. K. Tamppari, L. Barnard, T. Z. Martin, and A. S. McEwen, Io's Thermal Emission from the Galileo Photopolarimeter- Radiometer, *Science*, *288*, 1198–1201, 2000b.

Spencer, J. R., E. Lellouch, M. J. Richter, M. A. López-Valverde, K. L. Jessup, T. K. Greathouse, and J. Flaud, Mid-infrared detection of large longitudinal asymmetries in Io's SO_2 atmosphere, *Icarus*, *176*, 283–304, 2005.

Spencer, J. R., K. L. Jessup, C. C. C. Tsang, N. Cunningham, and K. Retherford, Evidence for Volcanic Support of Io's Jupiter-Facing Atmosphere from Constraints on Post-Eclipse Atmospheric Changes, in *Lunar and Planetary Institute Science Conference Abstracts*, vol. 43, p. 2420, 2012.

Spencer, J. R., et al., Io Volcanism Seen by New Horizons: A Major Eruption of the Tvashtar Volcano, *Science*, *318*, 240–243, 2007a.

Spencer, J. R., et al., New Horizons Observes Io's Volcanic Activity, in *Bulletin of the American Astronomical Society*, vol. 38, 2007b.

Spohn, T., and G. Schubert, Oceans in the icy Galilean satellites of Jupiter?, *Icarus*, *161*, 456–467, 2003.

Strobel, D. F., and B. C. Wolven, The Atmosphere of Io: Abundances and Sources of Sulfur Dioxide and Atomic Hydrogen, *Astrophys. Space Sci.*, *277*, 271–287, 2001.

Strobel, D. F., X. Zhu, and M. F. Summers, On the vertical thermal structure of Io's atmosphere, *Icarus*, *111*, 18–30, 1994.

STScI, *STIS Data Handbook*, Space Telescope Science Institute, 2007.

STScI, *Space Telescope Imaging Spectrograph Instrument Handbook*, Space Telescope Science Institute, 2011.

Summers, M. E., and D. F. Strobel, Photochemistry and Vertical Transport in Io's Atmosphere and Ionosphere, *Icarus*, *120*, 290–316, 1996.

Tayal, S. S., Oscillator Strengths of Allowed and Intercombination Transitions in Neutral Sulfur, *Astrophys. J.*, *497*, 493, 1998.

Tennyson, J., *Astronomical spectroscopy : an introduction to the atomic and molecular physics of astronomical spectra*, Imperial College Press, 2005.

Trafton, L., Detection of a potassium cloud near Io, *Nature*, *258*, 690–692, 1975.

Trafton, L. M., C. H. Moore, D. B. Goldstein, P. L. Varghese, and M. A. McGrath, HST/STIS observations and simulation of Io's emission spectrum in Jupiter shadow: Probing Io's Jupiter-facing eclipse atmosphere, *Icarus*, *220*, 1121–1140, 2012.

Trauger, J. T., K. R. Stapelfeldt, G. E. Ballester, J. T. Clarke, and WFPC2 Science Team, HST Observations of [O I] Emissions from Io in Eclipse, in *AAS/Division for Planetary Sciences Meeting Abstracts #29*, *Bulletin of the American Astronomical Society*, vol. 29, p. 1002, 1997.

Tsang, C. C. C., J. R. Spencer, E. Lellouch, M. A. López-Valverde, M. J. Richter, and T. K. Greathouse, Io's atmosphere: Constraints on sublimation support from density variations on seasonal timescales using NASA IRTF/TEXES observations from 2001 to 2010, *Icarus*, *217*, 277–296, 2012.

Turtle, E. P., et al., Mountains on Io: High-resolution Galileo observations, initial interpretations, and formation models, *J. Geophys. Res.*, *106*, 33,175–33,200, 2001.

Vatti Palle, P., J. Ajello, and A. Bhardwaj, High-resolution far ultraviolet spectrum of electron-excited SO_2, *J. Geophys. Res.*, *109*, A02310, 2004.

Walker, A. C., S. L. Gratiy, D. B. Goldstein, C. H. Moore, P. L. Varghese, L. M. Trafton, D. A. Levin, and B. Stewart, A comprehensive numerical simulation of Io's sublimation-driven atmosphere, *Icarus*, *207*, 409–432, 2010.

Walker, A. C., C. H. Moore, D. B. Goldstein, P. L. Varghese, and L. M. Trafton, A parametric study of Io's thermophysical surface properties and subsequent numerical atmospheric simulations based on the best fit parameters, *Icarus*, *220*, 225–253, 2012.

Weiss, J. W., Appendix 2: Planetary parameters, in *Jupiter. The Planet, Satellites and Magnetosphere*, edited by F. Bagenal, T. E. Dowling, and W. B. McKinnon, pp. 699–706, Cambridge University Press, 2004.

Williams, D. A., and R. R. Howell, Active volcanism: Effusive eruptions, in *Io After Galileo: A New View of Jupiter's Volcanic Moon*, edited by R. M. C. Lopes and J. R. Spencer, p. 133, Springer Praxis Books / Geophysical Sciences, 2007.

Williams, D. A., L. P. Keszthelyi, D. A. Crown, J. A. Yff, W. L. Jaeger, P. M. Schenk, P. E. Geissler, and T. L. Becker, Volcanism on Io: New insights from global geologic mapping, *Icarus*, *214*, 91–112, 2011.

Williams, D. J., and R. M. Thorne, Energetic particles over Io's polar caps, *J. Geophys. Res. (Space Physics)*, *108*, 1397–1403, 2003.

Williams, D. J., R. M. Thorne, and B. Mauk, Energetic electron beams and trapped electrons at Io, *J. Geophys. Res.*, *104*, 14,739–14,754, 1999.

Williams, D. J., et al., Electron Beams and lon Composition Measured at lo and in Its Torus, *Science*, *274*, 401–403, 1996.

Wolf-Gladrow, D. A., F. M. Neubauer, and M. Lussem, Io's interaction with the plasma torus - A self-consistent model, *J. Geophys. Res.*, *92*, 9949–9961, 1987.

Wolven, B. C., H. W. Moos, K. D. Retherford, P. D. Feldman, D. F. Strobel, W. H. Smyth, and F. L. Roesler, Emission profiles of neutral oxygen and sulfur in Io's exospheric corona, *J. Geophys. Res.*, *106*, 26,155–26,182, 2001.

Wong, M. C., and W. H. Smyth, Model Calculations for Io's Atmosphere at Eastern and Western Elongations, *Icarus*, *146*, 60–74, 2000.

Woods, T. N., et al., Validation of the UARS solar ultraviolet irradiances: Comparison with the ATLAS 1 and 2 measurements, *J. Geophys. Res.*, *101*, 9541–9570, 1996.

Woodward, R. C., F. L. Roesler, R. J. Oliversen, W. H. Smyth, H. W. Moos, and F. Bagenal, The Structure and Variability of Extended S II 1256Å Emission Near Io, *AGU Spring Meeting Abstracts*, p. 41, 2001.

Zatsarinny, O., and S. S. Tayal, Electron impact collision strengths and rates for neutral sulphur using the B-spline R-matrix approach, *Journal of Physics B Atomic Molecular Physics*, *35*, 2493–2503, 2002.

Zhang, J., D. B. Goldstein, P. L. Varghese, N. E. Gimelshein, S. F. Gimelshein, and D. A. Levin, Simulation of gas dynamics and radiation in volcanic plumes on Io, *Icarus*, *163*, 182–197, 2003.

Zimmer, C., K. K. Khurana, and M. G. Kivelson, Subsurface Oceans on Europa and Callisto: Constraints from Galileo Magnetometer Observations, *Icarus*, *147*, 329–347, 2000.

Danksagung

Ich möchte mich ganz besonders bei Professor Joachim Saur, dem Betreuer meiner Arbeit, bedanken. Zum einen hat er mir in den letzten knapp vier Jahren der Doktorarbeit stetig beigebracht, wie man sorgfältig wissenschaftlich arbeitet. Seine Erfahrung sowie seine Art Probleme zu erfassen und klar darzustellen haben in vielen Momenten sehr geholfen. Zum anderen hat er aber auch meine eigenen Ideen und Wünsche unterstützt. Ganz speziell möchte ich dabei meinen Aufenthalt an der Johns Hopkins University in Baltimore erwähnen, der nur durch seine Unterstützung und Mithilfe in der Art möglich wurde. Das halte ich nicht für selbstverständlich und möchte ganz ausdrücklich meinen Dank aussprechen.

With this in mind, my deep gratitude goes to Professor Darrell Strobel and Professor Paul Feldman for their warm hospitality and the inspiring collaboration. By sharing their extensive experience, they contributed significantly to the success of this thesis. And, I enjoyed my stay in Baltimore a lot. Thank you very much!

I would also like to thank Kurt Retherford for a very fruitful collaboration over the last years, which I am very happy to continue.

Professor Bülent Tezkan danke ich für die Übernahme des Koreferats. Das Interesse an meiner Arbeit freut mich sehr.

Ganz speziell danken möchte ich auch den Korrekturlesern dieser Arbeit, Anne Schreiner, Fabrizio Musacchio, Michael von Papen, Emmanuel Chané und Stefan Duling. Sie alle haben sehr zum Gelingen der Arbeit beigetragen.

Außerdem bedanke ich mich herzlich bei den Leuten, die mit mir das Büro geteilt haben. Besonders hervorheben möchte ich dabei Mario Seufert, der mich vom ersten bis zum letzten Tag hier am Institut ertragen und quasi alles mit mir durchgemacht hat. Aber auch Sven Jacobsen und Rudi Eröss sei herzlich gedankt für die vielen lustigen Momente hier im Büro. Ich hatte immer das Gefühl, Glück zu haben mit meinen Zimmernachbarn.

Sven Simon möchte ich für seine freundliche, selbstlose Bereitschaft sein großes Wissen mit anderen zu teilen herzlich danken.

Letztenendes verdanke ich das Gelingen dieser Doktorarbeit meiner Freundin Annika. Sie hat mich in meiner Arbeit die ganze Zeit über unterstützt, mir über schwierige Momente hinweggeholfen und mir in den letzten Wochen alles abgenommen, damit das Ganze auch ein Ende findet. Meinem kleinen Sohn Kaspar bin ich endlos dankbar dafür, dass er mir mit seiner lustigen und lieben Art täglich wieder zeigt, dass es viel schönere Dinge im Leben gibt als die Wissenschaft.

Versicherung

Ich versichere, dass ich die von mir vorgelegte Dissertation selbständig angefertigt, die benutzten Quellen und Hilfsmittel vollständig angegeben und die Stellen der Arbeit - einschließlich Tabellen, Karten und Abbildungen -, die anderen Werken im Wortlaut oder dem Sinn nach entnommen sind, in jedem Einzelfall als Entlehnung kenntlich gemacht habe; dass diese Dissertation noch keiner anderen Fakultät oder Universität zur Prüfung vorgelegen hat; dass sie - abgesehen von unten angegebenen Teilpublikationen - noch nicht veröffentlicht worden ist sowie, dass ich eine solche Veröffentlichung vor Abschluss des Promotionsverfahrens nicht vornehmen werde. Die Bestimmungen der Promotionsordnung sind mir bekannt. Die von mir vorgelegte Dissertation ist von Professor Joachim Saur betreut worden.

Köln, August 2012

Teilpublikation

Roth, L., J. Saur, K. D. Retherford, D. F. Strobel, and J. R. Spencer, Simulation of Io's auroral emission: Constraints on the atmosphere in eclipse, *Icarus*, *214*, 495–509, 2011.